Conceptual Aspects of Structure–Property Correlations and Electronic Instabilities, with Applications to Low-Dimensional Transition-Metal Oxides

ENRIC CANADELL*

Laboratoire de Chimie Théorique, Université de Paris-Sud, 91405 Orsay, France

MYUNG-HWAN WHANGBO*

Department of Chemistry, North Carolina State University, Raleigh, North Carolina 27695-8204

Received November 29, 1990 (Revised Manuscript Received March 14, 1991)

Contents

0009-2665/91/0791-0965$09.50/0

Enric Canadell was born in Catalonia, Spain and was educated at Universitat de Barcelona. He pursued his graduate work at Universidad Autonoma de Madrid, where he received his Ph.D. degree in 1976. After post-doctoral work with Lionel Salem at Université de Paris-Sud, Orsay, France, he returned to Catalonia as an Associate Professor at the Chemistry Faculty of Tarragona. In 1983 he spent a year at the University of Chicago with J. K. Burdett. Since 1984 he has been with the CNRS working at Université de Paris-Sud where he is now Directeur de Recherche. He is currently interested in understanding the relationship between the crystal structure and physical properties of solids.

M.-H. Whangbo, born in Korea, studied at Seoul National University. He received his Ph.D. degree in 1974 from Queen's University, Canada. After post-doctoral work at Cornell University, he joined the faculty at North Carolina State University in 1978, where he is Professor of Chemistry. His primary research interests lie in understanding the structural and electronic properties of solid state materials on the basis of electronic structure calculations.

1. Introduction

Binary and ternary molybdenum oxides have become a subject of numerous experimental and theoretical studies due largely to the fact that most of them are low-dimensional metals and consequently exhibit interesting physical properties associated with their electronic instabilities.[1] Red bronzes $A_{0.33}MoO_3$ (A = Li, K, Rb, Cs, Tl) are semiconductors, while the blue bronzes $A_{0.3}MoO_3$ (A = K, Rb, Tl), the purple bronzes $A_{0.9}Mo_6O_{17}$ (A = Li, Na, K) and $TlMo_6O_{17}$, the Magnéli phases Mo_4O_{11} and Mo_8O_{23}, and the rare-earth bronze $La_2Mo_2O_7$ are all metals at room temperature. All these oxides contain molybdenum–oxygen (Mo–O) layers made up of edge- and corner-sharing MoO_6 octahedra, with large and structurally complex unit cells.[2] A series of tungsten oxides,[3] i.e., monophosphate and diphosphate tungsten bronzes, possess crystal and electronic properties quite similar to those of the molybdenum oxides. In understanding the physical properties of such complex molybdenum and tungsten oxide systems, it is necessary to have a few guidelines by which to single out the parts of their crystal structures and chemical bonding essential for the description of their electronic properties.[4]

Solid-state materials are classified according to how their electrical resistivities ρ vary as a function of temperature T. Metals and semiconductors have positive and negative slopes in their ρ vs T plots as shown in 1.1 and 1.2, respectively. For certain compounds, their metallic states are stable only in a certain region of temperature. Thus a metal may become a semiconductor (1.3) or a superconductor (1.4) when the temperature is lowered. In understanding such phase

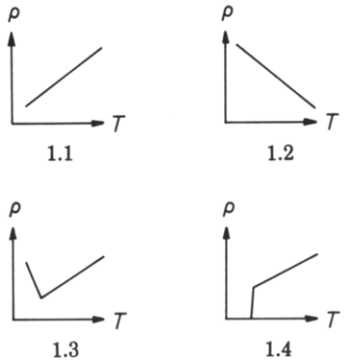

transitions of solid-state materials, it is crucial to know their electronic structures. The electronic structure of a molecule is characterized by discrete energy levels (1.5), and that of a solid by energy bands (1.6). Each

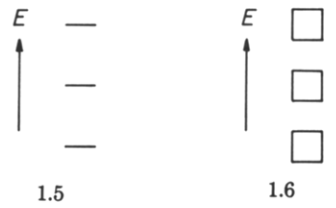

rectangular box of 1.6 represents a continuously allowed region of energy (i.e., an energy band). As illustrated in 1.7, any given energy band consists of N discrete levels, where N is the total number of unit cells in a solid. Because $N \rightarrow \infty$, all energy levels falling within a band are allowed. In a one-electron band picture, electron–electron repulsion is neglected so that each band level can be filled with two electrons. Therefore, a semiconductor (or insulator) contains only completely filled and completely empty bands (1.8), so an energy gap (i.e., band gap E_g) exists between the highest occupied and the lowest unoccupied band levels. (An insulator is a semiconductor with a large band gap, and a metal–semiconductor transition 1.3 is commonly referred to as a metal–insulator transition.) A metal has at least one partially filled band (1.9), so there is no energy gap between the highest occupied level (i.e., the Fermi level e_f) and the lowest unoccupied level. Thus

in understanding the electrical properties of solids, it is necessary to know how their electronic band structures are determined.

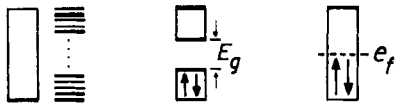

1.7 1.8 1.9

Low-dimensional metals often possess electronic instabilities toward a metal–insulator transition (see 1.3), which occur when the Fermi surfaces of their partially filled bands are nested.[4,5] For most molybdenum and tungsten oxides examined in the present review, the average d-electron count on transition metal is less than d^1. This means that, in those oxides with several nonequivalent transition-metal atoms per unit cell, only a limited number of transition-metal atoms can have d electrons and consequently become responsible for their metallic properties. In discussing the structural and electronic properties of the molybdenum and tungsten oxides, therefore, one needs to analyze[4] how the transition-metal atoms possessing d electrons can be identified on the basis of their crystal structures, which d orbitals of such transition-metal atoms contribute to form the highest-occupied bands, what kinds of dispersion relations and Fermi surfaces those bands have, and how the Fermi surfaces are related to their electronic instabilities. In the present review, we discuss theoretical, conceptual and practical aspects of those questions and show that the electronic properties of such low-dimensional molybdenum and tungsten oxides can be readily understood by analyzing how the nature of their highest occupied bands is related to the crystal structures.

The electronic structures of the low-dimensional transition-metal oxides discussed in the present review are all obtained on the basis of extended Hückel[6] tight binding (EHTB) band calculations.[7] With this semiempirical method, total energy differences are approximated by orbital energy differences, so that this method does not allow reliable geometry optimization but describes low-lying excitations of metallic states reasonably well. In addition, the nature of the partially filled bands of the transition-metal oxides reponsible for their metallic properties does not strongly depend upon the atomic parameters used in the EHTB calculations, as will be shown in some detail in terms of orbital interaction analyses. Consequently, for the transition-metal oxides with known crystal structures, EHTB calculations have been invaluable in studying the properties of their metallic states.[4]

The present review is organized as follows: Theoretical developments necessary for our discussion of the low-dimensional transition-metal oxides are given in Chapters 2–7. Fundamental concepts of electronic and vibrational energy bands are discussed in Chapters 2 and 3, respectively, on the basis of one-dimensional examples. Chapter 4 discusses how to deal with the electronic structures of two- and three-dimensional crystal systems. Fermi surfaces and electronic instabilities associated with partially filled bands are examined in Chapters 5 and 6, respectively. Chapter 7 describes various computational aspects of electronic band structure calculations. After a brief survey of typical structural patterns of the low-dimensional transition-metal oxides in Chapter 8, we examine their electronic properties in Chapters 9–16. Important findings of this review are summarized in Chapter 17.

2. Electronic Band Structure

In the present section, we discuss how the electronic band structures of solids come about by considering one-dimensional (1D) systems as examples. Though based upon 1D systems, theoretical concepts introduced in this section are readily applicable to two-dimensional (2D) or three-dimensional (3D) systems, as will be shown in later sections.

2.1 Formation of Energy Band

Let us consider a 1D lattice 2.1 with repeat distance a, where each unit cell (represented by a dot) contains a set of atomic orbitals (AO's) $\{\chi_1, \chi_2, ..., \chi_M\}$. An AO

2.1

χ_μ ($\mu = 1, 2, ..., M$) located at the n-th unit cell is written as $\chi_\mu(r - na)$. To determine the electronic energy bands arising from such AO's, one defines the Bloch orbital (BO) ϕ_μ for each AO χ_μ as follows:

$$\phi_\mu(k) = N^{-1/2}\sum_n \exp(ikna)\chi_\mu(r - na) \qquad (2.1)$$

where N refers to the number of unit cells in a crystalline solid under consideration. The exact expression of each BO $\phi_\mu(k)$ depends on the value of the wave vector k because the coefficient $\exp(ikna)$ for $\chi_\mu(r - na)$, which is introduced to satisfy the periodic boundary condition, varies with k. The coefficient $\exp(ikna)$ is a periodic function of k, so only those k values of the region

$$-\pi/a \le k \le \pi/a \qquad (2.2)$$

may be used to construct the BO's $\phi_\mu(k)$. The importance of the BO's lies with the fact that the crystal orbitals (CO's) ψ_i ($i = 1, 2, ..., M$) for 2.1 are constructed as linear combinations of the BO's:

$$\psi_i(k) = \sum_{\mu=1}^{M} C_{\mu i}(k)\phi_\mu(k) \qquad (2.3)$$

The energies $e_i(k)$ of the CO's $\psi_i(k)$ are eigenvalues associated with the effective Hamiltonian H^{eff}:

$$H^{\text{eff}}\,\psi_i(k) = e_i(k)\,\psi_i(k) \qquad (2.4)$$

The requirement that $\partial e_i(k)/\partial C_{\mu i}(k) = 0$ for $\mu = 1, 2, ..., M$ leads to the $M \times M$ secular determinant

$$|H_{\mu\nu}(k) - e_i(k)S_{\mu\nu}(k)| = 0 \qquad (2.5)$$

where the matrix elements $H_{\mu\nu}(k)$ and $S_{\mu\nu}(k)$ are defined as

$$H_{\mu\nu}(k) = \langle\phi_\mu(k)|H^{\text{eff}}|\phi_\nu(k)\rangle \qquad (2.6)$$

and

$$S_{\mu\nu}(k) = \langle\phi_\mu(k)|\phi_\nu(k)\rangle \qquad (2.7)$$

The allowed energy region for each CO ψ_i can be determined by solving eq 2.5 for a mesh of k-points covering the region $-\pi/a \le k \le \pi/a$. Because of the relationship, $e_i(k) = e_i(-k)$, one needs to solve eq 2.5 for

a mesh of k-points covering only the region $0 \leq k \leq \pi/a$. By the use of eq 2.1, the matrix elements $H_{\mu\nu}(k)$ and $S_{\mu\nu}(k)$ are expressed as

$$H_{\mu\nu}(k) = \langle\chi_\mu(r)|H^{\text{eff}}|\chi_\nu(r)\rangle + \sum_{n=1}^{\infty}[\exp(ikna)\langle\chi_\mu(r)|H^{\text{eff}}|\chi_\nu(r-na)\rangle + \exp(-ikna)\langle\chi_\mu(r-na)|H^{\text{eff}}|\chi_\nu(r)\rangle] \quad (2.8)$$

and

$$S_{\mu\nu}(k) = \langle\chi_\mu(r)|\chi_\nu(r)\rangle + \sum_{n=1}^{\infty}[\exp(ikna)\langle\chi_\mu(r)|\chi_\nu(r-na)\rangle + \exp(-ikna)\langle\chi_\mu(r-na)|\chi_\nu(r)\rangle] \quad (2.9)$$

In the n-th nearest neighbor approximation, the terms of eq 2.8 and 2.9 with indices greater than n are truncated. The choice of an appropriate n value depends upon whether or not the integrals such as $\langle\chi_\mu(r)|H^{\text{eff}}|\chi_\nu(r-na)\rangle$ and $\langle\chi_\mu(r)|\chi_\nu(r-na)\rangle$ are negligible. It should be clear from this discussion that energy band calculations for solids are quite similar to energy level calculations for molecules. For solids, however, the secular determinant needs to be solved for a set of different k points covering the region $0 \leq k \leq \pi/a$.

2.2 Orbital Interactions in Solids[6]

We now examine the essence of the energy band formalism described in the previous section from the viewpoint of orbital interaction. Let us consider the 1D system 2.2 which has one AO χ on each site. Since each

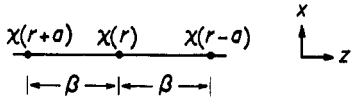

2.2

unit cell has only one AO, the BO $\phi(k)$ is identical with the CO $\psi(k)$. From eq 2.5, one obtains

$$e(k) = \frac{H(k)}{S(k)} \quad (2.10)$$

$$= \frac{\alpha + 2\beta\cos ka + \ldots}{1 + 2S\cos ka + \ldots} \quad (2.11)$$

where α is the Coulomb integral, $\alpha = \langle\chi(r)|H^{\text{eff}}|\chi(r)\rangle$, β is the nearest neighbor resonance integral, $\beta = \langle\chi(r)|H^{\text{eff}}|\chi(r-a)\rangle$, and S is the nearest neighbor overlap integral, $S = \langle\chi(r)|\chi(r-a)\rangle$. When the overlap integrals are neglected within the first nearest neighbor approximation, eq 2.11 is simplified as

$$e(k) = \alpha + 2\beta\cos ka \quad (2.12)$$

The dispersion relation of the band given by eq 2.12 is shown in 2.3. Within the approximations introduced

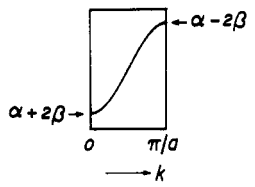

2.3

above, the bandwidth W is given by $W = 4|\beta|$. In other words, the energy level of the AO χ (i.e., α) is spread into a band of width $4|\beta|$, as depicted in 2.4.

TABLE 2.1. Bloch Orbital Coefficients for a 1D Chain

k point	exp($ikna$)
$\Gamma = 0$	$(1)^n$
$X = \pi/a$	$(-1)^n$

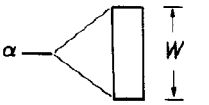

2.4

Although there are in principle an infinite number of k values to consider, the essence of the band dispersion given by eq 2.12 can be shown by examining only two special k points (i.e., $k = 0$ and π/a). As listed in Table 2.1, the coeffcients $\exp(ikna) = (1)^n$ at $k = 0$ (i.e., Γ), but $\exp(ikna) = (-1)^n$ at $k = \pi/a$ (i.e., X). This simply means that the BO at Γ is obtained by repeating the AO's with an identical sign, while the BO at X is obtained by repeating the AO's with alternating signs. This is shown in 2.5 for the case when χ is an s orbital.

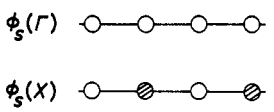

2.5

Note that the BO's at Γ and X refer to the maximum bonding and antibonding interactions possible for the 1D system. Therefore the s-orbital band should have a dispersion relation as shown in 2.3. (Hereafter, p_x, p_y, p_z, $d_{x^2-y^2}$, d_{z^2}, d_{xz}, d_{yz}, and d_{xy} orbitals will be simply referred to as x, y, z, x^2-y^2, z^2, xz, yz, and xy orbitals, respectively). When χ is an x orbital, the BO's at Γ and X are given by 2.6 so that the x-orbital band will have a dispersion relation as shown in 2.3. When χ is a z orbital, the BO's at Γ and X are given by 2.7. In

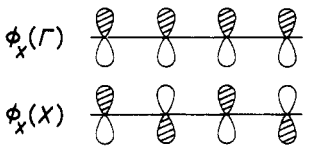

2.6

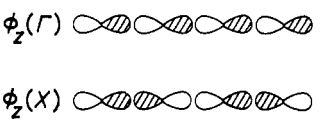

2.7

contrast to the cases of 2.5 and 2.6, the maximum bonding and antibonding interactions of the z orbital band occur at X and Γ, respectively. Therefore, the dispersion relation of the z-orbital band follows the pattern of 2.8. In addition, the width of the z-orbital band should be greater than that of either the s- or x-orbital band because the σ overlap between adjacent

2.8

z orbitals is larger in magnitude than either the π-overlap between adjacent x orbitals or the σ overlap between adjacent s orbitals. Thus, for 1D systems, consideration of orbital arrangements at Γ and X provides essential clues to the dispersion patterns and the bandwidths.

2.3 Band Gap and Symmetry Lowering

As a more complex example, we examine the 1D system 2.9 in which a unit cell contains two atoms with one AO each. If the overlap integrals are neglected,

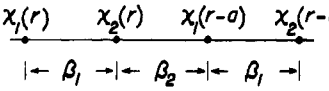

2.9

eq 2.5 for the lattice 2.9 becomes

$$\begin{vmatrix} H_{11}(k) - e_i(k) & H_{12}(k) \\ H_{21}(k) & H_{22}(k) - e_i(k) \end{vmatrix} = 0 \qquad (2.13)$$

Given the Coulomb integrals of the AO's χ_1 and χ_2 as α_1 and α_2, respectively, and the first nearest neighbor resonance integrals as defined in 2.9, the matrix elements $H_{\mu\nu}(k)$ are written as

$$H_{\mu\mu}(k) = \alpha_\mu \qquad (\mu = 1,2) \qquad (2.14)$$

$$H_{12}(k) = H_{21}^*(k) = \beta_1 + \beta_2 \exp(-ika) \qquad (2.15)$$

Equation 2.15 is obtained by the first nearest neighbor approximation. By the use of these matrix elements in eq 2.13, we obtain the following expression for $e_i(k)$

$$e_i(k) = (\alpha_1 + \alpha_2)/2 \pm [(\alpha_1 - \alpha_2)^2/4 + (\beta_1^2 + \beta_2^2 + 2\beta_1\beta_2 \cos ka)]^{1/2} \qquad (2.16)$$

A special case of interest for the above equation is defined in case I:

$$\text{case I} \quad \alpha_1 = \alpha_2 = \alpha < 0, \quad \beta_1 = \beta_2 = \beta < 0 \qquad (2.17)$$

for which eq 2.16 is rewritten as

$$e_i(k) = \alpha \pm 2\beta \cos(ka/2) \qquad (2.18)$$

Case I is identical with 2.2 except that its unit cell is doubled in size with respect to 2.2. Each dimer unit of 2.9 has the bonding and antibonding levels at $\alpha + \beta$ and $\alpha - \beta$, respectively, as depicted in 2.10. The dispersion

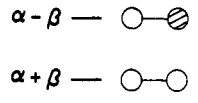

2.10

relation of eq 2.18, shown in 2.11, is simply obtained by folding the dispersion curve of 2.3 at the midpoint along $k = 0 \rightarrow k = \pi/a$ (It is important to notice that the repeat distance of 2.9 for case I is twice that of 2.2). In

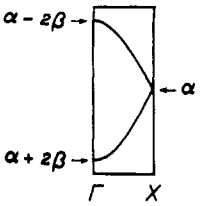

2.11

general, when a unit cell size increases n times without lowering the symmetry of the lattice, the resulting band dispersion is folded n times. This is illustrated in 2.12 for $n = 4$.

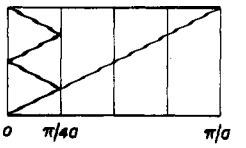

2.12

To describe the essence of the band dispersion relation of 2.11, the orbitals χ_μ ($\mu = 1, 2$) may now be assumed to be s orbitals. The BO's ϕ_i ($i = 1, 2$) at Γ are shown in 2.13. The CO's ψ_i ($i = 1, 2$) at Γ are linear

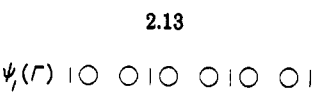

2.13

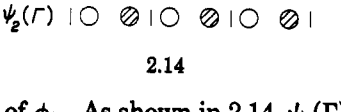

2.14

combinations of ϕ_i. As shown in 2.14, $\psi_1(\Gamma)$ is bonding, but $\psi_2(\Gamma)$ is antibonding, within a unit cell and between

$$\psi_1(\Gamma) \propto \phi_1(\Gamma) + \phi_2(\Gamma)$$

$$\psi_2(\Gamma) \propto \phi_1(\Gamma) - \phi_2(\Gamma) \qquad (2.19)$$

unit cells. Namely, $\psi_1(\Gamma)$ is a bonding combination of the dimer bonding orbitals, and $\psi_2(\Gamma)$ is an antibonding combination of the dimer antibonding orbitals. The BO's ϕ_i at X are shown in 2.15, and the corresponding CO's ψ_i are given as linear combinations. As depicted

$$\psi_1(X) \propto \phi_1(X) + \phi_2(X)$$

$$\psi_2(X) \propto \phi_1(X) - \phi_2(X) \qquad (2.20)$$

in 2.16, $\psi_1(X)$ is bonding within a unit cell but antibonding between unit cells while $\psi_2(X)$ is antibonding within a unit cell but bonding between unit cells. That

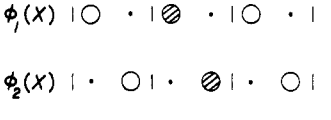

2.15

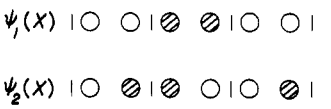

2.16

is, $\psi_1(X)$ is an antibonding combination of the dimer bonding orbitals, but $\psi_2(X)$ is a bonding combination of the dimer antibonding orbitals. Consequently, $\psi_1(X)$ and $\psi_2(X)$ are nonbonding in nature. This can also be shown in terms of their linear combinations

$$\psi_+(X) \propto \psi_1(X) + \psi_2(X)$$

$$\psi_-(X) \propto \psi_1(X) - \psi_2(X) \qquad (2.21)$$

As illustrated in 2.17, $\psi_+(X)$ has orbital character only on the first atom sites, and $\psi_-(X)$ only on the second atom sites. Therefore, $\psi_+(X)$ and $\psi_-(X)$ are each nonbonding in nature.

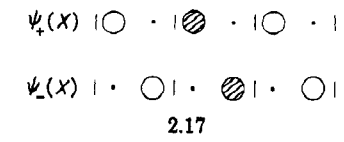

2.17

We are now ready to consider two examples for which eq 2.16 leads to a band gap. One typical case is shown in case II:

$$\text{case II} \qquad \alpha_1 = \alpha_2 = \alpha < 0 \qquad \beta_1 < \beta < \beta_2 < 0 \qquad (2.22)$$

That is, the resonance integral is greater in magnitude within a unit cell than between unit cells, while the two atoms of a unit cell are equivalent. A very common

2.18

situation leading to case II is a dimerization distortion 2.18. For case II, eq 2.16 is simplified as

$$e_i(k) = \alpha \pm [\beta_1^2 + \beta_2^2 + 2\beta_1\beta_2 \cos ka]^{1/2} \qquad (2.23)$$

which has the dispersion relation shown in 2.19. Case II produces two bands of width $2|\beta_2|$ separated by a

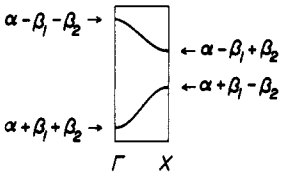

2.19

band gap of $2(\beta_2 - \beta_1)$. In other words, the dimer levels $\alpha + \beta_1$ and $\alpha - \beta_1$ are each spread into bands of width $2|\beta_2|$. The occurrence of band gap in 2.19 can be easily explained in terms of the CO's $\psi_i(X)$ shown in 2.16: When the intraunit resonance integral becomes larger (and the interunit resonance integral becomes smaller) in magnitude, $\psi_1(X)$ is lowered in energy but $\psi_2(X)$ is raised (see 2.20). Another case leading to a band gap

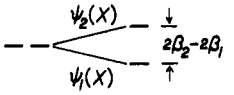

2.20

from eq 2.16 is given in case III:

$$\text{case III} \qquad \alpha_1 < \alpha < \alpha_2 < 0 \qquad \beta_1 = \beta_2 = \beta < 0 \qquad (2.24)$$

This situation occurs when two atoms of a unit cell are made nonequivalent. For case III, eq 2.16 becomes

$$e_i(k) = (\alpha_1 + \alpha_2)/2 \pm [(\alpha_1 - \alpha_2)^2/4 + 4\beta^2 \cos^2(ka/2)]^{1/2} \qquad (2.25)$$

The dispersion relation of this equation is shown in 2.21, where $D = (\alpha_1 - \alpha_2)^2/4 + 4\beta^2$, and the two bands are separated by a band gap of $\alpha_2 - \alpha_1$. When $|\alpha_1 - \alpha_2| \gg$

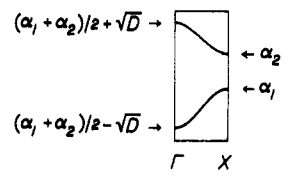

2.21

$|\beta|$, each band of 2.21 has a width of $4\beta^2/|\alpha_1 - \alpha_2|$. The occurrence of a band gap for case III is easily explained in terms of the CO's $\psi_+(X)$ and $\psi_-(X)$ shown in 2.17: When the Coulomb integral of χ_1 is lowered (and that of χ_2 is raised) in energy, $\psi_+(X)$ is stabilized but $\psi_-(X)$ is destabilized as depicted in 2.22. This leads to a band gap of $\alpha_2 - \alpha_1$.

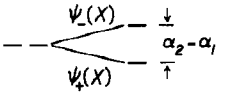

2.22

Either case II or case III results from case I by an appropriate perturbation. The essential outcome of such a perturbation, which lowers the symmetry of the lattice, is to open an energy gap in the middle of the band as depicted in 2.23. This band splitting becomes important when the band is half-filled, because the band gap opening at the Fermi level lowers the electronic energy of the half-filled system (see 2.24). The

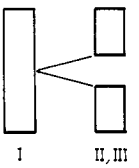

2.23

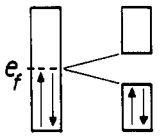

2.24

dimerization 2.18 in a half-filled band system provides a situation appropriate for 2.24. In general, when a unit cell size is increased n-fold by a distortion or an external potential (which introduces nonequivalent lattice sites), the band is split into n subbands. This is illustrated for $n = 4$ in 2.25, which can be easily explained on the basis of the folded band dispersion shown in 2.12, because symmetry lowering will split the degeneracies at Γ ($k = 0$) and X ($k = \pi/4a$) thereby introducing band gaps. Consequently, a 1D system having a partially filled band of occupancy $1/n$ or $(n - 1)/n$ is likely to undergo a distortion which increases the unit cell size n times (see 2.26 and 2.27). This general phenomenon is known as a Peierls distortion or a $2k_f$ distortion (see sections 6.1 and 6.2).

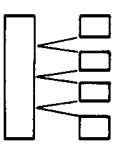

2.25

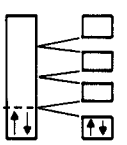

2.26

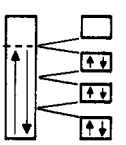

2.27

2.4 Dispersion Patterns of the t_{2g}-Block Bands

Low-dimensional transition-metal oxides have a crystal structure constructed from MO_6 octahedra via corner- or edge-sharing. In describing the d-block band structures of those compounds, it is important to know how the metal d orbitals interact directly or indirectly through the p-orbitals of the bridging oxygen atoms. For a regular MO_6 octahedron, the metal d orbitals are split into the t_{2g}- and e_g-block levels as shown in 2.28.

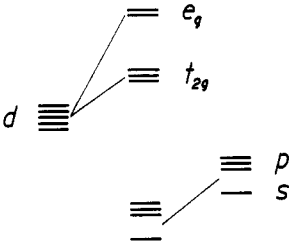

2.28

Between the metal and the oxygen atoms, the t_{2g}-levels have π-type antibonding interactions while the e_g-levels have σ-type antibonding interactions. Due to high oxidation states of the metal atoms in those oxides, only the d-block bands arising from the t_{2g}-levels may become filled. Thus we consider only their t_{2g}-block bands.

For a regular MO_6 shown in 2.29, the equatorial and axial oxygen atoms may be referred to as O_{eq} and O_{ax}, respectively. For the coordinate system used in 2.29,

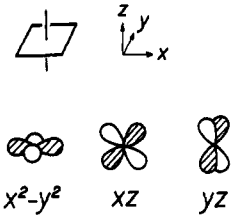

2.29

the t_{2g}-block levels arise from the x^2–y^2, xz, and yz orbitals. The x^2–y^2 orbital does not interact with the O_{ax} atoms (2.30), but it does with the O_{eq} atoms (2.31). If

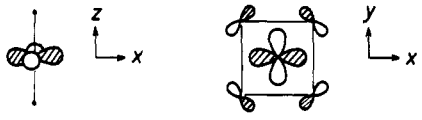

2.30 2.31

the antibonding interaction in each M–O_{eq} bond is denoted by the symbol (Y_t), where the subscript t indicates that the oxygen of the M–O bond is a terminal ligand, then the x^2–y^2 level has 4(Y_t) interactions. The xz and yz orbitals each make 2(Y_t) interactions with the O_{ax} atoms (2.32). With the O_{eq} atoms, the xz and yz

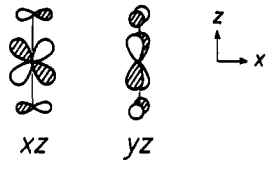

2.32

orbitals interact as shown in 2.33. Unlike in 2.31 and 2.32, each M–O_{eq} bond of 2.33 is not contained in the d-orbital plane, so the M–O_{eq} bond of 2.33 has a weaker antibonding. The presence of such an antibonding

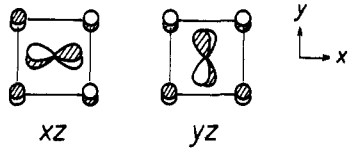

2.33

interaction in each M–O_{eq} bond may be denoted by (y_t). Then the xz and yz levels each have 2(Y_t) + 4(y_t) interactions. These two levels are degenerate with the x^2–y^2 level, so that 2(y_t) antibonding interactions are equal in magnitude to one (Y_t) antibonding interaction.

2.4.1 Corner-Sharing Octahedral Chain[8a]

As an example to illustrate how t_{2g}-block bands are constructed, we examine the corner-sharing MO_5 octahedral chain 2.34. To simplify our presentation, all

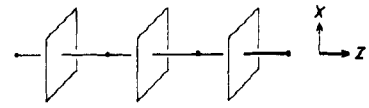

2.34

oxygen atom orbitals may be suppressed except for those of the bridging oxygen atoms. The BO's of the metal xz orbital at Γ and X are given in 2.35. The bridging oxygen atom orbital that can overlap with the adjacent xz orbital is the x orbital. The BO's of the x orbital at Γ and X are shown in 2.36. Due to the large

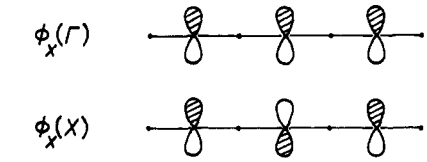

2.35

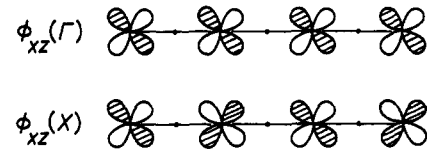

2.36

distances involved, direct metal-metal interactions are negligible, and so are direct interactions between the bridging oxygen atoms. Therefore, as shown in 2.37 by dashed lines, the BO energies of the xz and x orbitals are each dispersionless. At Γ, ϕ_{xz} and ϕ_x do not overlap

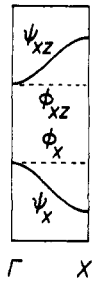

2.37

due to their different symmetry, while at X they do to give rise to the CO's $\psi_{xz}(X)$ and $\psi_x(X)$ shown in 2.38.

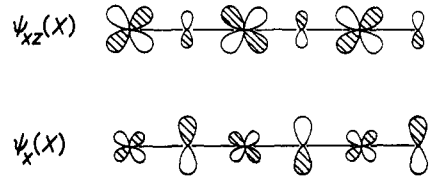

2.38

Between the metal and the bridging oxygen atoms, $\psi_x(X)$ has the maximum bonding interactions while $\psi_{xz}(X)$ has the maximum antibonding interactions. Thus the xz- and x-orbital bands have the dispersion relations shown by the solid lines in 2.37. The dispersion relations for the yz- and y-orbital bands of the MO_5 chain are similarly described. The BO's of the metal x^2–y^2 orbital at Γ and X are shown in 2.39. The

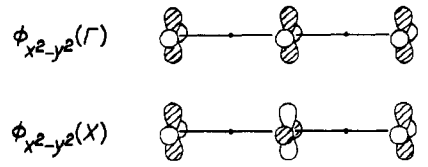

2.39

x^2-y^2 orbitals are δ-orbitals with respect to the chain axis, and therefore do not interact with any orbitals of the bridging oxygen atoms. Thus the BO's $\phi_{x^2-y^2}$ are the CO's themselves, so the x^2-y^2 band is dispersionless as shown in 2.40.

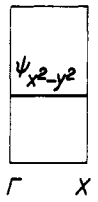

2.40

As in the case of the t_{2g}-block levels of a regular MO_6 octahedron, the occurrence of antibonding interaction between the metal d orbital and the bridging oxygen p orbital may be denoted by the symbol (Y_b) or (y_b) (depending upon whether or not the M–O bond is contained in the metal d-orbital plane), where the subscript b indicates that the oxygen of the M–O bond is a bridging ligand. The absence of an oxygen p orbital at the bridging position may then be represented by the symbol (N) and by a dot in orbital diagrams. According to these (Y_b), (y_b), and (N) notations, the essence of the dispersion relations of the xz, yz, and x^2-y^2 block bands can be summarized as in Table 2.2. Figure 2.1 shows the dispersion relations of the t_{2g}-block bands calculated for an ideal MoO_5 chain (with Mo–O = 1.96 Å). As expected, the x^2-y^2 band is almost dispersionless. The x^2-y^2 band at Γ and X is characterized by $4(Y_t)$ interactions. The degenerate xz and yz bands are characterized by $2(Y_t)$ interactions at Γ, but by $2(Y_t) + 2(Y_b)$ interactions at X. Since the flat x^2-y^2 band lies approximately in the middle of the xz and yz bands, two (Y_t) interactions are approximately equal in magnitude to one (Y_b) interaction. This relationship between (Y_b) and (Y_t) is not necessarily applicable to systems more complicated in structure than the MoO_5 chain. In general, the magnitudes of the antibonding interactions between the metal d and the oxygen p orbitals satisfy the following relationships:

$$(Y_b) \cong 2(y_b)$$

$$(Y_t) \cong 2(y_t) \qquad (2.26)$$

In the applications to be discussed later, we deal mostly with the (Y_b) and (y_b) interactions associated with bridging oxygen ligands. To simplify our notations, the (Y_b) and (y_b) interactions will be referred to as the (Y) and (y) interactions, respectively. There are two typical cases of corner-sharing between two MO_6 octahedra, i.e., 2.41 and 2.42. All possible phase relationships between

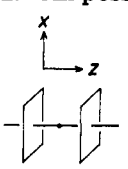

2.41

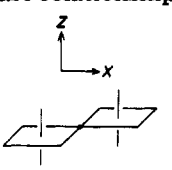

2.42

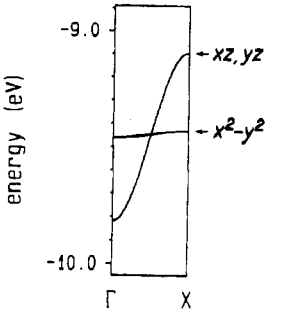

Figure 2.1. Dispersion relations of the t_{2g}-block bands calculated for a corner-sharing MoO_5 chain.

TABLE 2.2. Antibonding Contributions of the Oxygen p Orbitals of the Mo–O–Mo Bridges in the t_{2g}-Block Bands of the MO_5 Chain

band	*k* points Γ	*k* points *X*
xz, yz	(N)	(Y_b)
x^2-y^2	(N)	(N)

the adjacent t_{2g}-block levels of 2.41 and 2.42 are shown in 2.43 and 2.44, respectively. As will be shown later,

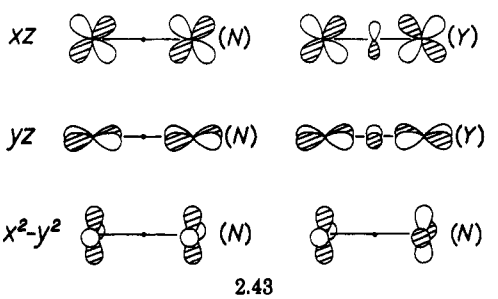

2.43

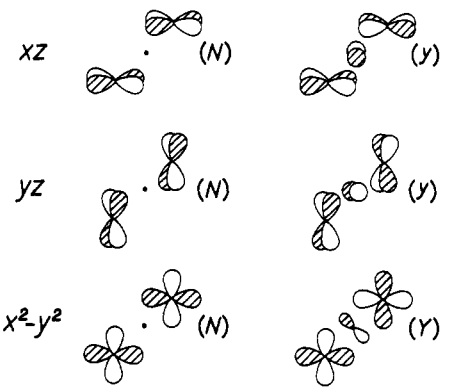

2.44

the dispersion relations of the t_{2g}-block bands of low-dimensional metal oxides are readily explained by simply analyzing whether or not the bridging oxygen p orbitals mix with their adjacent metal d orbitals [i.e., by counting the number of (Y), (y), and (N) interactions].

2.4.2 Edge-Sharing Octahedral Chain[28]

We now examine the t_{2g}-block bands of the edge-sharing MO_4 octahedral chain 2.45. The metal–metal distances through the shared edges are short, so direct metal–metal interactions can become strong. There-

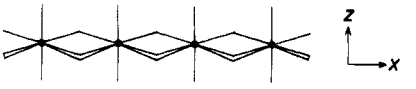

2.45

fore, the dispersion relations of the t_{2g}-block bands for the edge-sharing chain 2.45 are slightly more complex than those for the corner-sharing chain 2.34. With the coordinate system chosen, the σ-band of 2.45 is constructed from the x^2-y^2 orbitals. The BO's of the metal x^2-y^2 orbital at Γ and X are shown in 2.46. Since the

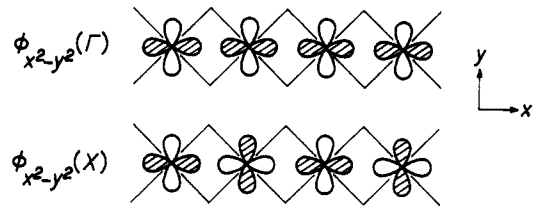

2.46

overlap between adjacent x^2-y^2 orbitals is strong, the BO of x^2-y^2 is dispersive as shown by the dashed line in 2.47. $\phi_{x^2-y^2}(\Gamma)$ and $\phi_{x^2-y^2}(X)$ interact with the

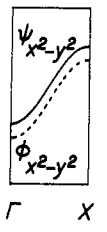

2.47

bridging oxygen orbitals $\phi_y(\Gamma)$ and $\phi_x(X)$ (see 2.48), respectively. Thus the CO of x^2-y^2, $\psi_{x^2-y^2}$, is raised in

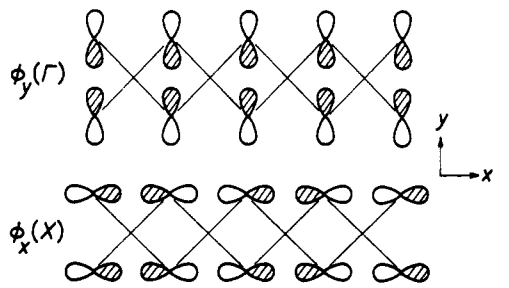

2.48

energy with respect to the BO of x^2-y^2, in 2.47. The π-band of 2.45 is derived from the xz orbitals. The BO's of xz at Γ and X are shown in 2.49. $\phi_{xz}(\Gamma)$ is metal–

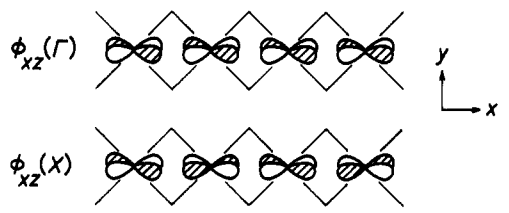

2.49

metal antibonding, while $\phi_{xz}(X)$ is metal–metal bonding. Thus $\phi_{xz}(k)$ varies as shown by the dashed line in 2.50. $\phi_{xz}(\Gamma)$ does not interact with any bridging oxygen

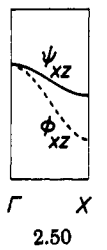

2.50

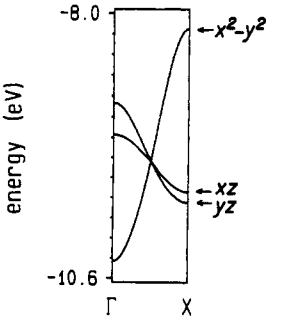

Figure 2.2. Dispersion relations of the t_{2g}-block bands calculated for an edge-sharing MoO_4 chain.

atom orbitals, while $\phi_{xz}(X)$ interacts with $\phi_z(X)$ shown in 2.51. Thus the CO of xz, $\psi_{xz}(k)$, is raised in energy

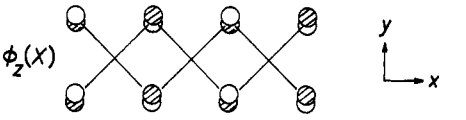

2.51

with respect to $\phi_{xz}(k)$, as k varies from Γ to X. Consequently, the xz band has a narrow bandwidth (2.50). The δ-band of 2.45 is constructed from the yz orbitals. The BO's of yz at Γ and X are shown in 2.52. Because

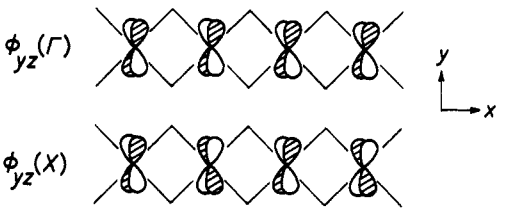

2.52

of the δ-orbital nature of yz, the BO $\phi_{yz}(k)$ is dispersionless as shown by the dashed line in 2.53. $\phi_{yz}(\Gamma)$

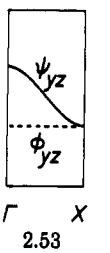

2.53

interacts with the bridging oxygen orbital $\phi_z(\Gamma)$ shown in 2.54, but $\phi_{yz}(X)$ does not interact with any bridging oxygen orbitals. Therefore the CO of yz, $\psi_{yz}(k)$, is

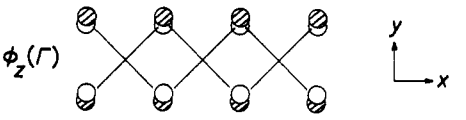

2.54

raised in energy as k varies from X to Γ. The width of the δ-band is determined solely by the metal-bridging oxygen interactions. In contrast, the width of the π-band is governed by two opposing effects, i.e., the metal–metal and the metal-bridging oxygen interactions. Consequently, the π-band becomes narrower than the δ-band in the edge-sharing MO_4 chain 2.45. Figure 2.2 shows the dispersion relations of the t_{2g}-block bands calculated for an ideal MoO_4 chain (with Mo–O = 1.96 Å).

When BO's are well separated in energy, the resulting CO's are well separated as well. In such cases, the essential aspects of band dispersion relations can be easily described by analyzing the nodal properties of the CO's at Γ and X. A more complex situation results when two BO's overlap in energy, as depicted by the dashed lines in 2.55. If these BO's can interact by symmetry along $\Gamma \rightarrow X$, the intended crossing of the dashed curves are avoided by orbital mixing thereby leading to two bands (represented by solid lines in 2.55) separated by a band gap. As a result, the two bands possess different orbital character before and after the intended crossing region. If the BO's do not interact by symmetry, the resulting bands cross as shown in 2.56.

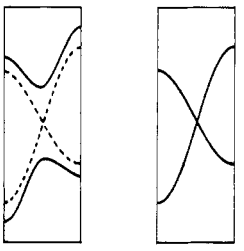

2.55 2.56

3. Vibrational Band Structure[9]

The vibrational energy levels of molecules are discrete while those of solids form energy bands. This situation is analogous to the difference in the electronic structures of molecules and solids. In the present section, we discuss how vibrational energy bands (i.e., phonon bands) are determined on the basis of a 1D chain and show that band formation and band gap occurrence for vibrational energies are quite similar to those for electronic energies.

3.1 Formation of Energy Bands

First, we note that a dimer 3.1 with atom mass M and stretching force constant f has the allowed vibrational frequency $\omega = \sqrt{2f/M}$ and the energy $h\omega/2\pi$. Allowed vibrational frequencies of a solid are a function of wave vector k, as are electronic energy levels. To simplify

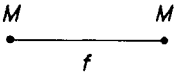

3.1

our discussion, we assume that the atoms of the 1D chain vibrate only along the chain direction (i.e., longitudinal vibration). For the monoatomic chain 3.2, the displacement function $U_{n,i}$ at the n-th lattice site represents the displacement of an atom i with mass M_i, at a certain time t, from the equilibrium position. For

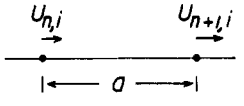

3.2

vibrational energy bands, those displacement functions $U_{n,i}$ have a role similar to the one that AO's play in constructing electronic band structures. Atoms at the lattice sites vibrate with frequency ω, and such vibrations satisfy the periodic boundary condition. Therefore $U_{n,i}$ is written as

$$U_{n,i} = U_i^{\circ}(M_i)^{-1/2} \exp(ikna) \exp(-i\omega t) \quad (3.1)$$

where U_i° is a constant, and the $\exp(ikna)$ term ensures that the displacement $U_{n,i}$ satisfies the translational symmetry of the 1D chain. As in section 2, the values of wave vector k to consider may be confined to $-\pi/a \leq k \leq \pi/a$. The vibrations are governed by a certain potential V, so each displacement function $U_{n,i}$ satisfies the equation of motion given by

$$M_i(\partial^2 U_{n,i}/\partial t^2) = -\sum_m \sum_j \Phi_{n,m}(i,j) \quad (3.2a)$$

where

$$\Phi_{n,m}(i,j) = \partial^2 V/\partial U_{n,i}\partial U_{m,j} \quad (3.2b)$$

Equation 3.2 eventually leads to the secular determinant

$$|D_{ij}(k) - \omega^2(k)\delta_{ij}| = 0 \quad (3.3)$$

where the matrix element $D_{ij}(k)$ is given by

$$D_{ij}(k) = (M_iM_j)^{1/2} \sum_m \Phi_{n,m}(i,j) \exp[ik(m-n)a] \quad (3.4)$$

The dimension of the secular determinant is equal to the number of atoms per unit cell.

Consider the monoatomic chain 3.3 with one atom (of mass M) per unit cell and force constant f between nearest neighbor atoms. We drop the index i in $U_{n,i}$

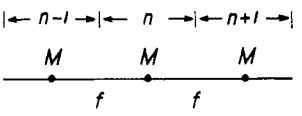

3.3

since there is one atom per unit cell, so eq 3.3 leads to the expression

$$\omega^2(k) = D(k) \quad (3.5)$$

Within the first nearest neighbor approximation, the potential V may be given as a harmonic function:

$$V = \sum_n f(U_n - U_{n+1})^2/2 \quad (3.6)$$

Since $\Phi_{n,n} = 2f$ and $\Phi_{n,n+1} = \Phi_{n,n-1} = -f$, $D(k)$ is written as

$$D(k) = (1/M)[2f - f\exp(-ika) - f\exp(ika)] = (4f/M)\sin^2(ka/2) \quad (3.7)$$

From eqs 3.5 and 3.7, we obtain

$$\omega(k) = \sqrt{4f/M}\sin(ka/2) \quad (3.8)$$

The dispersion relation of eq 3.8 is shown in 3.4, which reveals that the allowed vibrational frequencies range from 0 to $\sqrt{4f/M}$. It is of interest to examine what

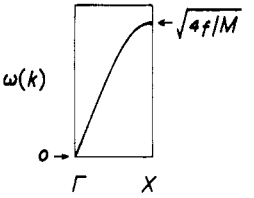

3.4

vibrational motions of the chain these two extreme cases correspond to. Imagine that, at a certain time t, an

atom of the reference site (i.e., $n = 0$) is displaced as shown in 3.5. At that instant, the vibration Bloch

3.5

functions at Γ and X are then obtained by repeating the displacement vector of the reference cell with a common sign and with alternating signs, respectively (see 3.6). Clearly, in $\phi(\Gamma)$, all atoms move in one direction without either shortening or lengthening any interatomic distances. That is, $\phi(\Gamma)$ describes a translation and does not involve any vibration, so the vibrational frequency for $\phi(\Gamma)$ is zero. On the other hand, $\phi(X)$ involves all atoms in stretching and squeezing every nearest neighbor interatomic contacts. Therefore, $\phi(X)$ describes the atom displacements associated with the highest possible vibrational frequency for the chain 3.3.

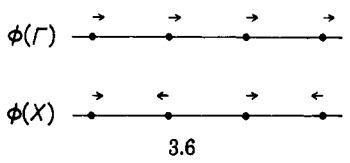

3.6

3.2 Band Gap and Symmetry Lowering

A slightly more complicated example is the chain 3.7, which has two atoms per unit cell. The most general situation for 3.7 results when the atoms 1 and 2 have different masses and also when the force constants for the atoms in a unit cell and between unit cells are different. Within the first nearest neighbor approximation, the harmonic potential for 3.7 is given by

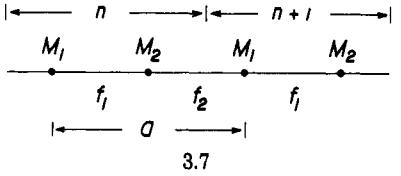

3.7

$$V = \sum_n [f_1(U_{n,1} - U_{n,2})^2 + f_2(U_{n-1,2} - U_{n,1})^2]/2 \qquad (3.9)$$

Since there are two atoms per unit cell, the secular determinant (eq 3.3) is written as

$$\begin{vmatrix} D_{11}(k) - \omega^2(k) & D_{12}(k) \\ D_{21}(k) & D_{22}(k) - \omega^2(k) \end{vmatrix} = 0 \qquad (3.10)$$

From eq 3.9, it is found that $\Phi_{n,n}(1,1) = \Phi_{n,n}(2,2) = f_1 + f_2$, $\Phi_{n,n}(1,2) = -f_1$, and $\Phi_{n,n-1}(1,2) = \Phi_{n,n+1}(2,1) = -f_2$. Consequently, the matrix elements $D_{ij}(k)$ are written as

$$D_{ii}(k) = (f_1 + f_2)/M_i \qquad (i = 1, 2)$$

$$D_{12}(k) = D_{21}^*(k) = -[f_1 + f_2 \exp(-ika)]/\sqrt{M_1 M_2} \qquad (3.11)$$

From eqs 3.10 and 3.11, the wave vector dependence of ω is expressed as

$$\mu\omega^2(k) = \frac{(f_1 + f_2)}{2}\left[1 \pm \sqrt{\frac{16 f_1 f_2 \mu^2 \sin^2(ka/2)}{(f_1 + f_2)^2 M_1 M_2}}\right] \qquad (3.12)$$

where $\mu = M_1M_2/(M_1 + M_2)$.

A particularly simple example for eq 3.12 is given by

case I $$M_1 = M_2 = M$$
$$f_1 = f_2 = f \qquad (3.13)$$

which is equivalent to 3.3 except that the unit cell size is doubled in case I. That is, the chain 3.7 for case I is obtained by repeating dimer units 3.1. For case I, eq 3.12 is simplified as

$$M\omega^2(k) = 2f[1 \pm \cos(ka/2)] \qquad (3.14)$$

which has the dispersion relation shown in 3.8, a folded version of 3.4. We now examine the essence of the band dispersion given by eq 3.14 by supposing that, at a certain time t, the atoms of the reference cell (i.e., $n = 0$) are each displaced as indicated in 3.5. Then, at that instant, the vibrational Bloch functions ϕ_i ($i = 1, 2$) at Γ are given by 3.9, and the vibrational crystal functions ψ_i at Γ are obtained as in-phase and out-of-phase combinations of ϕ_i as shown in 3.10. $\psi_1(\Gamma)$ involves no vibration, and its frequency is zero. $\psi_2(\Gamma)$ involves all atoms in stretching and squeezing all nearest neighbor contacts, and therefore describes the highest frequency vibration. If we apply the same reasoning, the "two" vibrational states of the dimer 3.1 can be represented as in 3.11 and 3.12. The former shows no vibration, and the latter shows a stretching vibration. It is clear that $\psi_1(\Gamma)$ and $\psi_2(\Gamma)$ are in-phase combinations of the dimer vibrations 3.11 and 3.12, respectively. The vibrational Bloch functions ϕ_i at X are given by 3.13, and their in-phase and out-of-phase combinations lead to the vibrational crystal functions ψ_i shown in 3.14. $\psi_1(X)$ and $\psi_2(X)$ are out-of-phase

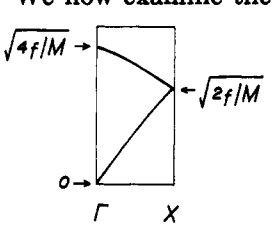

3.8

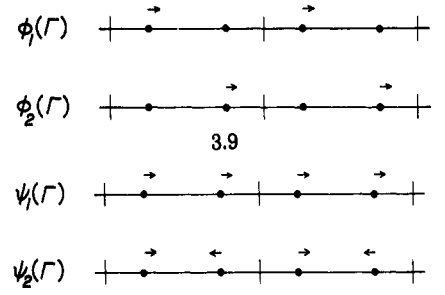

3.9

3.10

3.11 3.12

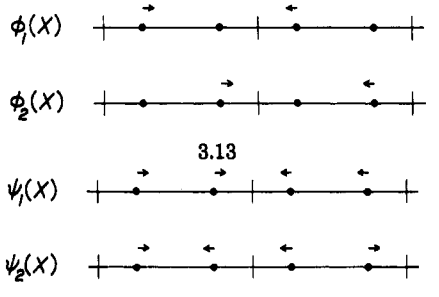

3.13

3.14

combinations of the dimer vibrations 3.11 and 3.12, respectively. It is noted that the vibration involves only the atoms between unit cells in $\psi_1(X)$, but only those within each unit in $\psi_2(X)$. For case I, $\psi_1(X)$ and $\psi_2(X)$ are degenerate, and their frequency is equal to that of an isolated dimer, i.e., $\omega = \sqrt{2f/M}$. The chain 3.7 for case I (or, equivalently, the chain 3.3) is constructed by repeating the dimer units. Therefore, the dimer vibrational level (i.e., $\omega = \sqrt{2f/M}$) spreads into a band of width $\sqrt{4f/M}$ as a result of forming the chain (see 3.15). Since $\psi_1(X)$ and $\psi_2(X)$ are degenerate, their

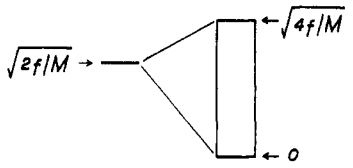

3.15

in-phase and out-of-phase combinations, shown in 3.16, are equally valid descriptions. This is so because the

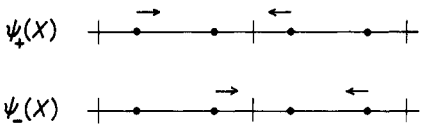

3.16

dimer vibration 3.17 is equivalent to 3.18, 3.19, or 3.20: Both atoms move simultaneously in 3.17 and 3.18 but only one moves in 3.19 and 3.20 with a displacement twice that found for 3.17 and 3.18.

3.17

3.18

3.19

3.20

One example of eq 3.12 leading to a band gap is defined in case II:

case II $$M_1 = M_2 = M$$
$$f_1 > f > f_2 \qquad (3.15)$$

for which eq 3.12 becomes

$$M\omega^2(k) = (f_1 + f_2)\left[1 \pm \sqrt{1 - \frac{4f_1f_2 \sin^2(ka/2)}{(f_1 + f_2)^2}}\right] \qquad (3.16)$$

As shown in 3.21, the dispersion relation of eq 3.16 leads to two separate bands. The band gap occurrence at

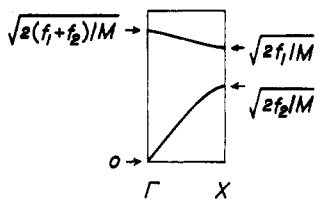

3.21

X can be easily explained in terms of the vibrational crystal functions $\psi_i(X)$ shown in 3.14. As depicted in 3.22, the frequency for $\psi_1(X)$ is lowered as the interdimer force constant decreases ($f_2 < f$) while the frequency for $\psi_2(X)$ is raised as the intradimer force constant increases ($f_1 > f$).

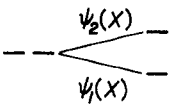

3.22

Another example of eq 3.12 leading to a band gap is defined in case III:

case III $$M_1 > M > M_2$$
$$f_1 = f_2 = f \qquad (3.17)$$

for which eq 3.12 is rewritten as

$$\mu\omega^2(k) = f\left[1 \pm \sqrt{1 - \frac{4\mu^2}{M_1M_2} \sin^2(ka/2)}\right] \qquad (3.18)$$

The dispersion relation of this equation is depicted in 3.23. The band gap occurrence in 3.23 is readily explained on the basis of the vibrational crystal functions shown in 3.16. As depicted in 3.24, $\psi_+(X)$ is lowered

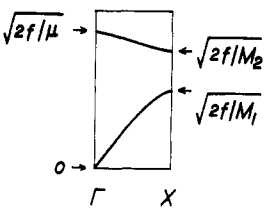

3.23

in frequency as the mass of the atom 1 increases, while $\psi_-(X)$ is raised in frequency as the mass of the atom 2 decreases.

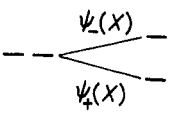

3.24

A vibrational energy band is called an acoustic band when its frequency decreases to zero as the wave vector approaches Γ, and an optical band otherwise. For example, the lower and upper bands of 3.21 or 3.23 are acoustic and optical bands, respectively.

4. Band Structure and Reciprocal Space

The basic concepts of electronic band structures were introduced in section 2 by taking 1D chains as examples. We now extend those concepts to 2D and 3D crystalline solids. For this purpose, the concepts of direct and reciprocal lattices[10] of a given solid are examined. Since electronic structures of centered 2D and 3D systems can be analyzed in terms of several different unit cells, we also discuss how different unit cell choices influence orbital analyses of the resulting band structures. Finally, we consider the concept of electronic density of states.

4.1 Electronic Structures of Multidimensional Systems

As an example of a 2D system, let us consider the rectangular lattice 4.1. An AO χ located at the (ma,

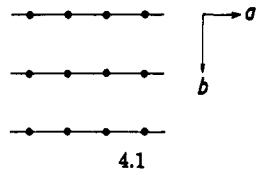

4.1

nb) site is written as $\chi(\mathbf{r} - m\mathbf{a} - n\mathbf{b})$, so the BO ϕ resulting from χ is expressed as

$$\phi(k_a,k_b) = N^{-1/2}\sum_m\sum_n \exp(ik_a ma)\exp(ik_b nb)\,\chi(\mathbf{r} - m\mathbf{a} - n\mathbf{b}) \quad (4.1)$$

where the two independent wave vectors k_a and k_b are necessary to allow all possible phase relationships between the AO's χ along the a and b directions, respectively. The coefficients $\exp(ik_a ma)$ and $\exp(ik_b nb)$ are periodic functions of k_a and k_b, respectively, so only the wave vectors (k_a, k_b) falling in the following region:

$$-\pi/a \le k_a \le \pi/a$$

$$-\pi/b \le k_b \le \pi/b \quad (4.2)$$

may be used in constructing the BO's. The wave vectors of equation 4.2 define the first Brillouin zone (FBZ) (see 4.2) of the 2D lattice 4.1. In 4.2, $\Gamma = (0,0)$, $X = (\pi/a, 0)$, $Y = (0, \pi/b)$, and $M = (\pi/a, \pi/b)$. When the overlap integrals are neglected within the first nearest neighbor approximation, the energy associated with the BO $\phi(k_a, k_b)$ is given by

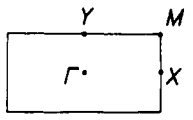

4.2

$$e(k_a, k_b) = \langle\phi(k_a,k_b)|H^{eff}|\phi(k_a,k_b)\rangle = \alpha + 2\beta_a \cos k_a a + 2\beta_b \cos k_b b \quad (4.3)$$

where β_a and β_b are the nearest neighbor resonance integrals along the a and b directions, respectively: $\beta_a = \langle\chi(\mathbf{r})|H^{eff}|\chi(\mathbf{r}-\mathbf{a})\rangle$ and $\beta_b = \langle\chi(\mathbf{r})|H^{eff}|\chi(\mathbf{r}-\mathbf{b})\rangle$. The wave vector dependence of $e(k_a, k_b)$ is often probed by plotting $e(k_a, k_b)$ as a function of (k_a, k_b) along several lines of the FBZ, e.g., $\Gamma \to X \to M \to Y \to \Gamma$.

Diagram 4.3 shows the $e(k_a, k_b)$ vs (k_a, k_b) plot based upon eq 4.3 under the assumption that $\beta_a < \beta_b < 0$ (i.e., the interaction along the a direction is stronger in magnitude than that along the b direction). The main

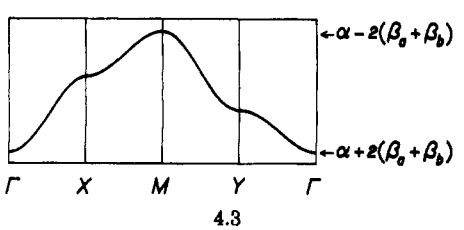

4.3

features of this band dispersion can be readily shown in terms of orbital interactions at a limited number of specific k points. The values of the coefficients $\exp(ik_a ma)$ and $\exp(ik_b nb)$ at Γ, X, Y, and M are listed in Table 4.1. Under the assumption that χ is an s orbital,

TABLE 4.1. Bloch Orbital Coefficients for a 2D Lattice

k point	$\exp(ik_a ma)\exp(ik_b nb)$
$\Gamma = (0, 0)$	$(1)^m (1)^n$
$X = (\pi/a, 0)$	$(-1)^m (1)^n$
$Y = (0, \pi/b)$	$(1)^m (-1)^n$
$M = (\pi/a, \pi/b)$	$(-1)^m (-1)^n$

the phase relationships between the AO's at those k points are illustrated in 4.4–4.7. At Γ, the AO's repeat

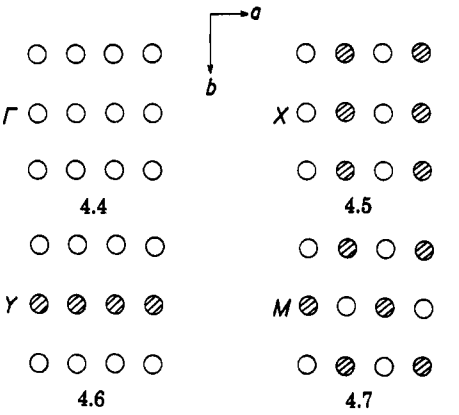

4.4 4.5 4.6 4.7

with a common sign along the a and b directions (4.4). At X, the AO's repeat with alternating signs along the a direction but with a common sign along the b direction (4.5). At Y, the AO's repeat with a same sign along the a direction but with alternating signs along the b direction (4.6). At M, the AO's repeat with alternating signs along the a and b directions (4.7). On the basis of 4.3–4.7, it is easy to explain the band dispersion relations of 4.3: For example, the energy $e(k_a, k_b)$ is lowest at Γ because this point allows bonding arrangements of the AO's for every nearest neighbor along the a and b directions. Along $\Gamma \to X$, the energy $e(k_a, k_b)$ increases because the nearest neighbor interaction along the a direction changes gradually from bonding to antibonding. Extension of our discussion to a 3D system is straightforward. As an example, consider the 3D orthorhombic lattice 4.8. Now an AO χ located at a

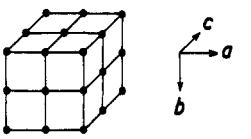

4.8

lattice site (ma, nb, pc) (m, n, p = integers) is given by $\chi(\mathbf{r} - m\mathbf{a} - n\mathbf{b} - p\mathbf{c})$, and the corresponding BO by

$$\phi(k_a,k_b,k_c) = N^{-1/2}\sum_m\sum_n\sum_p \exp(ik_a ma)\exp(ik_b nb)\exp(ik_c pc)\chi(\mathbf{r} - m\mathbf{a} - n\mathbf{b} - p\mathbf{c}) \quad (4.4)$$

where the three independent wave vectors k_a, k_b, and k_c are needed to describe all possible phase relationships between the AO's along the a, b, and c directions, respectively. Due to the periodic nature of the coefficients $\exp(ik_a ma)$, $\exp(ik_b nb)$, and $\exp(ik_c pc)$, only the wave vectors (k_a, k_b, k_c) in the following region may be used in constructing the BO's:

$$-\pi/a \le k_a \le \pi/a$$

$$-\pi/b \le k_b \le \pi/b \quad (4.5)$$

$$-\pi/c \le k_c \le \pi/c$$

TABLE 4.2. Bloch Orbital Coefficients for a 3D Lattice

k point	$\exp(ik_a ma)\ \exp(ik_b nb)\ \exp(ik_c pc)$
$\Gamma = (0, 0, 0)$	$(1)^m\ (1)^n\ (1)^p$
$X = (\pi/a, 0, 0)$	$(-1)^m\ (1)^n\ (1)^p$
$Y = (0, \pi/b, 0)$	$(1)^m\ (-1)^n\ (1)^p$
$Z = (0, 0, \pi/c)$	$(1)^m\ (1)^n\ (-1)^p$

These wave vectors define the FBZ (4.9) of the 3D lattice 4.8. In 4.9, $\Gamma = (0, 0, 0)$, $X = (\pi/a, 0, 0)$, $Y = (0, \pi/b, 0)$, and $Z = (0, 0, \pi/c)$. When the overlap integrals are neglected within the first nearest neighbor approximation, the energy $e(k_a, k_b, k_c)$ of the BO $\phi(k_a, k_b, k_c)$ is given by

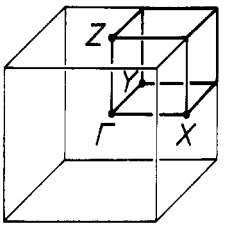

4.9

$$e(k_a, k_b, k_c) = \langle\phi(k_a,k_b,k_c)|H^{eff}|\phi(k_a,k_b,k_c)\rangle = \alpha + 2\beta_a \cos k_a a + 2\beta_b \cos k_b b + 2\beta_c \cos k_c c \quad (4.6)$$

where β_c is the nearest neighbor resonance integral along the c direction: $\beta_c = \langle\chi(\mathbf{r})|H^{eff}|\chi(\mathbf{r}-\mathbf{c})\rangle$. The width of the band given by eq 4.6 is $4(|\beta_a| + |\beta_b| + |\beta_c|)$. As in the cases of 1D and 2D systems, dispersion relations for 3D systems can be easily explained by knowing the coefficients $\exp(ik_a ma)$, $\exp(ik_b nb)$, and $\exp(ik_c pc)$ at a limited number of specific k points such as Γ, X, Y, and Z, which are summarized in Table 4.2.

4.2 Direct and Reciprocal Lattices[10]

To extend our descriptions of electronic band structures to general 3D systems, it is convenient to introduce the concepts of the direct and reciprocal lattices. For a general 3D lattice with repeat vectors **a**, **b**, and **c**, the positions of lattice sites (ma, nb, pc) can be represented as vectors **R**

$$\mathbf{R} = m\mathbf{a} + n\mathbf{b} + p\mathbf{c} \quad (4.7)$$

A set of these vectors is often called the direct lattice. For a given direct lattice, its reciprocal lattice is defined as a set of vectors **K** satisfying the relationship

$$\exp(\mathbf{K}\cdot\mathbf{R}) = 1 \quad (4.8)$$

Then any vector **K** of the reciprocal lattice is expressed as

$$\mathbf{K} = m\mathbf{a}^* + n\mathbf{b}^* + p\mathbf{c}^* \quad (4.9)$$

where **a***, **b***, and **c*** are the so-called reciprocal vectors. For the orthorhombic lattice 4.8, the lengths of **a***, **b***, and **c*** are given by $2\pi/a$, $2\pi/b$, and $2\pi/c$, respectively, and their directions are along **a**, **b**, and **c**, respectively.

Let us consider a direct lattice generated by three repeat vectors **a**, **b**, and **c** which are not necessarily orthogonal to each other, as shown in 4.10, where the volume V of the parallelepiped defined by the three vectors **a**, **b**, and **c** is given by $V = \mathbf{a}\cdot\mathbf{b}\times\mathbf{c}$. Then the reciprocal lattice vectors **a***, **b***, and **c*** are given as follows:

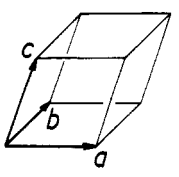

4.10

$$\mathbf{a}^* = (2\pi/V)\ \mathbf{b}\times\mathbf{c}$$
$$\mathbf{b}^* = (2\pi/V)\ \mathbf{c}\times\mathbf{a} \quad (4.10)$$
$$\mathbf{c}^* = (2\pi/V)\ \mathbf{a}\times\mathbf{b}$$

The lengths and directions of the vectors $\mathbf{b}\times\mathbf{c}$, $\mathbf{c}\times\mathbf{a}$, and $\mathbf{a}\times\mathbf{b}$ of eq 4.10 are easily determined. For example, the vector $\mathbf{a}\times\mathbf{b}$ has the length equal to the area of the parallelogram defined by the vectors **a** and **b** and has the direction perpendicular to both **a** and **b**, as shown in 4.11. The positive direction of $\mathbf{a}\times\mathbf{b}$ is obtained according to the right-handed screw convention: rotate **a** around the axis of $\mathbf{a}\times\mathbf{b}$ toward **b** as if to advance a right-handed screw. Then the screw-advancing direction is the positive direction of $\mathbf{a}\times\mathbf{b}$.

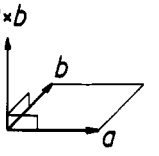

4.11

It is convenient to express a general position, **k**, of the reciprocal space (i.e., the space defined by the reciprocal lattice vectors **K**) in units of the reciprocal vectors, that is

$$\mathbf{k} = x\mathbf{a}^* + y\mathbf{b}^* + z\mathbf{c}^* \quad (4.11)$$

where x, y, and z are dimensionless numbers. Then, for any general 3D lattice, the term $\exp(i\mathbf{k}\cdot\mathbf{R})$ can be written as

$$\exp(i\mathbf{k}\cdot\mathbf{R}) = \exp(ik_a ma)\ \exp(ik_b nb)\ \exp(ik_c pc) \quad (4.12)$$

where $k_a = x(2\pi/a)$, $k_b = y(2\pi/b)$, and $k_c = z(2\pi/c)$. Therefore, the 3D wave vectors (k_a, k_b, k_c) introduced to construct the BO's of a 3D orthorhombic lattice are also valid for any other nonorthorhombic lattice. The wave vector **k** is often represented by (x, y, z). Thus for the FBZ 4.9, $\Gamma = (0, 0, 0)$, $X = (1/2, 0, 0)$, $Y = (0, 1/2, 0)$, and $Z = (0, 0, 1/2)$. The primitive unit cell of reciprocal space defined by equation 4.13 contains all

$$-1/2 \le x \le 1/2$$
$$-1/2 \le y \le 1/2 \quad (4.13)$$
$$-1/2 \le z \le 1/2$$

wave vectors needed for constructing the BO's. This primitive cell of reciprocal space may now be referred to as the first primitive zone (FPZ). For orthorhombic lattices, the FPZ is identical with the FBZ. This is not the case for other lattices, as will be discussed later.

Our notations for BO's and their related expressions are considerably simplified by the use of **k** and **R**. An AO χ_μ located at **R** is given by $\chi_\mu(\mathbf{r}-\mathbf{R})$. Therefore, the BO ϕ_μ is written as

$$\phi_\mu(\mathbf{k}) = \frac{1}{\sqrt{N}}\sum_{\mathbf{R}} \exp(i\mathbf{k}\cdot\mathbf{R})\chi_\mu(\mathbf{r}-\mathbf{R}) \quad (4.14)$$

and the CO's ψ_i are given as linear combinations of the BO's ϕ_μ

$$\psi_i(\mathbf{k}) = \sum_\mu C_{\mu i}(\mathbf{k})\ \phi_\mu(\mathbf{k}) \quad (4.15)$$

The energies $e_i(\mathbf{k})$ of the CO's $\psi_i(\mathbf{k})$ are eigenvalues associated with H^{eff}

$$H^{\text{eff}}\psi_i(\mathbf{k}) = e_i(\mathbf{k})\psi_i(\mathbf{k}) \tag{4.16}$$

which leads to the secular determinant

$$|H_{\mu\nu}(\mathbf{k}) - e_i(\mathbf{k})S_{\mu\nu}(\mathbf{k})| = 0 \tag{4.17}$$

The matrix elements $H_{\mu\nu}(\mathbf{k})$ and $S_{\mu\nu}(\mathbf{k})$ are then expressed as

$$\begin{aligned} H_{\mu\nu}(\mathbf{k}) &= \langle\phi_\mu(\mathbf{k})|H^{\text{eff}}|\phi_\nu(\mathbf{k})\rangle \\ &= \langle\chi_\mu(\mathbf{r})|H^{\text{eff}}|\chi_\nu(\mathbf{r})\rangle + \sum_{\mathbf{R}}[\exp(-i\mathbf{k}\cdot\mathbf{R})\langle\chi_\mu(\mathbf{r}-\mathbf{R}) \\ &\quad |H^{\text{eff}}|\chi_\nu(\mathbf{r})\rangle + \exp(i\mathbf{k}\cdot\mathbf{R})\langle\chi_\mu(\mathbf{r})|H^{\text{eff}}|\chi_\nu(\mathbf{r}-\mathbf{R})\rangle] \end{aligned} \tag{4.18}$$

and

$$\begin{aligned} S_{\mu\nu}(\mathbf{k}) &= \langle\phi_\mu(\mathbf{k})|\phi_\nu(\mathbf{k})\rangle \\ &= \langle\chi_\mu(\mathbf{r})|\chi_\nu(\mathbf{r})\rangle + \sum_{\mathbf{R}}[\exp(-i\mathbf{k}\cdot\mathbf{R})\langle\chi_\mu(\mathbf{r}-\mathbf{R}) \\ &\quad |\chi_\nu(\mathbf{r})\rangle + \exp(i\mathbf{k}\cdot\mathbf{R})\langle\chi_\mu(\mathbf{r})|\chi_\nu(\mathbf{r}-\mathbf{R})\rangle] \end{aligned} \tag{4.19}$$

4.3 Unit Cell Choice and Band Dispersion

Let us consider the body-centered 2D lattice shown in 4.12 as a practical example. For a unit cell, one

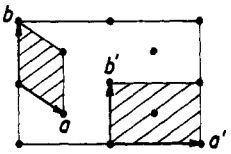

4.12

might choose the primitive cell defined by the nonorthogonal repeat vectors **a** and **b**. Diagram 4.13 shows the reciprocal vectors **a*** and **b*** corresponding to **a** and **b**, which are obtained according to equation 4.10 after adding a unit vector (**c**) at the origin along the **a** × **b** direction. Diagram 4.14 shows the reciprocal lattice

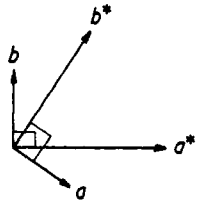

4.13

generated by the vectors **a*** and **b***, where the parallelogram represents the FPZ, $\Gamma = (0, 0)$, $X = (1/2, 0)$, $Y = (0,1/2)$, and $M = (1/2, 1/2)$. The FBZ of the

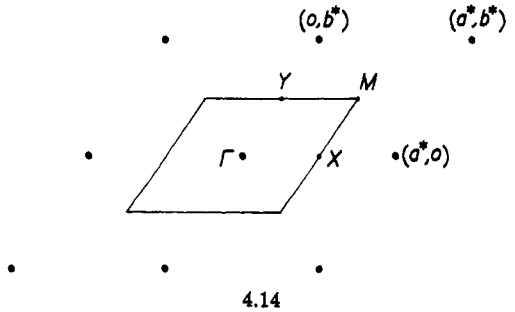

4.14

reciprocal lattice 4.14, shown in 4.15, is obtained as the smallest region around the origin enclosed by planes bisecting every straight line that connects the origin to its neighbor sites (i.e., the Wigner–Seitz cell). Obviously, the FPZ and the FBZ have the same area. The wave vectors of either the FPZ or the FBZ are equally valid in constructing the BO's and CO's.

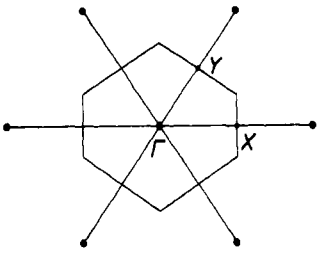

4.15

As a unit cell of the body-centered 2D lattice 4.12, one may choose the body-centered cell defined by the orthogonal vector **a'** and **b'**. The area of the unit cell defined by **a'** and **b'** is twice that defined by **a** and **b**. The reciprocal lattice generated by **a'*** and **b'*** is shown in 4.16, where the rectagular box around the origin is the FPZ. In this case, the FBZ is identical with the

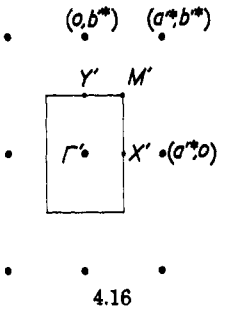

4.16

FPZ. In units of **a'*** and **b'***, $\Gamma' = (0, 0)$, $X' = (1/2, 0)$, $Y' = (0, 1/2)$, and $M' = (1/2, 1/2)$. For the purpose of comparison, the FPZ of 4.14, the FBZ of 4.15, and the FPZ of 4.16 are combined together in 4.17. The FPZ

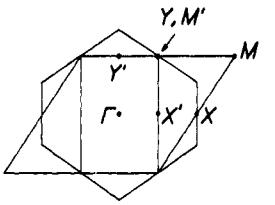

4.17

area of 4.16 is half that of 4.14, because the area of the real space unit cell defined by **a'** and **b'** is twice that defined by **a** and **b**. In 4.16, the $\Gamma' \rightarrow X'$ and $\Gamma' \rightarrow Y'$ directions are equal to the a' and b' directions, respectively. In 4.14 and 4.15, the $\Gamma \rightarrow X$ direction is equal to the a' direction, but the $\Gamma \rightarrow Y$ direction is not identical with the b' direction. The Y' point of 4.16 is equivalent to the point (−0.25, 0.5) in units of **a*** and **b*** in 4.14.

We now examine subtle differences in BO constructions arising from different choices of unit cells. To simplify our discussion, each lattice site of the 2D lattice 4.12 is assumed to have one s orbital. The body-centered unit cell consists of a dimeric unit, so each unit cell has dimer bonding and antibonding levels (4.18 and 4.19, respectively). To clarify our discussion in the

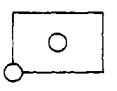

4.18

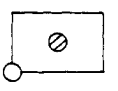

4.19

CHART 4.1

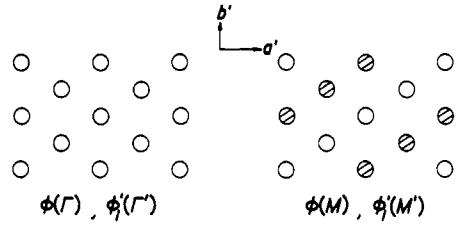

4.20

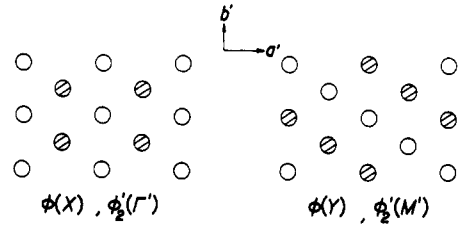

4.21

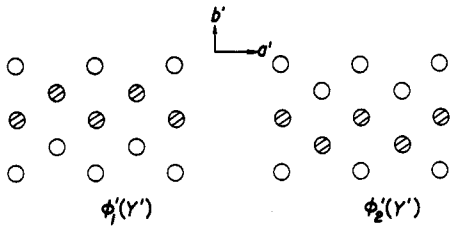

4.22

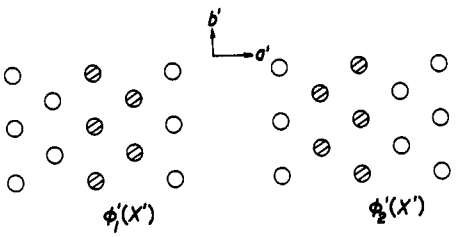

4.23

following, the BO's constructed from the primitive and body-centered cells will be represented by $\phi(\mathbf{k})$ and $\phi'(\mathbf{k}')$, respectively. In addition, the BO's $\phi'(\mathbf{k}')$ constructed from the dimer bonding and antibonding levels will be denoted by $\phi_1'(\mathbf{k}')$ and $\phi_2'(\mathbf{k}')$, respectively. The BO's $\phi(\Gamma)$ and $\phi(M)$ are shown in 4.20 (see Chart 4.1). Inspection of their nodal properties show that $\phi(\Gamma)$ and $\phi(M)$ are equivalent to $\phi_1'(\Gamma')$ and $\phi_1'(M')$, respectively. The BO's $\phi(X)$ and $\phi(Y)$ are shown in 4.21 (Chart 4.1), and are identical with $\phi_2'(\Gamma')$ and $\phi_2'(M')$, respectively. With the body-centered unit cell, the BO's $\phi_1'(Y')$ and $\phi_2'(Y')$ generated from the dimer bonding and antibonding levels are shown in 4.22 (Chart 4.1). These levels are degenerate and are obtained as linear combinations of two degenerate BO's $\phi(\mathbf{k})$ constructed for $\mathbf{k}$ = (0.25, 0.5) and (−0.25, 0.5). The BO's $\phi_1'(X')$ and $\phi_2'(X')$ are shown in 4.23 (Chart 4.1) and are obtained as linear combinations of two degenerate BO's $\phi(\mathbf{k})$ constructed for $\mathbf{k}$ = (0.25, 0) and $\mathbf{k}$ = (−0.25, 0). As can be seen from the above examples, it is important to note that orbital phase relationships given by wave vector points such as Γ, X, Y, and M depend on how unit cell repeat vectors are chosen. Consequently, to analyze the nature and strength of interactions along a certain real space direction for a given crystal, one needs to select a proper wave vector direction, which depends upon the reciprocal vectors associated with the chosen unit cell repeat vectors.

As a second example concerning the choice of reciprocal unit cell, we consider a 2D hexagonal lattice generated by the two vectors **a** and **b** shown in 4.24. The

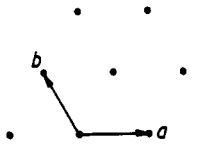

4.24

reciprocal lattice, the FPZ (parallelogram) and the FBZ (regular hexagon) are shown in 4.25, where L = (1/3, 1/3). The band dispersion relations of a 2D hexagonal system are typically shown by plotting $e(\mathbf{k})$ along the edges of the triangle of the FBZ defined by the three points Γ, X, and L. (The X, L, and M points are often

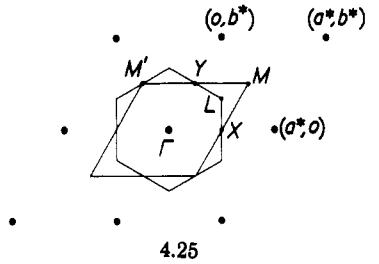

4.25

referred to as M, K, and K', respectively.) According to eq 4.8, $e(\mathbf{k} + \mathbf{K}) = e(\mathbf{k})$. In 4.25, M' = (−0.5, 0.5) = (0.5, 0.5) − (1.0, 0.0) = M − (1.0, 0.0) so that $e(M') = e(M)$. Since $e(M') = e(X)$ by symmetry, $e(M) = e(X)$. Therefore the band dispersion along $L \rightarrow M$ is equivalent to that along $L \rightarrow X$. Thus the band dispersion relation of a 2D hexagonal system can be examined by plotting $e(\mathbf{k})$ along $\Gamma \rightarrow X$ and $\Gamma \rightarrow M$. In band orbital analysis, the use of the $\Gamma \rightarrow M$ line is more convenient than that of $\Gamma \rightarrow L \rightarrow X$ because it provides an easier representation of orbital phase changes. An example of a 2D hexagonal lattice is the graphite layer 4.26, which has two carbon atoms per unit cell. Let us

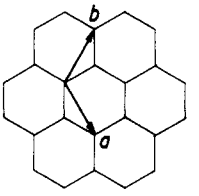

4.26

consider only the bands resulting from the π and π^* orbitals (shown as projection views perpendicular to the layer in 4.27) of each unit cell. The BO's $\phi_1(\mathbf{k})$ and

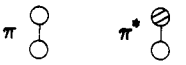

4.27

$\phi_2(\mathbf{k})$ (resulting from π and π^* orbitals, respectively) at Γ are shown in 4.28, those at X in 4.29, and those at M in 4.30. In 4.28–4.30 (Chart 4.2) the BO's are classified as symmetric (S) or antisymmetric (A) with respect to the horizontal mirror plane. As shown in 4.31, the $\phi_1(\mathbf{k})$ and $\phi_2(\mathbf{k})$ levels do not cross along $\Gamma \rightarrow X$ but they do

CHART 4.2

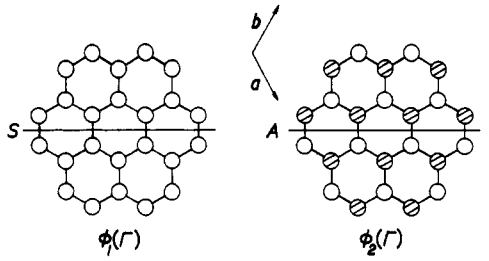

4.28

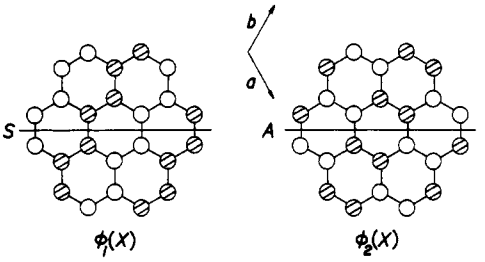

4.29

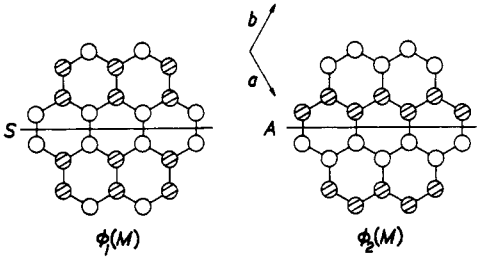

4.30

along $\Gamma \rightarrow M$, thereby leading to the degeneracy at L. Since the graphite layer has two π electrons per unit cell, the resulting bands become half filled.

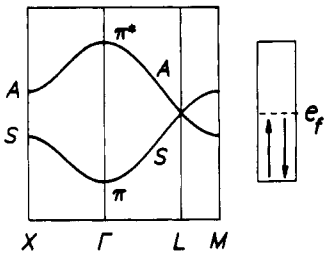

4.31

4.4 Density of States[10]

There are an infinite number of **k** points in the FPZ of reciprocal space. For a given energy band $e_i(\mathbf{k})$, it is practically impossible to examine $e_i(\mathbf{k})$ for all **k** in the FPZ. For simplicity, one may plot $e_i(\mathbf{k})$ vs **k** along several directions of **k** (e.g., $\Gamma \rightarrow X$, $\Gamma \rightarrow Y$ and $\Gamma \rightarrow Z$) so as to estimate the width of the band along those directions. In reciprocal space, all **k** points of the FPZ represent equally allowed states. Of course, it is possible that by symmetry several different **k** values may lead to a same energy value for $e_i(\mathbf{k})$. For example, in the hexagonal FBZ of 4.25, the points X, Y, and M' all lead to an identical set of $e_i(\mathbf{k})$ values. Provided that the energies of a given band are calculated for a fine mesh of **k** points covering the FBZ or FPZ, therefore, the energy levels of the band do not necessarily have the same probabilities thereby leading to the concept known as the density of states (DOS), $n(e)$. The DOS value $n(e)$ refers to the probability of the energy level e. Thus $n(e)$ is nonzero within the allowed energy region of a band, and vanishes in the forbidden energy region. Since a band can accommodate two electrons per unit cell, the $n_i(e)$ values of a given band i satisfy the normalization condition

$$\int_{-\infty}^{\infty} n_i(e)\, de = 2 \qquad (4.20)$$

The electronic structures of solids may be discussed solely on the basis of their DOS values. In such an approach, the band orbital information is completely absent. Details of DOS calculations are described later. For the moment, it is sufficient to observe typical patterns of 1D and 2D lattice. As shown in 4.32, the DOS values of a 1D band peak at the bottom and the top of the band. For a 2D square lattice with equal magnitudes of interaction along the a and b directions, the DOS values peak in the middle of the band as shown in 4.33. The DOS shape for a 3D lattice depends upon the nature of the lattice, but high DOS values generally occur in the middle of the band. An important DOS value in describing the physical properties of metals is the DOS value at the Fermi level, i.e., $n(e_f)$.

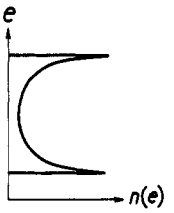

4.32

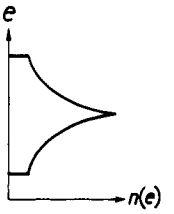

4.33

5. Partially Filled Bands

5.1. Fermi Surface[11]

To examine the concept of Fermi surface, we consider the band dispersion relation of eq 4.3 for a 2D lattice 4.1. Diagrams 5.1a–5.1e (Chart 5.1) show the band dispersion relations along $\Gamma \rightarrow X \rightarrow M \rightarrow Y \rightarrow \Gamma$ for cases a ($\beta_a < \beta_b = 0$), b ($\beta_a < \beta_b < 0$), c ($\beta_a < -\beta_b < 0$), d ($\beta_a = \beta_b < 0$), and e ($\beta_a = -\beta_b < 0$), respectively. There is no interaction along the b direction in case a, so that the band is dispersionless along $\Gamma \rightarrow Y$ and $X \rightarrow M$. In cases b and c, the interaction along the b direction is weaker in magnitude than that along the a direction. In cases d and e, the interactions along the a and b directions are equally strong. The dashed lines of 5.1a–5.1e refer to the Fermi level appropriate for when the band is half filled. For a partially filled band, wave vectors in a certain region of the FPZ lead to occupied band levels (i.e., levels below the Fermi level), and wave vectors in the remaining region of the FPZ lead to unoccupied band levels (i.e., levels above the Fermi level). For simplicity, wave vectors leading to occupied and unoccupied levels of a partially filled band may be referred to as occupied and unoccupied wave vectors, respectively. The occupied and unoccupied wave vectors of the FPZ for 5.1a–5.1e are shown in 5.2a–5.2e (Chart 5.2), respectively, where the occupied wave vectors are shown by shading. Since all k points of the

CHART 5.1

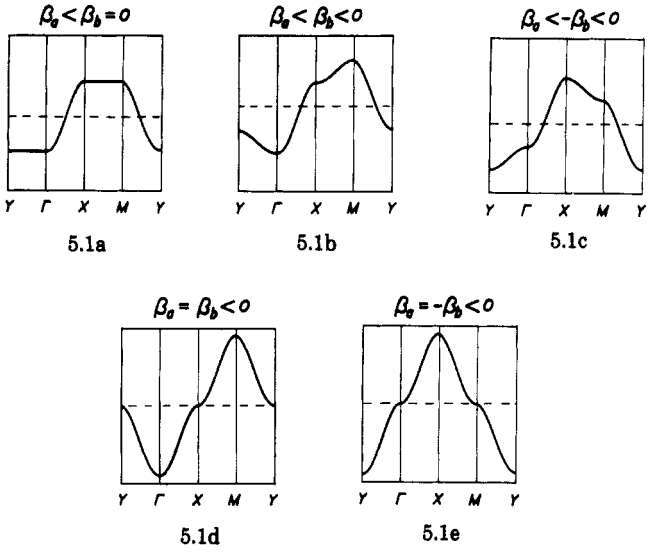

5.1a 5.1b 5.1c

5.1d 5.1e

CHART 5.2

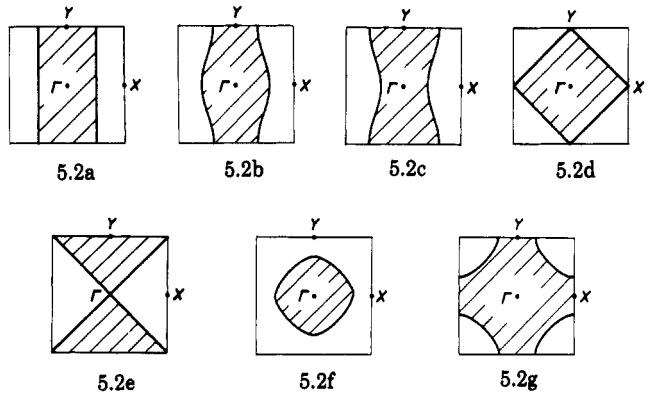

5.2a 5.2b 5.2c 5.2d

5.2e 5.2f 5.2g

CHART 5.3

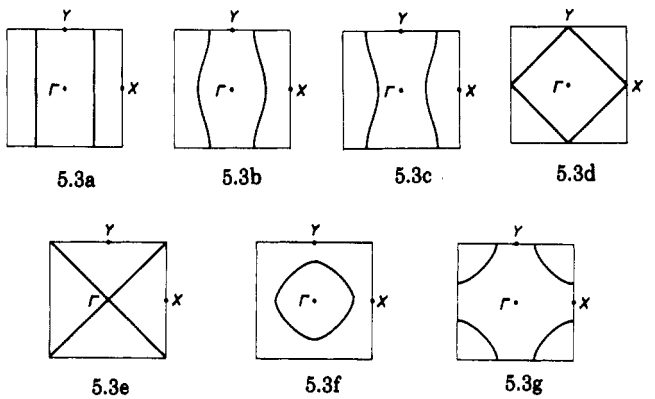

5.3a 5.3b 5.3c 5.3d

5.3e 5.3f 5.3g

FPZ are equally allowed, the occupied region in each of 5.2a–5.2e is one half the area of the FPZ. For a completely filled band, all the wave vectors of the FPZ are occupied. Diagrams 5.2f and 5.2g show the occupied and unoccupied wave vectors of case d when the band is less-than-half and more-than-half filled, respectively.

The boundary surfaces dividing the occupied and unoccupied wave vectors are known as Fermi surfaces. Thus a Fermi surface occurs as a surface in a 3D band description, a line in a 2D band description, and a point in a 1D band description. The wave vectors lying on the Fermi surface are called the Fermi vectors, which are denoted by $\mathbf{k}_f$. Thus the Fermi surfaces of 5.2a–5.2g are given by 5.3a–5.3g (Chart 5.3), respectively. The Fermi surfaces of 5.3a–5.3c each consist of isolated lines, and hence are 1D Fermi surfaces. The Fermi surfaces of 5.3d–5.3g are closed loops, and therefore define 2D Fermi surfaces. (For 5.3e and 5.3g, the Fermi surface patterns of the FPZ need to be repeated in reciprocal space to recognize their closed loops.) Carriers of metals are those electrons at the Fermi level. When a certain wave vector direction does not cross a Fermi surface (e.g., $\Gamma \rightarrow Y$ in 5.3a), there are no electrons at the Fermi level having momentum along that direction, so that the system is not metallic along that direction. Therefore the Fermi surfaces of 5.3a–5.3c refer to 1D metals with metallic properties along the a direction, while those of 5.3d–5.3g represent 2D metals. Fermi surfaces resulting from less-than-half and more-than-half filled bands are often referred to as electron and hole Fermi surfaces, respectively. For example, the Fermi surfaces of 5.3f and 5.3g (see also 5.2f and 5.2g) are electron and hole Fermi surfaces, respectively.

We now generalize our discussion of Fermi surface. With the 1D representation (eq 2.12), the Fermi surface of a half-filled band is given by two k points ($\pm 0.25\ \mathbf{a}^*$ or, equivalently, $\pm\mathbf{k}_f$) as shown in 5.4. With the 2D

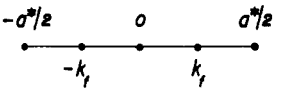

5.4

representation (eq 4.3), the Fermi surface of the half-filled 1D metal for $\beta_a < \beta_b = 0$ is given by two lines perpendicular to $\Gamma \rightarrow X$, as already seen from 5.3a. With the 3D representation (eq 4.6), the Fermi surface of the half-filled 1D band for $\beta_a < \beta_b = \beta_c = 0$ is given by two parallel planes, i.e., $(\pm 0.25, y, z)$, perpendicular to $\Gamma \rightarrow X$ (see 5.5). Likewise, the 2D Fermi surface

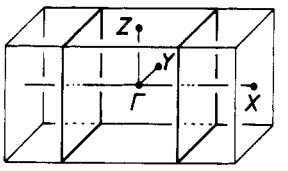

5.5

of 5.3f will be given by a cylinder in the 3D representation ($\beta_a = \beta_b < \beta_c = 0$ with eq 4.6) as shown in 5.6.

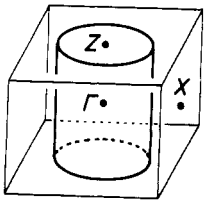

5.6

5.2 Fermi Surface Nesting[4,5]

In addition to the dimensionality of metallic properties, Fermi surfaces are also important in explaining the electronic instabilities of partially filled band systems. When a piece of a Fermi surface can be translated by a vector $\mathbf{q}$ and superimposed on another piece of the Fermi surface, the Fermi surface is said to be nested by the vector $\mathbf{q}$. Since the Fermi surface of 5.3a

consists of two parallel lines, it is nested by an infinite number of wave vectors, two examples of which are shown in 5.7. In discussing Fermi surface nesting, it

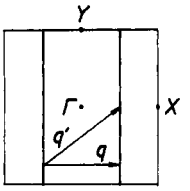

5.7

is important to consider Fermi surfaces in the entire reciprocal space, which is achieved by repeating the Fermi surface pattern of the FPZ in reciprocal space. For example, the Fermi surface of 5.3b is repeated once along $\Gamma \rightarrow Y$ to generate 5.8. Then it is evident that

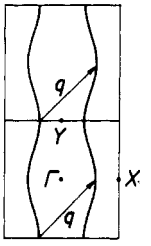

5.8

the Fermi surface of 5.8 is nested by the vector **q** shown. The Fermi surface of 5.3d is a square. Thus when this pattern is repeated in reciprocal space, one finds that the Fermi surface contains two sets of parallel lines orthogonal to each other (see 5.9). Consequently, a

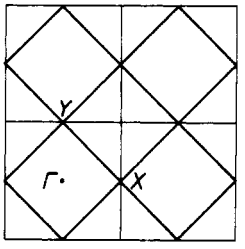

5.9

large number of nesting vectors are possible as in the case of 5.7.

As slightly more complicated examples of Fermi surface nesting, consider the two partially filled 1D bands shown in 5.10 and 5.11. In 5.10 the two bands

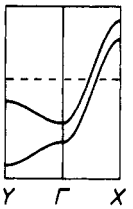

5.10

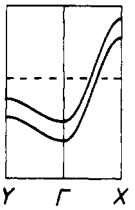

5.11

have an identical slope along $\Gamma \rightarrow X$ but opposite slopes along $\Gamma \rightarrow Y$. In 5.11 the two bands have a same slope along $\Gamma \rightarrow X$ as well as along $\Gamma \rightarrow Y$. Then the Fermi surfaces resulting from the two bands of 5.10 and 5.11 are each found to have four separate pieces as shown in 5.12 and 5.13, respectively. In 5.12 and 5.13, the

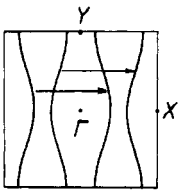

5.12

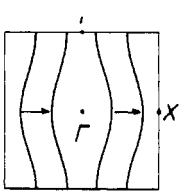

5.13

inner two pieces of the Fermi surface result from the upper band, and the outer two pieces from the lower band. In 5.12 or 5.13, there are two pairs of nested pieces with an identical nesting vector. The importance of Fermi surface nesting lies with the fact that a metallic system with a nested Fermi surface possesses electronic instability and therefore is likely to undergo a metal–insulator phase transition. The latter opens a band gap at the Fermi level thereby destroying the Fermi surface. This topic is discussed in detail in the next section.

6. Electronic States Derived from a Metallic State

In discussing metal–insulator and metal–superconductor transitions, it is convenient to describe the insulating and the superconducting states as a consequence of perturbation on the metallic state. In the following we first examine why Fermi surface nesting is likely to induce a metal–insulator transition from the viewpoint of band orbital mixing. Then we discuss how the phenomenon of electron localization may be understood and also how a superconducting state can be described in terms of band orbital mixing.

6.1 Orbital Mixing and Fermi Surface Nesting[4,5b,12]

A metallic state predicted by one-electron band theory (i.e., a normal metallic state) is not stable when its Fermi surface is nested, and becomes susceptible to a metal–insulator transition under a suitable perturbation. We now examine the nature of the nonmetallic states that are derived from a normal metallic state upon mixing its occupied and unoccupied band levels. For simplicity, consider the 2D representation of a nested Fermi surface shown in 6.1, where the vector **q** is one of many possible nesting vectors. To simplify

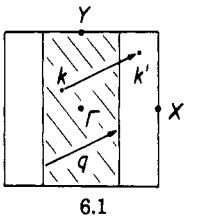

6.1

our notations, the occupied and unoccupied wave vectors are denoted by **k** and **k'**, respectively. Each unit cell will be assumed to contain one AO χ, so the BO's ϕ defined in eq 4.14 are the CO's as well. Suppose we choose the **k** and **k'** values to satisfy the relationship

$$\mathbf{q} = \mathbf{k} - \mathbf{k}' \qquad (6.1)$$

The orbitals $\phi(\mathbf{k})$ and $\phi(\mathbf{k}')$ are eigenfunctions of the unperturbed Hamiltonian H°. If a certain perturbation H' is introduced, these orbitals may not be eigenfunc-

tions of $H^\circ + H'$ anymore, so that they interact to give modified orbitals $\psi(\mathbf{k})$ and $\psi(\mathbf{k}')$

$$\psi(\mathbf{k}) \propto \phi(\mathbf{k}) + \gamma\phi(\mathbf{k}') \qquad (6.2)$$

$$\psi(\mathbf{k}') \propto -\gamma\phi(\mathbf{k}) + \phi(\mathbf{k}')$$

where γ is a mixing coefficient. These orbital mixings are possible when the interaction matrix elements $\langle\phi(\mathbf{k})|H'|\phi(\mathbf{k}')\rangle$ are nonzero. If the $\mathbf{k}$ and $\mathbf{k}'$ values are chosen from the Fermi surface, $\phi(\mathbf{k})$ and $\phi(\mathbf{k}')$ are degenerate (6.2), and nondegenerate otherwise (6.3). The

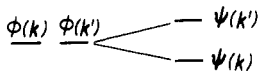

6.2

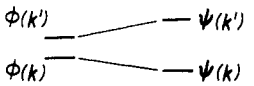

6.3

energy difference between $\phi(\mathbf{k})$ and $\phi(\mathbf{k}')$ become smaller as $\mathbf{k}$ approaches the Fermi surface.

We now examine how the electron density distributions of $\psi(\mathbf{k})$ and $\psi(\mathbf{k}')$ differ from those of the unmodified orbitals $\phi(\mathbf{k})$ and $\phi(\mathbf{k}')$. The electron density distributions associated with $\psi(\mathbf{k})$ and $\psi(\mathbf{k}')$ are given by

$$\psi(\mathbf{k})\psi^*(\mathbf{k}) \propto \phi(\mathbf{k})\phi^*(\mathbf{k}) + \gamma^2\phi(\mathbf{k}')\phi^*(\mathbf{k}') + \Delta\rho$$

$$\psi(\mathbf{k}')\psi^*(\mathbf{k}') \propto \gamma^2\phi(\mathbf{k})\phi^*(\mathbf{k}) + \phi(\mathbf{k}')\phi^*(\mathbf{k}') - \Delta\rho \qquad (6.3)$$

where

$$\Delta\rho = \gamma[\phi^*(\mathbf{k})\phi(\mathbf{k}') + \phi(\mathbf{k})\phi^*(\mathbf{k}')] \qquad (6.4)$$

If we expand $\phi^*(\mathbf{k})\phi(\mathbf{k}')$ and $\phi(\mathbf{k})\phi^*(\mathbf{k}')$ using eq 4.14 and keep only the diagonal terms $\chi(\mathbf{r}-\mathbf{R})\,\chi^*(\mathbf{r}-\mathbf{R})$, it can be shown that

$$\Delta\rho \propto \sum_{\mathbf{R}} \cos(\mathbf{q}\cdot\mathbf{R})\,\chi(\mathbf{r}-\mathbf{R})\,\chi^*(\mathbf{r}-\mathbf{R}) \qquad (6.5)$$

Therefore, with respect to $\phi(\mathbf{k})$ or $\phi(\mathbf{k}')$, $\psi(\mathbf{k})$ and $\psi(\mathbf{k}')$ each have density wave character whose periodicity in real space is governed by the term $\cos(\mathbf{q}\cdot\mathbf{R})$. According to eqs 6.3 and 6.4, $\psi(\mathbf{k})$ leads to density accumulation where $\psi(\mathbf{k}')$ has density depletion, and vice versa. If the density distribution arising from $\phi(\mathbf{k})$ or $\phi(\mathbf{k}')$ is represented by a straight line, then the density accumulation and depletion associated with $\psi(\mathbf{k})$ and $\psi(\mathbf{k}')$ occur as a wave form as shown in 6.4, where shaded and unshaded half waves represent density accumulation and depletion, respectively.

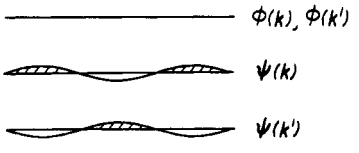

6.4

Suppose that the orbital mixings defined in eq 6.2 are carried out for all occupied $\mathbf{k}$ of the FPZ under the condition $\mathbf{q} = \mathbf{k} - \mathbf{k}'$ to obtain sets of modified orbitals $\{\psi(\mathbf{k})\}$ and $\{\psi(\mathbf{k}')\}$ from sets of unmodified orbitals $\{\phi(\mathbf{k})\}$ and $\{\phi(\mathbf{k}')\}$. The normal metallic state is one in which all the $\phi(\mathbf{k})$ orbitals are doubly occupied (6.5). Then as illustrated in 6.6 for a 1D chain, each site has no magnetic moment and has an identical amount of charge. A charge density wave (CDW) state occurs

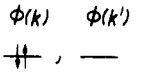

6.5

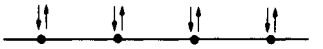

6.6

when the $\psi(\mathbf{k})$ orbitals are doubly occupied (6.7). As illustrated in 6.8 for a 1D chain, a CDW state has no local magnetic moment but charge densities on atomic sites which vary in a wave manner. When $\psi(\mathbf{k})$ and

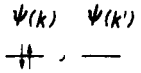

6.7

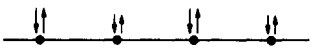

6.8

$\psi(\mathbf{k}')$ are each singly occupied by up-spin and down-spin electrons (6.9), respectively, a spin density wave (SDW) state results. As shown in 6.10 for 1D chain, the SDW state has a local magnetic moment at atomic sites but the total charge density on each atomic site is identical.

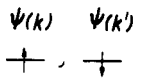

6.9

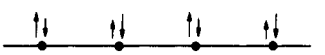

6.10

Unless $\phi(\mathbf{k})$ and $\phi(\mathbf{k}')$ are degenerate, which occurs when $\mathbf{k}$ is on the Fermi surface, the mixing of the unoccupied orbital $\phi(\mathbf{k}')$ into the occupied level $\phi(\mathbf{k})$ has an energy-raising effect, although it can be more than compensated by the energy lowering associated with the interaction energy $\langle\phi(\mathbf{k})|H'|\phi(\mathbf{k}')\rangle$. Thus the orbital mixing between $\phi(\mathbf{k})$ and $\phi(\mathbf{k}')$ becomes more favorable as the energy difference between them decreases, i.e., when the $\mathbf{k}$ value approaches the Fermi surface. The orbital mixing lifts the degeneracy between $\phi(\mathbf{k})$ and $\phi(\mathbf{k}')$ when $\mathbf{k}$ is on the Fermi surface (6.2) and increases the energy difference between $\phi(\mathbf{k})$ and $\phi(\mathbf{k}')$ when $\mathbf{k}$ does not lie on the Fermi surface (6.3). As illustrated in 6.11 for a partially filled 1D band system, the orbital mixing between $\phi(\mathbf{k})$ and $\phi(\mathbf{k}')$ changes their energies in the vicinity of the Fermi level most significantly and opens a band gap at the Fermi level. In 6.11 the band gap is given by 2Δ, where $\Delta =$

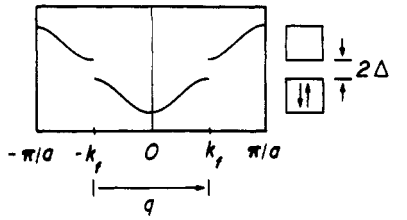

6.11

$\langle\phi(\mathbf{k})|H|\phi(\mathbf{k}')\rangle$ evaluated for $\mathbf{k} = \mathbf{k}_f$. When there exists a Fermi surface nesting, the favorable orbital mixing can be achieved for a large region of $\mathbf{k}$ values in the vicinity of the Fermi surface. This explains why a metal with nested Fermi surface is susceptible toward a phase transition that leads to orbital mixing between the levels around the Fermi level thereby creating a band gap.

By definition, Fermi surfaces disappear when a band gap opens at the Fermi level. So far in our discussion, a complete Fermi surface nesting (e.g., 6.1) has been assumed. In such a case, all the Fermi surface is removed by an appropriate orbital mixing. In certain cases, a Fermi surface nesting may be incomplete, as illustrated in 6.12, if some parts of the Fermi surface have different curvatures. In this case, only the nested

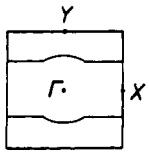

6.12

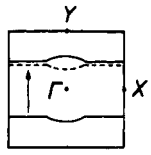

6.13

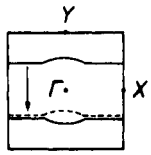

6.14

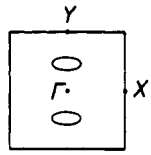

6.15

portion of the surface is removed by orbital mixing as illustrated in 6.13 and 6.14, so that the unnested portion is left as small Fermi surface pockets as shown in 6.15.[4] Since 6.15 has Fermi surfaces, it represents a metallic state as well. Compared with 6.12, 6.15 has a smaller Fermi surface area and hence a smaller number of carriers (i.e., those electrons at the Fermi level). Suppose that a phase transition induced by temperature lowering gives rise to the Fermi surface change 6.12 → 6.15. Such a phase transition is likely to exhibit a resistivity vs temperature plot as shown in 6.16. However, if a Fermi surface nesting is complete, 1.3 will be observed.

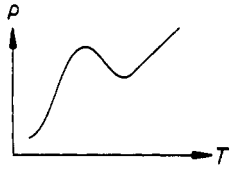

6.16

6.2 CDW Instability[5]

So far we have implicitly assumed that a band level below e_f is completely filled (i.e., occupancy of 1), and that above e_f is completely empty (i.e., occupancy of 0). This picture is valid for all levels when $T = 0$, but only for the levels lying outside the vicinity of the Fermi level (e.g., $e < e_f - 4k_BT$ and $e > e_f + 4k_BT$, where k_B is the Boltzmann constant) when $T > 0$. For the levels lying close to the Fermi level (e.g., $e_f - 4k_BT < e < e_f + 4k_BT$), whose orbital mixing plays a crucial role in lowering the energy of a metal with nested Fermi surface, thereby leading to a metal–insulator transition, their orbital occupancy f(e) at nonzero temperature is given by the Fermi–Dirac distribution function

$$f(e) = 1/[1 + \exp[(e - e_f)/k_BT]] \qquad (6.6)$$

Thus, $f(e) < 1$ for $e < e_f$, and $f(e) > 0$ for $e > e_f$. For example, in the vicinity of the Fermi level of 6.1, the occupancy of $\phi(\mathbf{k})$ is less than 1, and that of $\phi(\mathbf{k}')$ is larger than 0 (at $T > 0$). Consequently, the energy gain resulting from the orbital mixing between $\phi(\mathbf{k})$ and $\phi(\mathbf{k}')$ is maximum at $T = 0$ and decreases as T is raised. Thus, only when T is lowered below a certain temperature does the energy gain associated with the orbital mixing become substantial enough to cause a metal–insulator transition.

Metal–insulator transition arising from a CDW instability is not abrupt, but typically undergoes a series of steps.[1a] This process can be illustrated by considering a 1D metal as composed of weakly interacting chains. At a high temperature, each chain has no tendency for CDW formation, so all chains have uniform density distributions, as illustrated by straight lines in 6.17a. Below a certain temperature T_{1D}, each chain has a tendency for CDW formation. As depicted in 6.17b,

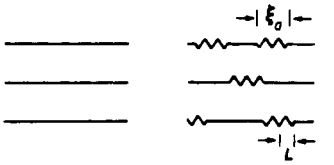

6.17a 6.17b

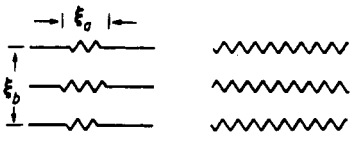

6.17c 6.17d

a CDW is formed and destroyed dynamically at many parts of each chain, and CDW formation in one chain is independent of those in other chains. The average length of a CDW segment (i.e., coherence length) is ξ_a. At a certain temperature T_x below T_{1D}, CDW segments among different chains begin to order along the interchain direction as shown in 6.17c, where ξ_b is the coherence length along the interchain direction. Finally, at a certain temperature T_c below T_x, CDW formation in each chain is complete and CDW's among different chains are ordered, as shwon in 6.17d. Therefore, a long-range order sets in. The coherence lengths ξ_a and ξ_b increase gradually upon lowering the temperature as the extents of long-range order along the intra- and interchain directions increase. These coherence lengths become infinite when a long-range order is complete in both directions.

The temperature dependence of CDW formation in real space, discussed above, is deduced typically from single-crystal X-ray diffraction measurements.[1a] At $T > T_{1D}$, the diffraction pattern of a 1D metal shows only Bragg peaks, as shown in 6.18a. At $T_x < T < T_{1D}$, the diffraction pattern shows diffuse lines (or sheets in 3D representation) perpendicular to the k_a direction, which are located at $\pm 2k_f$ from the rows of the Bragg peaks, as shown in 6.18b. The thickness of the diffuse line is given by ξ_a^{-1}. At $T_c < T < T_x$, the diffuse lines are transformed into diffuse spots (or rods in 3D representation) centered at $(2k_f, q_b)$ and its equivalent positions, as shown in 6.18c. The thickness of a diffuse spot along the k_a and k_b-directions is given by ξ_a^{-1} and ξ_b^{-1}, respectively. Below $T < T_c$, a long-range order sets in so that the diffuse spots are converted into superlattice spots, as shown in 6.18d. The diffuse spot thicknesses along the intra- and interchain directions are inversely

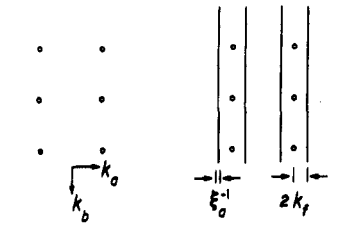

6.18a 6.18b

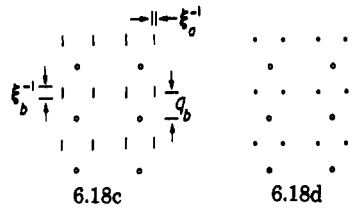

6.18c 6.18d

proportional to the coherence lengths ξ_a and ξ_b, respectively. Thus the diffuse spots become smaller as the extent of long-range order along the two directions increases, and eventually become superlattice spots after a long-range order sets in along both directions.

The perturbation causing the CDW state associated with a nesting vector **q** is a lattice vibration with the wave vector **q**. When the CDW state is formed, the lattice distorts so that the lattice vibration of wave vector **q** is softened. Consequently, the vibrational energy band shows a frequency lowering in the vicinity of the nesting value **q** as shown in 6.19, which is known as the Kohn anomaly.[5i,13] For a Fermi surface consisting of parallel lines (in 2D representation) as in 6.1, an infinite number of nesting vectors **q** are present. However, only one specific **q** value is likely to be adopted by the partially filled band system because distortion induces lattice strain. Thus the chosen **q** value is the one that leads to an optimum energy lowering for the system by balancing the electronic energy gain and the lattice strain. When CDW vectors **q** are integer fractions (i.e., 1/2, 1/3, 1/4, etc.) of reciprocal lattice vectors, the CDW's are said to be commensurate. Otherwise, they are called incommensurate.

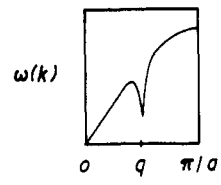

6.19

6.3 Electron Localization[14]

As discussed in section 6.1, new electronic states such as CDW and SDW are derived from a normal metallic state as a consequence of orbital mixing between the occupied and unoccupied levels in the vicinity of the Fermi level. The perturbation causing a CDW state is lattice vibration, as already discussed. The perturbation inducing an SDW state is the on-site electron–electron repulsion U, which may be understood by discussing the relative energies of the low- and high-spin states of a dimer. Consider a dimer with one orbital and one electron on each atomic site (6.20), the MO's of which are expressed as

$$\psi_1 = (\chi_1 + \chi_2)/\sqrt{2}$$

$$\psi_2 = (\chi_1 - \chi_2)/\sqrt{2} \qquad (6.7)$$

provided that the overlap integral $\langle\chi_1|\chi_2\rangle$ is neglected.

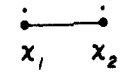

6.20

Then, the energies of these orbitals are given by $e_1 = \alpha + \beta$ and $e_2 = \alpha - \beta$, where β is the resonance integral $\langle\chi_1|H^{\text{eff}}|\chi_2\rangle$. With two electrons, one may construct the low-spin state 6.21 or the high-spin state 6.22. In a one-electron picture, in which electron–electron repulsion is neglected, the low-spin state is always more stable than the high-spin state. However, this is not necessarily the case when electron–electron repulsion is taken into consideration. To simplify our discussion, we neglect all repulsion integrals but the on-site repulsion $U = (\chi_1\chi_1|\chi_1\chi_1) = (\chi_2\chi_2|\chi_2\chi_2)$. Then, in any electronic state, an atomic site with the up- and down-spin electron densities $n\uparrow$ and $n\downarrow$, respectively, contributes the amount of repulsion given by $n\uparrow n\downarrow U$.[12] The on-site charge densities associated with the low-spin (6.21) and high-spin (6.22) states are depicted in 6.23 and 6.24, respectively. In terms of the on-site repulsion, the low-spin state is less stable than the high-spin by $U/2$. In terms of the orbital energies, however, the low-spin state is more stable than the high-spin state by $2|\beta|$, which is equal to $W/2$, where W is the bandwidth (see 2.4) of the corresponding 1D chain 2.1. Therefore, when electron–electron repulsion is taken into consideration, the high-spin state becomes more stable if $U > W$. In general, for a solid in which $U > W$, the total energy can be lowered by introducing spin polarization on each lattice site (i.e., $n\uparrow \neq n\downarrow$) because it reduces the contribution of on-site repulsion to the total energy. This situation is realized in an SDW state discussed in section 6.1 (see 6.10). A CDW or an SDW state constructed from a completely nested Fermi surface has a band gap, and therefore is an insulating state. A phase transition from a metallic state to an insulating state is sometimes referred to as electron localization.

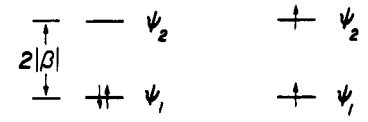

6.21 6.22

6.23 6.24

So far our discussion has been limited to those electronic states that originate from a normal metallic state and is therefore appropriate when the on-site repulsion is small compared with the band width (i.e., $W > U$). When $U \gg W$, electrons are localized on lattice sites. Consider the 1D lattice 6.25a that has one orbital and one electron per site, a typical half-filled band system.

6.25a 6.25b

When $U \gg W$, favorable electronic states are those in which each site has one electron with either up or down spin. All these states are insulating in nature, because electron hopping from one site to another leads to a situation in which two electrons reside on a single site thereby causing on-site repulsion (see 6.25b). Such insulating states resulting from partially filled bands are referred to as Mott–Hubbard localized states. Diagrams 6.26 and 6.27 represent ferromagnetic and antiferromagnetic arrangements of spins, respectively.

6.26

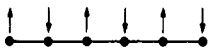

6.27

6.28

These two states have a long-range order. The spin arrangement of 6.28 is an example with no long-range order. Within the one-electron band picture, the ferromagnetic state 6.26 is represented by the electronic structure that results when all the band levels are singly occupied with an identical spin, as depicted in 6.29, which is a solid-state analogue of the dimer high-spin state 6.22. If one neglects electron–electron repulsion terms except for the on-site and the nearest neighbor intersite Coulomb repulsions, the electronic energies of the three states 6.26–6.28 are identical. Consequently, the high-spin band filling scheme 6.29 may be used to represent any localized electronic state arising from a half-filled band. This high-spin band filling scheme

6.29

is useful. For instance, if a quarter-filled band system adopts a low-spin band filling (i.e., each band level is occupied by up- and down-spin electrons), as shown in 2.26, it is susceptible to a tetramerization. However, when this system adopts a high-spin band filling, it would undergo a dimerization instead of tetramerization because band gap opening at the Fermi level can be achieved only by a dimerization (see 6.30).[8b] In 1D

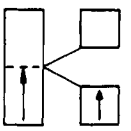

6.30

systems, the distortion (e.g., 2.26) arising from a low-spin band filling ($U < W$) is called a $2k_f$ distortion, since the nesting vector is given by $q = k_f - (-k_f) = 2k_f$. The distortion arising from a high-spin band filling ($U > W$) (e.g., 6.30) is referred to as a $4k_f$ distortion.[5i]

For a half-filled metallic system, the low-spin band filling 6.31 is appropriate since $U < W$ in such a case.

6.31

The energies for the low-lying excited states of the metallic state 6.31 are well described by the band orbital energy differences in the vicinity of the Fermi level. In contrast, it is difficult to describe the energies for the low-lying excited states of a Mott–Hubbard localized state (e.g., the energy differences between the states 6.26–6.28) within a band electronic structure theory, because this theory is based upon the assumption that electrons are delocalized throughout the lattice. Localized electronic systems are typically examined in terms of model Hamiltonians (e.g., spin and Hubbard Hamiltonians) designed to study their low-lying excited states.[14b]

In addition to Mott–Hubbard localization, there is another common source of electron localization, which arises when a lattice is under a random potential (e.g., a random distribution of alkali-metal ions in alkali-metal containing transition-metal oxides). For a metal, a practical consequence of a random potential is to open a band gap at the Fermi level. Insulating states induced by random potentials are referred to as Anderson localized states.[15]

6.4 Superconducting State[16,17]

When the temperature is lowered, a metal may become susceptible to another type of electronic instability, i.e., formation of a superconducting state. For a metal to become superconducting, it should avoid the electronic instability toward a metal–insulator transition leading to a CDW or an SDW state. In general, the Fermi surface of a 1D metal is well-nested, so a 1D metal rarely undergoes a metal–superconductor transition. From the viewpoint of one-electron band theory, a superconducting state also involves orbital mixing among band levels above and below the Fermi level. However, the way this orbital mixing comes about is quite different from that discussed for CDW and SDW states.

Charge carriers of a superconducting state are not individual electrons as in a normal metallic state, but pairs of electrons (called Cooper pairs) having opposite momenta (i.e., opposite wave vectors). Thus, Cooper pairs are described by product functions $\phi(\mathbf{k})\phi(-\mathbf{k})$ and $\phi(\mathbf{k}')\phi(-\mathbf{k}')$, where $\mathbf{k}$ and $\mathbf{k}'$ refer to occupied and unoccupied wave vectors of a normal metallic state, respectively.[5b,16] The energy lowering that brings about superconductivity is induced by the interaction of an occupied pair function $\phi(\mathbf{k})\phi(-\mathbf{k})$ with an unoccupied pair function $\phi(\mathbf{k}')\phi(-\mathbf{k}')$, i.e., $\langle\phi(\mathbf{k})\phi(-\mathbf{k})|H'|\phi(\mathbf{k}')\phi(-\mathbf{k}')\rangle$, where the perturbation H' causing this mixing is electron–phonon interaction in traditional superconductors described by the BCS theory.[17] As a consequence of the interaction between the pair functions, the character of the unoccupied pair function is mixed into that of the occupied pair function. In this indirect way, a superconducting state incorporates unoccupied orbital character into the occupied orbital character. Interactions between the pair functions $\phi(\mathbf{k})\phi(-\mathbf{k})$ and $\phi(\mathbf{k}')\phi(-\mathbf{k}')$ introduce an energy gap at the Fermi level, as do the interactions between $\phi(\mathbf{k})$ and $\phi(\mathbf{k}')$ informing CDW and SDW states. It should be recalled that charge carriers of a superconducting state are Cooper pairs. A superconducting energy gap prevents Cooper pairs from breaking up when there is no excitation energy greater than the gap. The latter is a few multiples

of k_BT_c at absolute zero temperature, where T_c is the superconducting transition temperature, and gradually decreases to zero at T_c.

For traditional superconductors, Cooper pair formation is induced by electron–phonon interaction:[17] As depicted in 6.32, a moving electron causes a slight, momentary lattice deformation around itself. The

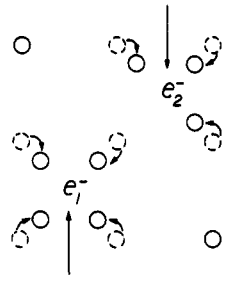

6.32

deformation affects the motion of a second electron (moving in the opposite direction) in the wake of the first in such a way that, effectively, the two electrons move as an entity as if bound together by an attractive force. The extent of electron–phonon coupling is measured by the electron–phonon coupling constant λ. The superconducting transition temperature T_c and the coupling constant λ are governed by the expression[17b]

$$T_c \propto \theta \exp\left(-\frac{1+\lambda}{\lambda+\mu^*}\right) \qquad (6.8)$$

where θ is the Debye temperature and μ^* is the effective Coulomb pseudopotential of the order of 0.1. Among the factors affecting the magnitude of T_c in eq 6.8, the most important one is the electron–phonon coupling constant λ: In general, T_c increases with increasing λ. For a lattice with atoms of mass M and with a vibrational band effective for electron–phonon coupling, the constant λ is given by[17b]

$$\lambda = \frac{n(e_f)\langle I^2\rangle}{M\langle\omega^2\rangle} \propto \frac{1}{M\langle\omega^2\rangle} \qquad (6.9)$$

where $\langle I^2\rangle$ is the square of the electron–phonon interaction element averaged over the Fermi surface, and $\langle\omega^2\rangle$ is the square of the phonon frequency averaged over the vibrational band. The $M\langle\omega^2\rangle$ term has the dimension of a force constant, so a large λ results when the lattice has a low-frequency phonon spectrum (i.e., soft phonons arising from vibrations with shallow potential wells). Therefore, when the lattice is soft toward the low-frequency phonons crucial for superconductivity, the electron–phonon coupling constant λ is large, thereby raising the T_c.[18]

Certainly, for a superconducting state to occur, the energy increase associated with the introduction of unoccupied orbital character should be smaller than the energy gain resulting from interaction among Cooper pair functions. Depending upon the nature and strength of the perturbations causing orbital mixing, a normal metallic state with nested Fermi surface may lead to a superconducting state when the temperature is lowered if CDW or SDW formation associated with the nesting can be prevented. Such a case occurs when the interaction matrix elements $\langle\phi(\mathbf{k})|H|\phi(\mathbf{k}')\rangle$ responsible for CDW or SDW formation are small compared with the interaction matrix elements $\langle\phi(\mathbf{k})\phi(-\mathbf{k})|H|\phi(\mathbf{k}')\phi(-\mathbf{k}')\rangle$ that cause a superconducting state. When the relative stabilities of CDW, SDW, and superconducting states are similar, preference of one state over the other is delicately balanced by a change in temperature and pressure.[19]

7. Computational Aspects[20]

7.1 Band Dispersion Relation

A study of the electronic band structure of a given solid requires solving the appropriate secular determinant (eq 4.17) for a set of k points. To obtain a dispersion relation for a band $\psi_i(\mathbf{k})$ along a specific direction of reciprocal space, one needs to calculate its energy $e_i(\mathbf{k})$ at a number of k points covering that direction. This is illustrated in 7.1 for a band of a 1D system, where the empty circles refer to the calculated energies at the chosen k values. The dispersion relation

7.1

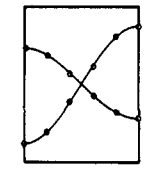

7.2

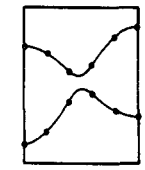

7.3

is then obtained by connecting those calculated energy values, as shown by the solid line in 7.1. A complicated situation arises when two bands overlap in energy as shown in 7.2. If the symmetries of the two band levels differ at all k points along $\Gamma \rightarrow X$, the two band dispersion curves cross as indicated in 7.2. However, if the two bands have an identical symmetry along $\Gamma \rightarrow X$, crossing of the dispersion curves is not possible so that there result in two narrower bands as illustrated in 7.3. To determine whether 7.2 or 7.3 is correct, one may calculate the $e_i(\mathbf{k})$ values for a fine mesh of k points in the vicinity of the crossing (or intended crossing) point.

For computational purposes, the meaning of an energy band needs to be examined further. Suppose that dispersion relations for a 2D lattice are calculated along a series of parallel wave vector directions $\Gamma \rightarrow X$, $A \rightarrow B$, $C \rightarrow D$, etc., as illustrated in 7.4. For simplicity, it

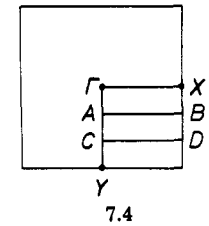

7.4

may be assumed that there are two energy bands, and their dispersion curves cross only along $\Gamma \rightarrow X$, as illustrated in 7.5–7.7. Then the energy surfaces of $e_i(\mathbf{k})$,

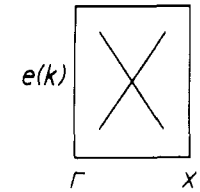

7.5

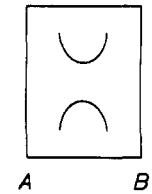

7.6

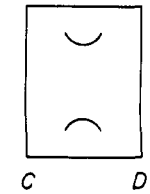

7.7

as a function of **k**, are given as depicted in 7.8. This

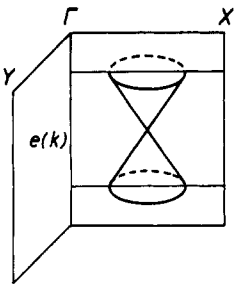

7.8

diagram describes a situation where two energy surfaces touch at one k point along $\Gamma \rightarrow X$. From the viewpoint of energy surfaces, it is more reasonable to consider the lower energy surface of 7.8 as one band and the upper surface as another band. Therefore, when band dispersions cross as in 7.5, one may classify the bands as shown in 7.9 in terms of the lower band (represented by the thick, solid line) and the upper band (represented by the thin, solid line). This classification is

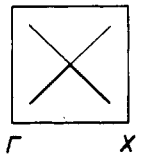

7.9

convenient in calculating Fermi surfaces of partially filled bands.

7.2 Fermi Level

We now discuss how the Fermi level of a partially filled band can be determined by considering a 2D square lattice, for which the FPZ is a square in reciprocal space. As indicated in 7.10, only the wave vectors in the shaded triangle are necessary to consider because the wave vectors of the remaining part of the FPZ are related to those of the shaded triangle by symmetry.

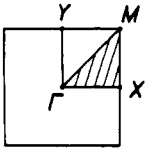

7.10

To examine the $e_i(\mathbf{k})$ vs **k** relationship for the **k** values of the shaded triangle, a set of L points $\{k_1, k_2, ..., k_L\}$ may be evenly distributed to cover the shaded triangle, as shown in 7.11 or 7.12 with a set of 10 k points. In

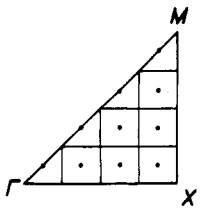

7.11

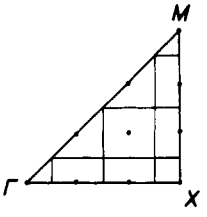

7.12

7.11 the k points avoid the boundary lines $\Gamma \rightarrow X$ and $X \rightarrow M$, while in 7.12 they do not. For a set of evenly distributed k points, each k point represents all the k values in the small square surrounding that point. Depending upon where the k point lies, it may represent only a fraction of the little square. For instance, each k point of 7.11 lying on the $\Gamma \rightarrow M$ line represents half the little square. Thus we define the weight of W_i of each $\mathbf{k}_i$ points such that W_i is proportional to the area $\mathbf{k}_i$ represents and satisfies the normalization condition

$$\sum_{i=1}^{L} W_i = 1 \tag{7.1}$$

For example, in 7.12, the weights of the k points (0, 0), (1/2, 0), (1/3, 0), and (1/3, 1/6) have the ratios 1/8:1/4:1/2:1.

When the crystal orbitals $\psi_n(\mathbf{k})$ are generated on the basis of a set of AO's $\{\chi_1, \chi_2, ..., \chi_M\}$ per unit cell, one obtains a set of M orbital energies $\{e_1(\mathbf{k}_i), e_2(\mathbf{k}_i), ..., e_M(\mathbf{k}_i)\}$ for each $\mathbf{k}_i$ point. Each band level $e_n(\mathbf{k}_i)$ has its probability of occurrence $p_n(\mathbf{k}_i)$ (see below), so there are a set of probabilities $\{p_1(\mathbf{k}_i), p_2(\mathbf{k}_i), ..., p_M(\mathbf{k}_i)\}$ to consider for each $\mathbf{k}_i$ point. Since the weight of the $\mathbf{k}_i$ point is W_i, one obtains

$$p_n(\mathbf{k}_i) = W_i \ (n = 1, 2, ..., M) \tag{7.2}$$

The probability $p_n(\mathbf{k}_i)$ has the meaning that a doubly occupied crystal orbital $\psi_n(\mathbf{k}_i)$ accounts for $2p_n(\mathbf{k}_i)$ electrons. If band calculations are performed for the L points of the set $\{\mathbf{k}_1, \mathbf{k}_2, ..., \mathbf{k}_L\}$, one obtains $M \times L$ band levels and their probabilities

$$\{e_1(\mathbf{k}_i), e_2(\mathbf{k}_i), ..., e_M(\mathbf{k}_i)\} \quad (i = 1, 2, ..., L) \tag{7.3}$$

$$\{p_1(\mathbf{k}_i), p_2(\mathbf{k}_i), ..., p_M(\mathbf{k}_i)\} \quad (i = 1, 2, ..., L) \tag{7.4}$$

The $M \times L$ band levels of eq 7.3 may now be rearranged in ascending order of energy. This ordered set of $M \times L$ levels may be simply written as

$$\{e_1, e_2, ..., e_M, e_{M+1}, ..., e_{2M}, ..., e_{M\times L}\} \tag{7.5}$$

The $M \times L$ probabilities of eq 7.4 may also be arranged as in the orbital energy sequence of eq 7.5 to give the ordered set of $M \times L$ probabilities, which may be written as

$$\{p_1, p_2, ..., p_M, p_{M+1}, ..., p_{2M}, ..., p_{M\times L}\} \tag{7.6}$$

As already mentioned, each doubly occupied level e_i of eq 7.5 would account for $2p_i$ electrons. Therefore if a unit cell contains N_{tot} electrons, then one can easily find the energy level e_{max} that satisfies the constraint

$$\sum_{i=1}^{max} 2p_i = N_{tot} \tag{7.7}$$

Then, e_{max} is the highest occupied band level, i.e., the Fermi level e_f.

It is important to note the difference between the two k point choices such as 7.11 and 7.12. Given an identical number of k points to evenly distribute, the mesh avoiding k points on the FPZ boundaries (e.g., 7.11) has a smaller square area to represent around each k point compared with the mesh including k points on the FPZ boundaries (e.g., 7.12). Thus, the former set provides a more accurate description if calculations involve averaging certain physical properties over the k points of the FPZ. Obviously, if calculations require information about the k points on the FPZ boundaries (e.g., Fermi surface), one must choose a k point mesh including the boundary points.

7.3 Density of States

Given the sets of the ordered orbital energies and their probabilities given by eqs 7.5 and 7.6, respectively, the DOS curves, i.e., $n(e)$ as a function of energy e, can be obtained by replacing each calculated level with a Gaussian function. For example, consider an energy level e_i which has the probability p_i as shown in 7.13.

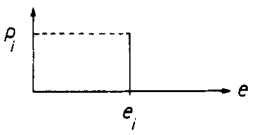

7.13

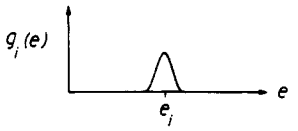

7.14

This discrete level at e_i may be replaced by the Gaussian function $g_i(e)$ centered at e_i shown in 7.14

$$g_i(e) = \frac{1}{\sqrt{\pi}\delta} p_i \exp\left[-\left(\frac{e - e_i}{\delta}\right)^2\right] \tag{7.8}$$

where δ is a constant to be chosen according to the size of the k points mesh. The Gaussian function $g_i(e)$ becomes flatter as δ increases, and satisfies the normalization condition

$$\int_{-\infty}^{\infty} g_i(e)\, de = p_i \tag{7.9}$$

The DOS, $n(e)$, at any given energy e is then obtained by summing contributions from all gaussian functions $g_i(e)$, i.e.

$$n(e) = \sum_{i=1}^{M \times L} 2g_i(e) \tag{7.10}$$

where the factor of 2 is introduced because each level can be occupied by two electrons. The quality of $n(e)$ is improved by using a small value of δ with a large set of k points. In terms of $n(e)$, the electronic energy E_{elec} of a system is written as

$$E_{elec} = \int_{-\infty}^{e_f} n(e) e\, de \tag{7.11}$$

Suppose one calculates the gross population of an atom A, $Q_A(e_i)$, and the overlap population between atoms A and B, $P_{AB}(e_i)$, on the basis of the band level e_i alone (one of the $M \times L$ levels in eq 7.5), assuming that this level is doubly occupied. Then by analogy with eqs 7.8 and 7.10, one might define the DOS-weighted gross and overlap populations as follows:[20,21]

$$Q_A(e) = \sum_i g_i(e) Q_A(e_i) \tag{7.12}$$

and

$$P_{AB}(e) = \sum_i g_i(e) P_{AB}(e_i) \tag{7.13}$$

Equation 7.12 defines the so-called local (or projected) DOS of atom A, $n_A(e)$, which satisfies the normalization condition

$$n(e) = \sum_{\text{all A}} n_A(e) \tag{7.14}$$

Equation 7.13 defines the crystal orbital overlap population.[21] The gross population of atom A, Q_A, and the overlap population between atoms A and B, P_{AB}, of a solid are then written as

$$Q_A = \int_{-\infty}^{e_f} Q_A(e)\, de \tag{7.15}$$

and

$$P_{AB} = \int_{-\infty}^{e_f} P_{AB}(e)\, de \tag{7.16}$$

7.4 Fermi Surface

We examine how to calculate a Fermi surface first by considering a 2D system as an example. To make our discussion general, this 2D system will be assumed to be neither hexagonal nor orthorhombic, so that the FBZ and FPZ are given by a hexagon (7.15) and a parallelogram (7.16), respectively. Suppose the n-th band is

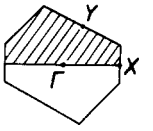

7.15

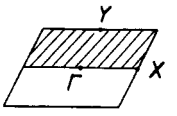

7.16

partially filled. With a set of k points $\{k_1, k_2, ..., k_L\}$ covering one half the FBZ or the FPZ (indicated by shading in 7.15 and 7.16), the Fermi level e_f can be determined. Given the n-th band energies $e_n(\mathbf{k}_i)$ calculated for this set of k points one can generate an analytical expression of $e_n(\mathbf{k})$ as a function of $\mathbf{k}$ by a 2D cubic spline fitting procedure.[22] For this fitting purpose the FPZ is more useful than the FBZ because the former provides a much simpler set of evenly distributed k points to calculate their weights. Once an analytical expression of $e_n(\mathbf{k})$ and the Fermi level e_f are obtained, it is easy to find the Fermi vector $\mathbf{k}_f$, for which $e_n(\mathbf{k}_f) = e_f$, along any wave vector direction desired (see 7.17).

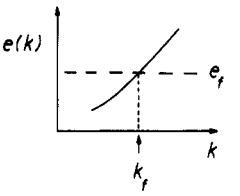

7.17

To present a Fermi surface as a contour in reciprocal space, one needs to find a large number of $\mathbf{k}_f$ values. This is achieved by examining the dispersion relations of the band $e_n(\mathbf{k})$ along several sets of parallel wave vector lines dividing the FPZ. This is illustrated with two sets of parallel wave vector lines in 7.18, where the $\mathbf{k}_f$ points found are represented by heavy dots. If one applies a finer mesh of parallel wave vector lines, more $\mathbf{k}_f$ points are found. Then, the Fermi surface is given by the contour line connecting those $\mathbf{k}_f$ points as shown by the solid line in 7.18.

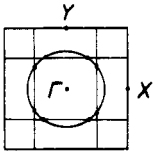

7.18

A 3D representation of a Fermi surface can be obtained by determining the cross sections of the Fermi

surface on a series of parallel wave vector planes dividing the FPZ. This is illustrated in 7.19 with three parallel wave vector planes $(x, y, 0)$, $(x, y, 0.25)$, and $(x, y, 0.5)$. One may carry out a similar analysis by

7.19a

7.19b

7.19c

choosing another set of parallel wave vector planes, e.g., $(0, y, z)$, $(0.25, y, z)$, and $(0.5, y, z)$. Then the shape of a Fermi surface is obtained by combining all these cross sections. For example, a 3D Fermi surface of spherical shape centered at Γ may then be represented in terms of two different sets of 2D contours as shown in 7.20.

7.20

8. Structural Patterns of Low-Dimensional Molybdenum Oxides and Their Related Tungsten Oxides[2,3]

In describing the electronic structures of low-dimensional molybdenum oxides and their related tungsten oxides, it is crucial to know how their crystal structures are built from MO_6 (M = Mo, W) octahedra. The crystal structures of these materials may be viewed as constructed from corner-shared octahedral chains. It is convenient to classify these materials according to whether the corner-shared chains are straight or zigzag.

8.1 Straight Octahedral Chains as Building Blocks

The single octahedral chain 8.1a may be represented by its side- and top-projection views 8.1b and 8.1c, respectively. Then 8.2a and 8.2b represent the side- and top-projection views of a double octahedral chain, which results from the corner-sharing of two single octahedral chains. The double chain 8.2 is converted to "eclipsed"

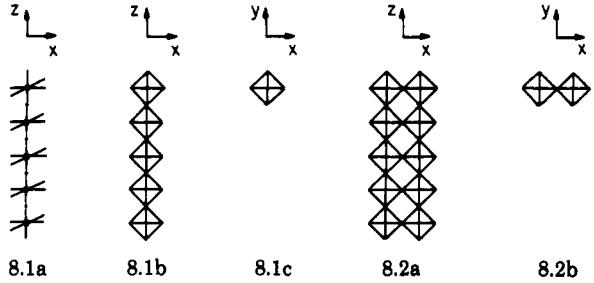

8.1a 8.1b 8.1c 8.2a 8.2b

and "staggered" hump-double chains 8.3a and 8.4a, respectively, by adding hump octahedra (shaded octahedra). The top-projection views of 8.3a and 8.4a can be shown by 8.3b and 8.4b, respectively. Similarly, the top-projection view of the hump-quadruple chain 8.5a is given by 8.5b.

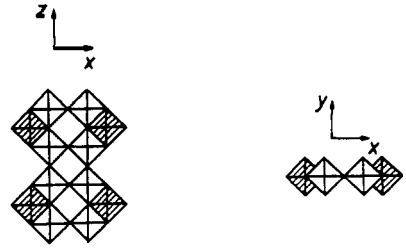

8.3a 8.3b

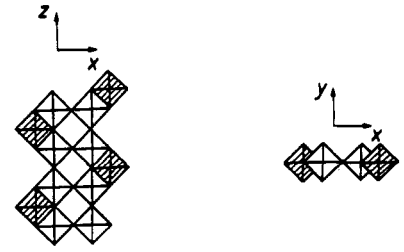

8.4a 8.4b

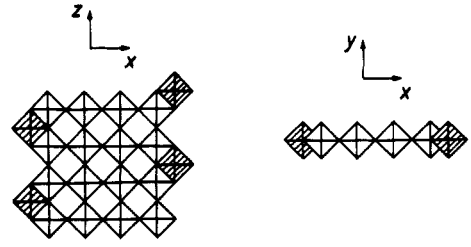

8.5a 8.5b

Edge-sharing of straight octahedral chains leads to important structural patterns, which we show by employing top-projection views. The double chains 8.2 may be edge-shared to form the quadruple chain 8.6 or the M_2O_7 layer 8.7. The latter is found in $La_2Mo_2O_7$.[23]

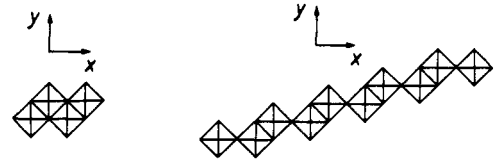

8.6 8.7

By edge-sharing the eclipsed and staggered hump-double chains (8.3 and 8.4, respectively), we obtain the $(MO_3)_6$ layers 8.8 and 8.9, respectively. The $(MO_3)_6$

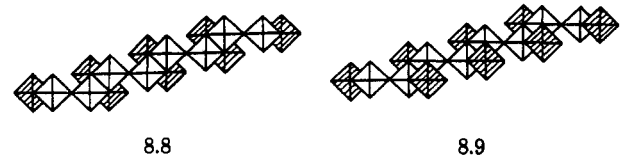

8.8 8.9

layer 8.8 is found in red bronze $K_{0.33}MoO_3$,[24] and the layer 8.9 in $Cs_{0.25}MoO_3$.[25] Blue bronze $K_{0.3}MoO_3$[26] contains the $(MO_3)_{10}$ layer 8.10, which is obtained from the staggered hump-quadruple chains 8.5 by edge-sharing.

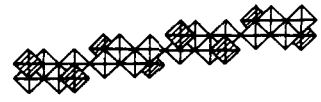

8.10

Corner-sharing of straight multiple octahedral chains leads to perovskite-type layers (i.e., those with only corner-sharing among MO_6 octahedra). For example, the quadruple chains 8.11 can be condensed by corner-sharing to form the layer 8.12, where the adjacent quadruple chains are joined in such a way that the first octahedron of one quadruple unit is condensed with the third octahedron of its adjacent quadruple unit. This

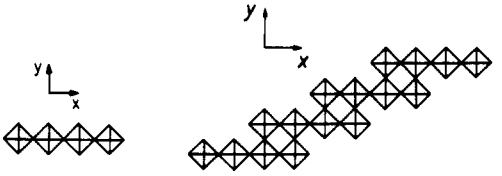

8.11 8.12

(13)-condensation can be carried out for any multiple octahedral chains to form perovskite-type layers of varying thickness. Thus the (13)-condensation of quintuple chain 8.13a gives rise to the perovskite-type layer 8.13b.

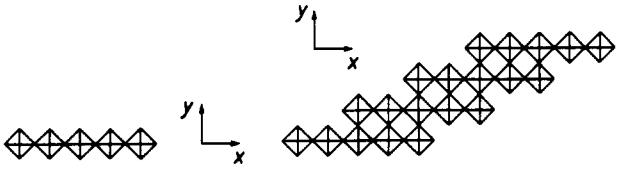

8.13a 8.13b

In Mo_8O_{23}[27] the perovskite-type layers 8.12 are linked by the quadruple chains 8.6 (shaded) as shown in 8.14, while in Mo_9O_{26}[27a] the perovskite-type layers 8.13b are linked by the quadruple chains 8.6. In diphosphate

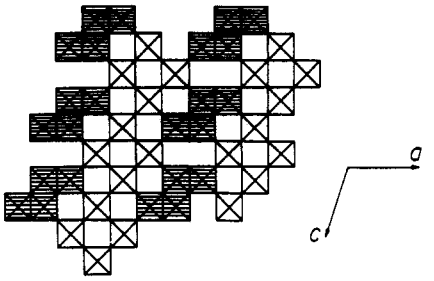

8.14

tungsten bronzes (DPTB's),[3,28] the perovskite-type layers [derived from the (13)-condensation of multiple octahedral chains] are linked by the diphosphate units P_2O_7 (8.15a). A single diphosphate unit may be represented by two tetrahedra sharing a corner (8.15b). In

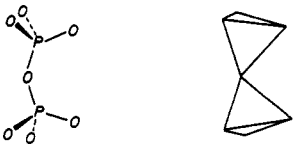

8.15a 8.15b

DPTB's the diphosphate units (shown by shading) link adjacent perovskite-type layers as shown in 8.16. A

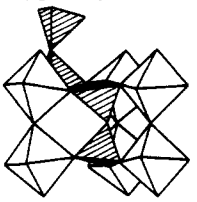

8.16

top-projection view of a DPTB is shown in 8.17, where each filled triangle represents a diphosphate unit.

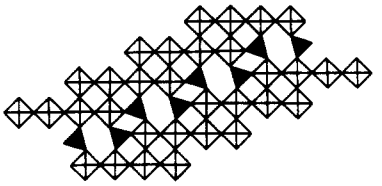

8.17

8.2 Zigzag Octahedral Chains as Building Blocks

The quadruple octahedral unit 8.18 is obtained by sharing the equatorial oxygen atoms of MO_6. As shown

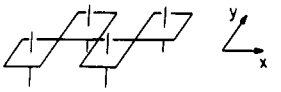

8.18

in 8.19a, these units may be repeated along one direction (i.e., the y-direction in 8.19a) by corner-sharing to form a chain. The projection view of 8.19a along the chain direction can be given by 8.19b, where shaded and unshaded octahedra indicate those closer to and farther away from the viewer, respectively. With this con-

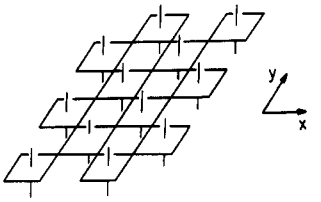

8.19a

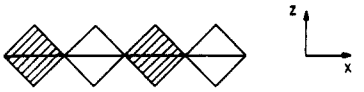

8.19b

vention, the step-layer 8.20a represents the perspective view 8.20b. The width of a step-layer increases with

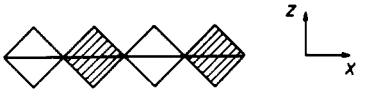

8.20a

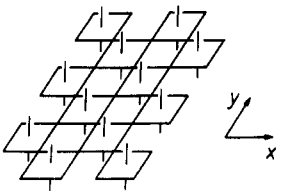

8.20b

the length of a multiple octahedral unit. For example, the sextuple units 8.21 lead to the step-chain 8.22.

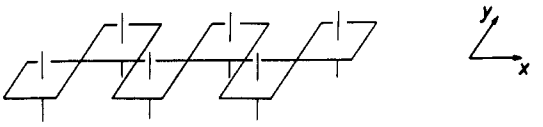

8.21

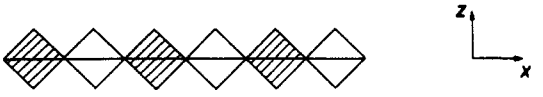

8.22

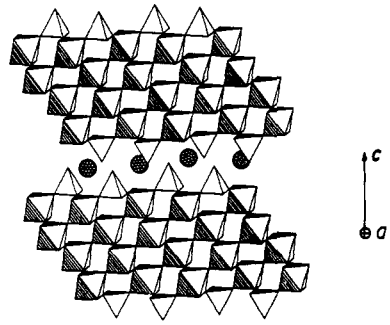

Figure 8.1. Perspective view of two adjacent Mo_6O_{17} layers of $K_{0.9}Mo_6O_{17}$. The c axis is perpendicular to the layer and the a axis is perpendicular to the plane of the figure (derived from ref 1f).

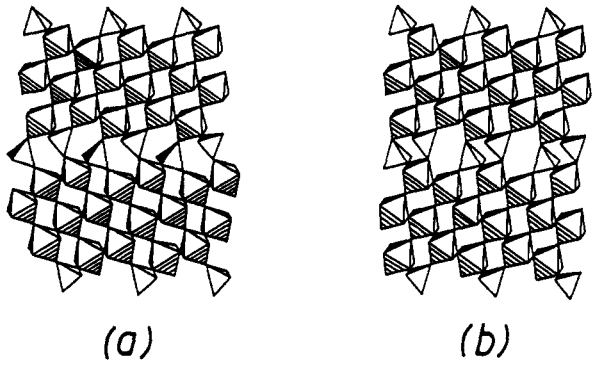

Figure 8.2. Perspective views of the crystal structures of the Magnéli phases: (a) γ-Mo_4O_{11} and (b) η-Mo_4O_{11} (derived from ref 1f).

Important layer patterns are obtained by corner-sharing of step-chains. For instance, (13)-condensation of the step-chains 8.19b provides the step-layer 8.23a, the perspective view of which is given by 8.23b. The

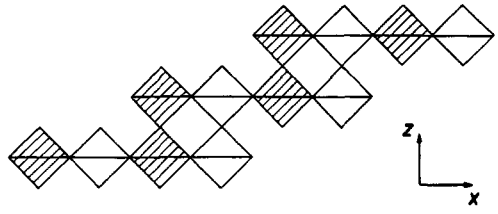

8.23a

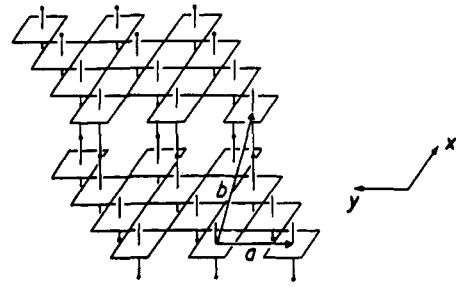

8.23b

step-layer 8.23 is found in monophosphate tungsten bronzes (MPTB's)[3,29] such as $(PO_2)_4(WO_3)_4(WO_3)_4$[30] and $A_x(PO_2)_4(WO_3)_4(WO_3)_4$ (A = alkali metal).[31] Likewise, (13)-condensation of the step-chains 8.22 leads to the step-layer 8.24, which is found in the Magnéli phases γ- and η-Mo_4O_{11}[32] as well as the MPTB's such as $(PO_2)_4(WO_3)_6(WO_3)_6$[33] and $A_x(PO_2)_4(WO_3)_6(WO_3)_6$.[31b]

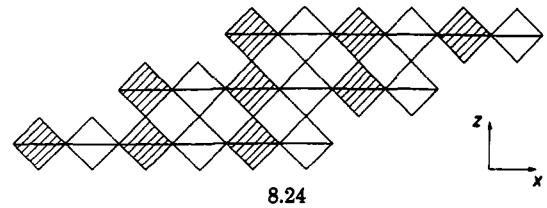

8.24

Two variations of step-chain condensation are shown in 8.25 and 8.26. The step-layer 8.25, found in lithium purple bronze $Li_{0.9}Mo_6O_{17}$,[34] is obtained from the step-chains 8.19 by applying (11)- and (13)-condensations. As indicated, this step layer consists of four nonequivalent metal atoms. In the step-layer 8.26, the step-chains 8.19 and 8.20 alternate and they are joined by (12)-condensation. It is important to note that the step-layer 8.26 is hexagonal in symmetry, which becomes clear when the layer is viewed along the direction perpendicular to the layer (indicated by the arrow in 8.26). This will be discussed later.

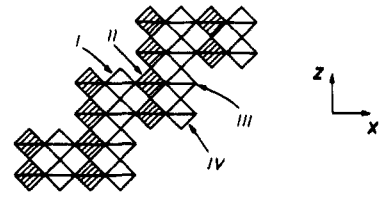

8.25

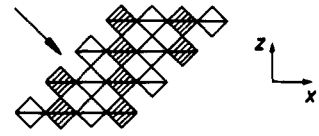

8.26

In actual compounds containing the step-layers, the surfaces of these layers are capped with MoO_4 or PO_4 tetrahedra. For instance, as schematically shown in Figure 8.1, the surfaces of the step-layers 8.26 in purple bronze $K_{0.9}Mo_6O_{17}$[35] are capped with MoO_4 tetrahedra such that the resulting Mo_6O_{17} layers are separated by potassium cations. As shown in Figures 8.2a and 8.2b, respectively, the step-layers 8.24 are linked by MoO_4 tetrahedra in γ- and η-Mo_4O_{11}, respectively.[32] The step-chain planes are parallel in adjacent step-layers for η-Mo_4O_{11}, but this is not the case for γ-Mo_4O_{11}. With the notation used for the MPTB's $(PO_2)_4(WO_3)_p(WO_3)_q$ (p, q = integers), Mo_4O_{11} is written as $(MoO_2)_4(MoO_3)_6(MoO_3)_6$. In the MPTB's, the step-layers made up of WO_6 octahedra are linked by PO_4 tetrahedra.[29]

9. Red Bronzes

Red bronzes $A_{0.33}MoO_3$ (A = K, Rb, Cs, Tl) consist of isolated layers of composition MoO_3 (8.8), and the A^+ cations lie in between these layers.[24,36] Hence they can be referred to as 2D red bronzes to distinguish from $Li_{0.33}MoO_3$[37] red bronze which has a 3D structure (see section 16). All these bronzes are found to be semiconductors.[36a,38] On the basis of structural considerations, it was proposed[39] that the 2D red bronze $K_{0.33}MoO_3$ is not a regular semiconductor (i.e., one that has no partially filled bands in a one-electron picture) but a Mott insulator[14] (i.e., a semiconductor despite the

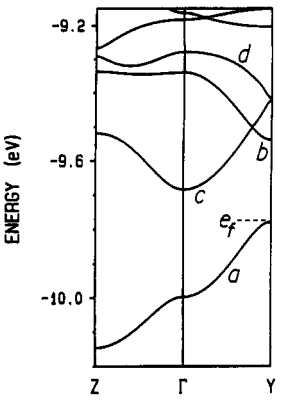

Figure 9.1. Bottom portion of the t_{2g}-block bands of the real Mo_6O_{18} layer. In units of the reciprocal vectors **a***, **b***, and **c***, the points Γ, *Y*, and *Z* are defined as Γ = (0, 0), *Y* = (*b**/2, 0), and *Z* = (0, *c**/2).

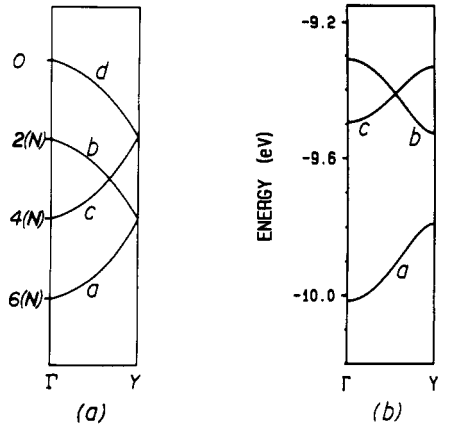

Figure 9.2. (a) *xz* bands of the ideal Mo_4O_{18} chains and (b) bottom portion of the t_{2g}-block bands of the real Mo_4O_{18} chains.

presence of partially filled bands in a one-electron picture). However, magnetic susceptibility and ESR studies suggest that the 2D red bronzes have delocalized d electrons and have very little spin density.[36a,40] These findings are not consistent with the proposal that the 2D red bronzes are Mott insulators.

The repeat unit of the MoO_3 slabs in 2D red bronzes contains six octahedra (Mo_6O_{18}, see 8.3 and 8.8), and hence there are two electrons to fill the bottom portion of the t_{2g}-block bands. Shown in Figure 9.1 are the dispersion relations calculated[41] for the bottom portion of the t_{2g}-block bands of $Tl_{0.33}MoO_3$.[36a] The lowest band a is separated by an indirect gap of about 0.12 eV from the next band c. In addition, as will be seen later, these bands are as dispersive as those calculated for other bronzes exhibiting metallic properties. Since the Mott insulators are characterized by partially filled narrow bands, the 2D red bronzes cannot be Mott insulators but regular semiconductors. This conclusion is consistent with several observations: the optical reflectivity of the red bronze $K_{0.33}MoO_3$ suggests a band gap of 0.5 eV,[38a] and the temperature dependence of the resistivity in $Cs_{0.33}MoO_3$[38b] and $Tl_{0.33}MoO_3$[36a] indicates a band gap of 0.24 and 0.52 eV, respectively.

9.1 Distortion and Lowest Lying t_{2g}-Block Levels[4]

In order to understand why an energy gap exists between bands a and c of the Mo_6O_{18} layer 8.8, it is necessary to analyze the nature of the bands. This task is considerably simplified by studying the different types of distortion present in the octahedra of the Mo_6O_{18} layer. The t_{2g}-block levels of a regular MoO_6 octahedron have antibonding combinations between molybdenum 4d and oxygen 2p orbitals. Therefore an Mo–O shortening raises any t_{2g}-block level if this level has an antibonding combination of Mo and O orbitals along the shortened Mo–O bond. Consequently, a distortion in which one Mo–O bond is shortened (see 9.1) leaves one t_{2g} level (i.e., *xy*, which is the δ orbital with respect to the shortened Mo–O bond axis) unaffected, but raises the remaining two levels (i.e., *xz* and *yz*, which are the π orbitals with respect to the shortened Mo–O bond axis). On the other hand, all three t_{2g}-block levels are raised by a distortion in which two or more Mo–O bonds are shortened (see 9.2). Thus inspection of the nature and extent of distortion in MoO_6 octahedra allows us to predict which MoO_6 octahedra of a given molybdenum oxide would have d

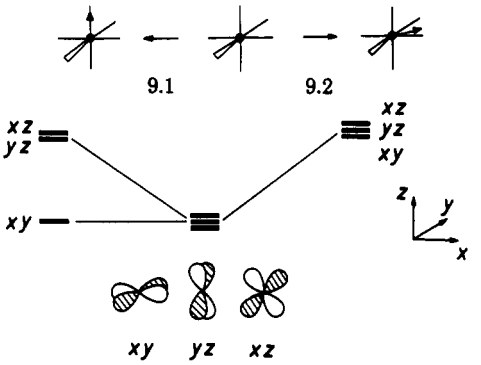

electrons and what kinds of d-block bands the oxide is likely to have.[4] Shown in 9.3 and 9.4 are the various Mo–O bond lengths found in the Mo_6O_{18} layers of $Tl_{0.33}MoO_3$.[36a] The hump octahedra have two strong

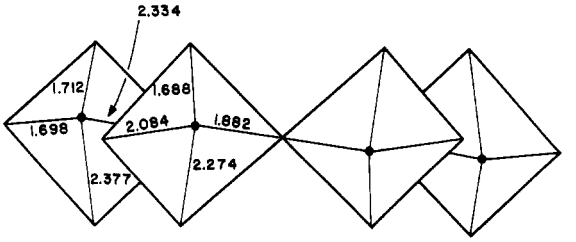

9.3

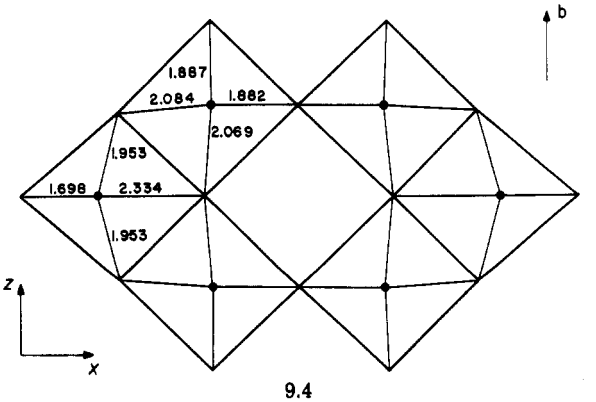

9.4

O–Mo···O bond alternations (i.e., distortion type 9.2), while only one strong O–Mo···O alternation occurs in the chain octahedra (i.e., distortion type 9.1). Thus, the t_{2g}-block levels of the hump octahedra are high in energy. The strong alternation in the chain octahedra occurs in a direction perpendicular to the chain direction, so that only the d orbital that is δ with respect to this direction will remain low in energy. This orbital, *xz* with the axis shown in 9.4, makes π-type overlap with the oxygen p orbital along the chain axis. Thus, it is

sufficient to consider the xz bands of the Mo_4O_{18} chain 8.2a in describing the low-lying d-block bands of the Mo_6O_{18} layer.[41]

9.2 Intrachain Interactions

In discussing the bottom d-block bands of the Mo_4O_{18} chains present in the Mo_6O_{18} layer, it is convenient to first examine the xz bands of the ideal Mo_4O_{18} chain 8.2a in which all MoO_6 octahedra are regular. These bands are shown in Figure 9.2a.[41] The cluster orbitals relevant for band orbital construction are shown in 9.5, where dots are used to indicate the absence of oxygen p orbital. For simplicity, the p orbitals of the nonshared oxygen atoms are not shown in 9.5. The energy ordering of these four levels is simply obtained by counting the number of dots [i.e., (N)-type interactions of 2.43 or 2.44] in the cluster orbitals, as shown in 9.6.

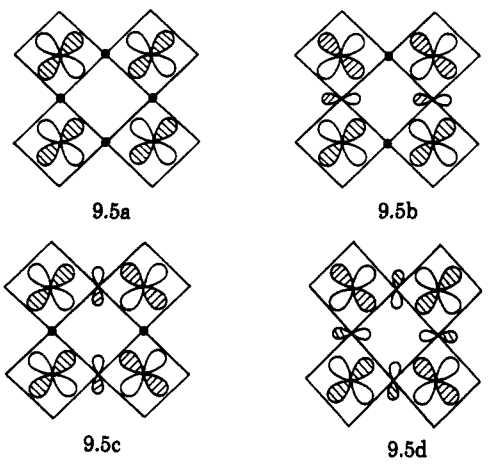

9.5a 9.5b 9.5c 9.5d

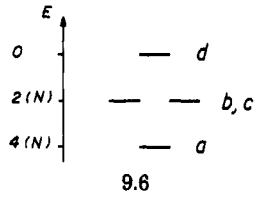

9.6

Band a at Γ has the nodal pattern of 9.7. Bands a and b at Y have the nodal patterns 9.8 and 9.9, respectively. Band c at Γ has the nodal pattern of 9.10. As discussed in section 2.4, the d-block band levels of a crystal structure obtained by sharing octahedral corners are raised in energy when the orbitals of the bridging ligand atoms are allowed by symmetry to mix with the metal d orbitals. There are three different types of oxygen bridges in the Mo_4O_{18} chain 8.2a: Within a four Mo atom unit cell, two oxygen atom bridges are parallel (∥) to the chain but the other two are perpendicular (⊥) to the chain. Between adjacent unit cells, there are two oxygen bridges parallel to the chain. The metal bridging-ligand antibonding interactions present in the orbitals of bands a–d at Γ and Y are summarized in Table 9.1. It is clear from this table and 9.8–9.10 that bands a and b at Y, and band c at Γ, are all degenerate. Likewise, bands c and d at Y, and band b at Γ, are all degenerate.

As can be seen from 9.4, there exists a bond length alternation of the type Mo···O···Mo–O–Mo along the real Mo_4O_{18} chain (i.e., 2.069, 2.069, 1.887, 1.887 Å), which therefore lifts the degeneracy between 9.8 and 9.9 (see Figure 9.2b). Since the long distances are associated with the presence of the hump octahedra, the lower

TABLE 9.1. Antibonding Contributions of the Oxygen p Orbitals of the Mo–O–Mo Bridges in the xz-Block Bands of the Mo_4O_{18} chains[a]

band	unit cell orbital	wave vector point	within a unit cell ∥	within a unit cell ⊥	between unit cells
a	**9.5a**	Γ	(N)	(N)	(N)
a	**9.5a**	Y	(N)	(N)	(Y)
b	**9.5b**	Γ	(Y)	(N)	(Y)
b	**9.5b**	Y	(Y)	(N)	(N)
c	**9.5c**	Γ	(N)	(Y)	(N)
c	**9.5c**	Y	(N)	(Y)	(Y)
d	**9.5d**	Γ	(Y)	(Y)	(Y)
d	**9.5d**	Y	(Y)	(Y)	(N)

[a] The presence of the antibonding contribution is indicated by the symbol (Y), and the absence of it by the symbol (N).

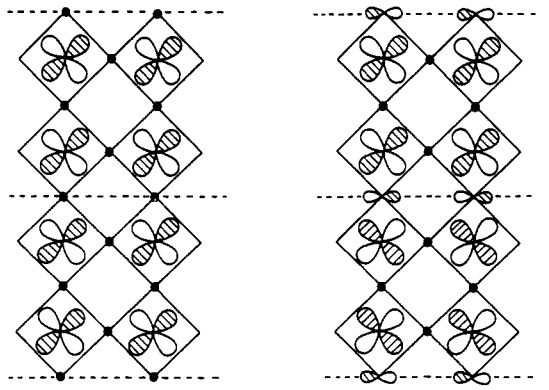

9.7 9.8

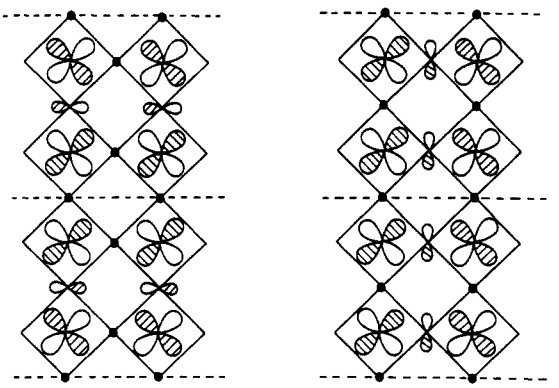

9.9 9.10

energy orbital is given by 9.11a, and the higher energy one by 9.11b. Band orbital 9.11a is built from the

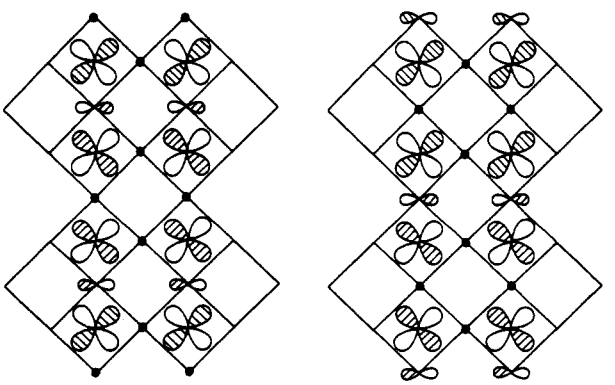

9.11a 9.11b

cluster orbital 9.5b and belongs to band b of the Mo_4O_{18} ideal chain, while 9.11b is built from the cluster orbital

9.5a and belongs to band a in the ideal Mo_4O_{18} chain. Therefore, in the real Mo_4O_{18} chain, there is an avoided crossing between bands a and b, as illustrated in 9.12.

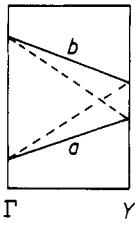

9.12

The short Mo–O bonds (1.882 Å) in the Mo–O–Mo linkages of 9.3 perpendicular to the chain are comparable to the short Mo–O bonds (1.887 Å) of 9.4 along the chain. Thus the extent of antibonding in 9.9 and 9.10 of the real Mo_4O_{18} chain are comparable. Therefore, when the Mo_4O_{18} chain distorts from ideal to the real structure, band a at Y is lowered, while both band b at Y and band c at Γ are raised. This is why, as shown in Figure 9.2b, the real Mo_4O_{18} chain has a band gap.[41]

9.3 Interchain Interactions

We now examine how the t_{2g}-block bands of the real Mo_4O_{18} chain are shifted in energy by the interchain interactions in the Mo_6O_{18} layer. Comparison of Figures 9.1 and 9.2b shows that band a remains unchanged in energy along Γ → Y but is lowered in energy along Γ → Z. Band c is shifted downward in energy along Γ → Y but is raised in energy along Γ → Z. When viewed along the chain, band orbitals 9.7–9.9 are represented by 9.13, and band orbital 9.10 by 9.14. With such

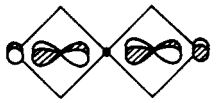

9.13

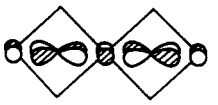

9.14

representations, bands a and b of Figure 9.1 at Γ are described by 9.15, while band c of Figure 9.1 at Γ is described by 9.16. Note from 9.15 and 9.16 that the

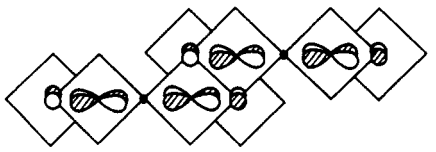

9.15

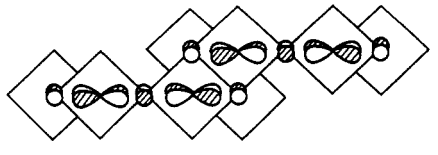

9.16

p orbital of each external oxygen atom of one Mo_4O_{18} chain is located along the nodal plane of the xz orbital of the adjacent Mo_4O_{18} chain. Thus, no strong direct interchain interactions are expected in the Mo_6O_{18} layer. The essential orbital patterns of 9.15 and 9.16 around the hump MoO_6 octahedra are given by 9.17 and 9.18, respectively. Since the d-block levels of the hump

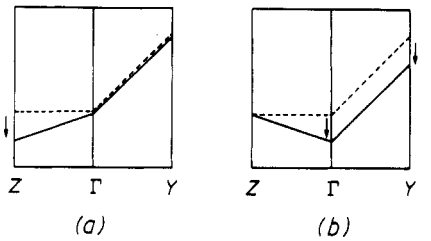

Figure 9.3. Correlation of the dispersion relations of an Mo_6O_{18} layer band (solid lines) with those of the corresponding Mo_4O_{18} chain band (dashed lines) for the cases when the interchain orbital patterns at Γ are given by 9.17 in a and by 9.18 in b.

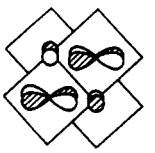

9.17

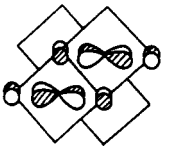

9.18

octahedra are higher lying in energy, they act as acceptor orbitals, i.e., they combine in-phase with the chain d-block levels if allowed by symmetry. As illustrated in 9.19 and 9.20, respectively, the symmetry of 9.17 does not allow such a mixing but that of 9.18 does.

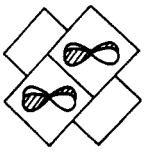

9.19

9.20

When this mixing occurs, the oxygen p orbital contribution of the inner two oxygen atoms of 9.18 decreases (because the p orbital is located close to the nodal plane of the xz orbital of the hump octahedron) thereby further lowering the band orbital energy.

Along Γ → Z (i.e., the interchain direction) the relative orbital phases between adjacent chains must change from in-phase to out-of-phase or vice versa. Therefore, bands with the orbital patterns 9.17 and 9.18 at Γ gradually pick up the orbital patterns of 9.18 and 9.17, respectively. Consequently, along Γ → Z, bands of the type 9.17 at Γ will be lowered in energy but bands of the type 9.18 at Γ will be raised in energy. Along Γ → Y, all bands retain the orbital patterns around the hump octahedra. Therefore, the whole band of the Mo_6O_{18} layer will be lowered with respect to that of the Mo_4O_{18} chain if the orbital pattern at Γ is 9.18 while the band remains unshifted if the orbital pattern at Γ is 9.17. Figures 9.3a and 9.3b show how the band dispersion relations of the Mo_6O_{18} layer (solid lines) are related to those of the Mo_4O_{18} chain (dashed lines) for the cases when the interchain orbital patterns at Γ are given by 9.17 and 9.18, respectively. As shown in Figure 9.4, whether there is a band gap between bands a and c or not depends critically on the relative strengths of the intrachain distortion effect (ΔE_{intra}) and the interchain interaction effect (ΔE_{inter}). The Mo–O distances associated with the antibonding interactions in band a at Y and band c at Γ are substantially different. For an isolated, real Mo_4O_{18} chain, the Mo–O bonds engaged in antibonding interactions are 2.069 and 2.084 Å for band a at Y, but 1.882 and 2.084 Å for band c at Γ. Due

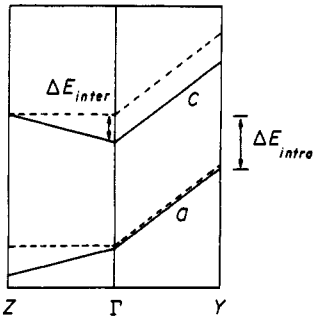

Figure 9.4. Dispersion relations of the Mo_6O_{18} layer bands a and c (solid lines) vs the corresponding Mo_4O_{18} chain bands (dashed lines).

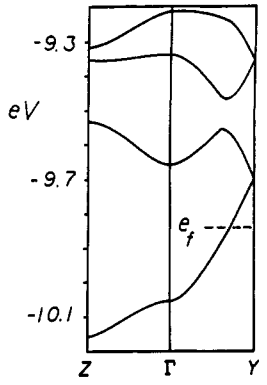

Figure 9.5. Bottom portion of the t_{2g}-block bands calculated for the Mo_6O_{18} layer of $Cs_{0.25}MoO_3$. The wave vectors Γ, Y, and Z are defined as Γ = (0, 0), Y = ($b^*/2$, 0), and Z = (0, $c^*/2$).

to the interchain interactions, the antibonding interaction of the Mo–O = 2.084 Å bond is removed in band c at Γ but retained in band a at Y in the Mo_4O_{16} layer. Although this makes smaller the energy difference between band c at Γ and band a at Y, (i.e., the band gap), band c at Γ still should lie above band a at Y in the Mo_6O_{18} layer because the intrachain antibonding of band c at Γ is associated with a much shorter Mo–O bond (i.e., 1.882 Å). Comparison of Figures 9.1 and 9.2b shows that the strength of the intrachain distortion is about twice that of the interchain interaction. This leads to a band gap between bands a and c of the Mo_4O_{18} layer, and consequently to the semiconducting properties of 2D red bronzes.

9.4 Crystal Symmetry and Band Gap

The above analysis makes it clear that although the hump octahedra do not participate in the lower t_{2g}-block bands of the 2D red bronzes, they play an extremely important role in determining their electronic structures by imposing a strong intrachain distortion. Another example showing the importance of these hump octahedra is provided by the cesium molybdenum bronze $Cs_{0.25}MoO_3$,[25] which is closely related to the 2D red bronze $Cs_{0.33}MoO_3$.[36b] As discussed in section 8, the crystal structure of these two bronzes differ in the way the hump octahedra are distributed. $A_{0.33}MoO_3$ contains MoO_3 layers 8.8 while $Cs_{0.25}MoO_3$ contains MoO_3 layers 8.9. This leads to slightly different distortions of the Mo_4O_{18} chains of the MoO_3 slabs. Since in $Cs_{0.25}MoO_3$ the hump octahedra are added to the Mo_4O_{18} chains in a zigzag way (8.4), the resulting Mo_6O_{24} chains have a symmetry element of 2-fold screw rotation.

Figure 9.5 shows the dispersion relations calculated[42] for the lower t_{2g}-block bands of the Mo_6O_{18} layer of $Cs_{0.25}MoO_3$. The essential difference between Figures 9.5 ($Cs_{0.25}MoO_3$) and 9.1 ($A_{0.33}MoO_3$) is that the bands are paired up at Y in the former but not in the latter. This difference, essential for the semiconducting properties of $A_{0.33}MoO_3$, originates from the fact that the distortions in the Mo_4O_{18} chains of $Cs_{0.25}MoO_3$ have the 2-fold screw rotation axis which makes orbitals 9.8 and 9.9 equivalent.

Figures 9.1 and 9.5 show that the layer 8.8 leads to a band gap but the layer 8.9 does not. From the viewpoint of the electronic energy stabilization associated with a band gap opening, therefore, $Cs_{0.33}MoO_3$ (which has two electrons to fill the t_{2g}-block bands) would be expected to adopt the layer structure 8.8 instead of 8.9, as found experimentally. To obtain a cesium bronze Cs_xMoO_3 with the layer structure 8.9, it would be necessary to have less than two electrons to fill the bands, thereby removing the possibility of electronic energy stabilization by a band gap opening at the zone edge. That is, a cesium bronze Cs_xMoO_3 with layer structure 8.9 would be more accessible for x smaller than 1/3. This is consistent with the original observation of $x \simeq 0.25$ by Mumme and Watts and may be one of the reasons why their phase has not been reproduced so far. Figure 9.5 suggests that any cesium molybdenum bronze Cs_xMoO_3 ($x < 1/3$) consisting of MoO_3 layers 8.9 would be a pseudo-1D metal and hence would exhibit a CDW phenomenon.

10. Blue Bronzes

Blue bronzes $A_{0.3}MoO_3$ (A = K, Rb, Tl) are layered type materials.[26,43] Early studies showed that the potassium blue bronze is metallic[44] and exhibits a metal–semiconductor transition at $T_p \simeq 180$ K.[45] Later studies noticed that the electrical conductivity in the plane of the layers is quite anisotropic.[46] On the basis of optical reflectivity data, it was suggested that the potassium blue bronze is a quasi-1D metal above T_p and the metal–semiconductor transition is of a Peierls type.[47] Evidence for the CDW in the blue bronze was found by an X-ray diffuse-scattering study.[48] Subsequent X-ray,[49] neutron[50] and electron diffraction[51] studies confirmed this finding. The wave vector component q_b of the CDW is incommensurate at room temperature (i.e., $q_b \simeq 0.72b^*$), where b is the repeat distance along the crystallographic b axis. A number of studies have shown that q_b gradually increases at low temperatures and approaches the commensurate value $0.75b^*$.[48-54] Similar results have been found for the rubidium and thallium blue bronzes.[1a-c,55-56] Nonlinear electrical conductivity attributed to sliding of the CDW have been found for the blue bronzes at temperatures below 183 K.[57]

As discussed in section 8, blue bronzes contain $Mo_{10}O_{30}$ layes 10.1. In the C-centered monoclinic cell,[26] each $Mo_{10}O_{30}$ layer is contained in a plane defined by the two orthogonal vectors **b** and **2d**, where **2d** = **2c** + **a**. As shown in 10.1 each $Mo_{10}O_{30}$ layer can be described in terms of either the two orthogonal vectors **b** and **2d** or the two primitive nonorthogonal vectors **b** and **d'**, where **d'** = **d** + **b**/2. As clearly seen in 10.1 the centered nature of the lattice is brought about by the arrangement of the hump octahedra (shaded in 10.1b) along the d direction of the layer.

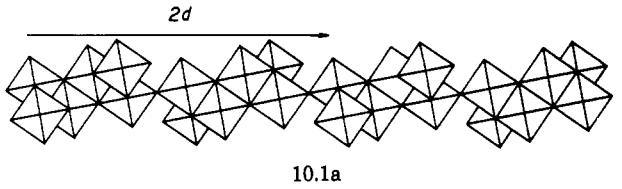

10.1a

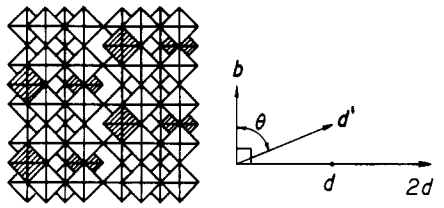

10.1b

With the formal oxidation states of Mo^{6+}, O^{2-}, and A^{+}, there are three electrons to fill the t_{2g}-block bands of the $Mo_{10}O_{30}$ layers. In the following, we examine how the nature of the bottom t_{2g}-block bands of the blue bronze is related to its crystal structure. The results of electronic structure calculations[58] described below are based upon the primitive unit cell (see the discussion of section 4.3).

10.1 Orbital Patterns of the Bottom d-Block Bands

Since there are 10 MoO_6 octahedra per repeat unit in a $Mo_{10}O_{30}$ layer of the blue bronze, there are 30 t_{2g}-block bands and only the bottom portion of these

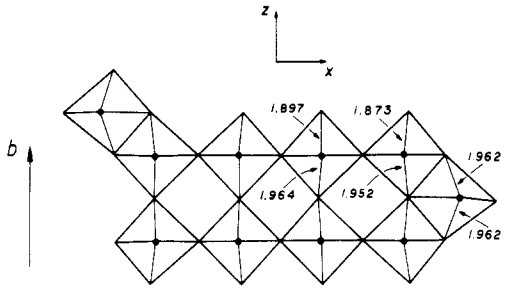

10.2a

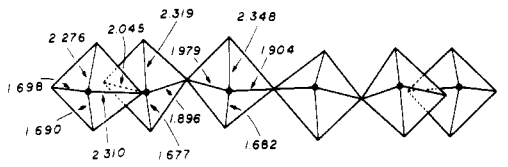

10.2b

bands is filled. Thus our analysis is simplified by considering the ideal distortions of the different oc-

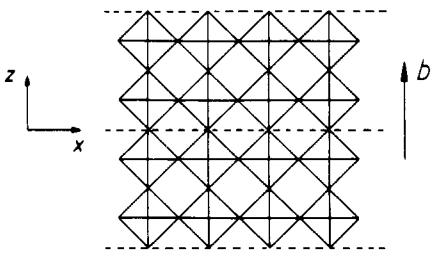

10.3

CHART 10.1

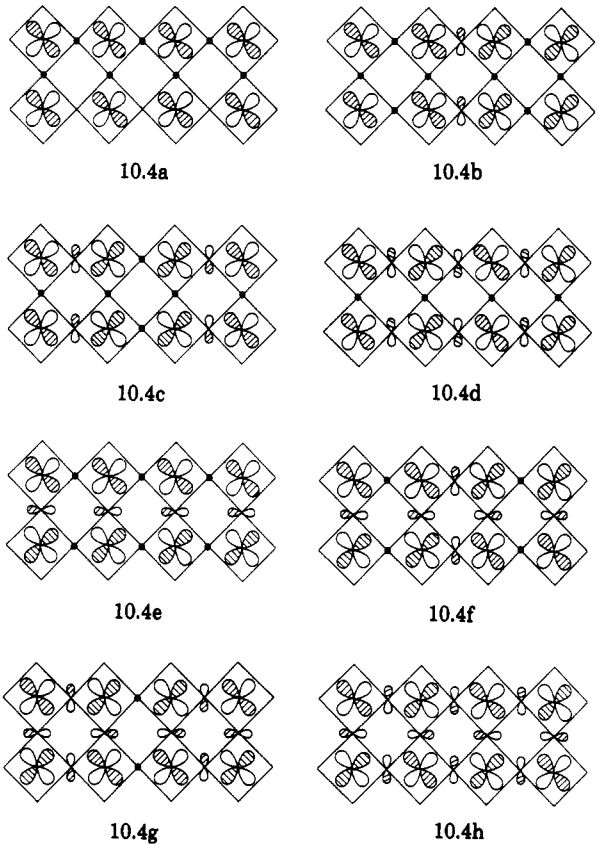

10.4a 10.4b 10.4c 10.4d 10.4e 10.4f 10.4g 10.4h

tahedra of the layer. Shown in 10.2 are the Mo–O bond lengths found in the $K_{0.3}MoO_3$ structure.[26] The hump octahedra have two strong O···Mo–O alternations so that their t_{2g} levels will be high in energy and will not contribute to the bottom d-block bands. All other octahedra have one strong O···Mo–O alternation perpendicular to the *b* direction. As a consequence, only the *xz* orbital of the nonhump octahedra (i.e., those of the Mo_8O_{34} chain 10.3) will remain low in energy and thus will lead to the low-lying d-block bands of the $Mo_{10}O_{30}$ layer.

In order to understand the bottom part of the band structure of the real Mo_8O_{34} chain 10.3, it is convenient to first consider the *xz* bands of the ideal Mo_8O_{34} chain. The cluster orbitals needed to build the *xz* CO's are shown in 10.4 (Chart 10.1). Just as in the case of the 2D red bronzes, the energy ordering of these eight levels can be obtained by counting the number of dots [i.e., (N)-type interactions]. The result is shown in 10.5.

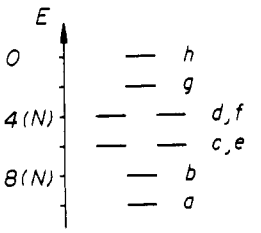

10.5

The CO's at Γ and *Y* generated by the cluster orbital 10.4a have the nodal patterns 10.6 and 10.7, respec-

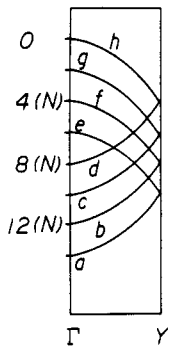

Figure 10.1. xz bands of the ideal Mo_8O_{34} chain 10.3.

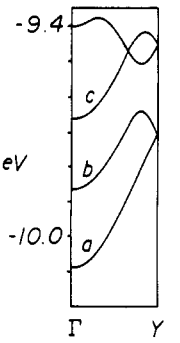

Figure 10.2. Bottom portion of the t_{2g}-block bands of the real Mo_8O_{34} chain.

tively. The numbers of (N)-type interactions per unit cell in 10.6 and 10.7 are 14 and 10, respectively. Namely, the number of (N)-type interactions in the CO's is the same as that in the initial cluster orbital at Y but increases by four at Γ. This stems from the

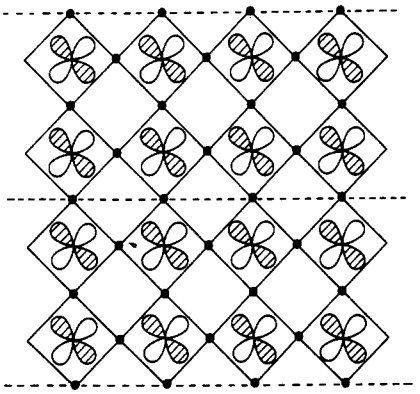

10.6

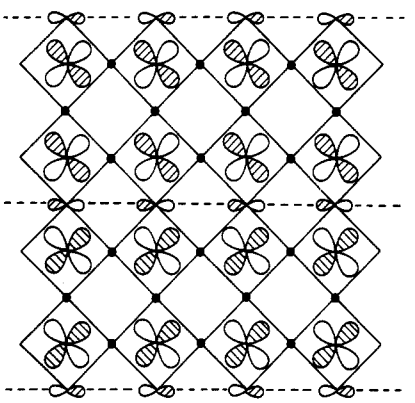

10.7

antisymmetric character of the cluster orbital 10.4a with respect to the horizontal symmetry plane. Consequently, the same is expected from the CO's obtained from the cluster orbitals 10.4b–d. The cluster orbitals 10.4e–h are symmetric with respect to the horizontal symmetry plane so that, in the CO's derived from any of those cluster orbitals, the number of (N)-type interactions is the same as that in the initial cluster orbital at Γ but increases by four at Y. Simple application of these counting rules leads to the schematic band structure shown in Figure 10.1.

In understanding the evolution of the CDW vector q_b of the blue bronze with temperature, it is important to note from Figure 10.1 that band c at Γ (10.9) is degenerate with bands a and e at Y (10.7 and 10.8, respectively). As in the case of $Cs_{0.25}MoO_3$, there is a

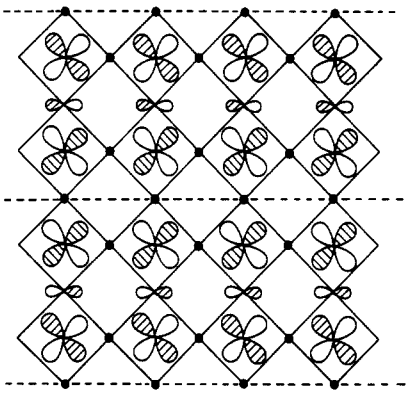

10.8

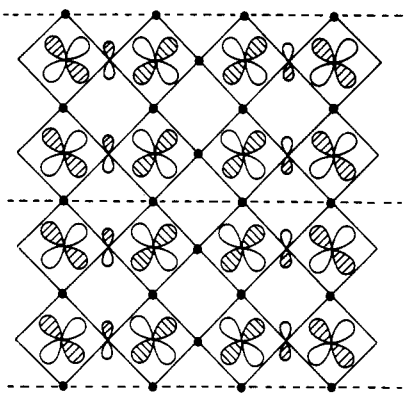

10.9

2-fold screw rotation axis along the Mo_8O_{34} chain direction (see 8.5a and 10.2). Consequently, the degeneracies at Y should be retained in the band structure of the real Mo_8O_{34} chain (Figure 10.2). In any of the CO's 10.7–10.9, there are four antibonding Mo–O–Mo type interactions [i.e., 4(Y)] per unit cell. As shown in 10.2, the Mo–O distances associated with the Mo–O–Mo bridges of both 10.7 and 10.8 are (1.873/1.873), (1.952/1.952), (1.897/1.897), and (1.964/1.964). In 10.9 the four antibonding interactions are identical and are associated with the Mo–O distances (1.896/1.979). The short and long Mo–O distances involved in 10.7 or 10.8 are similar to those involved in 10.9. This is why, as shown in Figure 10.2, band c at Γ and bands a and e at Y differ only slightly in energy (i.e., about 0.05 eV).

10.2 Interchain Interactions

As shown in section 9.2, the effect of the interchain interactions can be predicted by examining the phase

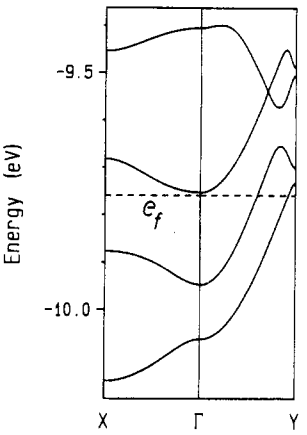

Figure 10.3. Bottom portion of the d-block bands calculated for a real $Mo_{10}O_{30}$ slab of the blue bronze along the $\Gamma \rightarrow X$ and $\Gamma \rightarrow Y$ directions of the FPZ defined by the vectors **d'** and **b** (see 10.1b). $\Gamma = (0, 0)$, $X = (d'^*/2, 0)$, and $Y = (0, b^*/2)$, where **d'** = **d** + **b**/2 (see the discussion of section 4.3). The dashed line refers to the Fermi level.

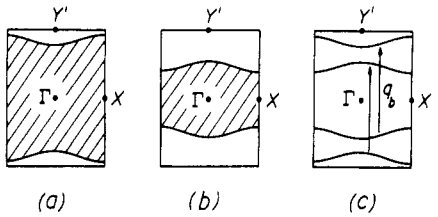

Figure 10.4. Fermi surfaces associated with the two partially filled d-block bands of a real $Mo_{10}O_{30}$ slab: (a) Fermi surface of the first band, where the wave vectors of the shaded and unshaded regions lead to occupied and unoccupied band levels, respectively, (b) Fermi surface of the second band, and (c) nesting of the Fermi surfaces of the first and second bands.

relation between the *xz* orbital of adjacent chains at the hump level in the CO's at Γ: If the orbital patterns around the hump octahedron are given by 10.10 and 10.11, the effects of the interchain interactions are described by Figure 9.3, parts a and b, respectively.

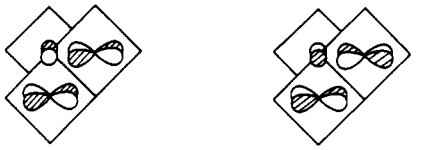

10.10 10.11

When viewed along the chain, band orbitals a, b, and c at Γ in Figure 10.1 are described by 10.12, 10.13, and 10.14, respectively. Consequently, band a will behave as in Figure 9.3a, but bands b and c as in Figure 9.3b. Thus, the band dispersion relations of the $Mo_{10}O_{30}$ layer (solid lines) are related to those of the Mo_8O_{34} chain (dashed line), as schematically shown in 10.15.

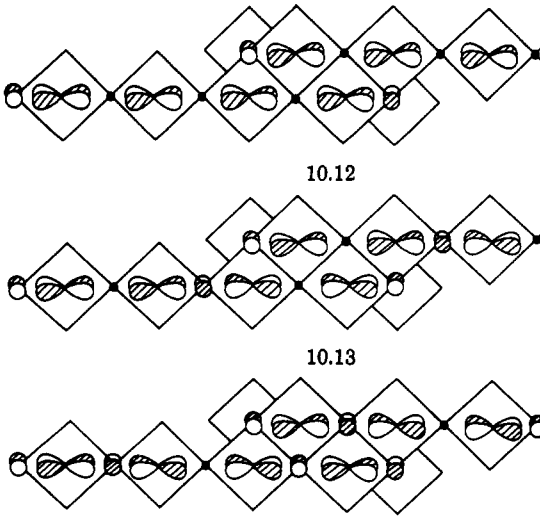

10.12

10.13

10.14

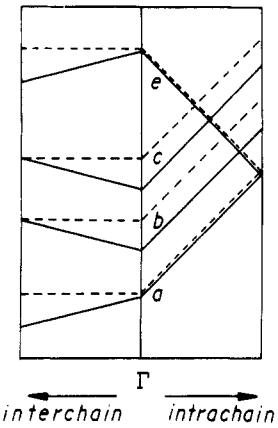

10.15

Two results of the above analysis are important to note: First, along $\Gamma \rightarrow X$ (i.e., the interchain direction), band a goes downward in energy while bands b and c go upward. Second, the bottom of band c lies near the top of band a in the Mo_8O_{34} chain so that the bottom of band c lies below the top of band a in the $Mo_{10}O_{30}$ layer. Figure 10.3 shows the calculated band structure for the real $Mo_{10}O_{30}$ layer of blue bronze.[58] From Figures 10.3 and 10.2, it is seen that the interchain interactions keep the energy difference between bands b and c at Γ almost constant but decrease that between bands c (or b) and a at Γ. Bearing in mind the discussion of section 4.3 and the avoided nature of some of the crossings in 10.15, the agreement between the calculated and schematic band structures is excellent.

10.3 Fermi Surfaces and Nesting

With three electrons per unit cell, the Fermi level cuts the two lowest d-block bands. The Fermi surfaces calculated[58] for the first and second bands of Figure 10.3 are shown in Figure 10.4, parts a and b, respectively. These two Fermi surfaces are open so that the blue bronze is predicted to be a 1D metal in agreement with experiment. Due to the interchain interactions, the Fermi surfaces of the two bands are curved. The two bands have opposite senses of curvature in their Fermi surfaces, as proposed by Pouget et al.,[53b] because, as discussed in the previous section, one band is lowered in energy but the other is raised in energy along the interchain direction ($\Gamma \rightarrow X$). The two Fermi surfaces can be combined together as in Figure 10.4c. The upper Fermi surface of the first band is nested to the lower Fermi surface of the second band by the wave vector $q_b = 0.75b^*$, and so is the lower Fermi surface of the first band to the upper Fermi surface of the second band. This explains why the blue bronze has only one CDW and undergoes a metal–semiconductor transition.

The Fermi level of Figure 10.3 is calculated to be only 0.012 eV below the bottom of the third band. This feature of the band electronic structure is crucial to explain the temperature dependence of q_b, as shown by Pouget et al.[53b] Because of the small energy difference, thermal excitation of electrons can occur from the first

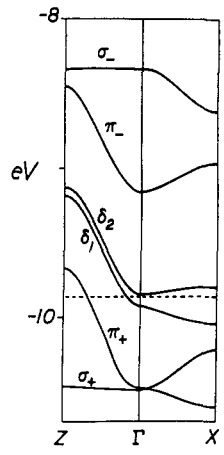

Figure 10.5. t_{2g}-block bands for the $Mo_2O_7^{6-}$ slab of $La_2Mo_2O_7$, where $\Gamma = (0, 0)$, $X = (a^*/2, 0)$, and $Z = (0, c^*/2)$. The dashed line refers to the Fermi level.

and second bands to the bottom portion of the third one. This thermal excitation, which increases with temperature, shrinks the occupied region of wave vectors in both Fermi surfaces. As a consequence, the two pieces of the Fermi surface of either the first and the second bands come closer to each other. Thus, the q_b value of the CDW should decrease upon increasing temperatures as observed.

10.4 Interchain Interactions and Nesting in $La_2Mo_2O_7$

Low-dimensional metallic compounds necessarily present stronger orbital interactions along a certain crystal direction and weaker interactions along the other directions. The latter can play an important role in determining the shape of the Fermi surfaces and hence its possible nesting vectors. For instance, the slopes of the two lower bands of the blue bronze along the interchain direction are similar in magnitude but opposite in sign. This is why the blue bronze exhibits a single CDW with nesting vector close to $0.75b^*$. An interesting contrast with the blue bronze is provided by rare-earth molybdenum bronze $La_2Mo_2O_7$,[59] which is a layered material with La^{3+} cations sandwiched in between $Mo_2O_7^{6-}$ layers 8.7.[23] $La_2Mo_2O_7$ is metallic down to 125 K, below which it undergoes a phase transition. This transition is also detected by magnetic susceptibility measurements.[23] According to the formal oxidations of $(La^{3+})_2(Mo_2O_7^{6-})$, each molybdenum is in the oxidation state Mo^{4+} (d^2). In each Mo_2O_{10} cluster 10.16 of $La_2Mo_2O_7$, the Mo–Mo distance across the shared edge is 2.478 Å, which is compatible with the Mo–Mo distance associated with a double bond between Mo atoms.[60] The bottom six d-block orbitals of an Mo_2O_{10}

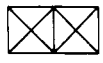

10.16

cluster,[61] derived primarily from the t_{2g} levels of each metal ion, consist of bonding orbitals σ_+ (10.17a), π_+ (10.18a), and δ_+ (10.19a) and antibonding orbitals σ_- (10.17b), π_- (10.18b), and δ_- (10.19b). Only the metal d orbitals are shown in 10.17–10.19 for simplicity.

The bottom six d-block bands calculated for a 2D $Mo_2O_7^{6-}$ slab[61] are shown in Figure 10.5. These bands

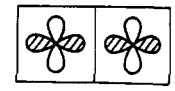

10.17a

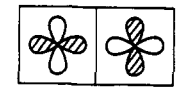

10.17b

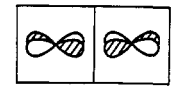

10.18a

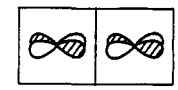

10.18b

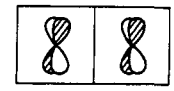

10.19a

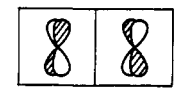

10.19b

are largely represented by the bottom six d-block orbitals of each Mo_2O_{10} cluster shown in 10.17–10.19, and their energy ordering is determined by the metal–metal interaction in the cluster. Along the chain direction $\Gamma \rightarrow Z$, the σ bands (σ_+ and σ_-) are flat whereas the π bands (π_+ and π_-) have a substantial dispersion as do the δ bands (δ_1 and δ_2). This is expected because both the π and δ orbitals make strong π-type overlaps with the p orbitals of the shared "axial" oxygen atoms along the chain direction while the σ orbitals do not overlap with any orbitals of the shared "axial" oxygen. The π and δ bands are much less dispersive along the interchain direction $\Gamma \rightarrow X$ than along the chain direction $\Gamma \rightarrow Z$, but the opposite is the case with the σ bands.

In each Mo_2O_{10} cluster, the σ_+, σ_-, π_+, and π_- bands have the metal character of the σ_+, σ_-, π_+, and π_- orbitals, respectively. The δ_1 and δ_2 bands have the metal character of δ_+ and δ_- orbitals, respectively, along $\Gamma \rightarrow Z$. Along $\Gamma \rightarrow X$, however, the δ_1 and δ_2 bands at X have the metal character of the δ_- and δ_+ orbitals, respectively. This switch of the orbital character is caused by the p orbitals of the shared "equatorial" oxygen atoms, whose participation in bonding depends upon the wave vector. The δ_1 and δ_2 bands at Γ have the orbital characters of 10.20a and 10.20b, respectively, but those at X have the orbital characters of 10.21a and 10.21b, respectively. When the oxygen p orbitals are

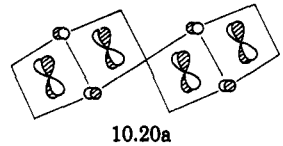

10.20a

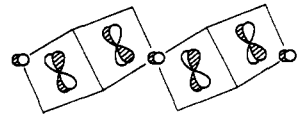

10.20b

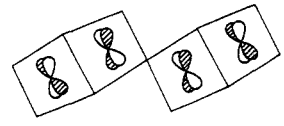

10.21a

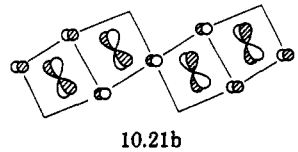

10.21b

allowed by symmetry to interact with the metal d orbitals, the former make an antibonding contribution to

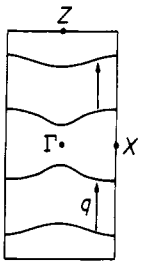

Figure 10.6. Combined Fermi surfaces for the $Mo_2O_7^{6-}$ slab of $La_2Mo_2O_7$.

the d-block levels, thereby raising their energies. Band π_+ at Γ has the orbital character 10.22a. Along $\Gamma \rightarrow X$ the antibonding contributions due to the equatorially shared oxygens is lost (10.22b). Consequently, band π_+ is lowered in energy along $\Gamma \rightarrow X$, as is δ_1. With four d electrons to fill the d-block bands of Figure 10.5, the σ_+ band is completely filled and the π_+ and δ_1 bands are partially filled.

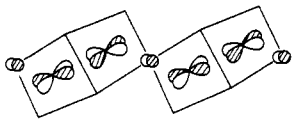

10.22a

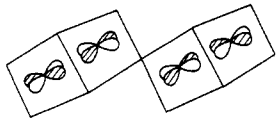

10.22b

The Fermi surfaces associated with the two partially filled bands of Figure 10.5 are shown in Figure 10.6, which consists of four separated curved lines along the direction perpendicular to the chains, as in the case of blue bronze. Thus, $La_2Mo_2O_7$ is a pseudo-1D metal with the best conductivity along the c direction (i.e., the chain direction).[61,62] However, there is an important difference from the blue bronze. The curvatures of the two upper lines (or the two lower ones) have the same sign in $La_2Mo_2O_7$ but opposite signs in blue bronze. Given the combined Fermi surfaces such as those in Figure 10.6, it is possible to consider nesting between two different bands (interband nesting) or within each band (intraband nesting). The first leads to a single nesting vector, and the second to two separate nesting vectors. However, the tendency to form a CDW is stronger as the area of the nested Fermi surface increases. The interband nesting in the Fermi surface of Figure 10.6 joins both the upper two and the lower two lines by a common vector $q \simeq (0, 0.27c^*)$ so that the interband nesting would be more important than the intraband nesting in $La_2Mo_2O_7$. It should be noted that the curvatures of the upper and lower two lines are slightly different in the region of the $\Gamma \rightarrow Z$ line so that some metallic character could remain after the CDW formation. According to this discussion it is likely that $La_2Mo_2O_7$ has CDW with wave vector $\mathbf{q} \simeq (0, 0.27c^*)$, and that such CDW is responsible for the phase transition at 125 K.[23]

Another important feature of the band structure of Figure 10.5 is that the bottom of the δ_2 band lies above but very close to the Fermi level (0.018 eV). Therefore, as in the case of the blue bronze, thermal excitation of electrons can occur from the π_+ and δ_1 bands into the bottom portion of the δ_2 band. This thermal excitation, which increases with temperature, shrinks the occupied region of wave vectors of both the π_+ and δ_1 bands. As a consequence, the two pieces of the Fermi surface of either the π_+ or the δ_1 band come closer to each other upon losing electrons by thermal excitation. Then, the CDW vector q would remain nearly temperature independent in contrast to the case of the blue bronze.

11. Magnéli Phase Mo_8O_{23} and Disphosphate Tungsten Bronzes $A_x(P_2O_4)_4(WO_3)_{4m}$

11.1 Magnéli Phase Mo_8O_{23}

Mo_8O_{23} is metallic[63] and exhibits no superlattice spots above 360 K, but shows incommensurate superlattice spots at $q_{ic} = (0.195a^*, 0.5b^*, -0.120c^*)$ between 360 and 285 K and commensurate superlattice spots at $q_c = (0, 0.5b^*, 0)$ below 285 K.[27c,64] The presence of the $0.5b^*$ component shows that the unit cell size of Mo_8O_{23} doubles along the b-axis direction as the temperature is lowered below 360 K. According to the electronic instability argument based upon Fermi surface nesting, the $0.5b^*$ component implies that Mo_8O_{23} has a half-filled band primarily dispersive along the b^* direction (i.e., the b direction, see 8.14). However, it seems unlikely: according to the usual oxidation formalism of O^{2-}, Mo_8O_{23} has only two d electrons per formula unit to fill its 24 t_{2g}-block bands. Furthermore, the Magnéli phase Mo_9O_{26}, which can be derived from the structure of Mo_8O_{23} (8.14) by replacing the Mo_4O_{15} layer 8.12 with the Mo_5O_{18} layer 8.13b, has also two d electrons to fill its 27 t_{2g} block bands, but it exhibits a superlattice modulation with $0.5b^*$ component.[65] Therefore, the structural modulation of Mo_8O_{23} may not originate from a Fermi surface nesting.

The crystal structure of Mo_8O_{23} determined at 370 K (i.e., the crystal structure without superlattice modulation)[27] shows that the MoO_6 octahedra are all distorted from an ideal, regular octahedron. Every MoO_6 octahedron of Mo_8O_{23} shows a strong O–Mo···O bond alternation (e.g., Mo–O = 1.69 Å and Mo···O = 2.37 Å) along the b axis. Every Mo atom of MoO_6 is located slightly out of the four O_{eq} atom plane, as depicted in 11.1, where the filled and empty circles represent the

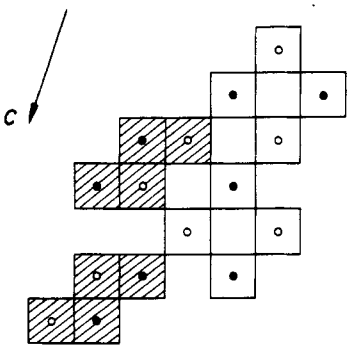

11.1

Mo atoms lying above and below the four O_{eq} atom planes, respectively. The senses of O–Mo···O alternation at these two kinds of Mo atoms are opposite (i.e., O–Mo···O at one and O···Mo–O at the other) so that the unit cell of Mo_8O_{23} is given by $(Mo_8O_{23})_2$. The Mo–O bonds associated with the O_{eq} atoms of the Mo_4O_{14} chains (11.2) and the Mo_4O_{15} slabs (11.3) are shown in 11.4 and 11.5, respectively. Note that every MoO_6

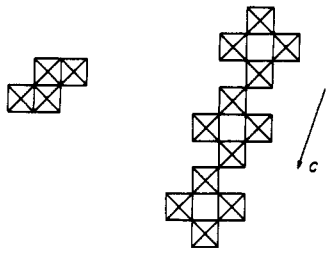

11.2 11.3

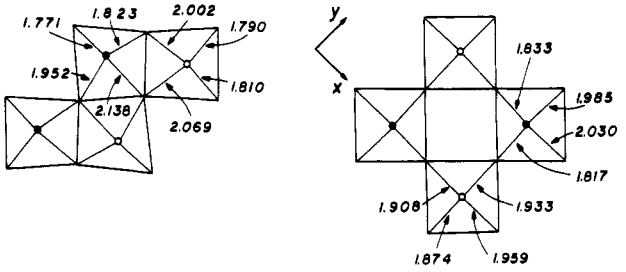

11.4 11.5

octahedron of the Mo_4O_{14} chain has one short Mo–O_{eq} bond (less than 1.80 Å), while that of the Mo_4O_{15} slab has Mo–O_{eq} bonds longer than 1.82 Å. Simply speaking, therefore, the MoO_6 octahedra of the Mo_4O_{15} slab 11.3 have a distortion in which one Mo–O bond is shortened, and those of the Mo_4O_{14} chains 11.2 have a distortion in which two Mo–O bonds are shortened. It is then expected that the bottom t_{2g}-block bands of Mo_8O_{23} will originate from the Mo_4O_{15} slab alone (i.e., the nonhatched part of 11.1).

Shown in Figure 11.1, parts a and b are the dispersion relations calculated for the bottom t_{2g}-block bands of the Mo_4O_{14} chain and Mo_4O_{15} slab in Mo_8O_{23}, respectively.[66] The lowest bands of the Mo_4O_{14} chain are quite high in energy with respect to the bottom bands of the Mo_4O_{15} slab in agreement with the above structural analysis. The main orbital character of the pairs of bands labeled a, b, and c in Figure 11.1b are those of the cluster orbitals 11.6a, 11.6b, and 11.6c, respectively.

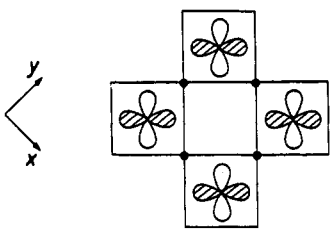

11.6a

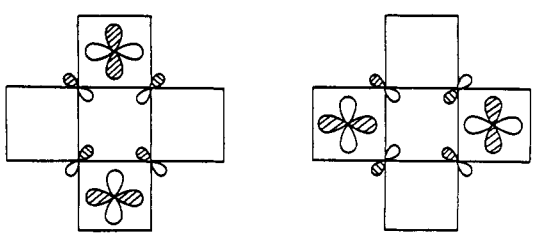

11.6b 11.6c

[Because of the opposite senses of the O···Mo–O alternations shown in 11.1, the unit of the Mo_4O_{15} slab is given by $(Mo_4O_{15})_2$, and all the bands contain two subbands.] Namely, the bottom portion of the t_{2g}-block bands of the Mo_4O_{15} layer is made up of the metal xy orbitals. Again, this result is in agreement with the

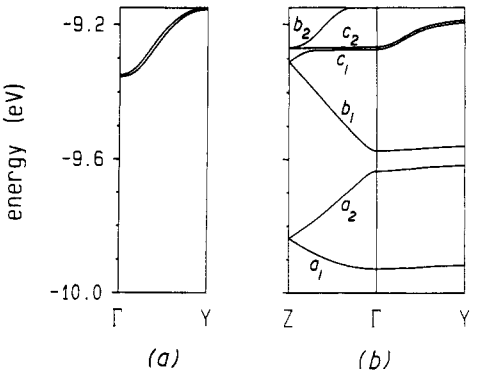

Figure 11.1. Dispersion relations of the bottom portion of the t_{2g}-block bands calculated for (a) the Mo_4O_{14} chain 11.2 and (b) the Mo_4O_{15} slab 11.3 in Mo_8O_{23}, where $\Gamma = (0, 0)$, $Y = (b^*/2, 0)$, and $Z = (0, c^*/2)$.

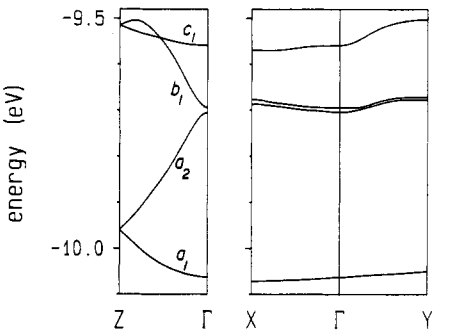

Figure 11.2. Dispersion relations of the bottom portion of the d-block bands calculated for Mo_8O_{23}. $\Gamma = (0, 0, 0)$, $X = (a^*/2, 0, 0)$, $Y = (0, b^*/2, 0)$, and $Z = (0, 0, c^*/2)$.

structural analysis since the xy orbital is the δ orbital with respect to the strong O–Mo···O alternation direction in the octahedra of the Mo_4O_{15} slab. Bands a_1 and a_2 are dispersive along the c^* direction, and so are bands b_1 and b_2 because the δ orbital (with respect to the b axis) at each MoO_6 octahedron is engaged in π-type interactions along the c-axis direction. For example, the nodal properties of bands a_1 and a_2 at Γ are given by 11.7a and 11.7b (Chart 11.1), respectively, and those of bands b_1 and b_2 at Γ by 11.8a and 11.8b (Chart 11.1), respectively. Bands c_1 and c_2 are not dispersive along the c^* direction, since the unit cell orbital 11.6c practically does not have any orbital contribution at the shared O_{eq} atoms (between unit cells). This is shown by 11.9a and 11.9b (Chart 11.1), which are the nodal properties of bands c_1 and c_2 at Γ, respectively. Bands a_1 and a_2 merge at Z because, by changing the relative phases between adjacent unit cells, band a_1 picks up but band a_2 removes oxygen p-orbital contribution from the shared O_{eq} atoms between unit cells. Similarly, bands b_1 and b_2 merge at Z, and so do bands c_1 and c_2.

If there is no appreciable interaction between the Mo_4O_{15} slabs and the Mo_4O_{14} chains in Mo_8O_{23}, superposition of Figure 11.1, parts a and b would be a good approximation for the t_{2g}-block bands of Mo_8O_{23}. With four d electrons per unit cell $(Mo_8O_{23})_2$, it is expected that only bands a_1 and a_2 of the Mo_4O_{15} slabs are occupied and all d-block bands of the Mo_4O_{14} chains are unoccupied. Figure 11.2 shows the bottom portion of the t_{2g}-block bands calculated for the three-dimensional lattice of Mo_8O_{23}.[66] There are two important observations to note from Figure 11.2: (a) Mo_8O_{23} is predicted to be a semimetal and does not have a half-filled band dispersive along the b^* direction. All the

CHART 11.1

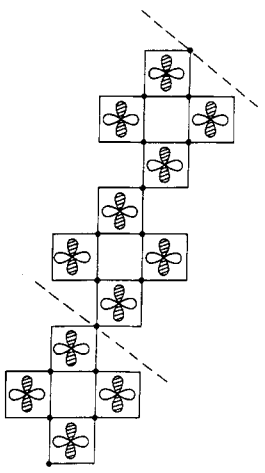

11.7a

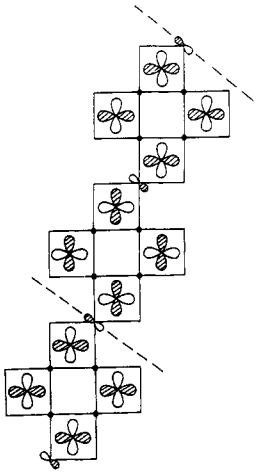

11.7b

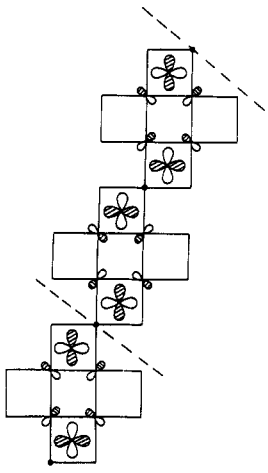

11.8a

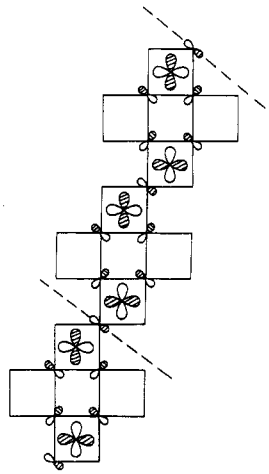

11.8b

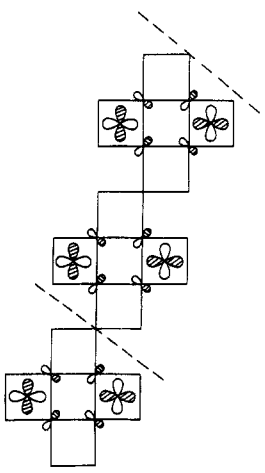

11.9a

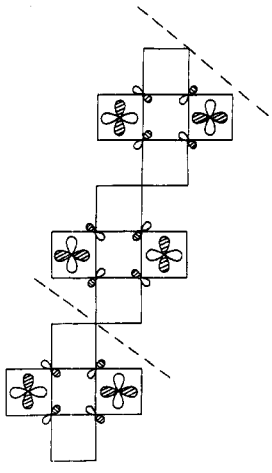

11.9b

bands of Figure 11.2 are not dispersive along the b^* direction, since they are largely based upon δ orbitals with respect to the b axis. (b) Only the bottom d-block bands of the Mo_4O_{15} slabs are filled, while the d-block bands of the Mo_4O_{14} chains are empty. Consequently, the Mo atoms of the Mo_4O_{15} slabs should be lower in their formal oxidation states than those of the Mo_4O_{14} chains (i.e., approximately, $Mo^{5.5+}$ for the Mo_4O_{15} slabs and Mo^{6+} for the Mo_4O_{14} chains). The Zachariasen analysis[67] for Mo_8O_{23} is found to give an unreasonable result; it predicts that all Mo atoms are nearly the same in their oxidation states (i.e., approximately $Mo^{5.75+}$).[65]

The Magnéli phase Mo_8O_{23} is thus a semimetal and has two partially filled bands resulting primarily from its structural components Mo_4O_{15} slabs. These two bands are not dispersive along the b^* and a^* directions but dispersive along the c^* direction. Namely, Mo_8O_{23} does not possess a half-filled band dispersive along the b^* direction, so that the $0.5b^*$ component of the superlattice modulation in Mo_8O_{23} does not originate from an electronic instability associated with Fermi surface nesting.[66] As suggested by Pouget,[1a] therefore, the cause for the $0.5b^*$ modulation is likely to be the well-known structural instability inherent in perovskite metal oxides, i.e., the concerted pairwise rotations of MO_6 octahedra within a layer of corner-shared MO_6 octahedra.[68] As illustrated in 11.10 for an Mo_4O_{17} quadruple chain (see 8.12 and the nonhatched part of 11.1), rotation of an MoO_6 octahedron around an O–Mo–O axis (perpendicular to the b axis) induces a concerted pairwise rotation of all MoO_6 octahedra within the Mo_4O_{17} chain. This doubles the unit cell size along the

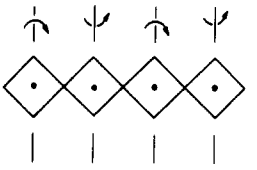

11.10

b direction and accounts for the $0.5b^*$ component. Indeed, the crystal structure of Mo_8O_{23} determined at 100 K[27c] and the inelastic neutron scattering data[69] of Mo_8O_{23} are consistent with the concerted pairwise octahedral rotation described above. It is expected that the $0.5b^*$ modulation observed for Mo_9O_{26} is also caused by the same mechanism.

11.2 Disphosphate Tungsten Bronzes

DPTB's $A_x(P_2O_4)_4(WO_3)_{4m}$ have slabs of ReO_3-type corner-sharing WO_6 octahedra terminated on both sides by insulating P_2O_7 groups.[28,70] Hence they are expected to be 2D conductors. Studies of the electrical properties of these materials in polycrystalline samples show[70e,71] that they are metallic and their electrical transport properties are almost independent of the nature of the A cation. Later, it was shown on the basis of single crystals that DPTB's are indeed quasi-2D metallic materials, with better conductivity along one of the two directions of the slabs.[72]

The slabs of corner-sharing WO_6 octahedra in the lowest member of the DPTB series (i.e., $m = 4$)[70d] (8.17) are similar to the Mo_4O_{15} slabs (8.12) of Mo_8O_{23}. However, the real structures of the DPTB's is more complex because the P_2O_7 groups (8.15) induce small tiltings of the WO_6 octahedra leading to a unit cell four times bigger than that of the ideal W_4O_{15} slabs. With the formal oxidation of A^+, P^{5+}, and O^{2-}, the average oxidation state of W in DPTB's $A_x(P_2O_4)_4(WO_3)_{4m}$ is given by $6 - (8 + x)/4m$. Since the x values are usually between 1 and 2, the number of d electrons per slab is usually between 9 and 10, so that the mean oxidation state of W increases with the thickness of the slab. In the case of the lowest reported member of the series (i.e., $m = 4$), the number of d electrons per W atom is 0.625. This is very similar to the value for the Mo atoms

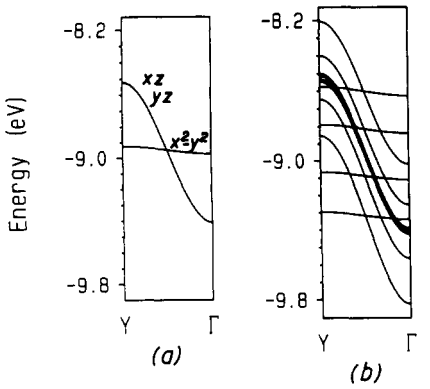

Figure 11.3. Dispersion relations for the bottom portion of the d-block bands calculated for (a) the ideal WO_5 chain 8.1 and (b) W_4O_{17} quadruple chain 11.3.

in the Mo_4O_{15} slabs of Mo_8O_{23} (i.e., 0.5). Hence, both structurally and electronically, the two systems are very similar. There is however one important difference: whereas Mo_8O_{23} exhibits a strong O···Mo–O alternation along the b direction, this is not the case for the DPTB's.[70] Consequently, all three t_{2g} orbitals of W can now lead to the low-lying t_{2g}-block bands. In the following, we study the band structure of an ideal W_4O_{15} slab 11.11.

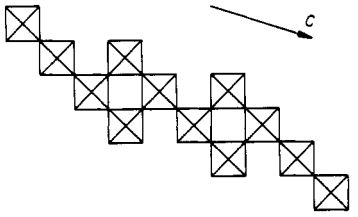

11.11

Shown in Figure 11.3a are the bottom three d-block bands of an ideal WO_5 chain (8.1b) constructed from WO_6 octahedra with W–O distances of 1.916 Å. With the coordinate system shown in 11.12, the two dispersive bands are built from the xz and yz orbitals, and the nondispersive one from the x^2–y^2 orbital. Figure

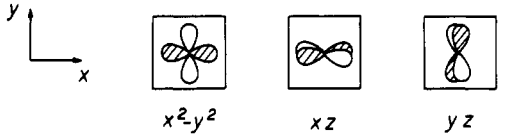

11.12

11.3b shows the bottom part of the d-block bands of a quadruple chain W_4O_{17}, 11.13, which consists of a set of four nondispersive δ bands and eight dispersive π bands. The four nondispersive ones originate from the four x^2–y^2 orbitals. Four of the dispersive bands are

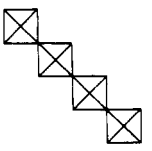

11.13

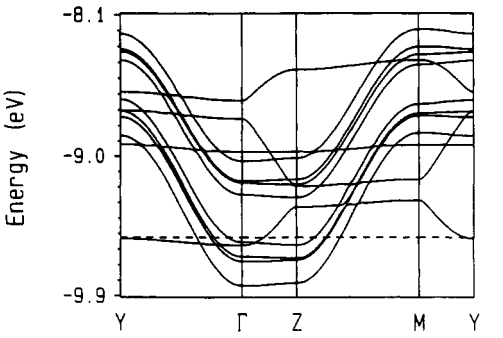

Figure 11.4. Dispersion relations of the bottom portion of the d-block bands calculated for the ideal W_4O_{15} slab. $\Gamma = (0, 0)$, $Y = (b^*/2, 0)$, $Z = (0, c^*/2)$, and $M = (b^*/2, c^*/2)$. The dashed line refers to the Fermi level corresponding to 2.5 electrons per unit cell.

almost degenerate and built from the cluster orbitals 11.14a–d. The latter have δ symmetry with respect to

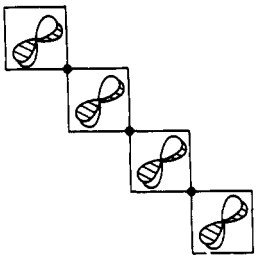

11.14a

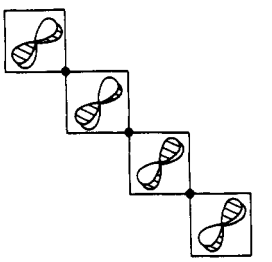

11.14b

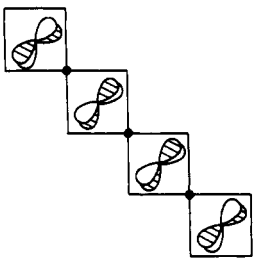

11.14c

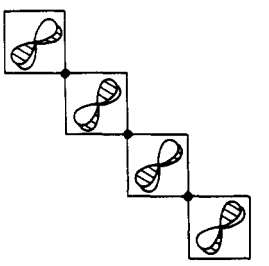

11.14d

the long axis of the cluster 11.3, so that the bands constructed from those cluster orbitals become practically degenerate. The remaining four dispersive bands are constructed from the cluster orbitals 11.15a–d, and hence are not degenerate.

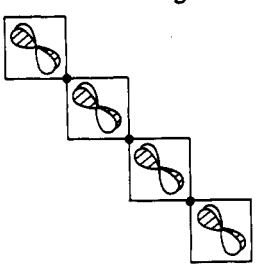

11.15a

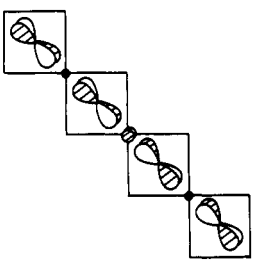

11.15b

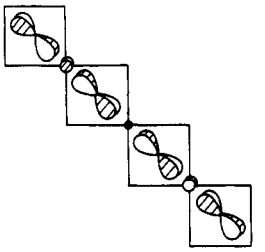

11.15c

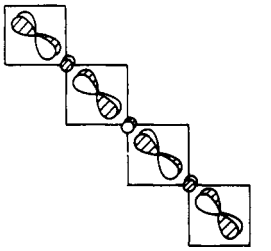

11.15d

Figure 11.4 shows the dispersion relations of the t_{2g}-block bands calculated for the ideal W_4O_{15} slab 11.11. Along $\Gamma \rightarrow Y$ (i.e., the intrachain direction), they are very similar to those of the ideal W_4O_{17} chain (Figure 11.3b) except that the four nearly degenerate bands of the W_4O_{17} chain split into two groups. Three of the four δ bands show dispersion along $\Gamma \rightarrow Z$ (i.e., the interchain direction), whereas all eight π bands are not dispersive only along $\Gamma \rightarrow Z$. Shown in 11.16 and 11.17 is the main orbital character of the lowest δ band at Γ and Z, respectively. Depending on the wave vector, the

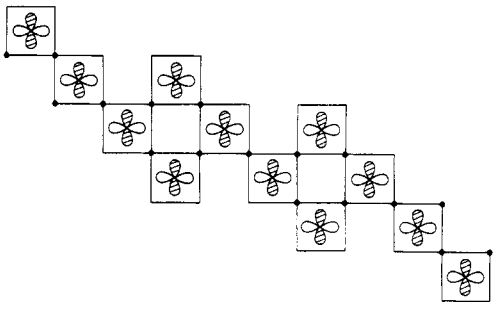

11.16

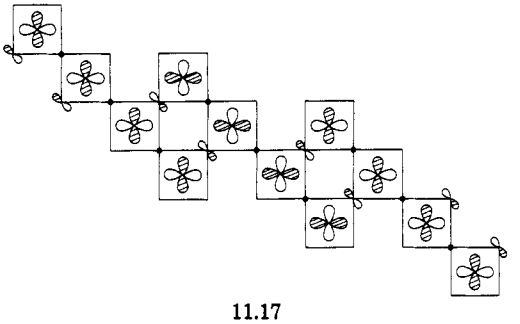

11.17

x^2-y^2 orbitals can make interchain in-plane π antibonding interactions and hence this band is dispersive along $\Gamma \rightarrow Z$. A similar reasoning applies to the other δ bands. Because of its δ character along the b direction, these bands are flat along $\Gamma \rightarrow Y$ so that the δ bands are 1D in character. Four of the π-type bands are built from the cluster orbitals 11.15, which lead to δ interactions between adjacent W_4O_{17} chains (11.13) in the W_4O_{15} slab. Thus these π bands are nondispersive along $\Gamma \rightarrow Z$. They are, however, dispersive along $\Gamma \rightarrow Y$ because the metal d orbitals make π-antibonding interactions with the bridging oxygen p orbitals along b

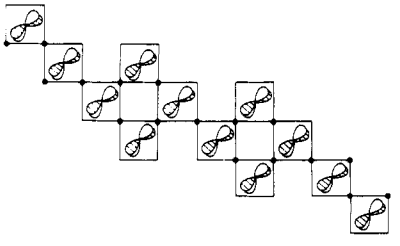

11.18

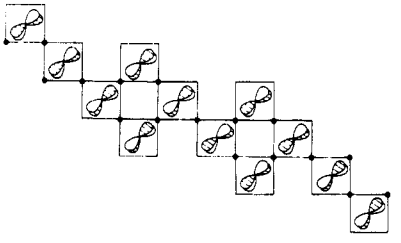

11.19

direction. Shown in 11.18 and 11.19 are the crystal orbitals at Γ and Z for the second π-type band of Figure 11.4, i.e., the lowest one originating from the set of four almost degenerate ones in Figure 11.3b. Essentially, 11.18 and 11.19 are generated by repeating the cluster orbital 11.20 in-phase and out-of-phase, respectively. Since the total number of (N)-type interactions does not change, the band is dispersionless along $\Gamma \rightarrow Z$. The same reasoning applies to the remaining three ones of the four nearly degenerate bands of Figure 11.3b.

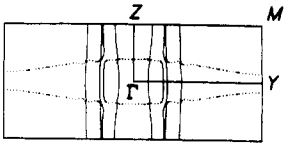

Figure 11.5. Combined Fermi surfaces associated with the partially filled bands of Figure 11.4.

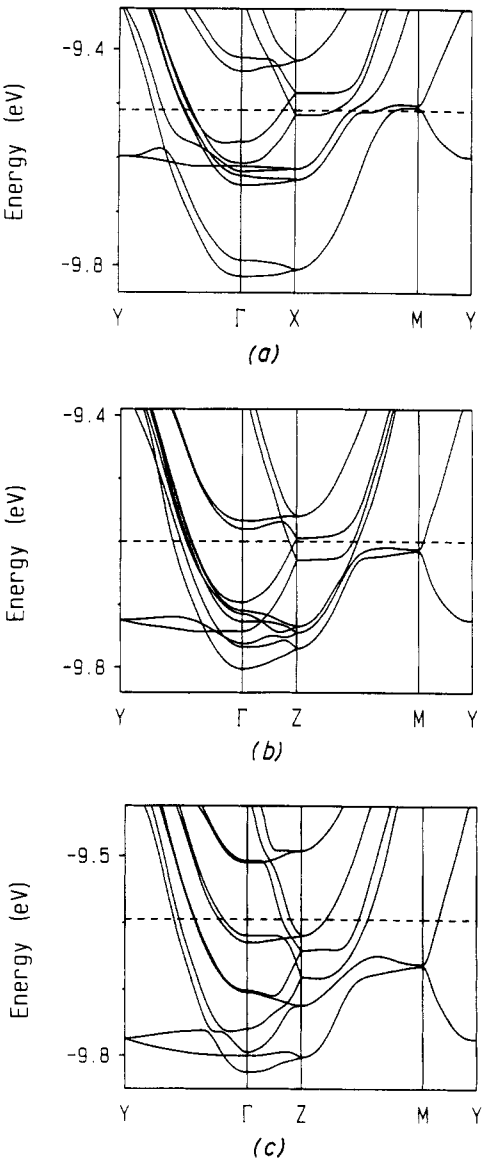

Figure 11.6. Dispersion relations of the bottom portion of the t_{2g}-block bands calculated for (a) the $W_{16}O_{60}$ slabs of $Rb_2(P_2O_4)_4(WO_3)_{16}$, (b) the $W_{24}O_{84}$ slabs of $Rb_{1.8}(P_2O_4)_4(WO_3)_{24}$ and, (c) the $W_{28}O_{96}$ slabs of $Rb_{1.74}(P_2O_4)_4(WO_3)_{28}$. The dashed lines refer to the appropriate Fermi levels for (a) $Rb_2(P_2O_4)_4(WO_3)_{16}$, (b) $K_2(P_2O_4)_4(WO_3)_{24}$, and (c) $K_2(P_2O_4)_4(WO_3)_{28}$, respectively.

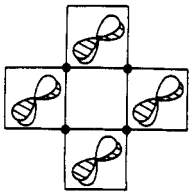

11.20

The calculated Fermi level for 2.5 electrons per unit cell (i.e., corresponding to the usual occupation of 10 d electrons per slab) cuts both the δ- and π-type bands, which are dispersive along the c and b directions, respectively. Consequently, the system should behave like a 2D metal. However, more bands are cut along the b direction (i.e., $\Gamma \rightarrow Y$ and $Z \rightarrow M$), so that the electrical conductivity should be greater along the b direction than along the c direction. It is interesting to note that the 2D metallic character of this system does not originate from the existence of genuine 2D bands but from that of 1D bands in orthogonal directions. This is clearly seen from Figure 11.5, which presents the combined Fermi surfaces associated with the partially filled bands of Figure 11.4.

Shown in Figure 11.6, parts a, b, and c are the band structures calculated[72] for the real W–O slabs in $Rb_2(P_2O_4)_4(WO_3)_{16}$,[70d] $Rb_{1.8}(P_2O_4)_4(WO_3)_{24}$,[70b] and $Rb_{1.74}(P_2O_4)_4(WO_3)_{28}$,[70c] respectively. Except for the band folding along the $\Gamma \rightarrow Y$ and $\Gamma \rightarrow Z$ directions, which is the consequence of the quadrupled unit cell found in the real slabs, these band structures are qualitatively similar to the ideal one of Figure 11.4. Hence, all these systems should be 2D metals with better conductivity along the b direction as found experimentally.[72] Some bands of Figure 11.6 have their flat portions lying very close to the Fermi level, and thus would have high DOS values in those energy regions. Therefore, the $n(e_f)$ value can be increased if the Fermi level is either raised or lowered to these flat regions. Such an increase in $n(e_f)$ may be responsible for the observed increase in the conductivity[72] of both the $K_xRb_y(P_2O_4)_4(WO_3)_{24}$ ($x + y < 2$, i.e., electron deficient) and $K_2Sn_x(P_2O_4)_4(WO_3)_{24}$ ($x > 0$, i.e., electron rich) systems (see Figure 11.6b) with respect to that of $K_2(P_2O_4)_4(WO_3)_{24}$. In contrast, according to Figure 11.6c, only electron-deficient samples $A_{2-x}(P_2O_4)_4(WO_3)_{28}$ ($x > 0$) are expected to show conductivity increase.

12. Lithium Purple Bronze $Li_{0.9}Mo_6O_{17}$ and Other Compounds Containing Zigzag Octahedral Chains as Conducting Paths

12.1 $Li_{0.9}Mo_6O_{17}$

Molybdenum purple bronzes $A_{0.9}Mo_6O_{17}$ (A = K, Na) and $TlMo_6O_{17}$ are 2D metals and exhibit CDW phenomena.[1b,c] In contrast, the lithium purple bronze $Li_{0.9}Mo_6O_{17}$ has a 3D crystal structure[34] and exhibits pseudo-1D metallic character.[34] It eventually becomes superconducting at ~2 K.[73] $(Li_{1-x}Na_x)_{0.9}Mo_6O_{17}$ ($x \leq 0.48$) and $(Li_{1-x}K_x)_{0.9}Mo_6O_{17}$ ($x \leq 0.40$) also exhibit superconductivity at ~2 K despite the random potentials expected from the presence of mixed alkali cations.[74]

$Li_{0.9}Mo_6O_{17}$ has 2.9 electrons per six molybdenum atoms and consequently, only the bottom portion of the d-block bands can be filled. In order to understand why

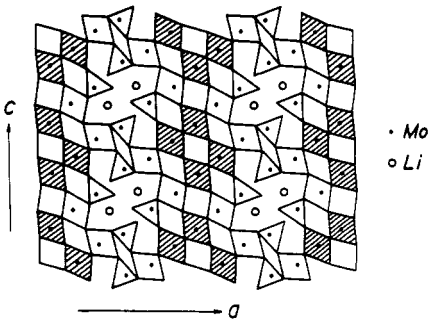

Figure 12.1. A schematic drawing of the crystal structure of $Li_{0.9}Mo_6O_{17}$, where each triangle or tetragon with an Mo atom represents an MoO_4 tetrahedron or MoO_6 octahedron, respectively.

a 3D crystal structure leads to pseudo-1D electrical properties, it is essential to determine how these 2.9 d electrons are distributed among the different Mo atoms. As shown in 8.25, the octahedral layers of $Li_{0.9}Mo_6O_{17}$ are step layers which have four different types of molybdenum atoms: Mo^I, Mo^{II}, Mo^{III}, and Mo^{IV}. The different MoO_6 octahedra in these layers share six to three of their oxygen atoms with MoO_4 tetrahedra. Consequently, each MoO_6 octahedron can be classified as an $(m + n)$ octahedron, where m and n are the oxygen atom numbers shared with MoO_6 octahedra and MoO_4 tetrahedra, respectively. Then, the four different molybdenum atoms Mo^I to Mo^{IV} are associated with octahedra of types (5 + 1), (6 + 0), (4 + 2), and (3 + 3), respectively (see 8.25 and Figure 12.1). The MoO_4 tetrahedra have in average much shorter Mo–O bonds than do the MoO_6 octahedra. All octahedra of the structure have three short and three long Mo–O distances. However, the short Mo–O bonds of the (3 + 3) and (4 + 2) octahedra are shorter than those of the (5 + 1) and (6 + 0) octahedra. Therefore, the lowest lying d-block bands of $Li_{0.9}Mo_6O_{17}$ are expected to be largely represented by the t_{2g} levels of the (5 + 1) and (6 + 0) octahedra (i.e., the t_{2g} levels of Mo^I and Mo^{II}). These two types of octahedra are hatched in Figure 12.1, which shows a projection view of the 3D structure of $Li_{0.9}Mo_6O_{17}$.[34] Therefore, according to the crystal structure analysis, the lowest lying d-block bands of $Li_{0.9}Mo_6O_{17}$ would be given by the t_{2g}-block bands of the isolated Mo_4O_{18} chains 12.1. Hence $Li_{0.9}Mo_6O_{17}$ is expected to

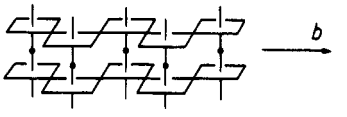

12.1a

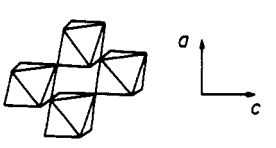

12.1b

exhibit pseudo-1D electrical properties. How the d electrons are distributed among the different Mo atoms is empirically estimated by performing a Zachariasen analysis[67] of the Mo–O bond lengths. This analysis revealed[34] that the Mo atoms of the tetrahedral sites as well as the Mo^{III} and Mo^{IV} atoms of the octahedral

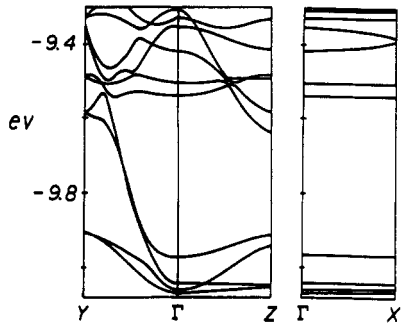

Figure 12.2. Dispersion relations of the d-block bands calculated for $Li_{0.9}Mo_6O_{17}$, where $\Gamma = (0, 0, 0)$, $X = (a^*/2, 0, 0)$, $Y = (0, b^*/2, 0)$, and $Z = (0, 0, c^*/2)$. The dashed line refers to the Fermi level.

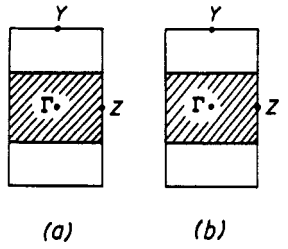

Figure 12.3. Fermi surfaces of the two partially filled d-block bands of $Li_{0.9}Mo_6O_{17}$. The wave vectors of the shaded and unshaded regions of the Brillouin zone give the occupied and unoccupied band levels, respectively.

sites have the oxidation state close to +6, but the Mo^{I} and Mo^{II} atoms of the octahedral sites have the oxidation state close +5, thereby confirming the above structure analysis.

Shown in Figure 12.2 are the dispersion relations of the bottom d-block bands calculated[75] for $Li_{0.9}Mo_6O_{17}$. As shown in Figure 12.1, the repeat unit of $Li_{0.9}Mo_6O_{17}$ is $(Li_{0.9}Mo_6O_{17})_2$ so that the d-block bands of Figure 12.2 are filled with 5.8 electrons. The four lowest bands of Figure 12.2 originate essentially from the Mo_4O_{18} double zigzag chains as predicted by the crystal structure analysis. The two partially filled bands in the $\Gamma \rightarrow Y$ region of Figure 12.2 are related in orbital character to the two flat bands in the $\Gamma \rightarrow Z$ region, although it is not apparent because of several avoided crossings. These partially filled bands give rise to the two almost perfect 1D Fermi surfaces shown in Figure 12.3. The most striking feature of the band electronic structure of $Li_{0.9}Mo_6O_{17}$ is the 1D nature of its partially filled bands. Since this feature is so critical in interpreting various physical properties of $Li_{0.9}Mo_6O_{17}$, we now examine how the bottom d-block bands come about from the viewpoint of orbital interaction analysis. Shown in Figure 12.4a is the band structure calculated[75] for the isolated Mo_4O_{18} chain 12.1 as found in the $Li_{0.9}Mo_6O_{17}$ structure. In order to trace the origin of these bands, we first study the band structure of an ideal Mo_4O_{18} double chain (i.e., the Mo_4O_{18} chain which is made up of regular MoO_6 octahedra). The t_{2g}-block bands of this chain, shown in Figure 12.4b, are similar to those of the real Mo_4O_{18} chain. The Mo_4O_{18} chain results from two Mo_2O_{10} chains 12.2 upon sharing their axial oxygens.

12.2

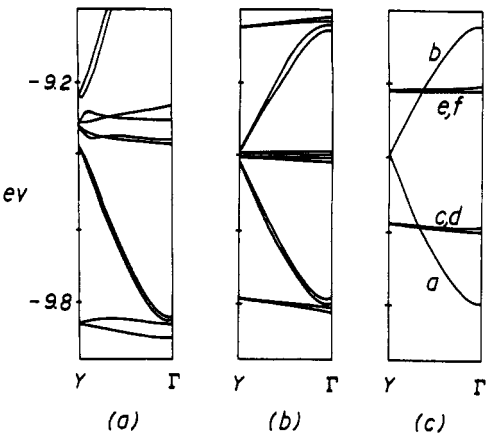

Figure 12.4. Dispersion relations of the d-block bands calculated for (a) the real Mo_4O_{18} chain, (b) the ideal Mo_4O_{18} chain, and (c) the ideal Mo_2O_{10} chain.

CHART 12.1

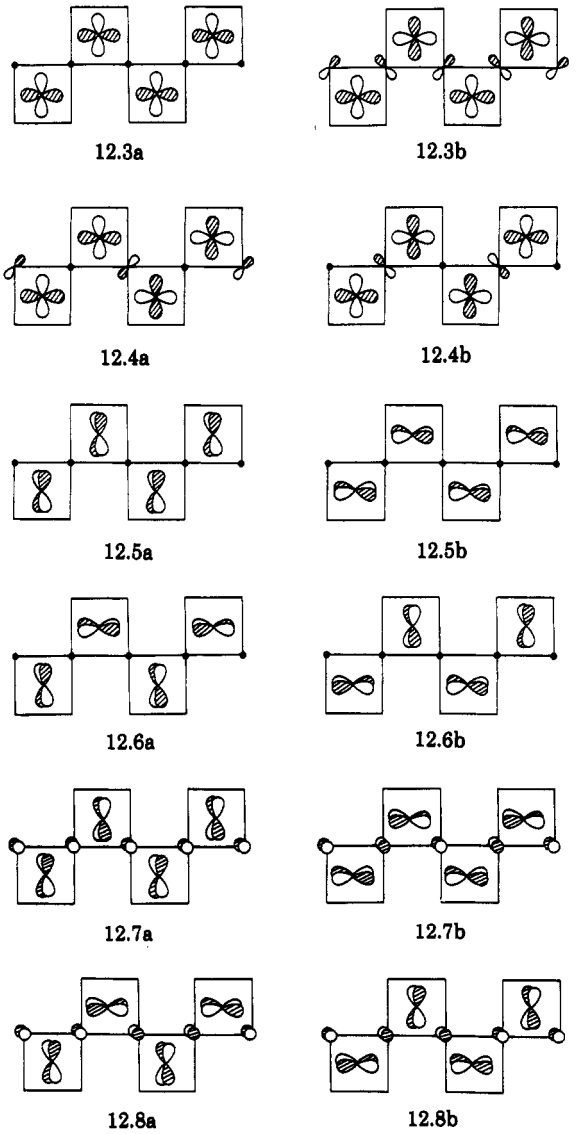

Figure 12.4c shows the t_{2g}-block bands calculated for the ideal Mo_2O_{10} chain. It is clear from Figure 12.4 that the bottom two dispersive d-block bands of $Li_{0.9}Mo_6O_{17}$ originate from the dispersive band a of each Mo_2O_{10}

TABLE 12.1. Antibonding Contributions of the Oxygen p Orbitals of the Mo–O–Mo Bridges in the t_{2g}-Block Band Orbitals of the Mo_2O_{10} chains[a]

band orbital	wave vector	bridging oxygen: within a unit cell	bridging oxygen: between nearest neighbor unit cells
12.3a	Γ	(N)	(N)
12.3b	Γ	(Y)	(Y)
12.4a	Y	(N)	(Y)
12.4b	Y	(Y)	(N)
12.5a	Γ	(N)	(N)
12.5b	Γ	(N)	(N)
12.6a	Y	(N)	(N)
12.6b	Y	(N)	(N)
12.7a	Γ	(y)	(y)
12.7b	Γ	(y)	(y)
12.8a	Y	(y)	(y)
12.8b	Y	(y)	(y)

[a] The presence of the antibonding contribution is indicated by the symbol (Y) or (y), and the absence of it by the symbol (N). The symbols (Y) and (y) refer to the stronger and the weaker antibonding contributions discussed in section 2.4.1.

chain, and the bottom two flat d-block bands of $Li_{0.9}Mo_6O_{17}$ originate from the flat bands c and d of each Mo_2O_{10} chain. Thus, in the following, we analyze the nature of the t_{2g}-block bands of the ideal Mo_2O_{10} and Mo_4O_{18} chains in some detail.[75]

12.1.1 Ideal Mo_2O_{10} Chain

The t_{2g}-block bands of the ideal Mo_2O_{10} chain are shown in Figure 12.4c. The orbitals of the dispersive bands a and b at Γ are given by 12.3a and 12.3b, respectively, and those at Y by 12.4a and 12.4b, respectively (Chart 12.1). The metal-bridging ligand antibonding interactions present in 12.3 and 12.4 are summarized in Table 12.1. 12.4a and 12.4b are degenerate so that the two bands a and b merge at Y. The orbitals of the two lower flat bands c and d of Figure 12.4c are given by 12.5 at Γ and by 12.6 at Y. Similarly, the orbitals of the two upper flat bands e and f are given by 12.7 at Γ and by 12.8 at Y. The metal-bridging ligand antibonding interactions present in 12.5–12.8 (Chart 12.1) are listed in Table 12.1. Bands c and d are flat since the orbitals of the bridging oxygen atoms do not mix into the d orbitals both at Γ and at Y, while bands e and f are flat because the orbital of the bridging oxygen atoms mix with the d orbitals both at Γ and Y.

According to Table 12.1 alone in which one considers only the metal bridging–ligand antibonding interactions, the energy level of 12.3a would be similar to that of either 12.5a or 12.5b. That 12.3a is lower in energy than either 12.5a or 12.5b arises from the difference in the extent of the molybdenum nonbridging–oxygen atom antibonding interactions. Each Mo atom of the Mo_2O_{10} chain has four (two axial and two equatorial) unshared oxygen atoms. As depicted in 12.9, the two equatorial oxygen atoms provide two strong Mo–O antibonding interactions to the x^2–y^2 orbital but two weak Mo–O

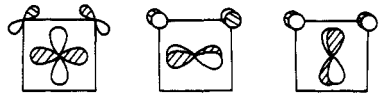

12.9a 12.9b 12.9c

antibonding interactions to the *xz* and *yz* orbitals. As shown in 12.10, however, the two axial oxygen atoms

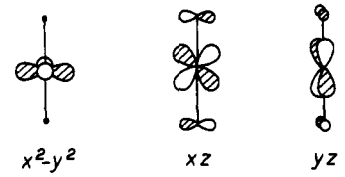

12.10a 12.10b 12.10c

do not contribute to the x^2–y^2 orbital but contribute two strong Mo–O antibonding interactions to the *xz* and *yz* orbitals. Since the sum of the two weak Mo–O antibonding corresponds to one strong Mo–O antibonding (see section 2.4.1), the overall antibonding contribution of the four unshared oxygen atoms is stronger in 12.5a or 12.5b than 12.3a. In a similar manner, it can be easily shown that the flat bands c and d lie in the middle of the band a, and the flat bands e and f lie in the middle of the band b.

12.1.2 Ideal Mo_4O_{18} Chain

The t_{2g}-block bands of the ideal Mo_4O_{18} chain are shown in Figure 12.4b. The Mo_4O_{18} chains are obtained from two Mo_2O_{10} chains by sharing the axial oxygen atoms. As discussed in the previous section, the x^2–y^2 orbital of an MoO_6 octahedron has no orbital contribution from the axial oxygen atoms. Thus, if two MoO_6 octahedra are joined together to make an Mo_2O_{11} unit by sharing an axial oxygen atom, the in-phase and out-of-phase combinations of the two x^2–y^2 orbitals are practically degenerate. Therefore, the dispersive bands a and b of the Mo_2O_{10} chain would remain the same in the Mo_4O_{18} chain. This explains the existence of the nearly degenerate, dispersive bands in Figure 12.4b.

The *xz* and *yz* orbitals (i.e., 12.10b and 12.10c, respectively) of each MoO_6 octahedron, which lead to the flat bands c–f of the ideal Mo_2O_{10}, have p-orbital participation from axial oxygen atoms. How the energy level of 12.10b (or 12.10c) of an MoO_6 octahedron is affected upon making an Mo_2O_{11} unit by sharing an axial oxygen atom is depicted in 12.11 with the *xz* orbital as an example. The $(xz)_-$ orbital 12.12a is lower

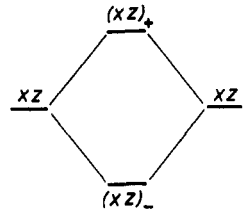

12.11

in energy than the *xz* level, since the orbital of the bridging oxygen atom does not mix into the $(xz)_-$. The $(xz)_+$ orbital 12.12b is higher in energy than the *xz* level, since the *p* orbital of the bridging oxygen atom mixes

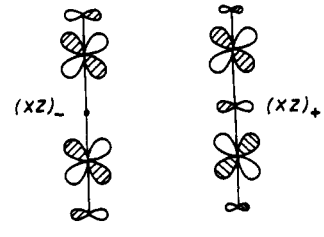

12.12a 12.12b

in with a greater coefficient than in the case of an MoO_6 octahedron 12.10b, which makes the $(xz)_+$ orbital normalized (see section 2.4.1). The set of bands c and d and that of the bands e and f each undergo the kind of level splitting depicted in 12.13, when two Mo_2O_{10} chains are condensed into one Mo_4O_{18} chain. Consequently, the two groups of nearly degenerate bands in each Mo_2O_{10} chain give rise to the three groups of nearly degenerate bands, as depicted in 12.13. As a result, we

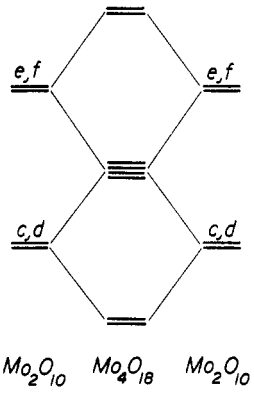

12.13

obtain the 12 t_{2g}-block bands of the ideal Mo_4O_{18} chain shown in Figure 12.4b. As can be seen from Figure 12.4, parts a and b, the d-block bands of the real Mo_4O_{18} chain are only slightly different from those of the ideal Mo_4O_{18} chain, which reflects the fact that in the real Mo_4O_{18} chain each MoO_6 octahedron deviates somewhat from a regular octahedral structure.

12.1.3 Interchain Interactions and Physical Properties

It is clear that the four filled d-block bands of $Li_{0.9}Mo_6O_{17}$ (Figure 12.2) arise primarily from the Mo_4O_{18} chains 12.1 parallel to the b axis. As can be seen from 12.14, the Mo_4O_{18} chains are linked to one another via the MoO_6 octahedra involving the Mo^{III} atoms. Note

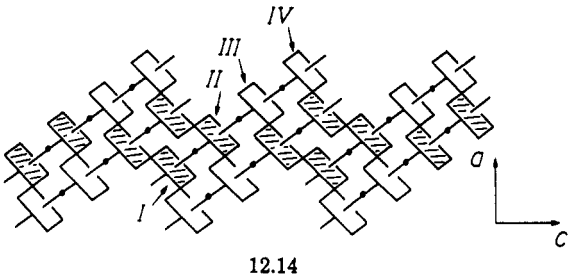

12.14

that each $Mo^{III}O_6$ octahedron is linked to two Mo_4O_{18} chains, one with sharing its axial oxygen atom and the other with sharing its equatorial oxygen atom. The x^2-y^2 orbital of each Mo^{II} atom makes a δ-type overlap interaction, and hence practically no overlap interaction, with the $Mo^{III}O_6$ octahedron through the shared axial oxygen atom. As far as the x^2-y^2 orbitals of the Mo^{II} atoms are concerned, therefore, the Mo_4O_{18} chains of $Li_{0.9}Mo_6O_{17}$ do not interact with one another. Consequently, the lower two dispersive bands of a single Mo_4O_{18} chain retain their 1D character in 3D $Li_{0.9}Mo_6O_{17}$. Each $Mo^{III}O_6$ octahedron provides a π-type overlap interaction not only with the Mo^{II} atom xz/yz orbitals through the shared equatorial oxygen atom but also with those through the shared axial oxygen atom. That is, as far as the xz/yz orbitals of the Mo^{II} atoms

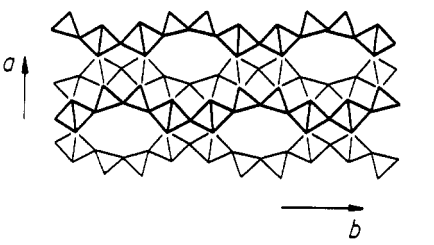

Figure 12.5. Projection view of the crystal structure of $Cs(P_2O_4)_4(WO_3)_8$. Cesium atoms (not shown) are present in the octagonal tunnels.

are concerned, the Mo_4O_{18} chains of $Li_{0.9}Mo_6O_{17}$ do interact to one another. This explains why two of the bottom four bands in $Li_{0.9}Mo_6O_{17}$ are almost equally dispersive, though not strongly, along $\Gamma \rightarrow Z$ and $\Gamma \rightarrow Y$ directions. Since only the x^2-y^2 based bands are partially filled, $Li_{0.9}Mo_6O_{17}$ is predicted to be a 1D metal in agreement with the results of the Zachariasen analysis.

The two pieces of the Fermi surfaces of Figure 12.3 are perfectly nested by the wave vector $q \simeq (0, 0.45b^*, 0)$. Consequently, $Li_{0.9}Mo_6O_{17}$ is expected to be susceptible to a 1D instability such as CDW or SDW formation associated with q.[75] The electrical resistivity of $Li_{0.9}Mo_6O_{17}$ decreases slowly as temperature is lowered down to 25 K, below which the resistivity gradually increases until it drops abruptly to zero around 1.9 K.[73] At 25 K there is also a heat capacity anomaly.[73a] It could be argued that the resistivity upturn is due to a localization effect[76] associated with the influence of the lithium cations. However, this would be inconsistent with the fact that $(Li_{1-x}Na_x)_{0.9}Mo_6O_{17}$ ($x \leq 0.48$) and $(Li_{1-x}K_x)_{0.9}Mo_6O_{17}$ ($x \leq 0.40$) exhibit both the resistivity upturn around 25 K and the superconductivity below 2 K despite the random potentials expected from the presence of mixed alkali cations. In addition, our study shows that the conducting electrons should be quite well screened from the influence of alkali cations.[75] In fact, recent magnetoresistance results do not seem to be consistent with a localization effect.[77] The resistivity upturn at 25 K could be due to a CDW formation.[77a] However, the magnetic susceptibility of $Li_{0.9}Mo_6O_{17}$ is observed to remain nearly constant upon lowering temperature below 25 K.[73b] This observation is not consistent with the possibility of a CDW instability. Alternatively, it may be suggested that the resistivity upturn of $Li_{0.9}Mo_6O_{17}$ at 25 K is caused by a SDW formation in the Mo_4O_{18} chains by analogy with the SDW $\rightarrow$ superconductor transition in the 1D organic metal $(TMTSF)_2PF_6$, which occurs under pressure.[78] This suggestion is consistent with the observation that an applied pressure suppresses the resistivity upturn of $Li_{0.9}Mo_6O_{17}$ and keeps the low-temperature superconducting state.[79] Formation of a SDW is not inconsistent with the observation of constant magnetic susceptibility. Hence, although the elucidation of the low-temperature behavior of $Li_{0.9}Mo_6O_{17}$ requires further experimental work, a SDW instability seems more likely to be responsible for the resistivity upturn at 25 K.

12.2 $Cs(P_2O_4)_4(WO_3)_8$ and $(P_2O_4)_4(WO_3)_{12}$

Double zigzag chains M_4O_{18} are also found in $Cs(P_2O_4)_4(WO_3)_8$[80] (Figure 12.5) where the W_4O_{18} chains are isolated from each other, so that $Cs(P_2O_4)_4(WO_3)_8$

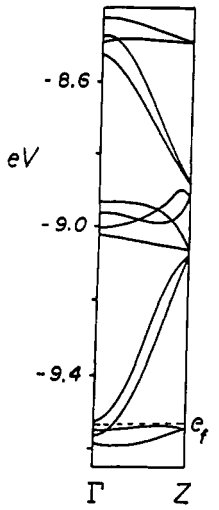

Figure 12.6. Dispersion relations of the t_{2g}-block bands of the W_4O_{18} chain, where $\Gamma = 0$ and $Z = c^*/2$. The Fermi level (dashed line) is for 4.5 d electrons per formula unit W_4O_{18}.

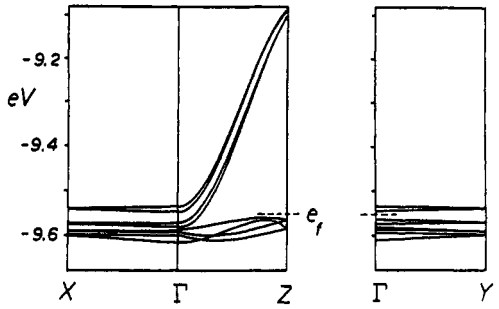

Figure 12.7. Dispersion relations of the bottom portion of the t_{2g}-block bands calculated for $Cs(P_2O_4)_4(WO_3)_8$, where $\Gamma = (0, 0, 0)$, $X = (a^*/2, 0, 0)$, $Y = (0, b^*/2, 0)$, and $Z = (0, 0, c^*/2)$. The Fermi level is for nine d electrons per unit cell.

is expected to be quasi 1D in electronic properties. Indeed, the electrical transport and magnetic properties are consistent with this picture.[81] The resistivity versus temperature plot of $Cs(P_2O_4)_4(WO_3)_8$ shows the presence of two resistivity anomalies at ~160 K and ~ 24 K: It is semiconducting from ~760 to 160 K, metallic between ~160 and ~24 K, and semiconductor below ~24 K. With the formal oxidation states Cs^+, O^{2-}, and $P_2O_7^{4-}$, the oxidation state of W in $Cs(P_2O_4)_4(WO_3)_8$ is 4.875. Thus, the electron counting on W is $d^{1.125}$, and there are 4.5 electrons to fill the d-block bands of the W_4O_{18} chain per formula unit (W_4O_{18}). The t_{2g}-block bands of the W_4O_{18} chain are shown in Figure 12.6, where the dashed line represents the Fermi level appropriate for 4.5 d electrons per unit cell. These bands are essentially identical in nature with those of the ideal Mo_4O_{18} chain described in section 12.1.2. Figure 12.7 shows the bottom portion of the t_{2g}-block bands of the $Cs(P_2O_4)_4(WO_3)_8$ lattice.[82] Since this lattice has two W_4O_{18} chains per unit cell, it has twice as many t_{2g}-block bands as does the W_4O_{18} chain and nine electrons to fill them. Except for the band doubling and a very small splitting in each pair of bands, the t_{2g}-block bands of the $Cs(P_2O_4)_4(WO_3)_8$ lattice are identical with those of the W_4O_{18} chain. The W_4O_{18} chains of $Cs(P_2O_4)_4(WO_3)_8$ are not as well screened as are the Mo_4O_{18} chains of $Li_{0.9}Mo_6O_{17}$, and hence their conduction electrons would be more susceptible to the electrical fields created by the cations. Hence order-disorder transitions of the Cs

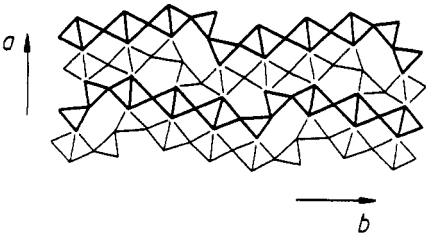

Figure 12.8. Projection view of the crystal structure of $(P_2O_4)_4(WO_3)_{12}$.

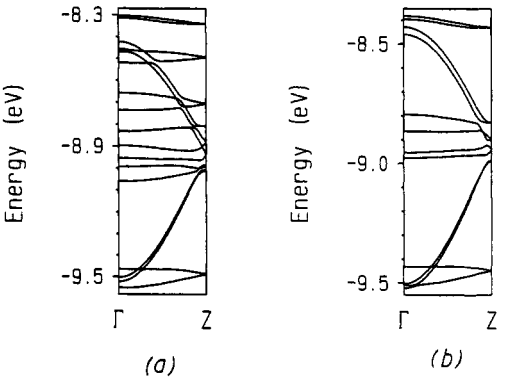

Figure 12.9. Dispersion relations of the t_{2g}-block bands of (a) the W_6O_{28} chain and (b) the W_4O_{18} chain, where $\Gamma = 0$ and $Z = c^*/2$.

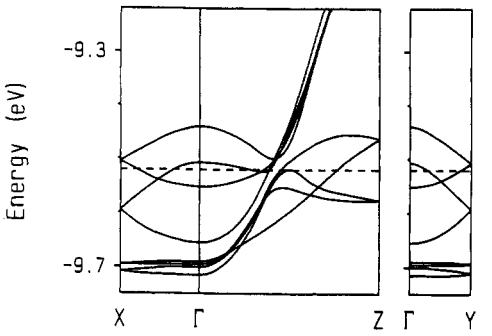

Figure 12.10. Dispersion relations of the bottom portion of the t_{2g}-block bands calculated for the $W_{12}O_{48}$ lattice of $(P_2O_4)_4(WO_3)_{12}$, where the dashed line refers to the Fermi level, $\Gamma = (0, 0, 0)$, $X = (a^*/2, 0, 0)$, $Y = (0, b^*/2, 0)$, and $Z = (0, 0, c^*/2)$.

cations could influence the conducting properties. Indeed, a partial interchannel ordering of the cations has been observed[83] near the temperature at which a metal–semiconductor transition occurs. Thus, the high-temperature semiconducting behavior may be associated with an Anderson localization (see section 6.3) of the electrons caused by an interchannel Cs^+ disorder. The resistivity upturn at ~24 K could be ascribed to a CDW associated with the one-fourth filled bands of Figure 12.7 since they are strongly one-dimensional ones. It should be possible to observe a CDW with vector $q \simeq 0.25c^*$. As the electron density in the partially filled dispersive bands increases, screening among the electrons of the band is increased so that electrons become less susceptible toward localization around Cs^+-rich neighbors. Thus, it would be of interest to study the electronic properties of $Tl_2(P_2O_4)_4(WO_3)_8$,[84] isostructural with $Cs(P_2O_4)_4(WO_3)_8$ but more electron rich. In fact, Wang et al. prepared alkali-metal substituted phases $A_yCs_x(P_2O_4)_4(WO_3)_8$ ($x + y > 1$) and

showed that as $x + y$ increases the resistivity hump at 160 K disappears whereas the upturn at 24 K remains.[82]

As shown in Figure 12.8, the crystal structure of $(P_2O_4)_4(WO_3)_{12}$[85] contains W_6O_{28} chains 12.15. These

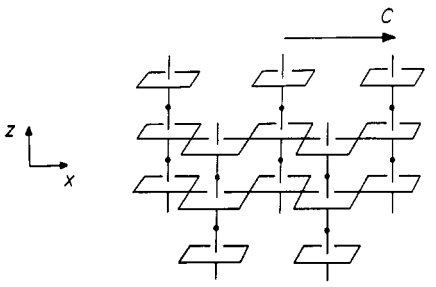

12.15a

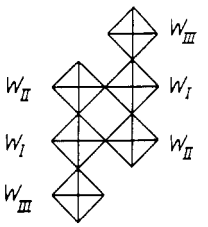

12.15b

chains contain three types of tungsten atoms: W^I, W^{II}, and W^{III}. It is noted that the W^IO_6 and $W^{II}O_6$ octahedra form a double zigzag chain W_4O_{18} 12.1. The 3D octahedral network of $(P_2O_4)_4(WO_3)_{12}$ can thus be described as a series of double zigzag W_4O_{18} chains interlinked by $W^{III}O_6$ octahedra. According to a Zachariasen-type analysis of the W–O bond lengths, the oxidation states of W^I, W^{II}, and W^{III} are calculated to be 5.19, 5.10, and 5.71, respectively.[84] The oxidation state for W^{III} is practically identical with those of the Mo^{III} and Mo^{IV} atoms (see 12.14) in $Li_{0.9}Mo_6O_{17}$, i.e., 5.72 and 5.76, respectively.[34] Thus one may expect a negligible contribution of W^{III} in the low-lying d-block bands of $(P_2O_4)_4(WO_3)_{12}$ and hence a low-dimensional electrical property. However, this is in disagreement with the observed 3D electrical properties.[84] With the formal oxidation states of O^{2-} and $P_2O_7^{4-}$, there are eight d electrons per 12 W atoms, i.e., four electrons per W_6O_{28} chain. Figure 12.9a shows the dispersion relations of the t_{2g}-block bands calculated[84] for the W_6O_{28} chain 12.15. With four electrons to fill these bands, the Fermi level lies near the top of the bottom flat band, and the bottom dispersive bands become partially filled as well. The partially filled bands are largely represented by the tungsten atoms W^I and W^{II}. This can be seen from Figure 12.9b, which shows the dispersion relations of the t_{2g}-block bands calculated for the W_4O_{18} chain obtained from the W_6O_{28} chain by removing $W^{III}O_6$ octahedra. Clearly, the bottom portions of Figure 12.9 parts a and b are nearly identical in nature. The t_{2g} orbitals of $W^{III}O_6$ octahedra represent the main orbital character of the three additional flat bands of Figure 12.9a. Consequently, the d electrons reside mainly in the W^IO_6 and $W^{II}O_6$ octahedra in agreement with the Zachariasen analysis.

From the band dispersions of the W_6O_{28} and W_4O_{18} chains, one might speculate a 1D character for $(P_2O_4)_4(WO_3)_{12}$. However, this is not the case as can be seen from Figure 12.10, which shows dispersion relations of the bottom portion of the t_{2g}-block bands calculated for the $W_{12}O_{48}$ lattice of $(P_2O_4)_4(WO_3)_{12}$. The essential features of the band dispersions of the $W_{12}O_{48}$ lattice are similar to those of the W_6O_{28} chain, except for an important difference that the π-type bands of the $W_{12}O_{48}$ lattice exhibit substantial dispersions in all three directions. Since the $W_{12}O_{48}$ lattice has two W_6O_{28} chains per unit cell, there are eight d electrons to fill the bands of Figure 12.10. Consequently, the π-type bands are cut by the Fermi level in all three directions, and $(P_2O_4)_4(WO_3)_{12}$ is a 3D metal. As shown in Figure 12.8 (see also 12.15b), the $W^{III}O_6$ octahedra of one W_6O_{28} chain share two oxygen atoms with another W_6O_{28} chain. Therefore, the π-type orbitals of an $W^{III}O_6$ octahedron provide π-type interactions not only within a W_6O_{28} chain but also between W_6O_{28} chains as schematically depicted in 12.16. This interaction is effec-

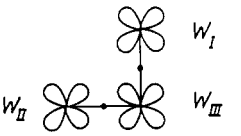

12.16

tive in the low-lying π-type bands of $(P_2O_4)_4(WO_3)_{12}$ as in $Li_{0.9}Mo_6O_{17}$ (section 12.1.3). A $W^{III}O_6$ octahedron of one W_6O_{28} chain is linked in a tilted manner, due to the diphosphate ions, to a $W^{II}O_6$ octahedron of the neighboring W_6O_{28} chain, which leads to a better interaction between the $W^{II}O_6$ and $W^{III}O_6$ octahedra. The essential difference with $Li_{0.9}Mo_6O_{17}$ lies in the number of d electrons per M_4O_{18} chain (M = Mo, W). Whereas in $Li_{0.9}Mo_6O_{17}$ there are 5.8 electrons per Mo_4O_{18} chain and the lower π bands are completely filled, in $(P_2O_4)_4(WO_3)_{12}$ there are only four electrons and both δ and π bands are partially filled. According to Figure 12.10, $(P_2O_4)_4(WO_3)_{12}$ will behave like a 1D metal if more electrons are added to its lattice so that the Fermi level lies above the top of the π bands. Our calculations[84] show that this change requires more than four electrons per formula unit, i.e., an electron count similar to that of $Li_{0.9}Mo_6O_{17}$. This explains why all the $A_x(P_2O_4)_4(WO_3)_{12}$ (A = Li, Na; $x < 1$) bronzes are 3D metals as found experimentally.[84] $Li_{0.9}Mo_6O_{17}$ and $(P_2O_4)_4(WO_3)_{12}$ contribute an example of two systems for which the Zachariasen-type analysis gives a similar distribution of the d electrons but have very different electrical conductivities. This observation originates from the fact that two types of bands with different dimensionality occur in the same energy range. In such cases, the dimensionality of the electrical conductivities will be a very sensitive function of the band filling, so that band structure calculations are necessary to determine the dimensionality or their electrical conductivities. This situation is likely to occur in low-dimensional systems built from octahedra condensation because of their δ- and π-type bands associated with the t_{2g}-block levels.

12.3 $(PO_2)_4(WO_3)_4$ and $CsMo_{4-x}O_{12}$

M_2O_{10} single zigzag chains (12.2) are found in the crystal structures of $(PO_2)_4(WO_3)_4$[86] and $CsMo_{4-x}O_{12}$.[87] In both compounds, however, these chains are distorted. Successive octahedra turn in opposite directions around their apical axis (12.17) in $(P_2O_4)_4(WO_3)_4$ and around the chain axis (12.18) in $CsMo_{4-x}O_{12}$. The W_2O_{10} chains

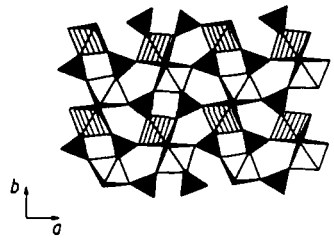

Figure 12.11. Projection view of the structure of $(PO_2)_4(WO_3)_4$.

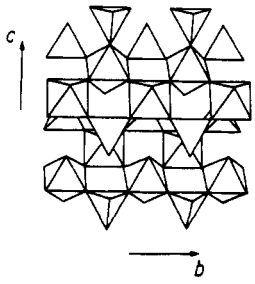

Figure 12.12. Projection view of the structure of $CsMo_{4-x}O_{12}$.

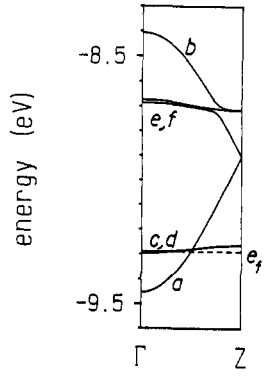

Figure 12.13. Dispersion relations of the t_{2g}-block bands calculated for the W_2O_{10} chains of $(PO_2)_4(WO_3)_4$.

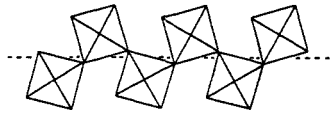

12.17

of the former are linked by PO_4 tetrahedra such that every chain can be considered isolated from one another (Figure 12.11). $CsMo_{4-x}O_{12}$ is a layered compound where the MoO_3 layers (Figure 12.12) are constructed from Mo_2O_{10} zigzag chains 12.18 linked by MoO_4 tetrahedra. Since the MoO_4 tetrahedra have in average

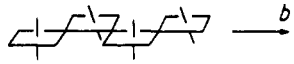

12.18

much shorter Mo–O distances than the MoO_6 octahedra, the tetrahedral Mo atoms should be in a +6 oxidation state, and therefore both $CsMo_{4-x}O_{12}$ and $(PO_2)_4(WO_3)_4$ should be 1D materials. It is noted that, according to the crystal structure refinement, the Cs sites in $CsMo_{4-x}O_{12}$ are fully occupied but the Mo sites, both tetrahedral and octahedral, are partially vacant (i.e., $x \simeq 0.13$).[87]

With the oxidation states of O^{2-} and P^{5+}, the d

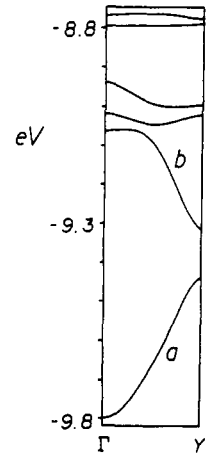

Figure 12.14. Dispersion relations of the t_{2g}-block bands calculated for the Mo_2O_{10} chains of $CsMo_{4-x}O_{12}$.

electron count of W in $(PO_2)_4(WO_3)_4$ is d^1. Namely, there are two electrons to fill the t_{2g}-block bands of Figure 12.13.[88] Therefore, the dispersive band a is nearly half-filled, and the nearly degenerate bands c and d are quarter-filled as a whole. In simple chemical terms, this implies that the two δ orbitals of a unit cell accommodate one electron, and so do the four π orbitals of a unit cell. Since bands c and d are extremely narrow, electrons in these bands are most likely to be localized. On the other hand, band a is quite dispersive so that electrons in this band are expected to be delocalized. Actual calculations[88] show that these observations remain valid for the 3D lattice of $(PO_2)_4(WO_3)_4$. As a result, $(PO_2)_4(WO_3)_4$ is expected to be metallic and possess magnetic properties associated with localized electrons. In addition, the 1D metallic band a may lead to an electronic instability such as CDW. It would be of interest to measure the physical properties of $(PO_2)_4(WO_3)_4$.

The dispersion relations for the Mo_2O_{10} zigzag chains of $CsMo_{4-x}O_{12}$ are shown in Figure 12.14. The main difference from the band structure of Figure 12.13 is that the four nondispersive bands have been pushed up in energy and that an energy gap opens at *Y*. The latter stems from the fact that the two Mo atoms of the octahedral zigzag chain are slightly different, while the former results from the fact that all octahedra have one very strong O···Mo–O distortion (i.e., 1.676 vs 2.211 Å or 1.694 vs 2.222 Å) along the apical axis. This leaves only one d orbital on the equatorial plane at low energy. Bands a and b have thus the same orbital character as do bands a and b of the ideal Mo_2O_{10} chain in Figure 12.4c. Assuming tetrahedral Mo atoms in a +6 oxidation state, there are $1 - 6x$ electrons to fill band a of Figure 12.14. Band a is as much dispersive as the partially filled bands of metallic oxides like blue bronze. Hence the semiconductive behavior of $CsMo_{4-x}O_{12}$[87,89] could result either from Anderson-like localization if vacant Mo sites occur only in MoO_4 tetrahedra or simply because the conduction path is cut if vacant Mo sites occur in both MoO_6 octahedra and MoO_4 tetrahedra. The crystal structure refinement study of Abrahams et al.[87] is consistent with the second possibility. Interestingly, if a nondefective $CsMo_4O_{12}$ with this structure could be prepared, it would have a half-filled 1D band a exactly as it does $(PO_2)_4(WO_3)_4$. However, the formal electron count on the octahedral

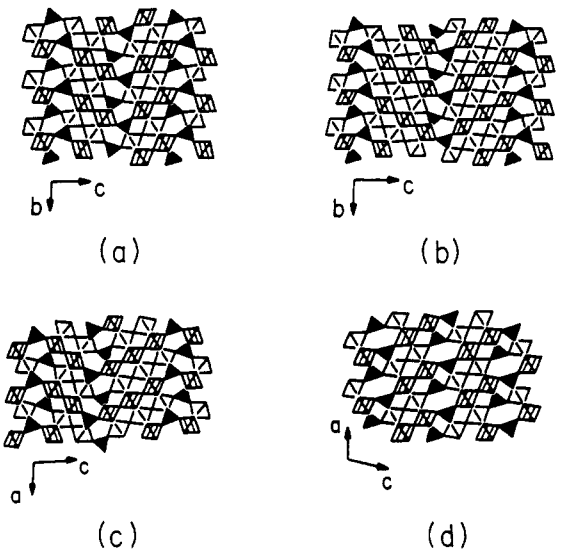

Figure 13.1. Projection views of representative MPTB phases: (a) $(PO_2)_4(WO_3)_4(WO_3)_4$, (b) $(PO_2)_4(WO_3)_6(WO_3)_6$, (c) $(PO_2)_4(WO_3)_4(WO_3)_6$, and (d) $Na_x(PO_2)_4(WO_3)_4(WO_3)_4$.

metal atom would be different in the two phases, i.e., $d^{0.5}$ in $CsMo_4O_{12}$ but d^1 in $(PO_2)_4(WO_3)$, as a result of the different structure of the MO_6 octahedra.

13. Compounds Containing Step-Layers as Conducting Paths

The Magnéli phases γ- and η-Mo_4O_{11}[32] are both 2D metals at room temperature and exhibit a resistivity anomaloy at low temperature (the phase transition temperature T_p = 100 and 109 K for γ- and η-Mo_4O_{11}, respectively).[90,91] Diffuse X-ray and electron-scattering studies on η-Mo_4O_{11} show that the resistivity anomaly originates from a CDW,[91b] which leads to the satellite peaks centered at (0, 0.23b^*, 0). Although the CDW affects the resistivity anisotropically, Mo_4O_{11} retains its 2D metallic character below T_p.

γ- and η-Mo_4O_{11} contain step-layers of composition Mo_6O_{22} (see 8.24). Such layers are linked via MoO_4 tetrahedra to form the 3D structures of Mo_4O_{11}. The γ- and η-Mo_4O_{11} phases differ slightly only in the way the Mo_6O_{22} layers are joined by the MoO_4 tetrahedra, as shown in Figure 8.2, parts a and b, respectively.[32] γ- and η-Mo_4O_{11} are instructural with the third members of MPTB the family.[31b,33] In the MPTB phases, the octahedral step layers are linked by PO_4 tetrahedra. The MPTB phases have either pentagonal or hexagonal tunnels between the W–O step-layers, and those with pentagonal and hexagonal tunnels are called $MPTB_p$ and $MPTB_h$, respectively.[3,28,29] The latter invariably occur with alkali-metal atoms Na or K in the hexagonal tunnels. Nearly all MPTB phases have two W–O layers per unit cell so that the general formula for the $MPTB_p$ phases can be written as $(PO_2)_4(WO_3)_p(WO_3)_q$, and that for the $MPTB_h$ phases as $A_x(PO_2)_4(WO_3)_p(WO_3)_q$ (A = Na, K). The indices p and q are even or odd integers, which are equal to the number of WO_6 octahedra per unit cell used to form the W–O layer. Usually, p and q are identical, thereby leading to the alternative formulas $(PO_2)_4(WO_3)_{2m}$ and $A_x(PO_2)_4(WO_3)_{2m}$. However, they can be different as in the case of $(PO_2)_4(WO_3)_4(WO_3)_6$,[92] which should be distinguished from $(PO_2)_4(WO_3)_5(WO_3)_5$. Figure 13.1 shows projection views of four representative MPTB phases, $(PO_2)_4(WO_3)_4(WO_3)_4$,[30] $(PO_2)_4(WO_3)_6(WO_3)_6$,[33] $(PO_2)_4(WO_3)_4(WO_3)_6$,[92] and $Na_x(PO_2)_4(WO_3)_4(WO_3)_4$,[31b] where the filled triangles represent the PO_4 tetrahedra.

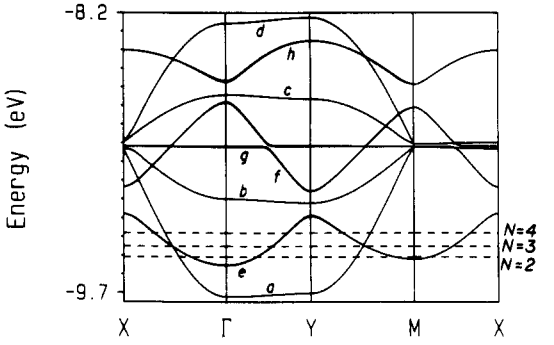

Figure 13.2. Dispersion relations of the t_{2g}-block bands calculated for an ideal W_4O_{16} layer, where the dashed lines refer to the Fermi levels for N = 2, 3, and 4. Γ = (0, 0), X = (a^*/2, 0), Y = (0, b^*/2), and M = (a^*/2, b^*/2).

For the purpose of d-electron counting, the general formula of the MPTB phases can be written as $A_x(PO_2)_4(WO_3)_p(WO_3)_q$. With the formal oxidation states of A^+, P^{5+}, and O^{2-}, the average oxidation state of W is given by $6 - (4 + x)/(p + q)$. Thus, a unit cell of an MPTB phase has $4 + x$ electrons or equivalently $2 + x/2$ electrons per W–O layer. Namely, there exist $2 + x/2$ electrons per unit cell to fill the t_{2g}-block bands of a W–O layer. In the Mo_4O_{11} phases ($x = 0$, $p = q = 6$), the average Mo–O bonds of the MoO_4 tetrahedra are much shorter than those of the MoO_6 octahedra. Consequently, the tetrahedral Mo atoms will have the formal oxidation state +6 so that there are eight d electrons per repeat unit or equivalently, four d electrons per octahedral Mo–O layer.

Recently, the $MPTB_p$ phase, $(PO_2)_4(WO_3)_6(WO_3)_6$, has been found to have resistivity anomalies[93] which originate from CDW instabilities.[94] Although the octahedral step-layers of Mo_4O_{11} and $(PO_2)_4(WO_3)_6(WO_3)_6$ are similar, the resistivity anomalies of the two phases are different. Presumably, this results from the different electron filling of the layer d-block bands. In the following, we examine how the electronic structure of octahedral step layers depend on both band filling and thickness of the slab.

13.1 Band Dispersion Relations of the Ideal Step-Layer M_4O_{16} (M = Mo, W)[95,96]

Figure 13.2 shows the dispersion relations of the t_{2g}-block bands calculated[96] for an ideal W_4O_{16} layer made up of regular WO_6 octahedra (with the average W–O distance of 1.916 Å), where the dashed lines refer to the Fermi levels appropriate for 2, 3, and 4 d electrons per unit cell, and the $\Gamma \rightarrow X$ and $\Gamma \rightarrow Y$ directions represent the intra- and interchain directions, respectively. The four bands a, b, c, and d are only dispersive along the intrachain direction and have 1D character (see also section 15.2 for further discussion). The four bands e, f, g, and h are each practically doubly degenerate. The bands e, f, and h are dispersive along the intra- and interchain directions and thus have 2D character. The Fermi level for any d-electron count between 2 and 4 per unit cell cuts the 1D band a as well as the two nearly degenerate 2D bands e. We now

probe the essential features of Figure 13.2 by examining the orbital character of bands a, b, and e.[95]

13.1.1 δ Bands

Band a of Figure 13.2 is constructed from the orbital 13.1a of the W_4O_{21} unit 13.2 (i.e., the lowest lying d orbital of the unit). Within this unit, the three equatorial bridging oxygen atoms have no contributions to 13.1a, i.e., they have the (NNN) contribution to 13.1a.

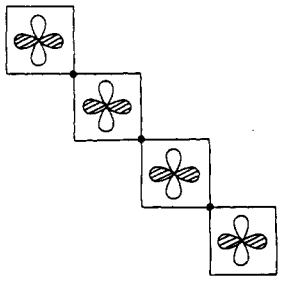

13.1a

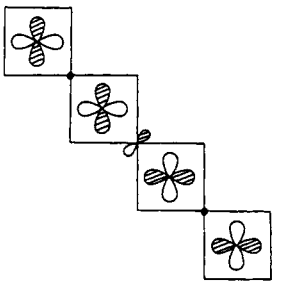

13.1b

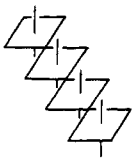

13.2

Band a at Γ and X is given by the step orbitals 13.3 and 13.4, respectively, which show the orbitals for one step of the W_4O_{16} layer (see 8.20). Between the W_4O_{21} units

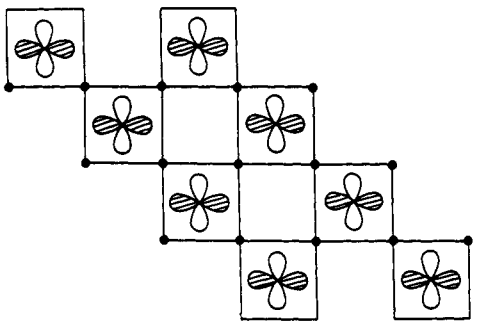

13.3

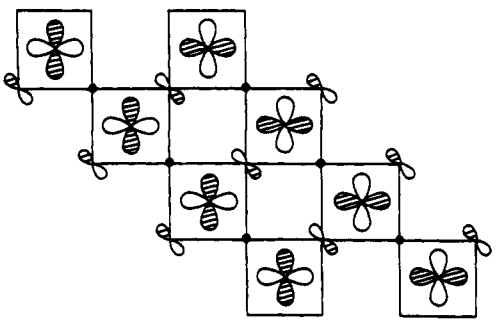

13.4

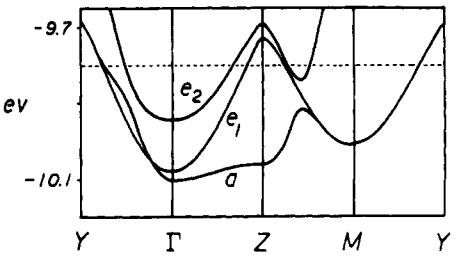

Figure 13.3. Dispersion relations of the t_{2g}-block bands calculated for the real Mo_8O_{22} layer of γ-Mo_4O_{11}. Γ, Y, Z, and M refer to the wave vectors (0, 0), ($b^*/2$, 0), (0, $c^*/2$), and ($b^*/2$, $c^*/2$). The dashed line refers to the Fermi level.

along the chain axis, the three equatorial bridging atoms have the (NNN) and (YYY) contributions to 13.3 and 13.4, respectively. Thus band a is less stable at X than at Γ by three (Y) interactions per W_4O_{21} unit. The step orbital of band a at Y is also given by 13.3. Along the interchain axis, the step orbitals 13.3 combine in-phase at Γ but out-of-phase at Y. The two bridging–axial atoms of each W_4O_{21} unit have the (NN) contribution to these band orbitals, due to the δ symmetry of the metal d orbitals. Therefore band a is dispersive along Γ → X and remains flat along Γ → Y.

Band b of Figure 13.2 is constructed from orbital 13.1b of the W_4O_{21} unit (i.e., the second lowest lying δ orbital of the unit 13.2. Within this unit, 13.1b has the (NYN) contribution from the three bridging–equatorial oxygen atoms. Band b at Γ and X has the step-orbitals 13.5 and 13.6, respectively. Between the W_4O_{21} units

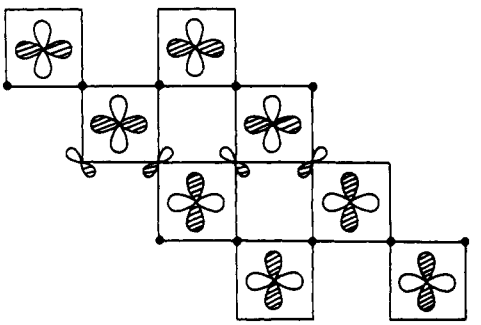

13.5

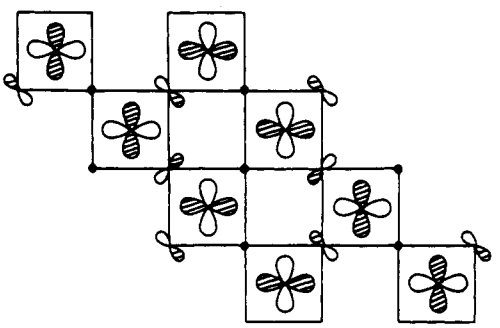

13.6

along the chain axis, 13.5 and 13.6 have the (NYN) and (YNY) contributions from the bridging–equatorial oxygen atoms, respectively. Therefore, 13.5 and 13.6 are less stable than 13.3 by two and three (Y) interactions per W_4O_{21} unit, respectively. Thus, with respect to

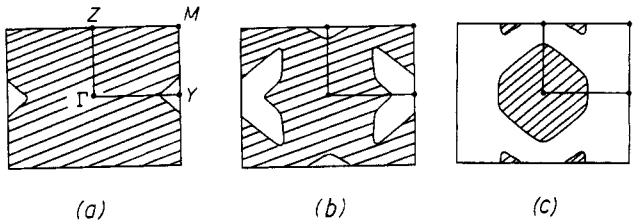

Figure 13.4. Fermi surfaces of the Mo_6O_{22} layer associated with (a) band a, (b) band e_1, and (c) band e_2. The wave vectors of the shaded and unshaded regions refer to filled and unfilled band levels, respectively.

band a, band b lies higher in energy and is less dispersive along $\Gamma \rightarrow X$. Band b is flat along $\Gamma \rightarrow Y$ for the same reason why band a is flat along $\Gamma \rightarrow Y$. Table 13.1 lists the contributions of the bridging oxygen p orbitals to bands a, b, and e at Γ, X, and Y.

13.1.2 π Bands

The nearly doubly degenerate band e of Figure 13.2 is constructed from the orbitals 13.7a and 13.7b. Both

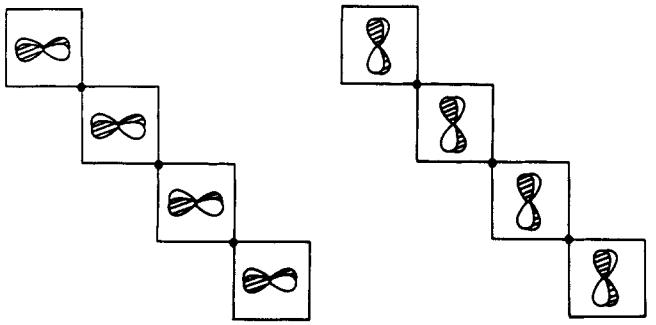

13.7a 13.7b

are the lowest lying π orbitals of the W_4O_{21} unit 13.2. Within this unit, the three bridging–equatorial oxygen

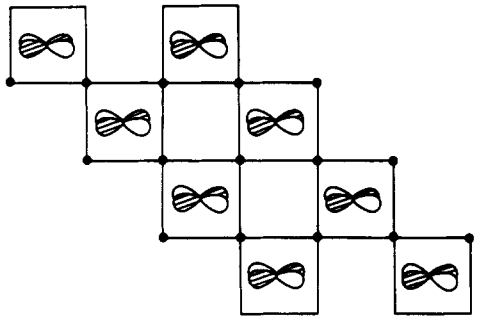

13.8

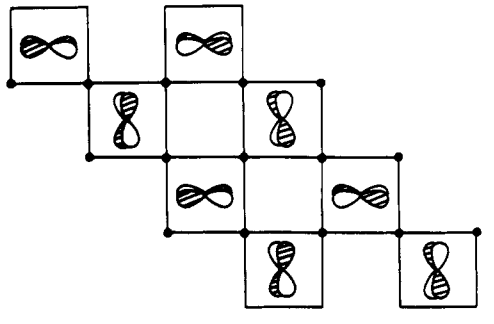

13.9

atoms have the (NNN) contribution to 13.7a and 13.7b. One of the two bands e has the step orbital 13.8 and 13.9 at Γ and Y, respectively. Between the W_4O_{21} units, 13.8 and 13.9 have the (NNN) contribution from the three bridging–equatorial oxygen atoms. At Γ and X, the step orbitals repeat with the same sign along the interchain axis, so that 13.8 and 13.9 have the (NN) and (YY) contributions, respectively, from the two bridging–axial oxygen atoms per W_4O_{21} unit. At Y, however, the step orbitals 13.8 repeat with alternating signs along the interchain axis. Thus band orbital e at Y has the (YY) contribution from the two bridging–axial oxygen atoms per W_4O_{21} unit. Therefore, as listed in Table 13.1, band e goes up in energy along both $\Gamma \rightarrow X$ and $\Gamma \rightarrow Y$. That is, band e is 2D-like. The same conclusion is obtained for the other member of the nearly degenerate band e. According only to the bridging oxygen contributions listed in Table 13.1, the 2D-like band e at Γ and the 1D-like band a at Γ would have the same energy. However, one must take into consideration the antibonding contributions from the eight nonbridging oxygen atoms of each W_4O_{21} (i.e., four axial and four equatorial oxygen atoms in 13.2). At Γ, band a (δ band) has $4(Y_t)$ interactions from the equatorial oxygen atoms, while band e (π band) has $4(Y_t)$ and $4(y_t)$ interactions from the axial and equatorial oxygen atoms, respectively. Therefore, band e should lie higher in energy than band a.

13.2 Magnéli Phases γ- and η-Mo_4O_{11}

The Mo_6O_{22} step layers 8.24 of Magnéli phases γ- and η-Mo_4O_{11}[32] contain three different types of molybdenum atoms (see 13.10). All octahedra have three short and

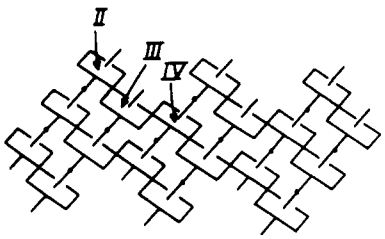

13.10

three long Mo–O bond lengths although the extent of the distortion is much stronger in the $Mo^{II}O_6$ octahedra. This suggests that d electrons are confined to the inner part of the layer (i.e., the $Mo^{III}O_6$ and $Mo^{IV}O_6$ octahedra). The Zachariasen analysis of the Mo–O bond lengths, in which the molybdenum oxidation state in the MoO_4 tetrahedral site is normalized to +6, shows that the Mo^{II}, Mo^{III}, and Mo^{IV} atoms have the oxidation states +5.8, +5.4, and +5.0, respectively,[32a] confirming the simple crystal structure analysis. Removal of the Mo^{II} octahedra from an Mo_6O_{22} layer leads to an Mo_4O_{16} step layer.

Shown in Figure 13.3 is the bottom portion of the t_{2g}-block bands calculated[95] for the real Mo_6O_{22} layer taken from the crystal structure of γ-Mo_4O_{11}. With four d electrons to fill these bands, the Fermi level cuts the bottom three bands a, e_1, and e_2. The main orbital characters of these bands are largely represented by the molybdenum atoms Mo^{III} and Mo^{IV}, in agreement with

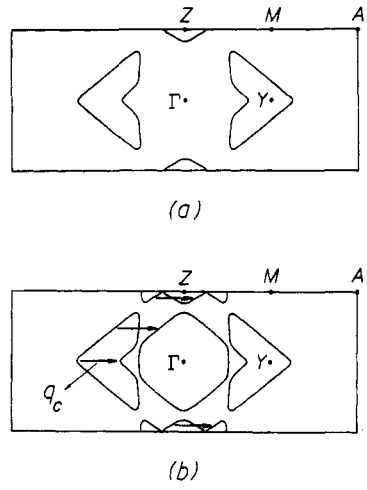

Figure 13.5. (a) Combined hole Fermi surfaces in the extended zone scheme for bands a and e_1 of the Mo_6O_{22} layer, where $A = (b^*, c^*/2)$. (b) Combined electron and hole surfaces in the extended zone scheme, where the nesting vector is given by $q_c \simeq (0.25b^*, 0)$.

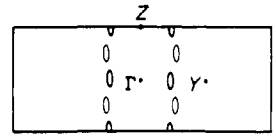

Figure 13.6. Fermi surface expected to result from Figure 13.5b after being partially destroyed by the CDW associated with q_c.

the crystal structure analysis. The nature of these three bands is very similar to the three lowest d bands of the ideal W_4O_{16} step-layer examined in section 13.1.

The Fermi surfaces associated with bands a, e_1, and e_2 are shown[95] in Figure 13.4, parts a, b, and c, respectively. Since bands a and e_1 merge into a single band (along $Z \rightarrow M \rightarrow Y$ of Figure 13.3), their Fermi surfaces should be combined into one in the extended zone scheme as illustrated in Figure 13.5a. Thus, the Mo_6O_{22} layer, and therefore Mo_4O_{11}, has the hole pockets given by Figure 13.5a and the electron pockets given by Figure 13.4c. All those Fermi surfaces are closed so that Mo_4O_{11} is predicted to be a 2D metal, as experimentally observed.[90,91] The hole Fermi surfaces of Figure 13.5a and the electron Fermi surface of Figure 13.4c are combined together in Figure 13.5b. In each heart-shaped hole surface, the "V-shaped" portions are related to each other by the translation $q_c \simeq (0.25b^*, 0)$, i.e., they are nested by q_c. The remaining portions of the hole surfaces, except for those parallel to the $\Gamma \rightarrow Z$ direction, are found to be nested to the appropriate portions of the electron surface by q_c as indicated by the arrows. This nesting[95] is the most likely reason for the electronic instability associated with the superlattice spots at $(0, 0.23b^*, 0)$.[91b] The nesting given by q_c is incomplete since the Fermi surface has some pieces not nested by q_c (i.e., those approximately parallel to $\Gamma \rightarrow Z$). In such a case, a CDW formation associated with q_c does not remove these pieces, but leads to elongated ellipse-like pockets comprising them as schematically shown in Figure 13.6. Nesting among such Fermi surface pockets would be responsible for another resistivity anomaly found for η-Mo_4O_{11} at 30 K.[91a-b,97] For further discussions of the Fermi surface nesting; see section 15.

TABLE 13.1. Antibonding Contributions of the Oxygen p Orbitals of the W–O–W Bridges in the t_{2g}-Block Band Orbitals of the W_4O_{16} Layer[a]

band	wave vector	step orbital	bridging oxygen: within a unit cell	bridging oxygen: between nearest neighbor unit cells, eq	bridging oxygen: between nearest neighbor unit cells, ax
a	Γ	13.3	(NNN)	(NNN)	(NN)
	X	13.4	(NNN)	(YYY)	(NN)
	Y	13.3	(NNN)	(NNN)	(NN)
b	Γ	13.5	(NYN)	(NYN)	(NN)
	X	13.6	(NYN)	(YNY)	(NN)
	Y	13.5	(NYN)	(NYN)	(NN)
e	Γ	13.8	(NNN)	(NNN)	(NN)
	X	13.9	(NNN)	(NNN)	(YY)
	Y	13.8	(NNN)	(NNN)	(YY)

[a] The presence of an antibonding contribution is indicated by the symbol (Y), and the absence of it by the symbol (N).

TABLE 13.2. Oxidation States of the W_I and W_{II} Atoms in the W_4O_{16} Layers Calculated by the Bond Valence Sum Analysis

compound	W_I	W_{II}
$(PO_2)_4(WO_3)_4(WO_3)_4$	5.82	5.18
$(PO_2)_4(WO_3)_4(WO_3)_6$	5.28	5.82
$Na_{1.5}(PO_2)_4(WO_3)_4(WO_3)_4$	5.24	5.38

13.3 Similarity of Band Structures in Monophosphate Tungsten Bronzes[96]

As discussed in previous sections, complex oxide metals often contain their d electrons only in a specific portion of their crystal structure. It is then important to estimate the oxidation states of nonequivalent metal atoms of the structure. As pointed out earlier, this question has been answered by a bond valence sum analysis, which allows one to estimate the oxidation state of a metal on the basis of the metal–oxygen bond lengths it makes with the surrounding oxygen atoms. This type of analysis (e.g., the Zachariasen-type analysis)[67] has been quite successful for molybdenum oxides. The parameters needed for the bond valence sum analysis of the MPTB phases have been developed by Domengès et al.[98] according to eq 13.1

$$S_i = (R_0/R_i)^n \qquad (13.1)$$

where S_i is the bond valence of the bond i with bond length R_i. In this equation, $n = 5.75$ and R_0 is determined so as to make the sum of all the bond valences associated with the W atoms equal to that expected from the formal tungsten oxidation states in the crystal. The bond valence sum of a W atom is then given by the sum of all the bond valences the W atom is associated with. For example, let us consider the W_4O_{16} layers present in several MPTB's. There are two nonequivalent W atoms (W^I and W^{II}) in the W_4O_{16} layers of $(PO_2)_4(WO_3)_4(WO_3)_4$,[30] $(PO_2)_4(WO_3)_4(WO_3)_6$,[92] and $Na_x(PO_2)_4(WO_3)_4(WO_3)_4$ ($x = 1.5$)[31b] shown in Figure 13.1. Every W^IO_6 octahedron shares five oxygen atoms with other WO_6 octahedra and one oxygen atom with a PO_4 tetrahedra, while every $W^{II}O_6$ octahedron shares three oxygen atoms with other WO_6 octahedra and three oxygen atoms with PO_4 tetrahedra. Table 13.2 summarizes the oxidation states of the W^I and W^{II} at-

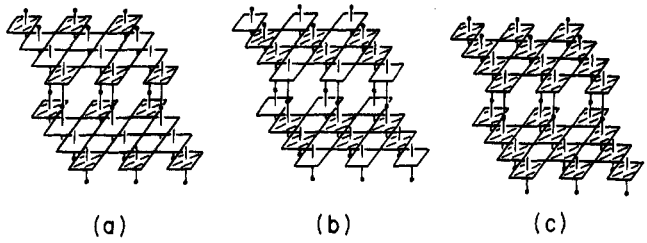

Figure 13.7. Perspective views of the W_4O_{16} layers found in (a) $(PO_2)_4(WO_3)_4(WO_3)_4$, (b) $(PO_2)_4(WO_3)_4(WO_3)_6$, and (c) $Na_{1.5}(PO_2)_4(WO_3)_4(WO_3)_4$. The shaded octahedra are predicted to contain d electrons by the bond valence sum analysis.

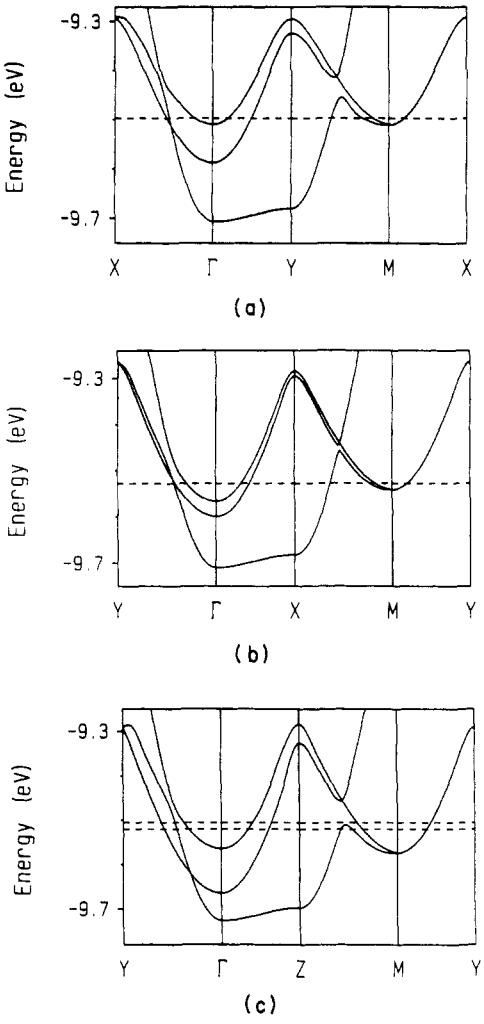

Figure 13.8. Dispersion relations of the bottom portions of the t_{2g}-block bands calculated for the W_4O_{16} layers of (a) $(PO_2)_4(WO_3)_4(WO_3)_4$, (b) $(PO_2)_4(WO_3)_4(WO_3)_6$, and (c) $Na_x(PO_2)_4(WO_3)_4(WO_3)_4$. $\Gamma = (0, 0)$, $X = (a^*/2, 0)$, $Y = (0, b^*/2)$ and $M = (a^*/2, b^*/2)$. The chain direction is given along $\Gamma \rightarrow X$ in a, but along $\Gamma \rightarrow Y$ in b and c. The dashed lines in a and b refer to the Fermi level corresponding to two d electrons per unit cell. In c the two dashed lines refer to the Fermi levels appropriate for 2.55 and 2.75 d electrons per unit cell (i.e., x = 1.1 and 1.5), respectively.

oms calculated for the three different W_4O_{16} layers by the bond valence sum analysis. For $Li_{0.9}Mo_6O_{17}$ and Mo_4O_{11}, it is reasonable to consider that the Mo atoms with oxidation state +5.7 or greater do not contain d electrons, and those with oxidation state +5.4 or smaller have d electrons. According to this approximation, the d-electron-containing WO_6 octahedra are isolated in the W_4O_{16} layer of $(PO_2)_4(WO_3)_4(WO_3)_4$ (shaded octahedra in Figure 13.7a), but form a continuous chain in the W_4O_{16} layer of $(PO_2)_4(WO_3)_4(WO_3)_6$ (shaded octahedra in Figure 13.7b). On the other hand, all WO_6 octahedra are expected to have d electrons in the W_4O_{16} layer of $Na_x(PO_2)_4(WO_3)_4(WO_3)_4$ (x = 1.5) (see Figure 13.7c). Therefore, Figure 13.7 suggests that the W_4O_{16} layers are nonmetallic in $(PO_2)(WO_3)_4(WO_3)_4$, 1D metallic in $(PO_2)_4(WO_3)_4(WO_3)_6$, and 2D metallic in $Na_{1.5}(PO_2)_4(WO_3)_4(WO_3)_4$.

The dispersion relations of the bottom portions of the t_{2g}-block bands calculated[96] for the W_4O_{16} layers in $(PO_2)_4(WO_3)_4(WO_3)_4$, $(PO_2)_4(WO_3)_4(WO_3)_6$, and $Na_x(PO_2)_4(WO_3)_4(WO_3)_4$ (x = 1.1–1.5) are shown in Figure 13.8, parts a, b, and c, respectively. All these bands are very similar to those of the ideal W_4O_{16} layer shown in Figure 13.2, except that bands e are split in the real W_4O_{16} layers because of their octahedral distortions. The most important aspect of Figure 13.8 is that the W_4O_{16} layers of $(PO_2)_4(WO_3)_4(WO_3)_4$ and $(PO_2)_4(WO_3)_4(WO_3)_6$ have both 1D and 2D metallic bands, as does that of $Na_x(PO_2)_4(WO_3)_4(WO_3)_4$.[99] This is in sharp contrast to the prediction of the bond valence sum analysis. This failure of the bond valence sum analysis is striking, in view of its general success in molybdenum oxide metals. The major reason for this failure is that the orbitals of bands a and e in the W_4O_{16} layers of $(PO_2)_4(WO_3)_4(WO_3)_4$ and $(PO_2)_4(WO_3)_4(WO_3)_6$ have nearly equal contributions from their W^I and W^{II} atoms, just as in the case of the corresponding bands in $Na_x(PO_2)_4(WO_3)_4(WO_3)_4$.

In the ideal W_4O_{16} layer, the bottoms of bands e are close in energy to that of band a (Figure 13.2) because, at Γ, their symmetric metal–oxygen–metal (M–O–M) bridges do not allow the p-orbital contributions from the bridging oxygen atoms when the adjacent two metal orbitals have a same sign (see 13.11a). If there was a strong M–O···M bond alternation (as a consequence of octahedral distortion), the bridging oxygen p orbital combines out-of-phase with the metal d orbital of the shorter M–O bond even if the adjacent two metal orbitals have a same sign (see 13.11b). Such an anti-

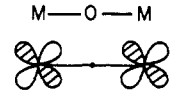

13.11a

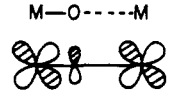

13.11b

bonding interaction raises the energy of 13.11b with respect to 13.11a. In the case of the MPTB phases, the W–O···W alternations are weak so that the bonding pattern of their W–O···W bridges at Γ are similar to that of 13.11a. Thus, in the t_{2g}-block bands of the W_4O_{16} layers (Figure 13.8), the bottoms of bands a and e are represented by W^I and W^{II} almost equally. In Mo_4O_{11}, of the three nonequivalent MoO_6 octahedra, one has a much stronger distortion than do the remaining two so that, 13.11b becomes appropriate. The existence of such a large difference in the magnitudes of octahedral distortion is necessary for the prediction of the bond

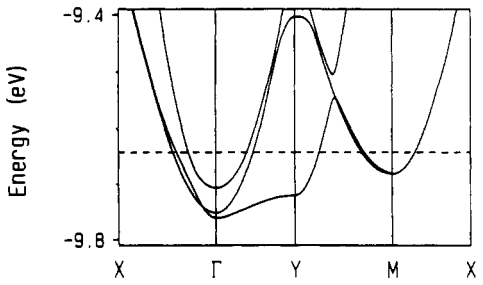

Figure 13.9. Dispersion relations of the bottom portion of the t_{2g}-block bands calculated for the W_6O_{22} layer of $(PO_2)_4(WO_3)_6(WO_3)_6$. The dashed line refers to the Fermi level corresponding to two d electrons per unit cell.

valence sum analysis to agree with that of band electronic structure calculations. This is not the case for the MPTB phases.

In the perovskite-type W–O layers, the W atoms interact via the W–O–W bridges. Thus, a d-block band orbital in which contributions of the bridging oxygen p orbitals are absent would have an energy close to that of the atomic d level. This should be the case regardless of how many WO_6 octahedra per unit cell are used to form a perovskite-type W–O layer. For example, band a of the W_4O_{16} layer is constructed from the orbital pattern 13.12a. Likewise, the corresponding band of the W_6O_{22} layer is constructed from the orbital pattern 13.12b. Since 13.12a and 13.12b have similar energies

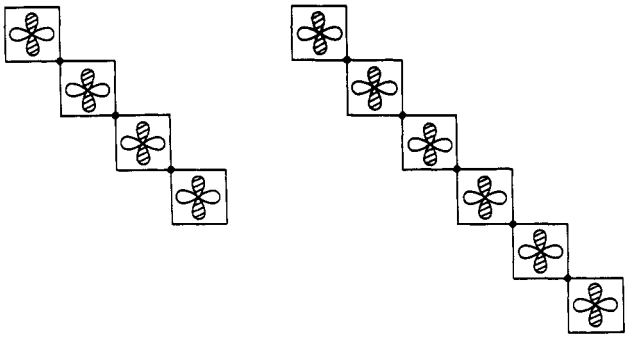

13.12a 13.12b

and similar nodal patterns, the resulting bands a of the W_4O_{16} and W_6O_{22} layers should be similar. According to the same reasoning, it is predicted that the bottom three t_{2g}-block bands of the W_4O_{16} layer should be similar to those of the W_6O_{22} layer or any other perovskite-type W–O step layer. Since the W–O step-layer of the MPTB phases have between 2 and 4 d electrons per unit cell, it is also predicted that all MPTB phases should have both 1D and 2D metallic bands. These predictions have been confirmed for all MPTB phases with known crystal structures. As a representative example we show in Figure 13.9 the dispersion relations of the t_{2g}-block bands calculated[96] for the W_6O_{22} step-layer of $(PO_2)_4(WO_3)_6(WO_3)_6$.

13.4 Fermi Surfaces of Octahedral Step-Layers as a Function of Electron Filling[100]

As shown in the preceding section, the band electronic structures of various MPTB phases are very similar, and their characteristic features are also exhibited by the ideal W–O layer made up of regular octahedra. The number of electrons, N, filling the

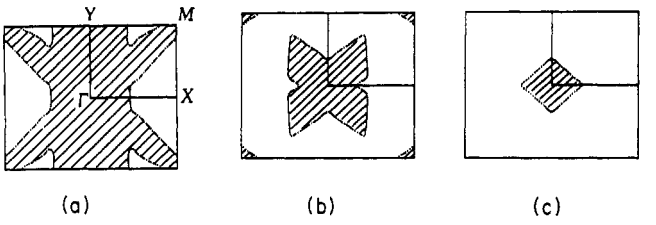

Figure 13.10. Fermi surfaces associated with the partially filled bands of Figure 13.2 for $N = 2$, where the filled regions of wave vectors are shown by shading.

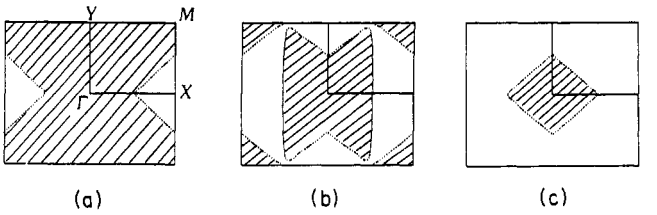

Figure 13.11. Fermi surfaces associated with the partially filled bands of Figure 13.2 for $N = 3$, where the filled regions of wave vectors are shown by shading.

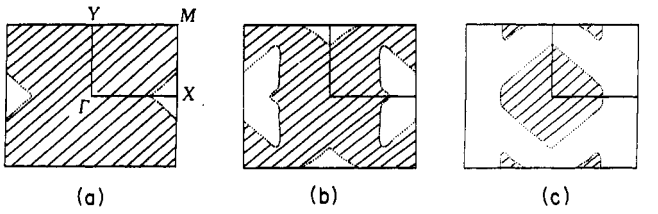

Figure 13.12. Fermi surfaces associated with the partially filled bands of Figure 13.2 for $N = 4$, where the filled regions of wave vectors are shown by shading.

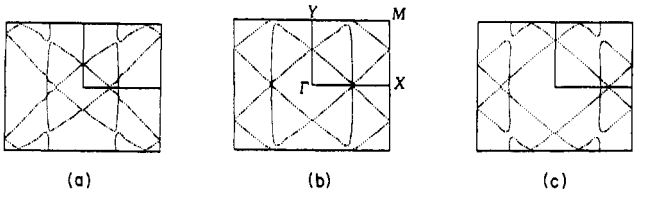

Figure 13.13. Combined Fermi surfaces of Figures 13.10, 13.11, and 13.12 in a, b, and c, respectively.

d-block bands of the step layers of MPTB's $A_x(PO_2)_4(WO_3)_p(WO_3)_q$ is given by $N = 2 + x/2$. Therefore, N is always 2 for all $MPTB_p$'s, but varies from 2 to 4 for $MPTB_h$'s. In this section we examine the Fermi surfaces of the ideal step layer W_4O_{16} for the N values between 2 and 4.

The electron and hole Fermi surfaces of the three partially filled bands calculated for the cases $N = 2$, 3, and 4 are shown in Figures 13.10, 13.11, and 13.12, respectively.[100] We combine the hole and electron Fermi surfaces of Figure 13.10 in Figure 13.13a, those of Figure 13.11 in Figure 13.13b, and those of Figure 13.12 in Figure 13.13c. The combined Fermi surfaces of Figure 13.13a originate from the 1D surface associated with the 1D band a (Figure 13.14a) and the two 2D surfaces associated with the 2D bands e (Figures 13.14b and 13.14c). These features are also present in the combined Fermi surfaces of Figures 13.13b and 13.13c. The Fermi surface of Figure 13.14b consists of rhombuses centered at Γ and M, while that of Figure 13.14c consists of rhombuses centered at X and Y. We now examine why these rhombus-shape Fermi surfaces

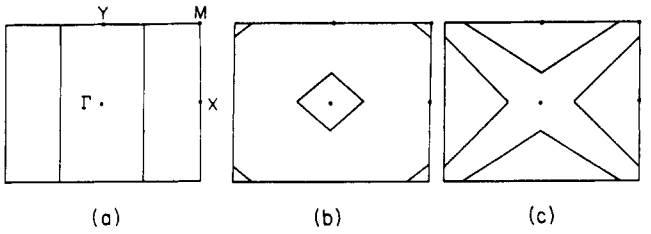

Figure 13.14. 1D and 2D Fermi surfaces leading to the combined Fermi surfaces of Figure 13.13a: (a) 1D Fermi surface, (b) 2D Fermi surfaces centered at Γ and M, and (c) 2D Fermi surfaces centered at X and Y. The rhombus-shape 2D Fermi surfaces centered at X, Y, and M can be readily constructed by repeating the patterns of b and c in an extended zone scheme.

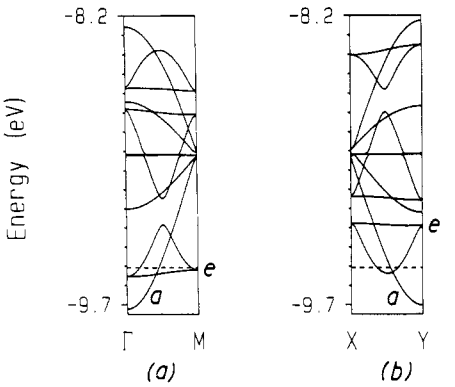

Figure 13.15. Dispersion relations of the t_{2g}-block bands of the ideal W_4O_{16} layer along (a) $\Gamma \rightarrow P \rightarrow M$ and (b) $X \rightarrow P \rightarrow Y$. The dashed line refers to the Fermi level for $N = 2$.

arise from the 2D band e of Figure 13.2. Figures 13.15a and 13.15b show dispersion relations of the t_{2g}-block bands along $\Gamma \rightarrow P \rightarrow M$ and $X \rightarrow P \rightarrow Y$. Here the wave vector P is the crossing point of the $\Gamma \rightarrow M$ and $X \rightarrow Y$ lines in the FBZ, 13.13. Band e consists of two

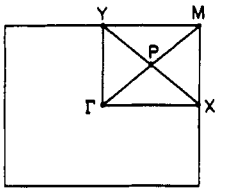

13.13

subbands. Along $\Gamma \rightarrow P \rightarrow M$ (Figure 13.15a), the lower subband is nearly flat but the upper subband is dispersive with a maximum at P. At Γ and M, the two subbands are degenerate. Along $X \rightarrow P \rightarrow Y$ (Figure 13.15b), however, the lower subband is dispersive with a minimum at P but the upper subband is nearly flat. At X and Y, the two subbands are degenerate. The two subbands have a lower energy at Γ and M than at X and Y. Consequently, along $X \rightarrow P \rightarrow M$, the upper subband is cut twice by the Fermi level nearly symmetrically around P, while along $X \rightarrow P \rightarrow Y$ the lower subband is cut twice by the Fermi level nearly symmetrically around P. This topology of the dispersion relations of the two subbands is responsible for the rhombus-shape 2D Fermi surfaces centered at Γ and M in Figure 13.14b and those at X and Y in Figure 13.14c.

We briefly examine why the above is the case on the basis of the orbital nodal properties of band e. The d-block orbitals of the W_4O_{21} unit appropriate for analyzing the behavior of bands e along $\Gamma \rightarrow P \rightarrow M$

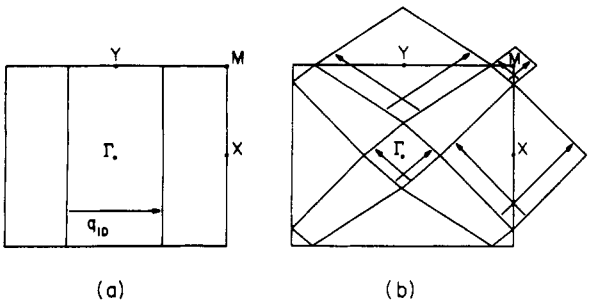

Figure 13.16. CDW nesting vectors associated with the Fermi surfaces of Figure 13.14: (a) q_{1D} and (b) q_Γ, q_M, q_X, and q_Y.

(Figure 13.15a) are shown in 13.14a–c, which have no orbital contribution from the equatorial–bridging oxygen atoms (O_{eq}). Note that the first and third AO's in

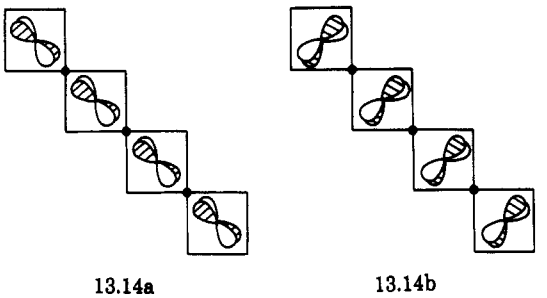

13.14a 13.14b

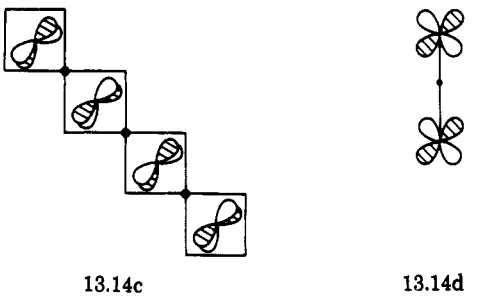

13.14c 13.14d

each of 13.14a–c have the same sign and so do the second and fourth AO's. Between the adjacent steps of the step layer 8.23, the third and fourth positions of one step are linked to the first and second positions of the other step, respectively, via the axial–bridging atoms (O_{ax}). Consequently, as long as the wave vector moves along $\Gamma \rightarrow P \rightarrow M$, every two metal AO's between adjacent steps joined by the O_{ax} atom have the same sign (e.g., as in 13.14d) when the W_4O_{21} unit orbitals 13.14a–c are employed to construct the CO's. Thus, the orbitals of the O_{ax} atoms cannot mix in with the orbitals of the steps so that there is essentially no orbital interaction between the steps. Therefore, only the intrastep interactions can change as the wave vector moves along $\Gamma \rightarrow P \rightarrow M$. The nodal properties of the flat subband of bands e at Γ and M are shown in 13.15 and 13.16, respectively. These orbitals have δ-type interactions

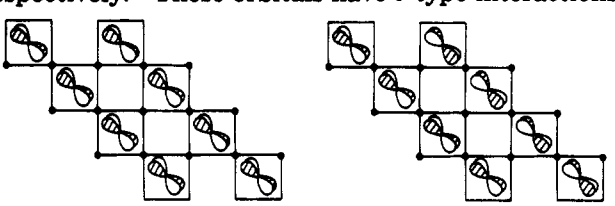

13.15 13.16

between the W_4O_{21} units across the O_{eq} atoms so that the orbitals of the O_{eq} atoms cannot mix with the W_4O_{21}

unit orbitals, thereby leading to the flat subband. The nodal properties of the dispersive subband of bands e at Γ and M are shown in 13.17 and 13.18, respectively.

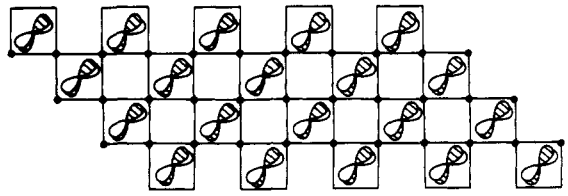

13.17

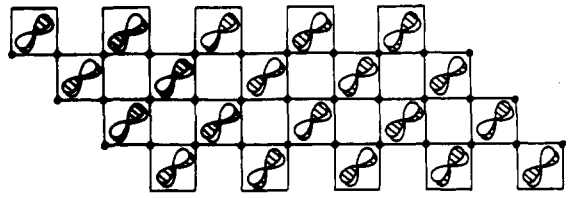

13.18

These orbitals have π-type interactions between the W_4O_{21} units across the O_{eq} atoms. At Γ and M, the p orbitals of the O_{eq} atoms cannot interact with the W_4O_{21} unit orbitals. However, this is not the case as the wave vector departs from Γ or M toward P, and the extent of the O_{eq} atom p orbital mixing with the W_4O_{21} unit orbitals is maximum at P. Thus, the energy of the dispersive subband of band e shows a maximum at P along $\Gamma \rightarrow P \rightarrow M$. In a similar way, one can explain the dispersion relations of bands e along $X \rightarrow P \rightarrow Y$ shown in Figure 13.15b.

The 1D Fermi surface of Figure 13.14a has the nesting vector q_{1D} as shown in Figure 13.16a. The rhombus-shape 2D Fermi surfaces centered at Γ, M, X, and Y in Figures 13.14b and 13.14c have the nesting vectors q_Γ, q_M, q_X, and q_Y, respectively, as shown in Figure 13.16b. If the sides of the rhombuses centered at Γ and M are parallel to the corresponding sides of the rhombuses at X and Y, one obtains a single nesting vector q_{2D} or q'_{2D} (instead of q_Γ, q_M, q_X, and q_Y) shown in Figure 13.17, parts a and b. Inspection of Figure 13.13, parts a, b, and c shows that the rhombuses are nearly parallel only when the N value (i.e., the number of d electrons per unit cell) is close to 4 (i.e., Figure 13.13c). The Mo–O step-layers of the Magnéli phases γ- and γ-Mo_4O_{11} correspond to this electron counting, and their Fermi surfaces (Figure 13.4) are very close to those shown in Figure 13.13c.

Calculations carried out for the various W–O step-layers of the $MPTB_p$ and $MPTB_h$ phases with known crystal structure show that their t_{2g}-block bands are qualitatively very similar to those of the ideal W_4O_{16} layer described in section 13.1.[93,99,100] This leads to Fermi surfaces very similar to those of Figures 13.10–13.12. As an example, the combined Fermi surfaces for the W_6O_{22} slab of $(PO_2)_4(WO_3)_6(WO_3)_6$ are shown in Figure 13.18.[93] The CDW nesting vectors q_i (i = 1D, Γ, M, X, Y) expected from the Fermi surfaces of these W–O step-layers may be expressed as

$$q_i = \alpha \mathbf{a}^* \pm \beta \mathbf{b}^* \qquad (13.2)$$

where the reciprocal vectors $\mathbf{a}^*$ and $\mathbf{b}^*$ correspond to the intrastep and interstep repeat vectors $\mathbf{a}$ and $\mathbf{b}$, respectively (see 8.23b). According to a description based

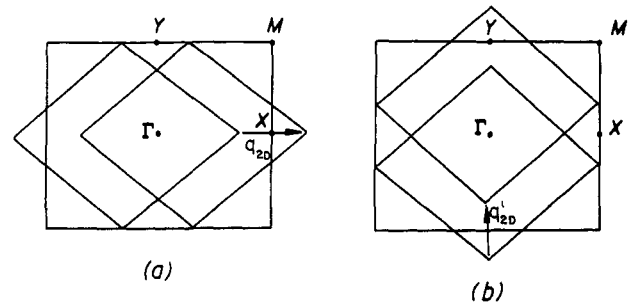

Figure 13.17. Alternative CDW nesting vectors (a) q_{2D} and (b) q'_{2D} constructed on the basis of Figure 13.13c.

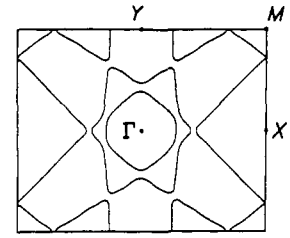

Figure 13.18. Combined Fermi surface for the W_6O_{22} layers of $(PO_2)_4(WO_3)_6(WO_3)_6$.

upon the ideal W–O layers, the α values of q_Γ and q_X (or q_Y and q_M), or the β values of q_Γ and q_Y (or q_X and q_M) add up to 0.5. The Fermi surfaces calculated for the real step-layers of MPTB can be summarized as follows:[100] (a) The "ideal" description of the CDW vectors given by eq 13.2 applies perfectly for the W_6O_{22} and W_7O_{25} layers. In general the W_4O_{16} layers deviate slightly from the ideal description in that α values of q_Γ and q_X (or q_Y and q_M) or the β values of q_Γ and q_Y (or q_X and q_M) do not exactly add up to 0.5. (b) The departure from the ideal description is caused by the distortion of the W–O layer from the ideal structure made up of regular WO_6 octahedra. The extent of distortion in the W–O layers is generally larger for the thin W–O layer (e.g., W_4O_{16} layer) than for the thick W–O layer (e.g., W_6O_{22} or W_7O_{25} layer). (c) The sides of the Fermi surface rhombuses at Γ and M become more parallel to the corresponding sides of the Fermi surface rhombuses at X and Y as the N value becomes close to 4. This is also the case for the W_4O_{16} layers, although their structures are generally more distorted than those of the W_6O_{22} or the W_7O_{25} layers. Therefore, the q_{2D} and q'_{2D} vectors become relevant when $N \simeq 4$. The reason for this can be understood on the basis of the Figure 13.15, which shows that bands e are slightly lower in energy at Γ than at M (i.e., as depicted in 13.19). This leads to a band dispersion with a slightly

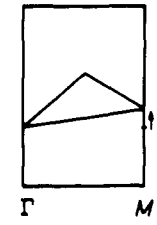

13.19

asymmetric shape. However, the degree of this asymmetry decreases when the Fermi level is raised (i.e., when the band filling increases), which ultimately leads to rhombuses with parallel sides. The reason for the

energy difference of bands e at Γ and M is that the metal orbitals involved in δ-type interactions are in-phase at Γ (13.17) but out-of-phase at M (13.18).

As discussed above, the MPTB phases have well-nested Fermi surfaces with nesting vectors q_{1D}, q_Γ, q_M, q_X, and q_Y. Thus these phases may in principle exhibit different CDW instabilities when their W–O step layers contain less than four d electrons per unit cell (e.g., $2 < N < 3$). When the value of N becomes close to 4, the four vectors q_Γ, q_M, q_X, and q_Y are expected to merge thereby leading to the alternative nesting vectors q_{2D} and q'_{2D}. Energy lowering associated with a CDW formation increases as the area of the nested Fermi surface increases. For the rhombus shape Fermi surfaces centered at Γ, M, X, and Y, the nested area increases with the size of the rhombus. Therefore, for the W–O step layers with N value close to 2, CDW's resulting from q_X and q_Y are more likely to be observable than are those from q_Γ and q_M. To confirm the CDW nesting vectors predicted on the basis of these calculations, diffuse X-ray scattering and/or neutron diffraction measurements would be necessary. Our analysis of the W–O layer band orbitals shows that their partially filled bands are represented by the orbitals of all the WO_6 octahedra including those of the W–O layer surfaces. This situation differs considerably from that found for many Mo–O layers, in which the MoO_6 octahedra of the Mo–O layer surfaces have practically no orbital contribution to their partially filled bands. Therefore, the CDW formation in the W–O layers of the $MPTB_h$, $A_x(PO_2)_4(WO_3)_p(WO_3)_q$, can be prevented by the random potentials that cation disorder in the hexagonal channels may create, because the alkali cations are close to the WO_6 octahedra of the W–O layer surfaces.[99] In observing CDW phenomena of the MPTB phases, therefore, it would be more fruitful to investigate the $MPTB_p$ phases $(PO_2)_4(WO_3)_p(WO_3)_q$ rather than the $MPTB_h$ phases $A_x(PO_2)_4(WO_3)_p(WO_3)_q$. The MPTB phases should exhibit rich CDW phenomena and therefore would be very exciting materials to study. For further discussions of the Fermi surface nesting, see section 15.

14. Purple Bronzes

The potassium purple bronze $K_{0.9}Mo_6O_{17}$ has separated metal–oxygen layers of composition Mo_6O_{17}, which are made up of both MoO_6 octahedra and MoO_4 tetrahedra (Figure 8.1).[35] The sodium purple bronze $Na_{0.9}Mo_6O_{17}$[101] and the thallium purple bronze $TlMo_6O_{17}$[102] are similar in structure to the potassium purple bronze. As discussed earlier, the lithium purple bronze differs from the other purple bronzes in that it has no separated metal–oxygen layers.[34] It was recently shown that the real composition of the sodium and potassium purple bronzes is not $A_{0.9}Mo_6O_{17}$, as initially proposed, but AMo_6O_{17} (A = K, Na)[103] so that hereafter we will refer to the 2D purple bronzes as AMo_6O_{17} (A = K, Na, Tl).

The potassium purple bronze is a 2D metal above 120 K at which temperature it undergoes a CDW phase transition.[104-105] In contrast to the case of the blue bronze, however, the potassium purple bronze remains 2D metallic after the CDW phase transition.[104] Diffuse X-ray scattering and electron diffraction studies show the occurrence of superlattice spots at $a^*/2$, $b^*/2$, and $(a^* - b^*)/2$ below 120 K.[105b] According to the thermoelectric power measurements, the major carriers for electrical transport are electrons and holes above and below 120 K, respectively, and the CDW removes about 50% of the carrier concentration.[104a] Hall effect measurements show that both electrons and holes are present below 120 K. According to these observations, several partially filled d-block bands are present in KMo_6O_{17}. In electrical, CDW, and other physical properties, $NaMo_6O_{17}$[106] and $TlMo_6O_{17}$[105] are similar to KMo_6O_{17}.

14.1 Crystal and Electronic Structures of AMo_6O_{17} Purple Bronzes

The crystal structure of KMo_6O_{17} contains hexagonal Mo_6O_{17} layers perpendicular to the c direction (Figure 8.1).[35] A convenient way to describe this Mo_6O_{17} layers is in terms of the building unit Mo_4O_{21} (14.1), which is constructed from four MoO_6 octahedra by sharing the axial oxygen atoms. Shown in 14.2 is a schematic

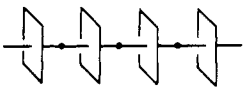

14.1

representation of the Mo_4O_{15} hexagonal layer (i.e., the Mo_6O_{17} layer without MoO_4 tetrahedra. See also 8.26) constructed from the Mo_4O_{21} cluster. Though not

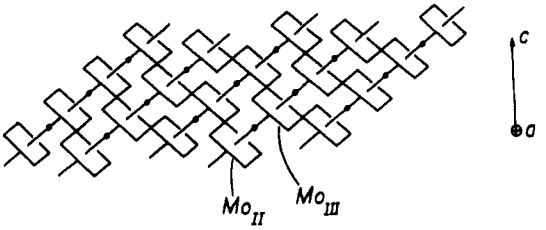

14.2

shown explicitly, every MoO_6 octahedron of 14.2 forms a zigzag chain Mo_2O_{10}, 14.3, along the crystallographic a direction (i.e., the direction perpendicular to the plane of the paper.). Consequently, along the crystallo-

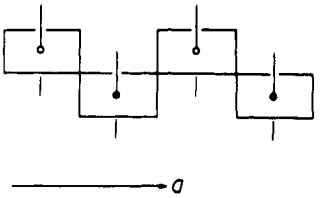

14.3

graphic a direction, every adjacent pair of Mo_4O_{21} clusters share the equatorial oxygens of three octahedra. This is also true along the crystallographic b direction ($a = b$, $\gamma = 120°$). When the Mo_4O_{15} layer 14.2, is viewed along the c axis (i.e., perpendicular to the layer shown in Figure 8.1), every three nearest neighbor MoO_6 octahedra of its outer octahedral sublayers from a triangle of oxygen atoms that can be used as a face of an MoO_4 tetrahedron. When all these triangles are capped by MoO groups to form MoO_4 tetrahedra, the Mo_6O_{17} layer of 2D purple bronzes is generated. It is between these Mo_6O_{17} layers that the K^+ cations reside. Thus there exist three different types of Mo atoms in K Mo_6O_{17}: The Mo atoms of the MoO_4 tetrahedra (Mo^I), those of the MoO_6 octahedra in the outer two sublayers

of the Mo_4O_{15} layers (Mo^{II} in 14.2), and those of the MoO_6 octahedra in the inner two sublayers of the Mo_4O_{15} layer (Mo^{III} in 14.2). According to a Zachariasen-type analysis of the metal–oxygen bond lengths in KMo_6O_{17} in which the oxidation state of Mo^{I} is adjusted to be +6, the oxidation state of Mo^{II} and Mo^{III} are calculated to be +5.8 and +5.1, respectively.[35] In other words, the d electrons of KMo_6O_{17} reside primarily in the MoO_6 octahedra in Mo^{III}. Therefore, the inner two sublayers of the Mo_4O_{15} layer are expected to play an important role in determining the electronic structure of the Mo_6O_{17} layer and hence that of KMo_6O_{17}.

The inner two sublayers of 14.2 are schematically shown in 14.4, which has the composition Mo_2O_9. This

14.4

layer may be considered to originate from the building unit Mo_2O_{11}, 14.5a. An alternative view of 14.5a is shown in 14.5b. A projection view of 14.5b along the direction perpendicular to a triangular face of the MoO_6 octahedra is given by 14.5c. With this representation

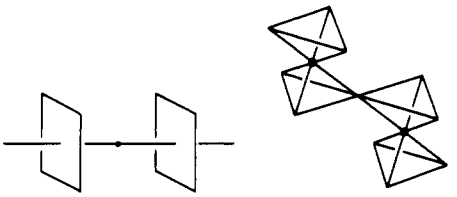

14.5a 14.5b

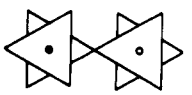

14.5c

of the Mo_2O_{11} unit, a projection view of the hexagonal Mo_2O_9 layer 14.4 along the c axis is given by 14.6. For

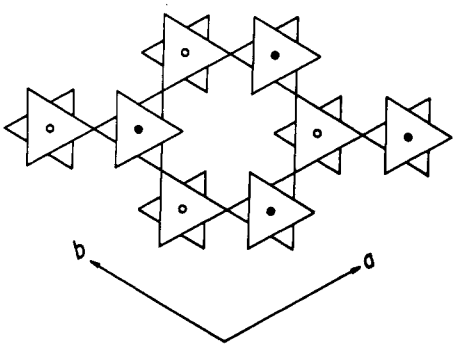

14.6

the discussion of its electronic structure, it is very important to recognize that the Mo_2O_9 layer 14.6 is constructed from the Mo_2O_{10} chains 14.3 upon sharing the axial oxygen atoms as illustrated in 14.7. Due to symmetry, there are three different ways of making Mo_2O_{10} chains in 14.6: The Mo_2O_{10} chains are aligned along the a-, b-, and $(a + b)$-axis directions in 14.7a, 14.7b, and 14.7c, respectively. This structural aspect of the Mo_2O_9 layer is crucial in understanding the low temperature CDW anomaly, as will be shown in section 15.1.

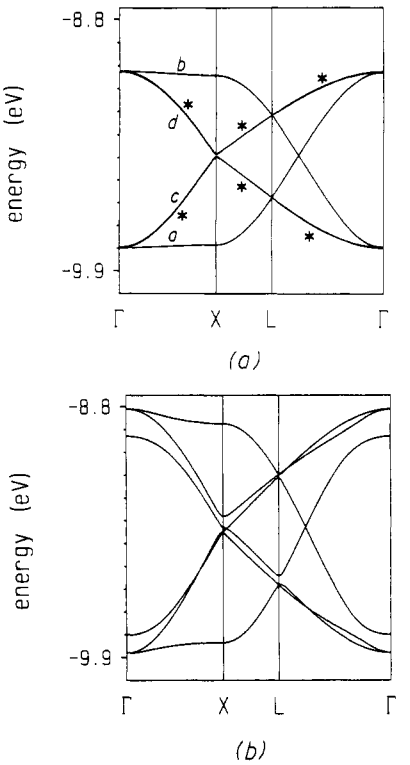

Figure 14.1. t_{2g}-block band structure of the (a) ideal and (b) real Mo_2O_9 hexagonal layer. Γ, X, and L refer to the wave vectors (0, 0), ($a^*/2$, 0), and ($a^*/3$, $b^*/3$), respectively.

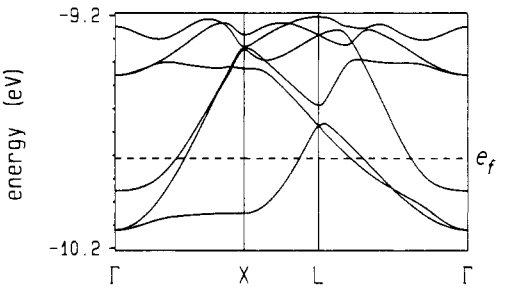

Figure 14.2. Bottom portion of the d-block band structure of the real Mo_6O_{17} layer in KMo_6O_{17}. The dashed line refers to the Fermi level.

For a 2D hexagonal lattice (i.e., $a = b$, $\gamma = 120°$) such as the Mo_2O_9 layer 14.6 or the Mo_6O_{17} layer, the FBZ of its reciprocal lattice is a regular hexagon centered at the origin Γ, as shown in 4.25. We now examine the d-block bands of the ideal and real structures of the Mo_2O_9 layer as well as that of the real Mo_6O_{17} layer.[107] In our discussion, an ideal layer refers to one in which the MoO_6 octahedra are regular in shape, while a real layer refers to one in which the MoO_6 octahedra (and MoO_4 tetrahedra) have the shapes as found in KMo_6O_{17}. Figure 14.1a show the t_{2g}-block bands calculated[107] for the ideal Mo_2O_9 layer 14.6, where the two bands marked with asterisks are each doubly degenerate. As expected from the presence of two metal atoms in the unit cell, there are six t_{2g}-block bands. The t_{2g}-block bands of the real Mo_2O_9 layer are shown in Figure 14.1b.[107] They are very close to those of the ideal Mo_2O_9 layer. The MoO_6 octahedra of the real Mo_2O_9 layer are slightly distorted from a regular octahedron, so the degeneracy in the t_{2g}-block bands of the ideal layer is somewhat lifted by the structural change in the real layer. Shown in Figure 14.2 is the bottom portion of the d-block bands calcu-

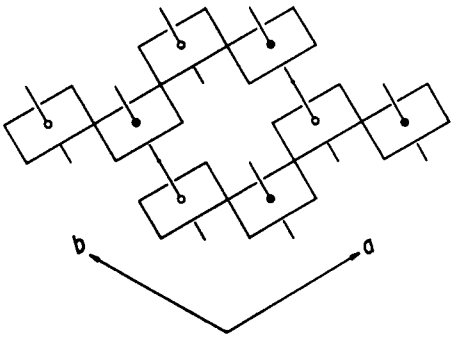

14.7a

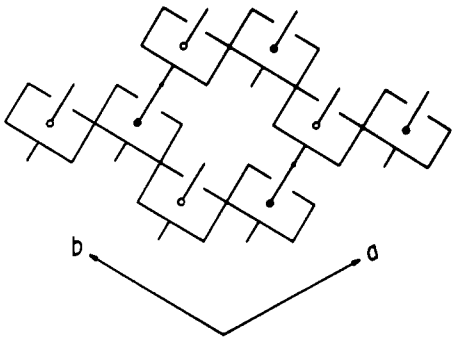

14.7b

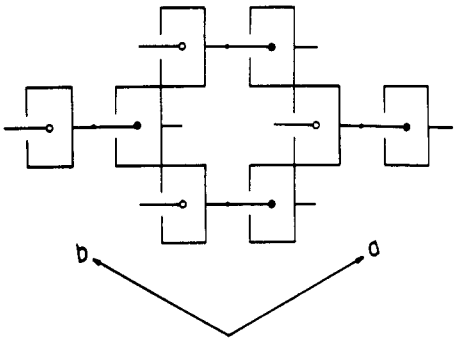

14.7c

lated[107] for the real Mo_6O_{17} layer. The bottom three d-block bands are essentially identical with those of the real Mo_2O_9 layer. The bottom three d-block bands of the Mo_6O_{17} layer have the d-orbital character of primarily Mo^{III} atoms. The d-block bands of primarily Mo^{I} and Mo^{II} character all lie above these three bottom d-block bands. With three electrons per KMo_6O_{17} (i.e., $K^+Mo_6O_{17}^-$) to fill the d-block bands of Figure 14.2, only the bottom three bands are partially filled. The Fermi surfaces calculated for the three partially filled bands of the Mo_6O_{17} layer are shown in Figure 14.3, where the shaded and unshaded regions refer to the occupied and unoccupied regions, respectively. As shown in Figure 14.3, parts a and c, the first and the third d-block bands (from the bottom) of the Mo_6O_{17} layer give hole pockets around L and an electron pocket around Γ, respectively. All three Fermi surfaces are closed, so that the potassium purple bronze is a 2D metal. How these Fermi surfaces are related to the CDW instability in 2D purple bronzes is discussed in section 15.1.

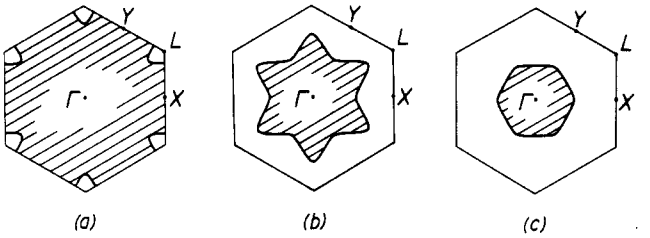

Figure 14.3. Fermi surfaces for the (a) first, (b) second, and (c) third d-block bands of the Mo_6O_{17} layer in KMo_6O_{17}.

14.2 t_{2g}-Block Bands of Hexagonal Mo_2O_9 Layers[107]

As discussed in Section 4.3, the point $M = (a^*/2, b^*/2)$ associated with an hexagonal lattice (see 4.25) is equivalent to $M' = (-a^*/2, b^*/2)$, since M' differs from M by an integral multiple of the reciprocal vector, i.e., $M' = M - (a^*, 0)$. By symmetry, M' is equivalent to X, so that the $L \rightarrow X$ line of the FBZ is equivalent to the $L \rightarrow M$ line. Thus, in our discussion, the $\Gamma \rightarrow L \rightarrow X$ line can be replaced by the $\Gamma \rightarrow M$ line. Then, essential features of the d-block bands of the ideal Mo_2O_9 layer in Figure 14.1a can be summarized as follows: (a) The nondegenerate bands a and b are flat along $\Gamma \rightarrow X$ but strongly dispersive along $\Gamma \rightarrow M$. In addition, the two bands cross each other along $\Gamma \rightarrow M$. (b) The doubly degenerate bands c and d are both equally dispersive along $\Gamma \rightarrow X$ and along $\Gamma \rightarrow M$, the extent of the dispersion being half that of the bands a and b along $\Gamma \rightarrow M$. In the following we examine these trends in terms of orbital interaction analysis.

On going from Γ to X, the phases between nearest neighbor unit cell orbitals remain in phase in one direction but change from in-phase to out-of-phase in the other direction. To simplify our representation of band orbitals, the building unit Mo_2O_{11}, of the Mo_2O_{10} chain may be represented as in 14.8. The two orbitals of this

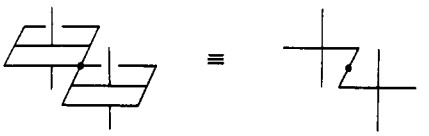

14.8

building unit that lead to bands a and b of the Mo_2O_9 layer are shown in 14.9. On the basis of the layer

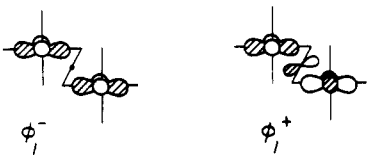

14.9

representation 14.7b, bands a and b at $\Gamma = (0, 0)$ are given by the orbitals 14.10a and 14.10b, respectively. The bands a and b at X are given by the orbitals 14.11a and 14.11b, respectively. Note that 14.10a and 14.11a are derived from the unit cell orbitals ϕ_1^- of 14.9, while 14.10b and 14.11b are derived from the unit cell orbitals ϕ_1^+ of 14.9. As summarized in Table 14.1, the oxygen

TABLE 14.1. Antibonding Contributions of the Oxygen p Orbitals of the Mo–O–Mo Bridges in the t_{2g}-Block Band Orbitals of the Mo_2O_9 Layer[a]

band orbital	wave vector	unit cell orbital	intrachain: within a unit cell	intrachain: between nearest neighbor unit cells	inter-chain
14.10a	Γ	ϕ_1^-	(N)	(N)	(N)
14.10b	Γ	ϕ_1^+	(Y)	(Y)	(N)
14.11a	*X*	ϕ_1^-	(N)	(N)	(N)
14.11b	*X*	ϕ_1^+	(Y)	(Y)	(N)
14.13a	Γ	ϕ_2^+	(N)	(N)	(N)
14.13b	Γ	ϕ_2^-	(Y)	(Y)	(N)
14.14a	*M*	ϕ_2^+	(Y)	(Y)	(N)
14.14b	*M*	ϕ_2^-	(N)	(N)	(N)
14.17a	Γ	ϕ_3^-	(N)	(N)	(N)
14.17b	Γ	ϕ_3^+	(y)	(y)	(Y)
14.18a	*X*	ϕ_3^-	(N)	(N)	(Y)
14.18b	*X*	ϕ_3^+	(y)	(y)	(N)

[a] The presence of the antibonding contribution is indicated by the symbol (Y) or (y), and the absence of it by the symbol (N). The symbols (Y) and (y) refer to the stronger and the weaker antibonding contributions discussed in section 2.4.1.

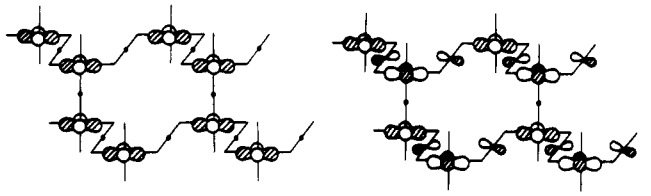

14.10a 14.10b

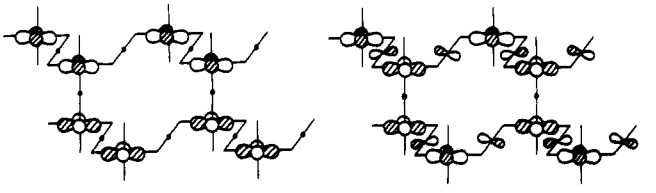

14.11a 14.11b

orbitals of the interchain Mo–O–Mo bridges do not contribute to 14.10 and 14.11. Those of the intrachain Mo–O–Mo bridges do not contribute to 14.10a and 14.11a, but they do to 14.10b and 14.11b. Thus energies of 14.10b and 14.11b are raised with respect to those of 14.10a and 14.11a. Since the chain orbitals do not overlap significantly across the interchain Mo–O–Mo bridges, 14.10a and 14.11a are nearly the same in energy, and so are 14.10b and 14.11b. On going from Γ to *M*, the phases between nearest neighbor unit cell orbitals change from in-phase to out-of-phase in both *a*- and *b*-axis directions. The Mo_2O_9 layer 14.7c has the unit cell orbitals ϕ_2^+ and ϕ_2^- shown in 14.12. The CO's

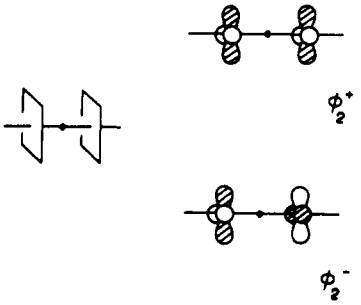

14.12

resulting from ϕ_2^+ and ϕ_2^- at Γ are given by 14.13a and 14.13b, respectively, and those at *M* by 14.14a and 14.14b, respectively. As can be seen from the p-orbital

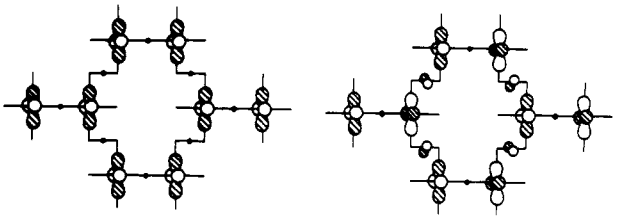

14.13a 14.13b

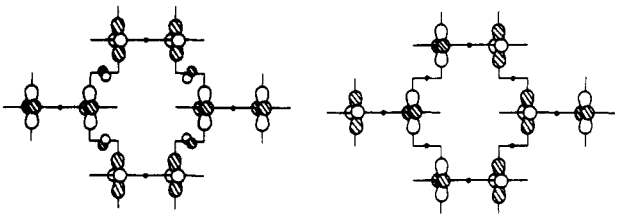

14.14a 14.14b

contributions of the bridging oxygens summarized in Table 14.1, 14.13a is lower in energy than 14.13b, but 14.14a is higher in energy than 14.14b. With respect to the 2-fold rotation around the (*a* + *b*)-axis of 14.7c, 14.13a and 14.14a are symmetric, while 14.13b and 14.14b are antisymmetric. Therefore, on going from Γ to *M*, 14.13a and 14.13b are correlated to 14.14a and 14.14b, respectively, and thus the two correlation curves (i.e., bands a and b) cross each other. This explains why bands a and b are highly dispersive along Γ → *M*. Given the translational symmetry of the Mo_2O_9 layer, 14.13a and 14.13b are identical with 14.10a and 14.10b, respectively, while 14.14a and 14.14b are identical with 14.11b and 14.11a, respectively. The latter observation is particularly interesting in that the CO's at *X* derived from the layer representation 14.7b are identical with those at *M* derived from the layer representation 14.7c. From the viewpoint of CO's, this is why the *X* and *M* points are equivalent for a hexagonal lattice.

On the basis of the Mo_2O_9 layer 14.7b, we now examine the degenerate bands c and d along Γ → *X*, which are derived from the unit cell orbitals ϕ_3^+ and ϕ_3^- in 14.15 and ϕ_4^+ and ϕ_4^- in 14.16. Since the set of ϕ_4^+

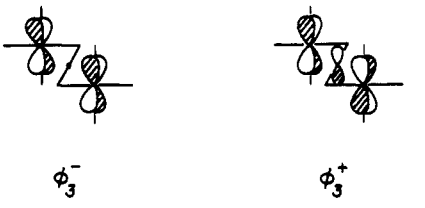

14.15

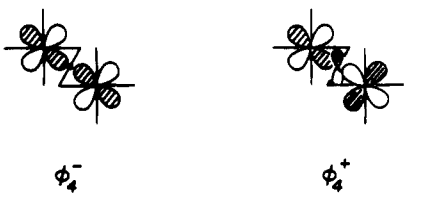

14.16

and ϕ_4^- leads to the same results as does that of ϕ_3^+ and ϕ_3^-, it is sufficient to consider only the CO's arising from

the latter. Bands c and d at Γ are represented by 14.17a and 14.17b, respectively, and those at X by 14.18a and 14.18b, respectively. The contributions of the oxygen

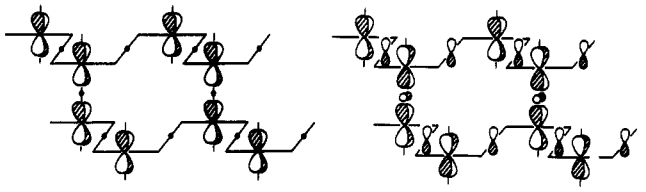

14.17a 14.17b

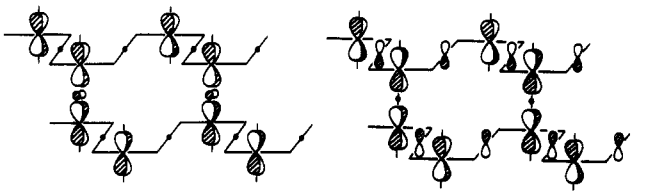

14.18a 14.18b

p orbitals of the Mo–O–Mo bridges in those CO's are summarized in Table 14.1. As discussed already (see 2.43 and 2.44), there are two different types of metal–ligand π overlap denoted by (Y) and (y) in Table 14.1. 14.17a has no oxygen p-orbital contribution from the Mo–O–Mo bridges and thus has the same energy as 14.10a. 14.17b has oxygen p-orbital contribution from all the intra- and interchain Mo–O–Mo bridges, unlike 14.10b, which has oxygen p-orbital contribution only from the intrachain Mo–O–Mo bridges. Nevertheless, 14.17b is degenerate with 14.10b since the sum of two (y) antibonding p-orbital contributions per unit cell is equivalent to one strong antibonding p-orbital contribution per unit cell. 14.18a has one (Y) antibonding p-orbital contribution per unit cell, while 14.18b has two (y) antibonding p-orbital contributions per unit cell. Consequently, 14.18a and 14.18b are nearly degenerate, and their energies lie at the midpoint between 14.17a and 14.17b. This explains why bands c and d are dispersive along $\Gamma \rightarrow X$ and why their dispersion is half as strong as that of bands a and b along $\Gamma \rightarrow M$. In a similar way, the Mo_2O_9 layer 14.7c can also be employed to show that bands c and d are equally dispersive along $\Gamma \rightarrow M$, and their dispersion is half as strong as that of bands a and b along $\Gamma \rightarrow M$.

15. Hidden Fermi Surface Nesting

In the previous sections, we have seen the importance of Fermi surface nesting in explaining the electronic instabilities of low dimensional metallic compounds. For 1D metallic systems (e.g., $Li_{0.9}Mo_6O_{17}$ and $K_{0.33}MoO_3$), it is straightforward to recognize the nesting vectors of their Fermi surfaces. In section 13, we have encountered somewhat complicated examples: The Magnéli phases Mo_4O_{11} and the MPTB's possess several partially filled bands and therefore several Fermi surfaces. When those surfaces are analyzed individually, detection of Fermi surface nesting is not immediately obvious. However, when they are combined together, it is possible to redraw them into nested 1D and 2D Fermi surfaces, which are intended but hidden because of weak band hybridization (i.e., noncrossing of band dispersion surfaces). Such hidden, nested Fermi surfaces lead to CDW's which destroy the nested portions of the combined Fermi surfaces. They may even give rise to a metal–insulator transition if the energy required for decoupling the weak band hybridization is smaller than the energy gain from a metal–insulator transition associated with the nesting of the hidden Fermi surfaces. In the following, we discuss this concept of hidden Fermi surface nesting in some detail.

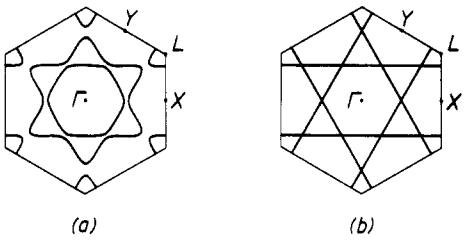

Figure 15.1. (a) Combined Fermi surfaces of potassium purple bronze KMo_6O_{17} and (b) hidden 1D Fermi surfaces associated with KMo_6O_{17}.

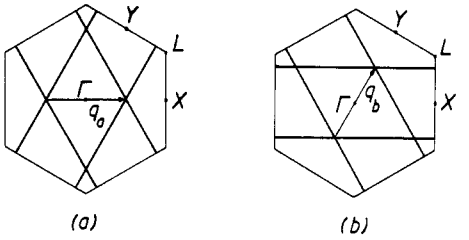

Figure 15.2. Nesting vectors common to two sets of the hidden 1D Fermi surfaces. The nesting vectors in a and b are parallel to the a^* and b^* directions, respectively.

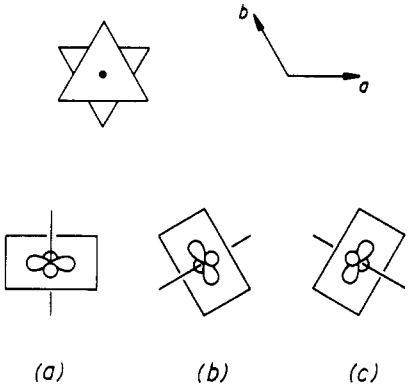

Figure 15.3. Perspective views of the three t_{2g} orbitals of an MoO_6 octahedron in the Mo_2O_9 layer 14.6. The d orbital containing planes are aligned along the a, b, and $(a + b)$ directions of the Mo_2O_9 layer in a, b, and c, respectively.

15.1 Hidden Nesting in KMo_6O_{17}[108]

The CDW instability of the purple bronze KMo_6O_{17} (section 14) may now be examined from the viewpoint of hidden nesting. The three Fermi surfaces of this phase (Figure 14.3) are combined into one in Figure 15.1a. A shown in Figure 15.1b, this combined Fermi surface may be decomposed into three sets of parallel lines (i.e., three sets of ideal 1D Fermi surfaces), if the weak noncrossing effects at the intended crossing points are neglected. Given such ideal 1D surfaces, one needs to find what nesting vectors are likely to be observed because, as discussed in section 5.2 (see 5.7), an ideal 1D Fermi surface possesses an infinite number of nesting vectors. The extent of electronic instability is enhanced with increasing the area of nested Fermi surface, so that nesting vectors appropriate for KMo_6O_{17} are the ones that simultaneously nest more than one

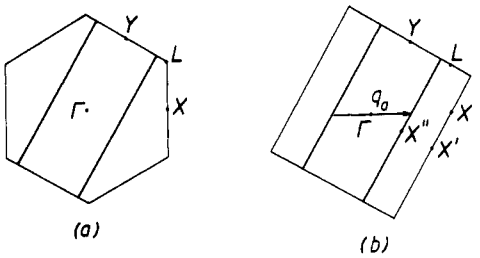

Figure 15.4. Representation of one hidden 1D Fermi surface of KMo_6O_{17} in (a) the FBZ and (b) the rectangular zone. The latter has the same area as the FBZ.

set of the 1D Fermi surfaces. Two examples of such nesting vectors are illustrated in Figure 15.2. The vectors q_a and q_b (in Figure 15.2, parts a and b, respectively) each nest two sets of the 1D Fermi surfaces, and they are parallel to the a^* and b^* directions, respectively. The magnitudes of these hidden nesting vectors are examined in the following.

As shown in 14.7, the d-electron-containing layer of KMo_6O_{17} (i.e., the Mo_2O_9 layer 14.6) can be decomposed into three sets of the zigzag Mo_2O_{10} chains (14.3) running along the a, b, and $(a + b)$ directions. The bottom three d-block bands of the Mo_2O_9 layer are derived from the t_{2g} orbitals of the MoO_6 octahedra. These three t_{2g} orbitals each make π-type interactions along the intrachain directions but δ-type interactions along the interchain directions. (For example, see 14.13 and 14.14.) Consequently, the band associated with each of the t_{2g} orbitals is dispersive along the associated intrachain direction but dispersionless along the associated interchain direction. As shown in Figure 15.3, each t_{2g} orbital of an MoO_6 octahedron is a δ orbital along the chosen axial Mo–O bond direction. Due to the orthogonality of the t_{2g} orbitals, the three chain bands resulting from the t_{2g} orbitals are practically independent of one another, to a first approximation. Thus, for qualitative purposes, the bottom three d-block bands of KMo_6O_{17} can be approximated by the three independent 1D bands resulting from the t_{2g} orbitals.

In a 2D representation, the Fermi surface of an ideal 1D metal is given by two parallel lines perpendicular to the chain direction (section 5). This is also the case for the ideal 1D Fermi surfaces of Figure 15.1b. For example, Figure 15.4a shows one set of the ideal 1D surface, which can be redrawn in a rectangular zone (Figure 15.4b) with the area identical with that of the FBZ. In Figure 15.4b, $\Gamma \rightarrow X'$ is perpendicular to $\Gamma \rightarrow Y$ and is therefore parallel to the a direction. Namely, the Fermi surface of Figure 15.4b is perpendicular to the a direction and therefore refers to the ideal 1D band associated with the Mo_2O_{10} chains running along the a direction (14.7a). In Figure 15.4b, the length of $\Gamma \rightarrow X'$ is $\sqrt{3}a^*/4$. In a similar manner, the remaining two of the ideal 1D Fermi surfaces are related to the Mo_2O_{10} chains running along the b and $(a + b)$ directions. KMo_6O_{17} has three electrons to fill its d-block bands, so that each of the three ideal 1D chain bands becomes half filled. Therefore, in Figure 15.4b, the length of $\Gamma \rightarrow X''$ becomes half that of $\Gamma \rightarrow X'$, and the nesting vector q_a is equal to $\Gamma \rightarrow X$. As a result, the nesting vector q_a is given by $a^*/2$. Likewise, the nesting vector q_b (Figure 15.2b) becomes $b^*/2$. This explains the superlattice spots at $a^*/2$, $b^*/2$, and $(a^* - b^*)/2$ observed for KMo_6O_{17} below 120 K.[105b] We note that KMo_6O_{17} remains metallic below 120 K,[104] which implies that the Fermi surface is not removed completely below 120 K. This is understandable because the nesting of the real Fermi surface is not complete due to the band hybridization.

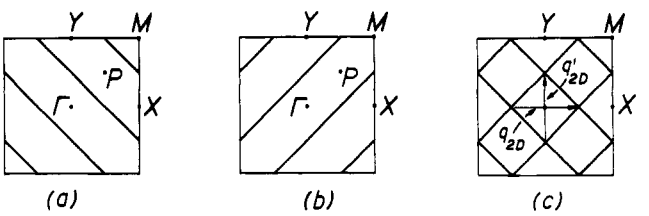

Figure 15.5. Construction of the rhombus-like 2D Fermi surfaces of the Magnéli phases Mo_4O_{11} and the MPTB phases with N = 4: (a) the 1D Fermi surface associated with the upper subband of band e (Figure 13.15a) and (b) that associated with the lower subband of band e (Figure 13.15b). The two 1D Fermi surfaces of a and b are combined into one in c.

15.2 Hidden Nesting in the Magnéli and the MPTB Phases

As discussed in section 13, the combined Fermi surfaces of the Magnéli and the MPTB phases are decomposed into nested 1D and 2D Fermi surfaces. Thus, the nesting vectors of those 1D and 2D Fermi surfaces are hidden nesting vectors. The 1D surface results from the δ band, and the 2D surfaces from the π bands (section 13.1). The 2D surfaces are described in terms of rhombuses centered at Γ, X, M, and Y (Figure 13.16b). We now show that, to a first approximation, these 2D Fermi surfaces can be further decomposed into two sets of hidden 1D surfaces.

As already discussed, those rhombus-like 2D Fermi surfaces originate from the fact that, along $\Gamma \rightarrow P \rightarrow M$, the upper subband of band e in Figure 13.15a has a maximum at P, so it is cut twice by the Fermi level. Thus, to a first approximation, this bands leads to the ideal 1D Fermi surface shown in Figure 15.5a, which consists of four parallel lines (perpendicular to $\Gamma \rightarrow P \rightarrow M$) within the FBZ. (In 5.1a the band dispersion along $\Gamma \rightarrow X$ is cut once by the Fermi level, so the resulting Fermi surface 5.3a consists of two parallel lines within the FBZ.) Likewise, along $X \rightarrow P \rightarrow Y$ (13.13), the lower subband of band e in Figure 13.5b is cut twice by the Fermi level and leads to the ideal 1D Fermi surface shown in Figure 15.5b. When the two sets of these ideal 1D surfaces are combined together, as shown in Figure 15.5c, one obtains rhombus-like 2D Fermi surfaces centered at Γ, X, Y, and M. To a first approximation, the rhombus-like 2D surfaces of the Magnéli and the MPTB phases discussed in section 13.4 originate essentially from two sets of such ideal 1D Fermi surfaces.

As discussed above, the upper and lower subbands of band e have 1D character along the $(a + b)$ and $(-a + b)$ directions, respectively. In order to understand this observation, it is necessary to redraw the MO_6 octahedra of the step-layer 8.23b such that two "basal" oxygen atoms of every MO_6 octahedron in the old representation are made "axial" in a new representation of MO_6. There are two sets of "basal" oxygen atoms to choose: One set contains two "basal" oxygen atoms trans to each other along the $(a + b)$ direction, and the other contains those along the $(-a + b)$ direction. According to these two new representations, the step-layer

8.23 is constructed from new octahedral chains (i.e., those formed upon sharing the new "basal" oxygen atoms of MO_6 octahedra) running along the $(a + b)$ or the $(-a + b)$ directions by sharing their "axial" oxygen atoms. These "new" octahedral chains differ in shape from the "old" step chains running along the a direction. The t_{2g} orbitals appropriate for band e at Γ are given by 13.15 and 13.17, where the d-orbital planes are aligned along the $(-a + b)$ and the $(a + b)$ directions, respectively. Thus the two t_{2g} orbitals each make π-type interactions along the new chain direction (i.e., the $(a + b)$ or the $(-a + b)$ direction) but δ-type interactions along the interchain direction. This accounts for the 1D nature of the two subbands of band e in Figure 13.15. The situation is very similar to that of purple bronze AMo_6O_{17} (A = Na, K) except that the step-layer 8.23 consists of two different types of 1D chains because of its lower symmetry. It should be noted that our analysis discussed above applies to any step-layer built on the basis of the (13)-condensation of step-chains, regardless of the width of the step-chain.

In Figure 15.5c, the two sets of 1D Fermi surfaces are nested by a common vector (q_{2D} or q'_{2D}). This situation is analogous to that found for KMo_6O_{17} in the previous section (see Figure 15.2). The CDW vector q_{2D} of Figure 15.5c corresponds to the observed CDW vector q_c of the Magnéli phases Mo_4O_{11} (Figure 13.5b) and also to the CDW vector q_{2D} of the MPTB phase with $N = 4$, where N is the number of electrons per unit cell of one W–O step-layer (see Figure 13.17a). In terms of the nested Fermi surface areas, the CDW's with vectors q_{2D} and q'_{2D} are equally probable. However, only the CDW with q_{2D} is observed. This implies that the CDW with q_{2D} induces less strain than does that with the q'_{2D}. This is due probably to the fact that the vector q_{2D} is parallel, but the vector q'_{2D} is perpendicular, to the step-chain direction. As discussed in section 13.4, the "2D" Fermi surface nesting of the MPTB phases is better described in terms of the vectors q_i ($i = \Gamma, X, Y, M$) associated with the rhombus-like Fermi surfaces (e.g., see Figure 13.16b), as N becomes smaller than 4. Nevertheless, the occurrence of the rhombus-like Fermi surfaces can be viewed in terms of two sets of "warped" 1D Fermi surfaces. If this Fermi surface warping is weak, it may be possible to observe a CDW vector q_{2D} instead of q_i ($i = \Gamma, X, Y, M$) even when $N < 4$.

The purple bronze KMo_6O_{17}, the Magnéli phase Mo_4O_{11} and the MPTB's possess 2D Fermi surfaces, and thus they are all 2D metals. However, these systems exhibit CDW phenomena typically observed for 1D metallic compounds because their 2D Fermi surfaces have hidden 1D nesting vectors. Therefore, when a 2D metallic system exhibits a CDW phenomenon, it would be interesting to examine whether or not such an electronic instability originates from hidden 1D Fermi surface nesting. From this viewpoint, it would be worthwhile to reexamine the electronic structures of layered transition-metal dichalcogenides.

16. Electronic Structures of Other Seemingly Complex Systems

A common feature of the compounds examined so far is a very low d-electron count, so that only the lowest lying portion of their t_{2g}-block energy bands are filled. If some of the octahedra are distorted such that certain M–O bond lengths become short, some or all t_{2g} orbitals of these octahedra are raised in energy and do not contribute significantly to the lowest lying t_{2g}-block bands. Thus, a detailed analysis of crystal structures is important in providing a qualitative understanding of the electronic structure of these materials. In particular, it can be very useful in the case of complex materials where only a certain part of the structure is responsible for their transport properties. As shown earlier, this approach is more powerful than the traditional bond valence sum analysis because the directionality of the low-lying orbitals is explicitly taken into account. In the present section, we consider the crystal and electronic structures of $Na_{0.25}TiO_2$[109a] and $Li_{0.33}MoO_3$,[37] two materials which have a seemingly complex 3D lattice but which are nevertheless pseudo-1D in physical properties.

16.1 $Na_{0.25}TiO_2$

The sodium titanium bronze $Na_{0.25}TiO_2$ undergoes a metal–insulator transition at 630 K.[109] Below 430 K, $Na_{0.25}TiO_2$ shows incommensurate superlattice spots centered at $(a^*, q_b^*, 0)$, suggesting that the transition is of a Peierls type.[109,110] The q_b^* is found to increase gradually from $0.230b^*$ at 430 K to $0.245b^*$ at room temperature. Such a temperature dependence of q_b^* is reminiscent of that in blue bronze (section 10). $Na_{0.25}TiO_2$ has a 3D lattice of TiO_6 octahedra.[109a] Since Peierls-type transitions are usually associated with low-dimensional systems, a particular distortion of some TiO_6 octahedra must exist to render a low-dimensional character to the 3D Ti–O lattice. Thus, it is important to understand how the electronic structure of $Na_{0.25}TiO_2$ is related to its crystal structure.

The essential building blocks of the 3D Ti–O lattice in $Na_{0.25}TiO_2$ are Ti_2O_8 double octahedral chains 16.1a. A Ti_2O_8 double chain is obtained from two TiO_5 chains 2.34 by sharing two edges per octahedron. 16.1b is a projection view of the Ti_2O_8 double chain 16.1a along the chain direction. In terms of such a projection view,

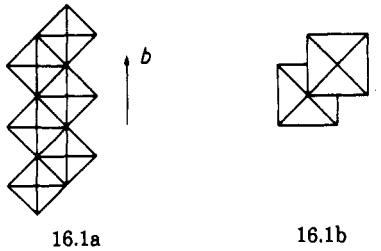

16.1a 16.1b

it is very easy to build the 3D Ti–O lattice of $Na_{0.25}TiO_2$. We obtain a Ti_4O_{12} quadruple chain 16.2 by sharing edges of the Ti_2O_8 double chains, a Ti_8O_{20} layer 16.3 by sharing edges of the Ti_4O_{12} quadruple chains, and finally the 3D Ti_8O_{16} lattice 16.4 by sharing corners of Ti_8O_{20} layers. The sodium cations are located in the

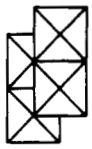

16.2

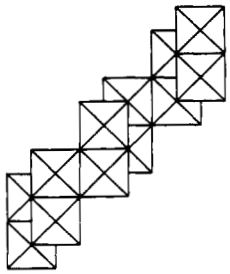

16.3

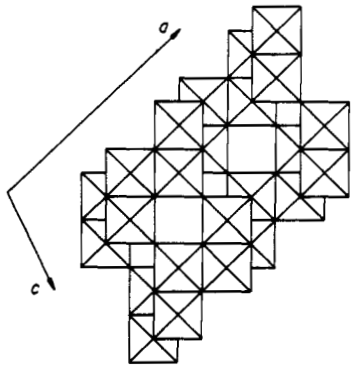

16.4

channels between Ti_8O_{20} layers.

There are two crystallographically different Ti atoms in $Na_{0.25}TiO_2$[109a] [i.e., Ti(1) and Ti(2)] and their TiO_6 octahedra are distorted from a regular octahedra as shown in 16.5. In the $Ti(1)O_6$ octahedron, there exists

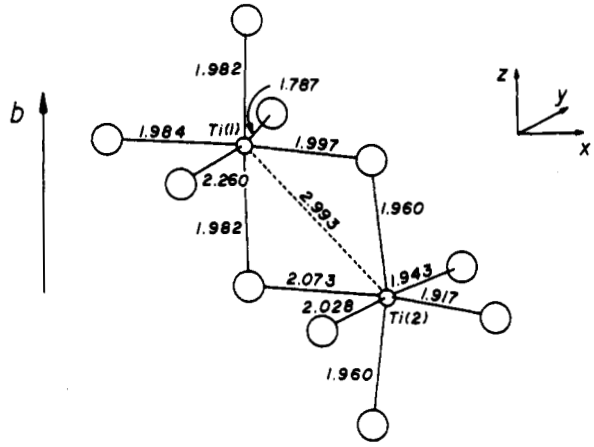

16.5

a strong O–Ti···O bond alternation (i.e., 1.787 vs 2.260 Å) along the direction perpendicular to the crystallographic b axis (i.e., the chain direction), and the remaining four Ti–O bonds have a similar length (i.e., ~1.986 Å on average). It is then clear that only the xz orbital of the $Ti(1)O_6$ octahedra will remain low in energy. Although each $Ti(2)O_6$ octahedron has four "short" and two "long" bonds, it has no strong O–Ti···O alternation unlike $Ti(1)O_6$. However, the four "short" bonds of $Ti(2)O_6$ are shorter in average (i.e., 1.945 Å) than the four intermediate bonds of $Ti(1)O_6$. Thus, the three t_{2g} levels of $Ti(2)O_6$ will lie higher in energy than

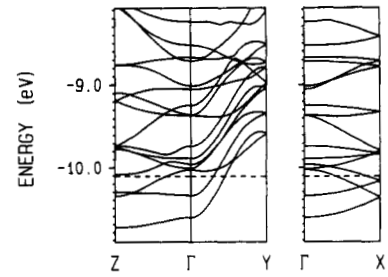

Figure 16.1. Dispersion relations of the bottom t_{2g}-block bands calculated for the $Ti_8O_{16}^{2-}$ lattice 16.4, where the dashed line refers to the Fermi level. $\Gamma = (0, 0, 0)$, $X = (a^*/2, 0, 0)$, $Y = (0, b^*/2, 0)$, and $Z = (0, 0, c^*/2)$.

the xz level of $Ti(1)O_6$. In addition, there is some Ti(1)···Ti(2) interaction perpendicular to the shared edge (i.e., 2.993 Å), which will provide some additional lowering of the Ti(1) xz level. It is then expected that the lowest t_{2g}-block levels of the Ti_8O_{16} lattice originate mainly from the xz orbitals of the $Ti(1)O_6$ octahedra.

Given the oxidation states of Ti^{4+} and O^{2-}, the t_{2g}-block bands of $Na_{0.25}TiO_2$ are filled due to the electrons donated by Na. The amount of electrons donated is not large, i.e., one electron per four Ti atoms or, equivalently, one electron per 12 t_{2g}-block levels. Therefore in $Na_{0.25}TiO_2$, only the bottom of the t_{2g}-block bands (i.e., the lowest xz bands) becomes occupied.

In the Ti_4O_{12} quadruple chain 16.2, the Ti(1) and Ti(2) atoms are found in the middle two and in the outer two TiO_5 chains, respectively. Consequently, the $Ti(1)O_6$ octahedra form $Ti(1)_2O_8$ double chains and these double chains are separated from one another as shown in 16.6. The xz orbitals of Ti(1) (i.e., those

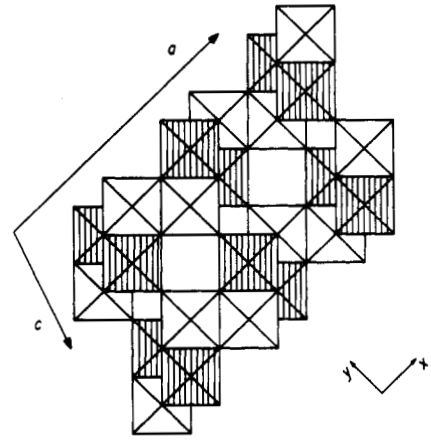

16.6

leading to the lowest t_{2g} bands) have strong π-type interaction with the oxygen x orbitals along the chain direction (i.e., the b axis), as illustrated in 16.7 for one TiO_5 chain. These xz orbitals are well oriented to

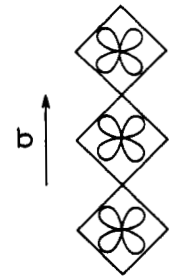

16.7

interact with the high-lying xz orbitals of the $Ti(2)O_6$ octahedra so that a weak coupling between the xz bands of the $Ti(1)_2O_8$ double chains can be expected. The Ti(1) xz orbitals of different Ti_2O_8 double chains along the c direction lead to δ-type interactions between $Ti(1)O_6$ and $Ti(2)O_6$ octahedra, which are extremely weak. Therefore, the lowest t_{2g}-block bands of the Ti_8O_{16} lattice should be pseudo-1D with strong dispersion along the b direction and weaker interaction along the a direction. Figure 16.1 shows the bottom portion of the t_{2g}-block bands calculated[111] for the 3D $Ti_8O_{16}^{2-}$ lattice of $Na_{0.25}TiO_2$, where the dashed line refers to the Fermi level. With only two electrons to fill them, the bottom two folded bands become partially filled. These bands are largely represented by the xz levels of the Ti(1) atoms and are mainly dispersive along $\Gamma \rightarrow Y$, as expected.

$Na_{0.25}TiO_2$ is pseudo-1D despite its 3D crystal lattice. This is reminiscent of the situation for lithium molybdenum purple bronze $Li_{0.9}Mo_6O_{17}$ (section 12). However, $Na_{0.25}TiO_2$ is even more striking because its lattice is exclusively built from TiO_6 octahedra. Since the Fermi surfaces associated with the partially filled bands of Figure 16.1 have a strong 1D character, it is expected that $Na_{0.25}TiO_2$ has some type of Peierls instability. According to the band structure of Figure 16.1, the Fermi surfaces for $Na_{0.25}TiO_2$ are not perfectly nested, which would be consistent with a metal-to-metal transition rather than the observed metal-to-insulator transition. However, it should be recalled that the available crystal structure for $Na_{0.25}TiO_2$ was solved at room temperature without considering the superlattice spots in the refinement.[109a] Consequently, this crystal structure should be considered as approximate, and only the gross features of the band structure calculated on the basis of this structure can be considered relevant.

16.2 $Li_{0.33}MoO_3$

The lithium bronze $Li_{0.33}MoO_3$[37,112] is violet blue and different in structure from the other $A_{0.33}MoO_3$ (A = K, Rb, Cs, Tl) bronzes (see section 9). A single-crystal X-ray diffraction study[37] reveals that it is triclinic, which is quiet unique among the known molybdenum bronzes. As in the case of other $A_{0.33}MoO_3$ bronzes, however, $Li_{0.33}MoO_3$ is a semiconductor.[113] Although its crystal structure is quite complex, a careful analysis of the distortions present in the lattice leads to a simple explanation for the origin of its semiconducting properties.

Schematically shown in 16.8 is a Mo_6O_{26} unit made up of six MoO_6 octahedra sharing their edges and corners. Such Mo_6O_{26} units form an Mo_6O_{24} chain 16.9 upon sharing their corners. When LiO_6 octahedra are fused into the Mo_6O_{24} chain between every two adjacent Mo_6O_{26} units, one obtains an $Li_2Mo_6O_{30}$ chain 16.10, where LiO_6 octahedra are indicated by shading. Such

16.8

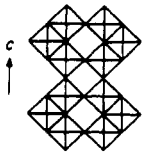

16.9

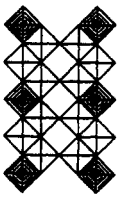

16.10

$Li_2Mo_6O_{30}$ chains share their octahedral corners to form an $Li_2Mo_6O_{28}$ layer 16.11. It is these layers that form

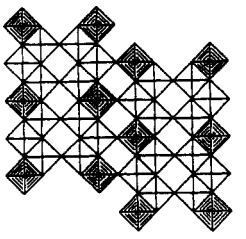

16.11

the 3D crystal structure of $Li_{0.33}MoO_3$ by sharing their octahedral corners and edges. Two $Li_2Mo_6O_{28}$ layers may share their octahedral corners as indicated in 16.12a or their octahedral edges as indicated in 16.12b, where LiO_6 octahedra of each $Li_2Mo_6O_{28}$ layer are omitted for clarity. In the layer stacking 16.12a,

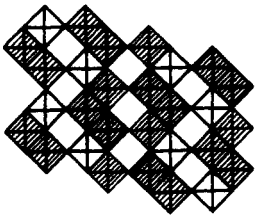

16.12a

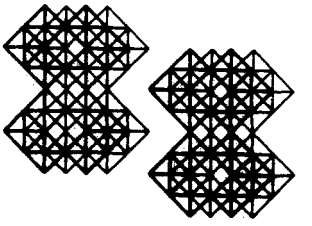

16.12b

Mo_6O_{24} chains (16.9) of one layer (16.10) are linked to one another via the Mo_6O_{24} chains of another $Li_2Mo_6O_{28}$ layer, while this is not the case in the layer stacking 16.12b. In $Li_{0.33}MoO_3$, the types of layer stacking 16.12a and 16.12b are both present. As schematically shown in 16.13, a unit cell of $Li_{0.33}MoO_3$ contains four shared $Li_2Mo_6O_{28}$ layers (I_a, II_a, II_b, and I_b). The layers II_a and

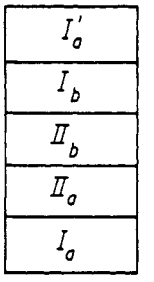

16.13

II_b share their octahedral edges as in 16.12b, while all other adjacent layers share their octahedral corners as in 16.12a. Thus a repeat unit cell of $Li_{0.33}MoO_3$ has the formula unit $(LiMo_3O_9)_8$. Due to the inversion symmetry of the crystal, the layers I_a and II_a are equivalent to I_b and II_b, respectively, so that only two unique $Li_2Mo_6O_{28}$ layers are present in $Li_{0.33}MoO_3$.

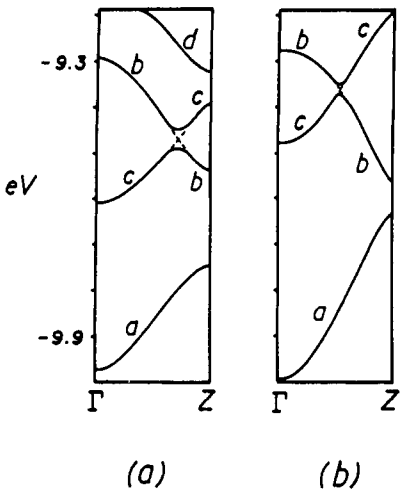

Figure 16.2. Dispersion relations of the bottom d-block bands calculated for the Mo_6O_{24} chains present in (a) layer I_a and (b) layer II_a of $Li_{0.33}MoO_3$.

In every $Li_2Mo_6O_{28}$ layer of $Li_{0.33}MoO_3$ (e.g., I_a and II_a in 16.13), each MoO_6 octahedron has a strong O–Mo···O bond length alternation perpendicular to the layer plane (e.g. ~1.7 vs ~2.4–2.5 Å in I_a and ~1.7 vs ~2.3–2.7 Å in II_a). Thus the *xz* and *yz* orbitals of each MoO_6 octahedron (see 16.14) are strongly raised in energy with respect to its *xy* orbital (i.e., the in-plane orbital), so that the bottom d-block bands of each $Li_2Mo_6O_{28}$ layer result from the *xy* orbitals of the MoO_6 octahedra. It is important to note that, between adjacent $Li_2Mo_6O_{28}$ layers, having the corner stacking shown in 16.12a, these *xy* orbitals give rise to δ-type interactions. Since these interactions practically vanish, such $Li_2Mo_6O_{28}$ layers do not interact each other as far as their *xy* orbitals are concerned. As will be discussed later, adjacent $Li_2Mo_6O_{28}$ layers having the edge stacking shown in 16.12b (i.e., II_a and II_b in 16.13) can also be considered noninteracting as far as their low-lying *xy* bands are concerned. Thus, the bottom d-block bands of $Li_{0.33}MoO_3$ can be approximated by superposing the bottom d-block bands of each $Li_2Mo_6O_{28}$ layer. As discussed already, there are only two unique $Li_2Mo_6O_{28}$ layers (e.g., I_a and II_a in 16.13) in $Li_{0.33}MoO_3$. In addition, each layer 16.11 consists of isolated Mo_6O_{24} chains. Thererfore, one needs to consider only the d-block bands of the Mo_6O_{24} chains present in layers I_a and II_a in order to deduce the bottom d-block bands of $Li_{0.33}MoO_3$.

Shown in Figure 16.2 are the bottom portions of the d-block bands calculated[114] for the Mo_6O_{24} chains present in layers I_a and II_a of $Li_{0.33}MoO_3$. These bands are largely derived from the *xy* orbitals of the MoO_6 octahedra and possess dispersion patterns that resemble those found for the ideal Mo_4O_{18} chain in Figure 9.2a. The CO degeneracies of the ideal Mo_4O_{18} chain observed in Figure 9.2a are all lifted in Figure 16.2 because of the distortions present in the real Mo_6O_{24}, as will be examined in this section. The two important features to note from Figure 16.2 are that the lowest lying band a is separated from other bands lying above in Figure 16.2, and that the top of band a in Figure 16.2b lies below the bottom of band c in Figure 16.2a. With two electrons per unit cell per chain to fill the d-block bands, the band structure of Figure 16.2a or that of Figure 16.2b has a band gap, and the band structure obtained by superposing Figure 16.2 a and b also gives a band gap although it is very small.

16.14a (16.14b) illustrates how the Mo_6O_{26} unit 16.8 of the Mo_6O_{24} chain in layer I_a (II_a) of $Li_{0.33}MoO_3$ differs from the corresponding ideal structure constructed from regular octahedra. For simplicity, the Mo–O distances associated with the axial oxygen atoms are not shown in 16.14. In 16.14a and 16.14b the hump MoO_6 oc-

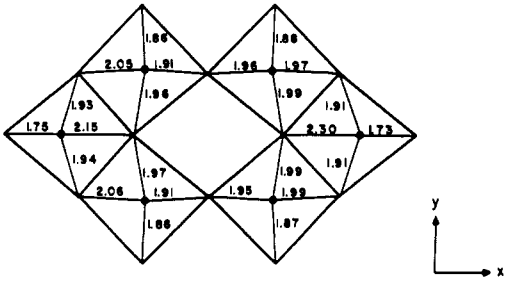

16.14a

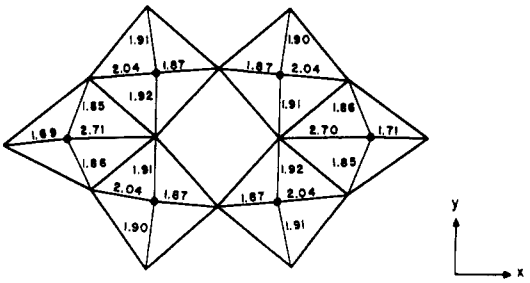

16.14b

tahedra have very short Mo–O distances (~1.7 Å), so that their *xy* orbitals are raised in energy beyond the energy region of Figure 16.2. Thus, the lowest lying *xy*-block bands of the Mo_6O_{24} chains should be largely represented by the bands of the Mo_4O_{18} chain 8.2. Let us now discuss how the band structures of Figure 16.2 deviate from that of Figure 9.2a corresponding to the ideal Mo_4O_{18} chain 8.2. For this purpose, both the orbital analysis in section 9.2 and the geometry distortions present in the real Mo_6O_{24} chains 16.14a and 16.14b should be taken into consideration.

Bands b and c in Figure 16.2 show noncrossing due to the symmetry lowering induced by the distortions. The essential result of Figure 16.2 is that the top of band a in Figure 16.2b lies slightly lower in energy than the bottom of band c in Figure 16.2a. The Mo–O bonds in 16.14a and 16.14b (excluding those of the hump octahedra) approximately parallel and perpendicular to the Mo_6O_{24} chain may be referred to as the Mo–O(∥) and Mo–O(⊥) bonds, respectively. The average lengths of the Mo–O(⊥) and Mo–O(∥) bonds are respectively 1.92 and 1.97 Å in 16.14a, and 1.91 and 1.95 Å in 16.14b. Since the average Mo–O(⊥) bond length is shorter than the average Mo–O(∥) bond length, the top of band a lies below the bottom of band c in Figure 16.2, parts a and b (see 9.9 and 9.10). The average Mo–O(⊥) and Mo–O(∥) bond lengths are both shorter in 16.14b than in 16.14a, so that the band a (top) and the band c (bottom) in Figure 16.2b both lie higher than the corresponding points in Figure 16.2a. Since the average Mo–O(∥) length in 16.14b is longer than the average Mo–O(⊥) length in 16.14a, the band a top of Figure 16.2b lies below the band c bottom of Figure 16.2a so that band c of Figure 16.2a does not overlap with band a of Figure 16.2b.

Finally, we note that band a is essentially obtained from the unit cell orbital 9.5a, which has no orbital contribution from the bridging oxygen atoms within a unit cell. In the layer stacking of 16.12b, the metal xy orbitals of each layer can in principle interact with those of the other layer via the bridging oxygen atoms. However, band a does not have any orbital contribution from the bridging oxygen atoms, so that the character of band a is not expected to change upon the layer stacking of 16.12b. Band c is obtained from the unit cell orbital 9.5c, which has p-orbital contribution from the O(||) atoms (i.e., those oxygen atoms on the Mo–O–Mo bridges parallel to the Mo_6O_{24} chain) within a unit cell. According to 16.12b, these O(||) atoms of one layer are located on top of the Mo atoms of the other layer so that there exists no orbital overlap between such Mo and O(||) atoms. Consequently, the character of band c is not expected to change upon the layer stacking of 16.12b. As a result, the energy gap between band a at Z in Figure 16.2b and band c at Γ in Figure 16.2a is expected to remain even if the layer stacking 16.12b is taken into consideration. As a result, $Li_{0.33}MoO_3$ was predicted to be semiconducting in all directions.[114] Since the valence and the conduction bands of Figure 16.2 are dispersive along $\Gamma \rightarrow Z$, the electrical conductivity of $Li_{0.33}MoO_3$ is expected to be largest along the c direction. These predictions were confirmed by single-crystal electrical resistivity measurements.[113]

17. Concluding Remarks

In the first half of this review, we have discussed theoretical and computational concepts necessary for understanding the electronic properties of low-dimensional metallic compounds. The electronic structures of crystalline solids are described in terms of band structures, the essence of which can be easily understood in terms of overlap, symmetry, and chemical bonding by analyzing the band orbitals at a few specific wave vector points. The phase transition from a normal metallic state to a CDW, SDW, or superconducting state is described in terms of orbital mixings between the occupied and unoccupied levels of the normal metallic state near the Fermi level. In the second half of this review, we have examined the structure–property correlations associated with the electronic instabilities of low-dimensional molybdenum and tungsten oxide metals. The CDW phenomena of these oxides originate from the Fermi surface nesting of their partially filled d-block bands. Those oxides have a very low d-electron counting on transition metal. Consequently, only certain parts of their crystal structures, i.e., the metal–oxygen layers made up of MO_6 octahedra, contain d electrons, and only the bottom portion of the t_{2g}-block bands associated with such layers become partially filled. The dispersion characteristics of these partially t_{2g}-block bands are easily explained by analyzing the octahedral distortions of the oxides and by counting in how many metal–oxygen–metal bridges the oxygen p orbitals can mix between adjacent metal t_{2g}-block orbitals at a few specific wave vector points.

For 1D metals such as $Li_{0.9}Mo_6O_{17}$ and $K_{0.33}MoO_3$, it is straightforward to identify their Fermi surface nesting. The 2D metals, purple bronze KMo_6O_{17}, the Magnéli phases Mo_4O_{11}, and the MPTB phases, all possess several 2D Fermi surfaces which, if viewed individually, do not give a clue to any Fermi surface nesting. When those 2D Fermi surfaces are combined together, it is easy to redraw them into nested 1D and nested 2D Fermi surfaces. Such a hidden nesting leads to an electronic instability when the energy required for decoupling the weak band hybridization, which produces "unnested" 2D Fermi surfaces, is small compared with the energy gain resulting from a CDW or SDW formation associated with the hidden nesting. The Fermi surfaces of every MPTB phase have several different hidden nesting vectors, so that the MPTB phases should exhibit rich CDW phenomena and are exciting materials to study.

Acknowledgments. This work was supported by the Office of Basic Energy Sciences, Division of Materials Sciences, U.S. Department of Energy, under Grant No. DE-FG05-86ER45259, by Scientific Affairs Division, NATO and by Centre National de la Recherche Scientifique, France. We express our appreciation for computing time made available by DOE. During the course of our studies on the low-dimensional molybdenum and tungsten oxide metals, we have benefited from invaluable discussions with Professor M. Greenblatt, Dr. J.-P. Pouget, and Professor C. Schlenker.

References

(1) (a) Pouget, J. P. In *Low-Dimensional Electronic Properties of Molybdenum Bronzes and Oxides*; Schlenker, C., Ed; Kluwer: Dordrecht, The Netherlands, 1989; p 87. (b) Schlenker, C.; Dumas, J.; Escribe-Filippini, C.; Guyot, H. In *Low-Dimensional Electronic Properties of Molybdenum Bronzes and Oxides*; Schlenker, C., Ed.; Kluwer: Dordrecht, The Netherlands, 1989; p 159. (c) Greenblatt, M. In *Low-Dimensional Electronic Properties of Molybdenum Bronzes and Oxides*; Schlenker, C., Ed.; Kluwer: Dordrecht, The Netherlands, 1989; p 1. (d) Fleming, R. M.; Cava, R. J. In *Low-Dimensional Electronic Properties of Molybdenum Bronzes and Oxides*; Schlenker, C., Ed.; Kluwer: Dordrecht, The Netherlands, 1989; p 259. (e) Greenblatt, M. *Chem. Rev.* **1988**, *88*, 31. (f) Schlenker, C.; Dumas, J.; Escribe-Filippini, C.; Guyot, H.; Marcus, J.; Fourcadot, J. *Philos. Mag. B* **1985**, *52*, 643.

(2) (a) Manthiram, A.; Gopalakrishnan, J. *Rev. Inorg. Chem.* **1984**, *6*, 1. (b) Vincent, H.; Marezio, M. In *Low-Dimensional Electronic Properties of Molybdenum Bronzes and Oxides*; Schlenker, C., Ed.; Kluwer, Dordrecht, The Netherlands, 1989; p 49. (c) Kihlborg, L. *Ark. Kemi* **1963**, *21*, 471.

(3) Raveau, B. *Proc. Indian Nat. Sci. Acad.* **1986**, *A52*, 67.

(4) Whangbo, M.-H.; Canadell, E. *Acc. Chem. Res.* **1989**, *22*, 375.

(5) (a) Wilson, J. A.; DiSalvo, F. J.; Mahajan, S. *Adv. Phys.* **1975**, *24*, 117. (b) Whangbo, M.-H. In *Electron Transfer in Biology and the Solid State: Inorganic Compounds with Unusual Properties*; Johnson, M. K., King, R. B., Kurtz, D. M., Kutal, C.; Norton, M. L., Scott, R. A., Eds.; American Chemical Society: Washington, DC, 1990; p 269. (c) Monceau, P. In *Electronic Properties of Inorganic Quasi-One-Dimensional Compounds*; Monceau, P., Ed.; Reidel: Dordrecht, The Netherlands, 1985; Part II, p 139. (d) Moret, R.; Pouget, J. P. In *Crystal Chemistry and Properties of Materials with Quasi-One-Dimensional Structures*; Rouxel, J., Ed.; Reidel: Dordrecht, The Netherlands, 1986; p 87. (e) Rouxel, J.; Schlenker, C. In *Charge Density Waves in Solids*; Gor'kov, L. P., Grüner, G., Eds.; Elsevier: Amsterdam, The Netherlands, 1989; p 15. (f) Meerschaut, A.; Rouxel, J. In *Crystal Chemistry and Properties of Materials with Quasi-One-Dimensional Structures*; Rouxel, J., Ed.; Reidel: Dordrecht, The Netherlands, 1986; p 205. (g) DiSalvo, F. J. In *Electron-Phonon Interactions and Phase Transitions*; Riste, T. Ed.; Plenum: New York, 1977; p 107. (h) Pouget, J. P.; Comes, R. In *Charge Density Waves in Solids*; Gor'kov, L. P.; Grüner, G., Eds.; Elsevier: Amsterdam, The Netherlands, 1989; p 85. (i) Kagoshima, S.; Nagasawa, H.; Sambongi, T. *One-Dimensional Conductors*; Springer-Verlag: Heidelberg, Germany, 1988.

(6) Hoffmann, R. *J. Chem. Phys.* **1963**, *39*, 1397. A modified Wolfsberg-Helmholz formula is used to calculate the off-diagonal H_{ij} values: Ammeter, J. H.; Bürgi, H.-B.; Thibeault, J.; Hoffmann, R. *J. Am. Chem. Soc.* **1978**, *100*, 3686.

(7) (a) Whangbo, M.-H.; Hoffmann, R. *J. Am. Chem. Soc.* **1978**, *100*, 6093. (b) Whangbo, M.-H.; Hoffmann, R.; Woodward, R. B. *Proc. Soc. London* **1979**, *A366*, 23.

(8) (a) Whangbo, M.-H. In *Crystal Chemistry and Properties of Materials with Quasi-One-Dimensional Structures*; Rouxel, J., Ed.; Reidel: Dordrecht, The Netherlands, 1986; p 205. (b) Whangbo, M.-H. In *Extended Linear Chain Compounds*; Miller, J. S., Ed.; Plenum: New York, 1982; Vol. 2, p 127. (c) Burdett, J. K. *Prog. Solid State Chem.* **1984**, *15*, 173. (d) Hoffmann, R. *Solids and Surfaces: A Chemist's View of Bonding in Extended Structures*; VCH: New York, 1988. (e) Albright, T. A.; Burdett, J. K.; Whangbo, M.-H. *Orbital Interactions in Chemistry*; Wiley: New York, 1985; Chapter 13.

(9) (a) DiBartolo, B.; Powell, R. C. *Phonons and Resonances in Solids*; Wiley: New York, 1976; Chapter 5. (b) Brüesch, P. *Phonons: Theory and Experiment*; Springer-Verlag: New York, 1982; Vol. I, Chapter 2.

(10) (a) Ashcroft, N. W.; Mermin, N. D. *Solid State Physics*; Holt, Rinehart and Winston: Philadelphia, 1985. (b) Christman, J. R. *Fundamentals of Solid State Physics*; Wiley: New York, 1988.

(11) (a) Cracknell, A. P.; Wong, K. C. *The Fermi Surface*. Oxford University Press: Oxford, England, 1973. (b) Jones, H. *The Theory of Brillouin Zones and Electronic States in Crystals*, 2nd ed.; North Holland: Amsterdam, The Netherlands, 1975.

(12) (a) Whangbo, M.-H. *J. Chem. Phys.* **1980**, *73*, 3854. (c) Whangbo, M.-H. *Acc. Chem. Soc.* **1983**, *16*, 95.

(13) (a) Kohn, W. *Phys. Rev. Lett.* **1959**, *2*, 393. (b) Kagoshima, S. *Extended Linear Chain Compounds*; Miller, J. S., Ed.; Plenum: New York, 1982; Vol. 2, Chapter 7.

(14) (a) Mott, N. F. *Metal-Insulator Transitions*; Barnes and Noble: New York, 1977. (b) Brandow, B. H *Adv. Phys.* **1977**, *26*, 651. (c) Whangbo, M.-H. *J. Chem. Phys.* **1979**, *70*, 4963.

(15) (a) Anderson, P. W. *Phys. Rev.* **1958**, *109*, 1492. (b) Hayes, W.; Stoneham, A. M. *Defects and Defect Processes in Nonmetallic Solids*; Wiley: New York, 1985; Chapter 8.

(16) (a) Solymar, L.; Walsh, D. *Lectures on the Electrical Properties of Materials*, 4th ed.; Oxford University Press: Oxford, England, 1988; Chapter 14. (b) Grassie, A. D. C. *The Superconducting State*; Sussex University Press: London, 1975; Chapter 2.

(17) (a) Bardeen, J.; Cooper, L. N.; Schrieffer, J. R. *Phys. Rev.* **1957**, *108*, 1175. (b) McMillan, W. L. *Phys. Rev.* **1968**, *167*, 331.

(18) Whangbo, M.-H.; Williams, J. M.; Schultz, A. J.; Emge, T. J.; Beno, M. A. *J. Am. Chem. Soc.* **1987**, *109*, 90.

(19) Nasu, K. *J. Phys. Soc. Jpn* **1985**, *54*, 1933.

(20) Whangbo, M.-H.; Evain, M.; Hughbanks, T.; Kertesz, M.; Wijeyesekera, S.; Wilker, C.; Zheng, C.; Hoffmann, R. *QCPE* **1989**, *9*, 61.

(21) Hughbanks, T.; Hoffmann, R. *J. Am. Chem. Soc.* **1983**, *105*, 3528.

(22) Press, W. H.; Flannery, B. P.; Teukolsky, S. A.; Vetterling, W. T. *Numerical Recipes*; Cambridge University Press: New York, 1987.

(23) Moioni, A.; Subramanian, M.; Clearfield, A.; DiSalvo, F. J.; McCarroll, W. H. *J. Solid State Chem.* **1987**, *66*, 136.

(24) Stephenson, N. C.; Wadsley, A. D. *Acta Crystallogr.* **1965**, *18*, 241.

(25) (a) Mumme, G.; Watts, J. W. *J. Solid State Chem.* **1970**, *2*, 16. (b) *Structure Reports*; Pearson, W. B., Ed.; Oosthoek, Scheltema, Hokkema: Utrecht, The Netherlands, 1957; Vol. 35A, p 227.

(26) (a) Graham, J.; Wadsley, A. D. *Acta Crystallogr.* **1966**, *20*, 93. (b) Ghedira, M.; Chenavas, J.; Marezio, M.; Marcus, J. *J. Solid State Chem.* **1985**, *57*, 300.

(27) (a) Magnéli, A. *Acta Chem. Scand.* **1948**, *2*, 501. (b) Kihlborg, L. *Ark. Kemi* **1963**, *21*, 461. (c) Fujishita, H.; Sato, M.; Sato, S.; Hoshino, S. *J. Solid State Chem.* **1987**, *66*, 40.

(28) (a) Hervieu, M.; Raveau, B. *J. Solid State Chem.* **1982**, *43*, 299. (b) Domengès, B.; Hervieu, M.; Raveau, B. *Acta Cryst.* **1984**, *B40*, 249. (c) Hervieu, M.; Raveau, B. *Chem. Scr.* **1983**, *22*, 117, 123.

(29) (a) Domengès, B.; Studer, F.; Raveau, B. *Mat. Res. Bull.* **1983**, *18*, 669. (b) Domengès, B.; Hervieu, M.; Raveau, B.; Tilley, R. J. D. *J. Solid State Chem.* **1984**, *54*, 10.

(30) Giroult, J. P.; Goreaud, M.; Labbé, P.; Raveau, B. *Acta Crystallogr.* **1981**, *B37*, 2139.

(31) (a) Giroult, J. P.; Goreaud, M.; Labbé, P.; Raveau, B. *J. Solid State Chem.* **1982**, *44*, 407. (b) Benmoussa, A.; Giroult, J. P.; Labbé, P.; Raveau, B. *Acta Crystallogr.* **1984**, *C40*, 573.

(32) (a) Ghedira, M.; Vincent, H.; Marezio, M.; Marcus, J.; Fourcadot, G. *J. Solid State Chem.* **1985**, *56*, 66. (b) Kihlborg, L. *Ark. Kemi* **1963**, *21*, 365. (c) Magnéli, A. *Acta Chem. Scand.* **1948**, *2*, 861.

(33) Labbé, P.; Goreaud, M.; Raveau, B. *J. Solid State Chem.* **1986**, *61*, 324.

(34) Onoda, M.; Toriumi, K.; Matsuda, Y.; Sato, M. *J. Solid State Chem.* **1987**, *66*, 163.

(35) Vincent, H.; Ghedira, M.; Marcus, J.; Mercier, J.; Schlenker, C. *J. Solid State Chem.* **1983**, *47*, 113.

(36) (a) Ganne, M.; Dion, M.; Boumaza, A. *C. R. Acad. Sci. Ser. 2* **1986**, *302*, 635. (b) Tsai, P. P.; Potenza, J. A.; Greenblatt, M. *J. Solid State Chem.* **1987**, *69*, 329. (c) Réau, J.-M.; Fouassier, C.; Hagenmuller, P. *Bull. Soc. Chim. Fr.* **1971**, *8*, 2884.

(37) Tsai, P. P.; Potenza, J. A.; Greenblatt, M.; Schugar, H. *J. Solid State Chem.* **1984**, *64*, 47.

(38) (a) Travaglini, G.; Wachter, P.; Marcus, J.; Schlenker, C. *Solid State Commun.* **1982**, *42*, 407. (b) Strobel, P.; Greenblatt, M. *J. Solid State Chem.* **1981**, *36*, 331. (c) Wold, A.; Kunnmann, W.; Arnott, R. J.; Ferretti, A. *Inorg. Chem.* **1964**, *3*, 545. (d) Bouchard, G. H.; Perlstein, J.; Sienko, M. J. *Inorg. Chem.* **1967**, *6*, 1682. (e) Morsli, M.; Bonnet, A.; Connan, A.; Ganne, M.; Jouanneaux, A. *Phys. Rev. B* **1989**, *39*, 3735.

(39) Travaglini, P.; Wachter, P. *Solid State Commun.* **1983**, *47*, 217.

(40) Bang, G.; Sperlich, G. *Z. Phys. B* **1975**, *22*, 1.

(41) Whangbo, M.-H.; Evain, M.; Canadell, E.; Ganne, M. *Inorg. Chem.* **1989**, *28*, 267.

(42) Canadell, E.; Whangbo, M.-H. *Inorg. Chem.* **1989**, *28*, 1609.

(43) Ganne, M.; Boumaza, M.; Dion, M.; Dumas, J. *Mat. Res. Bull.* **1985**, *20*, 1297.

(44) Wold, A.; Kunnmann, W.; Arnott, R. J.; Ferretti, A. *Inorg. Chem.* **1964**, *3*, 345.

(45) (a) Bouchard, G. H.; Perlstein, J. H.; Sienko, M. J. *Inorg. Chem.* **1967**, *6*, 1682. (b) Fogle, W.; Perlstein, J. H. *Phys. Rev. B* **1972**, *6*, 1402.

(46) (a) Perloff, D. S.; Vlasse, M.; Wold, A. *J. Phys. Chem. Solids* **1969**, *30*, 1071. (b) Brusetti, R.; Chakraverty, B. K.; Deveny, Y.; Dumas, J.; Marcus, J.; Schlenker, C. *Recent Developments in Condensed Matter Physics*; Devreese, J. T., Ed.; Plenum: New York, 1981; Vol. 2, p 181.

(47) Travaglini, G.; Wachter, P.; Marcus, J.; Schlenker, C. *Solid State Commun.* **1981**, *37*, 599.

(48) Pouget, J. P.; Kagoshima, S.; Schlenker, C.; Marcus, J. *J. Phys. Lett.* **1983**, *44*, L113.

(49) Fleming, R.; Schneemeyer, L. F.; Moncton, D. E. *Phys. Rev. B* **1985**, *31*, 899.

(50) (a) Sato, M.; Fujishita, H.; Hoshino, S. *J. Phys. C* **1983**, *16*, L877. (b) Sato, M.; Fujishita, H.; Hoshino, S. *J. Phys. C.* **1985**, *18*, 2603.

(51) Chen, C. H.; Schneemeyer, L. F.; Fleming, R. M. *Phys. Rev. B* **1984**, *29*, 3765.

(52) (a) Fleming, R. M.; Schneemeyer, L. F. *Bull. Am. Phys. Soc.* **1984**, *29*, 470. (b) Dieker, S. B.; Lyons, K. B.; Schneemeyer, L. F. *Bull. Am. Phys. Soc.* **1984**, *29*, 469.

(53) (a) Escribe-Filippini, C.; Pouget, J. P.; Currat, R.; Hennion, B.; Marcus, J. *Lect. Notes Phys.* **1985**, *217*, 71. (b) Pouget, J. P.; Noguera, C.; Moudden, A. H.; Moret, R. *J. Phys. (Les Ulis, Fr.)* **1985**, *46*, 1731.

(54) Tamegai, T.; Tsutsumi, K.; Kagoshima, S.; Kanai, Y.; Tani, M.; Tomozawa, H.; Sato, M.; Tsuji, K.; Harada, J.; Sakata, M.; Nakajima, T. *Solid State Commun.* **1984**, *51*, 585.

(55) Collins, B. T.; Ramanujachary, K. V.; Greenblatt, M.; Waszczak, J. V. *Solid State Commun.* **1985**, *56*, 1023.

(56) Schlenker, C.; Dumas, J. *Crystal Structures and Properties of Materials with Quasi-One-Dimensional Structures*; Rouxel, J., Ed.; Reidel: Dordrecht, The Netherlands, 1986; p 135.

(57) (a) Dumas, J.; Schlenker, C.; Marcus, J.; Buder, R. *Phys. Rev. Lett.* **1983**, *50*, 757. (b) Schlenker, C.; Filippini, C.; Marcus, J.; Dumas, J.; Pouget, J. P.; Kagoshima, S. *J. Phys. (Les Ulis, Fr.)* **1983**, *44*, C3-1757. (c) Schneemeyer, L. F.; DiSalvo, F. J.; Fleming, R. M.; Waszczak, J. V. *J. Solid State Chem.* **1984**, *54*, 538. (d) Dumas, J.; Schlenker, C. *Solid State Commun.* **1983**, *45*, 885. (e) Fleming, R. M.; Schneemeyer, L. F. *Phys. Rev. B* **1983**, *28*, 6996.

(58) Whangbo, M.-H.; Schneemeyer, L. F. *Inorg. Chem.* **1986**, *25*, 2424.

(59) McCarroll, W. H.; Darling, C.; Jakubicki, G. *J. Solid State Chem.* **1983**, *48*, 1989.

(60) Cotton, F. A.; Walton, R. A. *Multiple Bonds between Metal Atoms*; Wiley: New York, 1982; p 287.

(61) Whangbo, M.-H.; Canadell, E. *Inorg. Chem.* **1987**, *26*, 842.

(62) Collins, B. T.; Greenblatt, M.; McCarroll, W. H.; Hull, G. W. *J. Solid State Chem.* **1988**, *73*, 507.

(63) (a) Sato, M.; Nakao, K.; Hoshino, S. *J. Phys. C* **1984**, *17*, L817. (b) Gruber, H.; Krautz, E.; Fritzer, H. P.; Gatterer, K.; Popitsch, A. *Solid State Commun.* **1986**, *58*, 133.

(64) (a) Sato, M.; Fujishita, H.; Sato, S.; Hoshino, S. *J. Phys. C* **1986**, *19*, 3059. (b) Komdeur, A. J. H.; DeBoer, J. L.; van Smaalen, S. *J. Phys. Condens. Matter* **1990**, *2*, 45.

(65) Onoda, M.; Fujishita, H.; Matsuda, Y.; Sato, M. *Synth. Met.* **1987**, *19*, 947.

(66) Canadell, E.; Whangbo, M.-H. *Inorg. Chem.* **1990**, *29*, 2256.

(67) Zachariasen, W. H. *J. Less-Common Met.* **1978**, *62*, 1.

(68) (a) Shirane, G.; Yamada, Y. *Phys. Rev.* **1969**, *177*, 858. (b) Fuji, Y.; Hoshino, S.; Yamada, Y.; Shirane, G. *Phys. Rev. B*

1974, *9*, 4549. (c) Sato, M.; Grier, B. H.; Shirane, G.; Akahane, T. *Phys. Rev. B* **1982**, *25*, 6876.
(69) Fujishita, H.; Sato, M.; Shapiro, S.; Hoshino, S. *Physica B* **1986**, *143*, 201.
(70) (a) Giroult, J. P.; Goreaud, M.; Labbé, P.; Raveau, B. *Acta Crystallogr.* **1980**, *B36*, 2570. (b) Giroult, J. P.; Goreaud, M.; Labbé, P.; Raveau, B. *Acta Crystallogr.* **1981**, *B37*, 1163. (c) Giroult, J. P.; Goreaud, M.; Labbé, P.; Raveau, B. *Acta Crystallogr.* **1982**, *B38*, 2342. (d) Giroult, J. P.; Goreaud, M.; Labbé, P.; Raveau, B. *Rev. Chim. Min.* **1983**, *20*, 829. (e) Labbé, P.; Ouacheé, D.; Goreaud, M.; Raveau, B. *J. Solid State Chem.* **1983**, *50*, 163.
(71) Giroult, J. P.; Goreaud, M.; Labbé, P.; Provost, J.; Raveau, B. *Mater. Res. Bull.* **1981**, *16*, 811.
(72) Wang, E.; Greenblatt, M.; Rachidi, I. E.-I.; Canadell, E.; Whangbo, M.-H. *J. Solid State Chem.* **1989**, *80*, 266.
(73) (a) Schlenker, C.; Schwenk, H.; Escribe-Filippini, C.; Marcus, J. *Physica* **1985**, *135B*, 511. (b) Greenblatt, M.; McCarroll, W. H.; Neifeld, R.; Croft, M.; Waszczak, J. V. *Solid State Commun.* **1984**, *51*, 671.
(74) (a) Ramanujachary, K. V.; Collins, B. T.; Greenblatt, M.; McNally, P.; McCarroll, W. H. *Solid State Ionics* **1986**, *22*, 105. (b) Matsuda, Y.; Onoda, M.; Sato, M. *Physica* **1986**, *143B*, 243.
(75) Whangbo, M.-H.; Canadell, E. *J. Am. Chem. Soc.* **1988**, *110*, 358.
(76) Sato, M.; Matsuda, Y.; Fukuyama, H. *J. Phys. C.* **1987**, *20*, L137.
(77) (a) Boujida, M.; Escribe-Filippini, C.; Beille, J.; Marcus, J.; Schlenker, C. *Fizika* **1990**, *23*, 151. (b) Boujida, M.; Escribe-Filippini, C.; Marcus, J.; Schlenker, *C. Physica* **1988**, *C153*, 465.
(78) (a) Jérome, D.; Mazaud, A.; Ribault, M.; Bechgaard, K. J. *Phys. Lett. (Les Ulis, Fr.)* **1980**, *41*, L195. (b) Torrance, J.; Pedersen, J. B.; Bechgaard, K. *Phys. Rev. Lett.* **1982**, *49*, 881. (c) Walsh, W. M., Jr.; Wudl, F.; Thomas, G. A.; Nalewajek, D.; Hauser, J. J.; Lee, P.; Poehler, T. O. *Phys. Rev. Lett.* **1980**, *45*, 829. (d) Pouget, J. P.; Moret, R.; Comes, R.; Shirane, G.; Bechgaard, K.; Fabre, J. M. *J. Phys. (Les Ulis, Fr.)* **1983**, *43*, C3-969. (e) Scott, J. C.; Pederson, H. J.; Bechgaard, K. *Phys. Rev. Lett.* **1980**, *45*, 2125.
(79) Escribe-Filippini, C.; Beille, J.; Boujida, M.; Marcus, J.; Schlenker, C. *Physica* **1989**, *C162–164*, 427.
(80) Goreaud, M.; Labbé, P.; Raveau, B. *J. Solid State Chem.* **1985**, *56*, 41.
(81) Wang, E.; Greenblatt, M. *J. Solid State Chem.* **1988**, *76*, 340.
(82) Wang, E.; Greenblatt, M.; Rachidi, I. E.-I.; Canadell, E.; Whangbo, M.-H. *Inorg. Chem.* **1989**, *28*, 2451.
(83) Foury, P.; Pouget, J. P.; Wang, E.; Greenblatt, M. *Synth. Met.*, in press.
(84) Canadell, E.; Rachidi, I. E.-I.; Wang, E.; Greenblatt, M.; Whangbo, M.-H. *Inorg. Chem.* **1989**, *28*, 2455.
(85) Domengès, B.; Goreaud, M.; Labbé, P.; Raveau, B. *Acta Crystallogr.* **1982**, *B38*, 1724.
(86) Wang, S. L.; Wang, C. C.; Lii, K. H. *J. Solid State Chem.* **1989**, *82*, 298.
(87) Abrahams, S. C.; Marsh, P.; Schneemeyer, L. F.; Rice, C. E.; Spengler, S. E. *J. Mater. Res.* **1987**, *2*, 82.
(88) Canadell, E.; Whangbo, M.-H. *J. Solid State Chem.* **1990**, *86*, 131.
(89) Schneemeyer, L. F.; Spengler, S. E.; DiSalvo, F. J.; Waszczak, J. V.; Rice, C. E. *J. Solid State Chem.* **1984**, *55*, 158.
(90) (a) Guyot, H.; Schlenker, C.; Fourcadot, G.; Konatè, K. *Solid State Commun.* **1985**, *54*, 909. (b) Schlenker, C.; Parkin, S. S. P.; Guyot, H. *J. Magn. Magn. Matter.* **1986**, *54–57*, 1313. (c) Sato, M.; Nakao, K.; Hoshino, S. *J. Phys. C* **1984**, *54*, 909.
(91) (a) Guyot, H.; Escribe-Filippini, C.; Fourcadot, G.; Konatè, K.; Schlenker, C. *J. Phys. C* **1983**, *16*, L1227. (b) Guyot, H.; Schlenker, C.; Pouget, J. P.; Ayroles, R.; Roucau, C. *J. Phys. C* **1985**, *18*, 4427. (c) Gruber, H.; Krautz, E.; Fritzer, H. P.; Gatterer, K.; Popitsch, A. *Phys. Stat. Sol. (a)* **1984**, *86*, 749.
(92) Benmoussa, A.; Labbé, P.; Giroult, D.; Raveau, B. *J. Solid State Chem.* **1982**, *44*, 318.
(93) Wang, E.; Greenblatt, M.; Rachidi, I. E.-I.; Canadell, E.; Whangbo, M.-H.; Vadlamannati, S. *Phys. Rev. B* **1989**, *39*, 12969.
(94) Foury, P.; Pouget, J. P.; Wang, E.; Greenblatt, M. *Europhys. Lett.*, submitted for publication.
(95) Canadell, E.; Whangbo, M.-H.; Schlenker, C.; Escribe-Filippini, C. *Inorg. Chem.* **1989**, *28*, 1466.
(96) Canadell, E.; Whangbo, M.-H.; Rachidi, I. E.-I. *Inorg. Chem.* **1990**, *29*, 3871.
(97) Inoue, M.; Ohara, S.; Horisaka, S.; Koyano, M.; Negishi, H. *Phys. Stat. Sol. (a)* **1988**, *148*, 659.
(98) Domengès, B.; McGuire, N. K.; O'Keeffe, M. *J. Solid State Chem.* **1985**, *56*, 94.
(99) Wang, E.; Greenblatt, M.; Rachidi, I. E.-I.; Canadell, E.; Whangbo, M.-H. *J. Solid State Chem.* **1989**, *81*, 173.
(100) Canadell, E.; Whangbo, M.-H. *Phys. Rev. B* **1991**, *43*, 1894.
(101) (a) Onoda, M.; Matsuda, Y.; Sato, M. *J. Solid State Chem.* **1987**, *66*, 163. (b) Stephenson, N. C. *Acta Crystallogr.* **1966**, *20*, 59.
(102) (a) Ganne, M.; Dion, M.; Boumaza, A.; Tournoux, M. *Solid State Commun.* **1986**, *59*, 137. (b) Ramanujachary, K. V.; Collins, B. T.; Greenblatt, M. *Solid State Commun.* **1986**, *59*, 647.
(103) DeBoer, J. L.; Meetsma, A. Unbublished results.
(104) (a) Buder, R.; Deveny, J.; Dumas, J.; Marcus, J.; Mercier, J.; Schlenker, C. *J. Phys. (Les Ulis, Fr.)* **1982**, *43*, L59. (b) Bervas, E.; Cochrane, R. W.; Dumas, J.; Escribe-Filippini, C.; Marcus, J.; Schlenker, C. *Lect. Notes Phys.* **1985**, *217*, 144.
(105) (a) Dumas, J.; Bervas, E.; Marcus, J.; Salomon, D.; Schlenker, C. *J. Magn. Magn. Mater.* **1983**, *31–34*, 535. (b) Escribe-Filippini, C.; Konate, K.; Marcus, J.; Schlenker, C.; Almairac, R.; Ayroles, R.; Roucau, C. *Philos. Mag. B*, **1984**, *50*, 321.
(106) Greenblatt, M.; Ramanujachary, K. V.; McCarroll, W. H.; Neifeld, R.; Waszczak, J. V. *J. Solid State Chem.* **1985**, *59*, 149.
(107) Whangbo, M.-H.; Canadell, E.; Schlenker, C. *J. Am. Chem. Soc.* **1987**, *109*, 6308.
(108) Whangbo, M.-H.; Canadell, E.; Foury, P.; Pouget, J. P. *Science* **1991**, *252*, 96.
(109) (a) Brohan, L. Ph.D. Thesis, Université de Nantes, 1986. (b) Brohan, L.; Marchand, R.; Tournoux, M. *J. Solid State Chem.* **1988**, *72*, 145.
(110) Colaitis, D.; Coene, W.; Amelinckx, S.; Brohan, L.; Marchand, R. *J. Solid State Chem.* **1988**, *75*, 156.
(111) Evain, M.; Whangbo, M.-H.; Brohan, L.; Marchand, R. *Inorg. Chem.* **1990**, *29*, 1413.
(112) (a) McCarroll, W. H.; Greenblatt, M. *J. Solid State Chem.* **1984**, *54*, 282. (b) Strobel, P.; Greenblatt, M. *J. Solid State Chem.* **1981**, *36*, 331. (c) Nair, K. R.; Wang, E.; Greenblatt, M. *J. Solid State Chem.* **1984**, *55*, 193. (d) Reau, J. M.; Fouassier, C.; Hagenmuller, P. *J. Solid State Chem.* **1970**, *1*, 326.
(113) Collins, B. T.; Ramanujachary, K. V.; Greenblatt, M.; McCarroll, W. H.; McNally, P.; Waszczak, J. V. *J. Solid State Chem.* **1988**, *76*, 319.
(114) Canadell, E.; Whangbo, M.-H. *Inorg. Chem.* **1988**, *27*, 228.